U N I V E R S I T Y O F S P L I T

FACULTY OF ELECTRICAL ENGINEERING, MECHANICAL ENGINEERING AND NAVAL ARCHITECTURE

DOCTORAL THESIS

STOCHASTIC-DETERMINISTIC MODELING OF THE THERMAL RESPONSE OF THE HUMAN BODY EXPOSED TO HIGH FREQUENCY RADIATION

Enida Cero Dinarević

Split, 2024.

U N I V E R S I T Y O F S P L I T

FACULTY OF ELECTRICAL ENGINEERING, MECHANICAL ENGINEERING AND NAVAL ARCHITECTURE

DOCTORAL THESIS

STOCHASTIC-DETERMINISTIC MODELING OF THE THERMAL RESPONSE OF THE HUMAN BODY EXPOSED TO HIGH FREQUENCY RADIATION

Enida Cero Dinarević

Split, 2024.

The research reported in this thesis was carried out at Department of Electronics and Computing, University of Split, Faculty of Electrical Engineering, Mechanical Engineering and Naval Architecture.

Supervisor: Prof. dr. sc. Dragan Poljak, University of Split, Faculty of Electrical Engineering, Mechanical Engineering and Naval Architecture, Croatia

Dissertation number:

BIBLIOGRAPHIC INFORMATION

Keywords: analytical approach, vertical dipole antenna, half space, electric field, internal field dosimetry, specific absorption, simple body models, parallelepiped, cylinder, thermal field modelling, stochastic analysis, steady-state, uncertainty quantification, stochastic collocation.

Scientific area: Technical sciences

Scientific field: Electrical engineering

Scientific branch: Electronics

Institution of PhD completion: Faculty of Electrical Engineering, Mechanical Engineering and Naval Architecture, Split

Supervisor of the thesis: Prof. dr.sc. Dragan Poljak

Number of pages: 168

Number of figures: 75

Number of tables: 9

Number of references: 160

Stochastic-deterministic modelling of the thermal response of the human body exposed to high frequency radiation

Abstract:

New generation of communication systems require the use of a frequency band above 3 GHz and below 6 GHz for fast data transmission over short distances with Line of Sight (LOS) and transmission with minimal refraction. One of the biggest obstacles for implementation of 5G systems from 2020. to 2025. is related to the potential effects of electromagnetic fields generated by 5G systems, but it is clear that the effects are thermal in nature. One of the simplest scenarios to assess the human exposure to high frequency radiation is the human body exposed to the field radiated by thin wire antennas. Even with the sophisticated new technologies coming along, a simple body model exposed to dipole antenna radiation is of interest for quick dosimetry procedures, aiming to get a rapid estimation of the phenomena.

The analysis of the radiation of the vertical dipole antenna requires numerical solution of the Pocklington equation, and with a known current distribution along the wire, the radiated electric field, and other dosimetric quantities can be determined. This process is demanding in terms of computer memory and calculation time, which is a problem if we want a fast dosimetric procedure.

The basic assumption of the doctoral thesis is that the application of the assumed current distribution along the vertical electric dipole antenna enables the determination of the values of E field close to the actual values. In this way, the numerical solution of Pocklington's integro-differential equation is avoided, thus reducing computer resources without significant loss of accuracy. Furthermore, the next assumption that enables the analytical solution of the radiated electric field is the use of the Fresnel refraction coefficient which is related to the first term in the asymptotic expansion of the Sommerfeld integrals, which additionally saves calculation time.

For the second step, i.e. internal dosimetry, an assumption is made about the use of a simple human model (parallelepiped or cylinder) positioned in the far field zone. Taking into account the maximum value of the field on the surface of the parallelepiped or cylinder and the transmission coefficient resulting from the Modified Image Theory (MIT) approach, the corresponding dosimetric quantities of interest can be quickly determined.

Finally, in the third step, the use of analytical methods enables a quick determination of the thermal response in parallelepiped human body model. Taking into account the maximum value of the field on the surface of the parallelepiped human body, a stationary solution of the Pennes' equation for temperature increase is calculated, assuming a

constant amount of power density in the tissue and assuming that the power density exponentially decays with the tissue depth. A homogeneous single-layer and 3-layer geometry of parallelepiped human body is used.

In fourth step stochastic-deterministic modelling of thermal response was performed. Stochastic-deterministic modelling takes into account the uncertainty of input parameters in thermal dosimetry analysis. In order to assess the influence of each of the input parameters (which become random variables) on the output variable of interest, a sensitivity analysis is performed.

The described, fully analytically solvable and simple, stochastic-deterministic model consisting of a vertical dipole antenna of finite length and of a simple model of the human body significantly saves computer resources, so the model can be used for rapid dosimetry of human exposure to radiation from new communication systems in the lower part of the frequency range.

Keywords:

analytical approach, vertical electric dipole, half space, electric field, internal field dosimetry, specific absorption, simple body model, parallelepiped, cylinder, thermal field modelling, stochastic analysis, steady-state, uncertainty quantification, stochastic collocation;

Stohastičko-determinističko modeliranje toplinskog odziva ljudskog tijela izloženog zračenju visokih frekvencija

Sažetak:

Komunikacijski sustavi novih generacija zahtijevaju uporabu frekvencijskog pojasa ispod 6 GHz i iznad 3 GHz za brzi prijenos podataka na kratkim udaljenostima uz postojanje linije vidljivosti (engl. *Line of Sight*, skraćeno LOS) i prenos s minimalnom refrakcijom. Jedna od najvećih prepreka za implementaciju 5G sustava od 2020. do 2025. odnosi se na potencijalne učinke EM polja koje generiraju 5G sustavi, ali je poznato da su oni u prirodi toplinski. Jedan od najjednostavnijih scenarija za procjenu izloženosti ljudi EM zračenju je ljudsko tijelo izloženo zračenju tankih žičanih antena. Čak i sa sofisticiranim novim tehnologijama koje dolaze, jednostavan model tijela izložen zračenju dipolne antene je zanimljiv za brze procjene i jednostavnije postupke dozimetrije.

Analiza zračenja vertikalne dipol antene zahtijeva riješavanje Poklinkton-ove jednadžbe numerički, a zatim uz poznatu struju izračeno električno polje, i ostale dozimetrijske veličine također se određuju numeričkim metodama. Ovaj proces je zahtijevan u smislu memorije računala ali i vremena računanja, što predstavlja problem ako želimo brz dozimetrijski postupak.

Temeljna pretpostavka doktorskog istraživanja je da primjena pretpostavljene raspodjele struje duž vertiklalno pozicionirane dipol antene omogućava određivanje izračenog E polja bliskog stvarnim vrijednostima. Na ovaj način izbjegava se numeričko rješavanje Pocklington-ove integro- diferencijalne jednadžbe, čime se smanjuju računarski resursi bez značajnog gubitka točnosti. Nadalje, sljedeća pretpostavka koja omogućuje analitičko rješenje izračenog električkog polja je upotreba Fresnel-ovog koeficijenata refleksije (engl. *Fresnel Refraction Coefficient*, skraćeno RCM) koja je povezana je s prvim članom u asimptotskoj ekspanziji Sommerfeld-ovih integrala, što dodatno štedi vrijeme računanja.

Za drugi korak, odnosno unutarnju dozimetriju, uvodi se pretpostvka o upotrebi jednostavnog ljudskog modela (kvadra ili cilindra) pozicioniranog u zoni dalekog polja. Uzimajući u obzir maksimalnu vrijednost polja na površini kvadra ili cilindra i koeficijent prijenosa koji proizlazi iz MIT pristupa mogu se brzo odrediti odgovarajuće veličine od interesa.

Konačno, u trećem koraku, upotreba analitičkih metoda omogućava brzo određivanje toplinskog odziva. Uzimajući u obzir maksimalnu vrijednost polja na površini kvadra, traži se stacionarno rješenje Pennesove jednadžbe za temperaturni prirast pretpostavljajući konstantan iznos gustoće snage te pretpostavljajući da gustoća snage eksponencijalno opada po dubini tkiva. Za toplinski model koristi se homogeni i višeslojni kvadar.

U četvrtom koraku proveden je postupak stohastičkog modeliranja toplinskog odziva. Njime se uzima u obzir nesigurnost ulaznih parametara u analizi toplinske dozimetrije. U svrhu procjene utjecaja svakog od ulaznih parametara (koji postaju slučajne varijable) na izlaznu veličinu od interesa provodi se analiza osjetljivosti.

Opisani, u potpunosti analitički riješiv i jednostavan, stohastičko-deterministički model koji se sastoji od dipol antene konačne duljine jednostavnog modela ljudskog tijela, značajno štedi računalne resurse, pa model može poslužiti za brzu dozimetriju izloženosti ljudi zračenju novih komunikacijskih sustava u nižem dijelu frekvencijskog raspona.

Ključne riječi:

analitički pristup, vertikalna dipolna antena, poluprostor, električno polje, dozimetrija unutarnjeg polja, specifična apsorpcija, jednostavni modeli tijela, paralelopiped, cilindar, modeliranje toplinskog polja, stohastička analiza, stacionarno stanje, kvantifikacija nesigurnosti, stohastička kolokacija;

Acknowledgments

First, foremost, and forever, thanks God Almighty. Thanks for blessing me much more than I deserve, thanks for everything.

Professor Dragan Poljak, thank you for this extraordinary trip. You have enriched my life with beautiful human and professional values. I can't thank you enough!

Many thanks go to co-authors of papers Professor Vicko Dorić.

Professor Dorić, it was honour to work with you.

I would like to thank prof. Zoran Blažević, Zvonimir Šipuš, Maja Škiljo, and Mario Cvetković, and– not only for their time and patience, but for their intellectual contributions to my development as a scientist. I consider Your feedback as valuable input for future work.

To my Family,

Mama i babo hvala Vam što ste baš vi moji roditelji.

Mirza, ponosna sam na naše partnertsvo. Hvala ti što si tu.

Enzo, hvala ti na ljubavi i prijateljstvu.

„Nothing in this world is to be feared … only understood. “

Marie Curie

“He who has led you so far will guide you further.”

Rumi

Contents

List of Figures

List of Tables

List of Abbreviations

Fifth Generation Networks	5G
ANalysis Of VAriance	ANOVA
American National Standards Institute	ANSI
Absorbed Power Density	*APD*
Boundary Condition	BC
Boundary Element Method	BEM
Basic Restriction	BR
Computer Aided Design	CAD
Computational Electromagnetics	CEM
DeoxyriboNucleic Acid	DNA
Electric Field Integral Equation	EFIE
Electromagnetic	EM
Finite Difference Method	FDM
Finite-Difference Time-Domain	FDTD
Finite Element Method	FEM
Finite Integration Technique	FIT
Galerkin-Bubnov Indirect Boundary Element Method	GB-IBEM
generalized Polynomial Chaos	gPC
High Frequency	*HF*
International Commission on Non-Ionizing Radiation Protection	ICNIRP
Committee on Electromagnetic Safety of the Institute of Electrical and Electronics Engineers	IEEE
Incident Power Density	*IPD*
Low Frequency	*LF*
Monte Carlo	MC
Medium Frequency	*MF*
Very HF	*VHF*
Ultra HF	*UHF*
Modified Image Theory	MIT
Method based on modified PBHE	MPBH
National Council on Radiation Protection and Measurements	NCRP
Numeric Electromagnetic Code	NEC
One-at-a-Time	OAT
Pennes' Bio-Heat transfer Equitation	PBHE
Partial Differential Equation	PDE
Perfectly Electric Conducting	PEC
Radio Frequency	*RF*
Reference Levels	RL
Random Variable	RV

Specific Absorption Rate	*SAR*
Stochastic Collocation	SC
Separation of Variables	SoV
Saddle Point Method	SPM
Thin Wire Approximation	TWA
Transmitted Power Density	*TPD*
Uncertainty Propagation	UP
Uncertainty Quantification	UQ
Vertical Electric Dipole	VED
Variational Iteration Method	VIM
Very LF	VLF
Volume Power Density	*VPD*

Biography

Enida Cero Dinarević was born in Konjic on March 29, 1990. She studied at the University of Sarajevo, and got Bachelor degree (2008-2011) and Master degree (2011-2013) in Electrical Engineering – department for Telecommunication. Obtained honors and awards include the best student of gymnasium – Ju "Srednja škola" Konjic (2008), Praise for the outstanding success achieved during studies at the Faculty of Electrical Engineering in Sarajevo, Department of Telecommunications (2011)– Silver badge of the University of Sarajevo (2013), and the best paper award - IFMBE Clinical Engineering Division and Global Clinical Engineering Alliance Awards (2021).

Her employment experience included the American University in Sarajevo, Codding Giants School for programing, and BH Telecom. As part of work expirence in BH Telecom she participates in the testing of IT and communication equipment and solutions, in the monitoring of standards and recommendations, in cooperation with higher education and scientific institutions and organizations, cooperation with other companies in terms of development and testing of new technological solutions and services, and preparation of procedures and instructions related to service tasks and other tasks in accordance with the order of the immediate manager, and participates in innovation support activities. Enida has teaching experience in topics: web technologies, fundamentals of programming, java artificial Intelligence, machine learning, communication networks, number systems, binary logic and information literacy.

Her special fields of interest include IoT (applications, design, protocols), Sensor networks 5G related topics, Biomedical Engineering, and Human Interactions with Electromagnetic fields.

CHAPTER 1

Introduction

1.1 Motivation

Electromagnetic (EM) fields are emitted by many human and natural sources daily, and the introduction of new frequencies and new technologies, such as in Fifth Generation (5G) networks, affects human exposure to these systems. More than 3 billion people are exposed to the influence of EM fields worldwide on a daily basis [1], and generations of new mobile technology require new methods for human exposure to EM fields analysis [2]. Considering the upcoming implementation of the 5G system, and the fear of the potential harmful effects of these systems on the overall health, the importance of electromagnetic-thermal dosimetry has increased significantly.

Various organizations have proposed guidelines for limiting exposure to EM field, and the most commonly used are defined by the International Commission on Non-Ionizing Radiation Protection (ICNIRP) [3] and Committee on Electromagnetic Safety of the Institute of Electrical and Electronics Engineers (IEEE) [4]. Guidelines are given in terms of Basic Restriction (BR) and/or Reference Levels (RL). BR are exposure indices inside the body that must not be exceeded, and the specification depends on the operating frequency. BRs must be respected when implementing the system, while compliance with RL does not mean that BRs are also respected.

Since BRs are frequency dependent, it is worth to mention that 5G systems use two main frequency bands: the frequency band below 6 GHz (Frequency Range 1, FR1) and the millimetre wave band (Frequency Range 2, FR2) [5]. The advantage of transmission below 6 GHz is the balance of capacity and coverage [5]. The SAR [4] is the BR defined for the high frequency (HF) area (FR1), and it is specified in terms of the maximum whole-body average SAR (SAR_{WB}) and peak spatial average SAR [3]. Above 6 GHz (FR2) EM fields are absorbed at the body surface, and exposure is described in terms of RLs for maximum externally applied electric and magnetic field strength, and in terms of power density. For local exposure to frequencies higher than 6 GHz, related to the temperature increase in the surface layer, the use of Absorbed Power Density (APD) is recommended in [6].

In FR1 and FR2, the dominant effect of excessive exposure to EM fields is tissue heating, with adverse effects occurring when the temperature is elevated between 1-2 ℃ [7]. A

SAR_{WB} value bellow 0.4 $\frac{W}{kg}$ is considered safe for professional exposure, and a value bellow 0.08 $\frac{W}{kg}$ is considered safe for public exposure [3]. Due to the different thermoregulatory properties of different tissues in the human body, the peak limits for spatially averaged SAR (1 g or 10 g, cubed) for exposure in controlled environments are 20 $\frac{W}{kg}$ for limbs and 8 $\frac{W}{kg}$ for head, neck and trunk. For exposure in uncontrolled environments, the peak limits of spatially averaged SAR are 4.0 $\frac{W}{kg}$ for limbs and 1.6 $\frac{W}{kg}$ for head, neck and trunk [4].

Electromagnetic dosimetry procedures provide the quantification of the energy absorbed by the human body or its part exposed to HF EM fields. The assessment of dosimetric quantities is based on theoretical or experimental techniques, and involves three steps: incident field dosimetry, internal field dosimetry and the thermal dosimetry.

The first step is the assessment of the distribution of the incident EM field (external field in the absence of the human body) which induces EM field inside the body (internal field). The field interaction with the human body depends on the ratio of wavelength to body size (human height at the resonance frequency is approximately 0.4 wavelengths of radio frequency (RF) waves in free space [8]), and in FR1 and FR2 the absorption is at the surface. Induced currents and fields can lead to thermal and non-thermal effects in general, and in the HF region thermal effects are dominant. Since the basic dosimetric quantity in FR1 is SAR, and direct experimental measurements of the thermal response in healthy humans are not possible, many computational studies aim to link SAR and temperature rise in the human body. Temperature elevation leads to third step in dosimetry also called thermal dosimetry usually based on the model proposed by Pennes' and related numerical simulation method.

On the other hand, analytical solutions are very interesting due to the simplicity and speed in the calculation of dosimetric quantities compared to experimental and numerical calculations [9-12]. Therefore, simplifications of EM problems providing a faster assessment and analytical solution are always welcome. Analytical solutions can be validated through comparison with numerical methods or measurements if possible.

Various antenna systems are the usual electromagnetic interference (EMI) sources. Ever since the beginning of the 19th century, vertical dipole antennas have been used in various applications in the field of wireless communications [13]. The need for interference reduction in the frequency band below 6 GHz in 5G systems, requires RF network implementation with a large number of small cells, and base stations equipped with small and directional antennas [14], such as a vertical electric dipole (VED). The simplest approach for EM modelling of VED radiation is the approximation of free space in which only the direct ray is considered, ignoring the field components reflected from surrounding objects. Such approach is presented in [15, 16]. On the other hand, neglecting the reflected

components can significantly reduce the calculated value of the irradiated electric field compared to the real-life scenarios. Therefore, to improve the accuracy of the calculation, the antenna is placed above the ground with losses, which is formulated in terms of Sommerfeld integrals. The traditional solution of Sommerfeld problem deals with Hertz potentials, which cannot be solved analytically without a set of approximations.

Analytically based internal field dosimetry can provide a satisfactory level of accuracy under certain conditions, which makes it attractive for engineering applications. In addition to simplicity and speed, these models provide relatively accurate results for the magnitude of the internal electric field even when canonical models of the human body are used.

As is the case with incident and internal EM field dosimetry procedures, thermal dosimetry procedures can be performed both analytically and numerically. Traditionally, numerical methods are used when analytical solutions are not available, while analytical methods are preferred because they are simple and fast [9]. Furthermore, analytical methods can also be used for benchmarking.

Computational models used to describe the interaction of EM and thermal fields are mostly deterministic in nature and thus provide results for a specific set of input parameters. As measurements in vivo are not possible there is an inherent uncertainty in the input data set [17]. This problem can be overcome by using stochastic modelling.

1.2 Scientific method and contribution

The goal of the research is to develop a simplified analytical deterministic-stochastic model for rapid assessment of thermal response of the human body due to exposure to external fields. The model consists of a VED placed at a height h above the real ground and a human body modelled in the form of a parallelepiped or cylinder. Note that VED could be considered as a simple representation of base station antenna. Plane wave exposure is assumed, and complete dosimetric procedure includes 3 steps: incident field dosimetry, internal field dosimetry and thermal dosimetry.

Within the incident field dosimetry, the electric field irradiated by finite-length dipole antenna at any point of the upper half-space is obtained, using a rigorous numerical approach, an approximate numerical approach with an assumed current distribution, and an analytical approach.

The irradiated electric field of a finite-length VED at any point of the upper half-space, is usually calculated numerically. The current distribution along the antenna is obtained by numerically solving the Pocklington equation. In this thesis such approach is referred as a rigorous numerical approach due to the minimum number of used approximations. If the

current distribution along the wire can be approximated by analytical expressions, including trigonometric functions, as in [18, 19], solving the Pocklington equation can be avoided without significant loss of accuracy. If the current distribution is assumed and field integrals are solved numerically the approach is refered as an approximate numerical approach with an assumed current distribution. If the current distribution is assumed and field integrals are solved analytically the approach is refered as an analytical approach with an assumed current distribution. In this thesis, within the framework of certain conditions, a sinusoidal or triangular current distribution, respectively, along the wire is assumed.

The results for the irradiated field in case of rigorous numerical approach, are obtained using the Numeric Electromagnetic Code (NEC) [20]. Having solved the Pocklington integral equation, numerical solution of the field integrals are performed. Within the framework of the thesis, for approximate numerical approach with assumed current distribution, a procedure for numerical solution of the field integral is developed. Comparison of the results for the irradiated electric fields obtained for rigorous numerical approach and the approximate numerical approach with assumed current distribution and for different values of the model parameters, allows to define the conditions in which the approximate approach can be applied. When used in proper conditions, approximate numerical approach with assumed current distribution reduces computational costs. Both models give similar results when the vertical dipole antenna is electrically short ($L \leq \frac{\lambda}{10}$) and when the ratio of the height of the antenna above the ground and wavelength satisfies $h \geq 10\lambda$. The results obtained on the basis of the previous two approaches are also valid in the near field, which means that they include the terms $\frac{1}{R^2}$ and $\frac{1}{R^3}$.

The analytical solution is based on the far-field approximation (only term which contains $\frac{1}{R}$ dependence is used). By comparing the results for all three approaches, an additional limitation is imposed. Namely, when the distance in the horizontal direction is above 60 m these three models agree satisfactorily. For small distances in the horizontal direction (x < 40 m), due to the far field approximation used in proposed analytical approach, the significant overestimation of the field values could be observed.

In the second step, the induced electric field, SAR and the TPD in the human body exposed to VED radiation are obtained. Two simple body models are considered: the parallelepiped human body model and the cylindrical human body model. In parallelepiped incident field decreases exponentially with tissue depth. On the other hand, the cylindrical model is based on solving Pocklington's integro-differential equation for the so-called thick wire, which is solved by applying the general expression for the total axial current in the form of the sum of sine functions. The procedure for determining the coefficient of sine functions in the general expression for the axial current distribution is represented in detail in [21]. The coefficients are expressed through integrals that are

calculated numerically, which makes cylindrical model difficult to apply in stochastic-deterministic thermal modelling.

The difference between the SAR_{WB} obtained in parallelepiped and cylindrical human body models in the x horizontal direction is less than 10 % at 80 m away from source VED antenna. A parallelepiped human body model can further simplify the internal dosimetry and further save computational cost, specifically if thermal dosimetry is of interest.

In thermal dosimetry, the stationary Pennes' equation of heat transfer in biological tissues is considered. The disadvantage of this approach is that it does not take into account time dependence, but the simplicity of the mathematical expression facilitates parametric analysis [102] and provides simpler analysis in multi-layer tissue modelling, since the internal structure of the skin plays a very important role in realistic calculation of temperature elevation in human body [22].

Within the framework of the thesis, a planar multi-layer human body model (skin-fat-muscle) is used. To solve the Pennes' Bio-Heat transfer Equation (PBHE) analytically, power density from external heat source related to the absorbed EM energy irradiated from VED antenna, is assumed to either be constant, or exponentially decreasing with the tissue depth. These two models are created under the assumption that the tissue is homogeneous and isotropic, that the properties of the tissue are temperature independent, that the heat generated by metabolism is constant, that the blood perfusion rate is spatially and temporally uniform and independent of the tissue temperature, and that arterial blood temperature is constant [23].

The PBHE can be solved by first reducing the number of parameters in the parametric analysis, in such a way as to observe the state before exposure to the EM field, presented by the initial temperature, and then introducing a new variable related to the temperature change in the stationary state in relation to the state before exposure to the EM field, instead of observing the final temperature in the stationary state. The resulting modified equation describing heat transfer can be solved analytically for multi-layer media using the classical theory of ordinary differential equations. Within each layer, the temperature increase is described by the superposition of the solution of the homogeneous linear equation and the solution of the particular linear equation (constant variation method). The value of the constants in the general solution in each tissue layer can be determined using appropriate boundary conditions (BCs) at the boundaries of the two layers. The method of variation of the constants is rather suitable for linear systems, while it is more difficult to apply this approach to non-linear systems [24].

The impossibility of in-vivo measurement of thermal parameters is the cause of uncertainties in the set of input parameters, that is, in the set of corresponding input variables. Namely, the input variables then can be modelled as random variables (RVs) with a certain probability density function associated with them. In the simplest case, a

uniform distribution of the value of the RV around the mean can be assumed. For each set of input variables, the calculation is performed, giving one output quantity. Output values are presented in the form of stochastic values such as mean, variance, standard deviation and confidence interval. For this purpose, within the stochastic part of the thermal models, the uncertainty of input parameters is quantified using stochastic collocation (SC). The thermal conductivity and the thickness of the tissues in three layers (skin-fat-muscle) are chosen to be input RVs.

Furthermore, a sensitivity analysis of the corresponding input parameters is carried out. The purpose of sensitivity analysis is to observe the influence of individual and collective input variables on the output variable of interest. In other words, the sensitivity analysis allows the ranking of the input parameters according to the level of influence on the output value. A simple approach in sensitivity analysis is called "One-at-a-Time" (OAT), which studies the variances of a one-dimensional problem. Thus, only one variable at the input is changed, while the other variables are treated as constants. The main advantage of this method is the ability to quickly rank the variables according to the level of influence on the output value. However, the OAT method cannot provide information on the collective influence of two or more input variables on the output quantity and mutual interaction between input RVs. This shortcoming can be overcome using ANalysis Of VAriance (ANOVA). Sensitivity analysis, based on variance decomposition in which the variance of the model is split into members depending on the input factors and their mutual interactions, provides the calculation of sensitivity indices of the first and higher orders [25].

1.3 Thesis outline

The thesis is organized in seven chapters. Chapter 2 describes the interaction of HF fields with living material. First, short explanation of interaction mechanisms is given, followed by the main effect of EM fields in different frequency bands. Safety guidelines are further elaborated. Chapter 2 ends up with some general aspects in dosimetry.

In Chapter 3 incident dosimetry methods are explained. Source of EM fields is VED antenna above a lossy half space at height h. After presentation of incident field calculation, some simplification from literature needed for analytical solution of incident field calculation are introduced. The analytical approach to incident dosimetry developed as part of thesis is explained along with the results obtained. The results from Chapter 3 are necessary for the next step related to the internal dosimetry procedure.

Chapter 4 provides an analysis of internal EM dosimetry. Coupling between external and internal fields, followed by theoretical dosimetry basics and approaches to internal EM dosimetry is given. This chapter, presents analytical approaches and simple human body models, which provide closed form solution of internal dosimetric quantities.

Furthermore, analytical approach to internal EM dosimetry in parallelepiped and cylindrical human body is explained in detail, and the calculated results are compared.

Chapter 5 deals with the thermal dosimetry based on the PBHE. Analytical approach to thermal dosimetry from this study will be explained on single-layer muscle tissue and 3-layer human body composed of skin, fat and muscle.

In Chapter 6 deterministic stochastic thermal dosimetry is presented. Starting from explanation of need for stochastic-deterministic modelling, through uncertainty propagation (UP) to basic concept of sensitivity analysis. Then approach to stochastic-deterministic thermal dosimetry from proposed study is explained on 3-layer human body composed of skin, fat and muscle. Concluding remarks are given in Chapter 7.

CHAPTER 2

Interaction of high frequency fields with living material

2.1 Interaction mechanisms

The interaction of EM waves with humans depends on the properties of the incident wave, the environment and the human body. Interacting with the human body, one part of the EM wave is absorbed and the other part is reflected. The absorbed part of the incident wave is the trigger for the possible occurrence of any detectable, reversible or irreversible changes in the organism. Harmful effects on human's health are often accumulative in nature, and are closely related to the time of exposure as well as the radiation dose [7]. Although it is currently known that certain levels of EM fields have a harmful effect on humans, the impact of long-term exposure to levels significantly lower than the limit given in the guidelines [3], is still being investigated.

Energy absorption is appriciately frequency dependent. At low frequencies (LFs) the dominant effect of EM fields (EMFs) is stimulation of muscles, nerves and sensory organs [26]. In HF region wavelengths of EM waves are comparable to dimensions of the human organs, so tissue heating is dominant EM effect.

Assessment of the environmental impact and health implications of EM waves, quantitative description of the EM fields and power deposition in the tissues is required. The penetration or skin depth is considered as the depth of EM waves at which the amplitude of transmitted power density (TPD) is attenuated by a value of $\frac{1}{e^2}$ [27]. The intensity of EMFs in the human body decreases exponentially from the surface to the interior of the tissue, which can be mathematically expressed:

$$I(z) = I_0 \, e^{-\alpha z} \tag{2.1}$$

where

- I stands for electric field intensity or magnetic field intensity as a function of depth z $[\frac{V}{m}]$,
- I_0 is the electric field intensity or magnetic field intensity at the surface $[\frac{V}{m}]$, and
- α is the attenuation coefficient $\left[\frac{Np}{m}\right]$.

The penetration depth is a function the wave frequency, the strength of the field and the electrical and dielectric properties of the human body [27]. The penetration depth is smaller at higher frequencies, i.e. inversely proportional to the frequency of the incident wave. The higher the frequency of the EMF the stronger the absorption at the human body surface, therefore the higher the frequency the shorter the distance the field can penetrate into the human body.

Dielectric and electrical properties play an important role in determining the energy deposition and hence, temperature elevation in biological matter. They depend of the composition of the tissues in the human body, and the amount of water in the tissue is the most important factor. It is clear that in HF frequency region muscle, with a typical water content of 75 %, exhibits a much higher permittivity and conductivity than does fat (which typically has a water content of some 5 - 20 %) [28].

The dielectric properties of materials are obtained from their measured complex relative permittivity [29].

$$\varepsilon^*{}_r = \varepsilon'_r - j\varepsilon''_r \tag{2.2}$$

$$\varepsilon''_r = \frac{\sigma}{\omega\varepsilon_0} \tag{2.3}$$

where

- ε'_r is the relative permittivity of the material and,
- ε''_r is the out-of-phase loss factor,
- ε_0 is the vacuum permittivity $[\frac{F}{m}]$,
- σ is conductivity $[\frac{S}{m}]$, and
- ω is the angular frequency $[\frac{1}{s}]$.

The relative permittivity of a tissue decreases at high frequencies, and may reach values of up to 10^7 at frequencies below 100 Hz [29]. More details about theoretical aspects and the main findings in this subject are described in [28, 30, 31]. In addition to the relative permittivity, the conductivity also depends on the frequency and increases with increasing frequency [32].

2.2 Biological effects

Due to the use of a large number of electronic devices in everyday life, the human body is simultaneously exposed to radiation of EM waves of different frequencies. As the frequency of the EM energy spectrum changes from extremely low to Gamma rays, the effects of EMFs on humans also change [33] (Fig. 2.1).

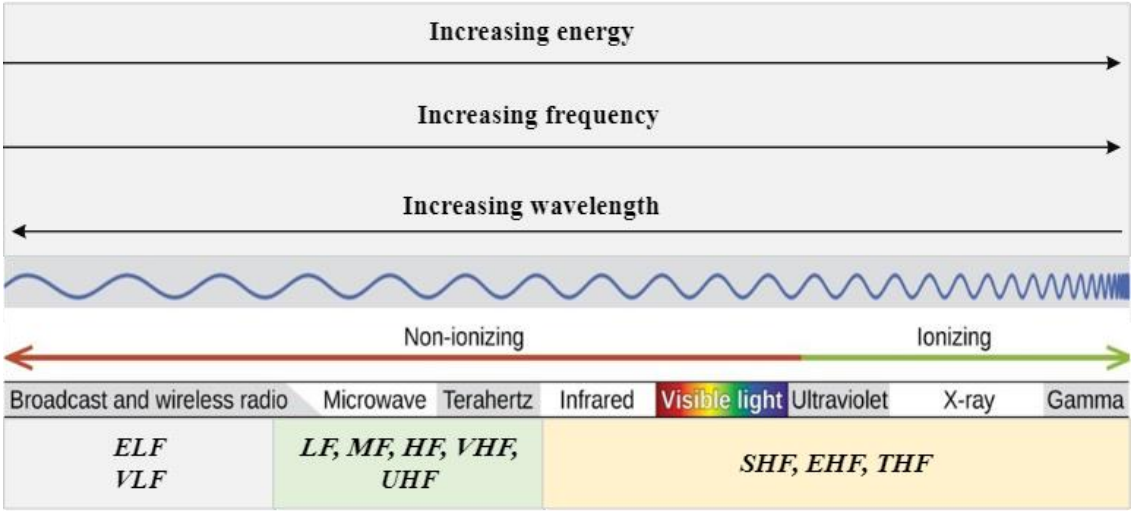

Figure 2.1 EMF effects vs frequency

Extreme LF (ELF) and Very LF (VLF) frequency band induce non-thermal effects, while LF, Medium Frequency (MF), HF, Very HF (VHF), Ultra HF (UHF) bends lead to heat generation (thermal effects) [33]. EMFs on aforementioned frequencies are classified as non-ionizing radiation.

Broadly, nonionizing field are categorized as low frequencies (LF), with frequencies $f < \sim 30$ kHz and high frequencies (HF) with frequencies $\sim 30\ \text{kHz} < f < \sim 300$ GHz. According to literature, LF fields may cause excitation of sensory, nerve and muscle cells [34]. Namely, in frequency range up to 10 MHz, time-varying electric and magnetic fields induce electric fields and currents inside the body, which cause stimulation of nerves and muscles [35].

HF fields are absorbed by the body, and the related heating effects are dominant [34]. Thermal effects are associated with the heat created by EMFs in a certain area, and it is possible that every interaction between HF fields and living tissues causes an energy transfer resulting in a temperature rise [1]. At frequencies above 100 MHz, absorption of EM energy results in an increase of body temperature, either general or local [35]. However, at frequencies above 10 GHz, the energy absorption is limited to the body surface [35].

At ultra violet, X-Ray and Gamma Rays frequencies ionizing radiation occurs, which may lead to different non-thermal effects, such as Deoxyribonucleic acid (DNA) damage,

cancer, mutation and birth defects [33].

The introduction of new technology, such as 5G recently, has led to public health concerns around the world. Two international organizations, ICNIRP and IEEE, have been addressing this issue for decades. The goal is to provide human exposure limits that many serve as a protection against established or substantiated adverse health effects, to be further explained in more detail below.

2.3 Safety guidelines

Various organizations have proposed guidelines for limiting exposure to EMFs for protection against all established adverse health effects. The most commonly used limits are defined by ICNIRP [3] and by IEEE [4]. Threshold levels are defined according to scientific and professional knowledge, which are often based on experimental research on phantoms, in which a harmful effect on the body is proven. At dosimetric levels with proven harmful consequences of EMFs, so-called safety factors (usually 2, 5, 10, or 50) are applied, depending on whether it is a whole-body exposure or a local exposure. Compared to occupational exposures, in the area of public, increased, and uncontrolled exposure, larger safety factors are applied [3].

Guidance are given in terms of BRs and/or RLs (Fig. 1.2). BRs are exposure indices within the body that should not be exceeded, and are specified in terms of non-measurable internal electric field [3] and the current density in LF range.

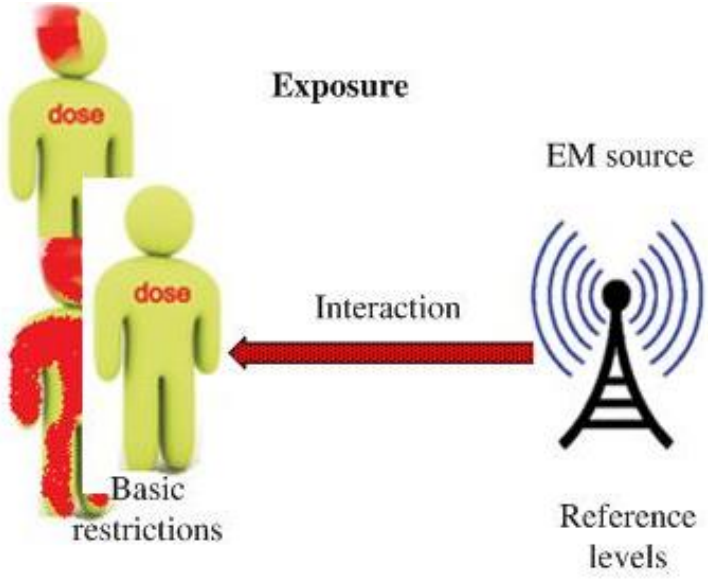

Figure 2.2 Quantities in the guidelines: BCs on the internal dose and RLs for the external exposure

The rate of RF energy absorption (SAR) [3] is the BR specified for HF range. Since measurements of the SAR or internal electric field strength are often difficult to perform, RLs for maximum human exposure to RF fields have also been specified. The RLs are specified in terms of unperturbed, externally applied electric and magnetic field strength, power density and in terms of electric currents in the body occurring from either induction or contact with energized metallic objects.

While compliance with the BRs is required, non-compliance with the RLs does not necessarily mean that the BRs are exceeded. In such cases, additional measurements or calculations may be required to assess compliance. Further on, BRs are mainly addressed, but additional information about RLs are offered in [3].

BRs are frequency dependent dosimetric quantities. For 3 kHz – 10 MHz frequency range BRs for the avoidance of non-thermal effects are specified in terms of maximum internal electric field strength within the body [3]. In the frequency range from 100 kHz to 300 GHz tissue heating must be restricted. Bellow 6 GHz limits are given in terms of specific energy absorption rate or maximum $\mathrm{SAR_{WB}}$ and peak spatially-averaged SAR (averaged over a small cubical volume) [3]. Above 6 GHz, EMFs are absorbed dominantly on the surface, and expressed in terms of RLs for maximum unperturbed, externally applied electric and magnetic-field strengths and in terms of power density.

In the frequency range $100\,\mathrm{kHz} < f < 6\,\mathrm{GHz}$, exposure longer than $t > 1\,\mathrm{h}$ with average $SAR_{WB} \sim 6\ \frac{\mathrm{W}}{\mathrm{kg}}$ is causes a core body temperature change of ~1 ℃ [3]. Adverse health effects (effect of vasodilation) may appear when body core temperature elevation is between 1-2 ℃ [7], while thermoregulatory changes in skin appear for local increases in skin temperature between 1-2 ℃. With the incorporation of the safety factor, a whole human body average SAR of 0.4 $\frac{\mathrm{W}}{\mathrm{kg}}$has been chosen as the restriction that provides adequate protection for occupational exposure [3]. An additional safety factor of 5 is introduced for public exposure, giving an whole human body average SAR limit of 0.08 $\frac{\mathrm{W}}{\mathrm{kg}}$ [3].

Due to the different thermoregulatory properties of different tissues in the human body, peak spatially-averaged SAR limits (1 g or 10 g, in the shape of a cube) for exposures in controlled environments are 20 $\frac{\mathrm{W}}{\mathrm{kg}}$ for the limbs and 8 $\frac{\mathrm{W}}{\mathrm{kg}}$ for the head, neck and trunk. For exposures in uncontrolled environments, the peak spatially-averaged SAR limits are 4 $\frac{\mathrm{W}}{\mathrm{kg}}$ for the limbs and 1.6 $\frac{\mathrm{W}}{\mathrm{kg}}$ for the head, neck and trunk [4].

Calculated dosimetric quantities are compared with BRs, to ensure that they are not exceeded. Some general dosimetry aspects in calculating dosimetric quantities are discussed in next section of this chapter.

2.4 Dosimetry – general aspects

Dosimetry relies on theoretical or experimental techniques, and as already mentioned, is carried out in three steps: incident field dosimetry, internal field dosimetry and thermal field dosimetry. By the definition, electromagnetic dosimetry represents the quantification of energy absorbed by the body or its part exposed to HF EMFs, where the first step is the evaluation of external EM field distribution necessary for the assessment of internal fields.

Antennas are most commonly EMI sources. Of particular interest are thin wire antennas. Various models of different antenna systems are used, such as: Norton model short VED at the surface of the earth [36], Wait model for line current source above the ground [37], King model for VED at height d in air [38, 39], Kurniawan and Wood model [18], analytical model for broadband Power line communication (PLC) by Chaaban, Drissi, and Poljak [19], Parise model for EMF of an overhead line current source [40], and Nazari asymptotic solution for the EM scattering of a VED over plasmonic and non-plasmonic half-spaces [41]. According to the differential and integral formulation of the problem, respectively, domain, boundary or source simulation, numerical methods can be used [17].

Furthermore, the distribution of the induced field strongly depends on various parameters, such as source (strength, frequency, polarization, direction of incidence, size, shape, etc.), distance and location of the source with respect to the body, outer anatomy, inner anatomy, body posture, and environment of the body (e.g. reflective objects). For the application of analytical approaches in internal field dosimetry simplified human body models are necessary. The most commonly used simplified models of the human body are the spherical, parallelepiped and cylindrical models. Main featured of of analytical methods are mathematical simplicity and low computational cost. Since, human body is complex in geometrical sense and non-homogeneous in nature, more accurate results can be obtained with numerical methods. A more detailed representation of the human body is provided in numerical dosimetry with much higher computational cost.

As stated earlier, induced currents and fields may give rise to thermal and non-thermal effects, and in HF range thermal effects are dominant. The basic dosimetric quantity is SAR, and as direct experimental measurements of thermal response on healthy human subjects is not possible, many computational studies aim to relate SAR and temperature elevation in human body, which leads us to third step in dosimetry.

Third step in dosimetry is thermal field dosimetry where numerous models can be used to describe the process of heat exchange, but the model proposed by Pennes' is widely used. The analytical solution using the Laplace transform method, a method based on modified PBHE, method based on Bessel functions, the method based on Green's function and the method based on Separation of Variables (SoV) are often used in analysed literature. Even analytical methods are preferable in this step, some of the numerical approaches used to solve PBHE are Boundary Element Method (BEM), the Finite Element Method (FEM),

the Finite Difference Method (FDM), the Dual Reciprocity BEM (DRMBEM), and the Monte Carlo (MC) method.

Research on the impact of EM radiation on the human body is based on the measurement of standardized dosimetric quantities and their comparison with defined limits. The dose of absorbed EMF energy is dependent of frequency. If the measured/calculated quantity is above the permissible limit, short-term/long-term effects of this exposure may occur. Even in the case of the mentioned effects, the studies are divided. Some have proven the existence of these effects, but the influence is mostly experimentally unconfirmed.

CHAPTER 3

Incident dosimetry methods for simple wire antennas

In this thesis EMI source of interest is VED. Analytical procedures for the assessment of the irradiated field by VED are presented in this chapter.

3.1 Vertical Electric Dipole

Less than a decade after Heinrich Hertz demonstrated, through a series of experiments, the existence and many of the properties of EM waves, Marconi explained their usage in applications of long-range wireless communication. Ever since the beginning of the 19th century, VED antennas have been used in various applications in the field of wireless communications [13]. The simplest approach for EM modelling of VED radiation is the approximation of free space in which only the direct beam of radiation is considered, ignoring the field components reflected from the substrate (soil) or surrounding objects. This approach is presented in [15, 16].

The waves that propagate along the surface of the earth differ from those that travel in free space. On the other hand, neglecting the reflected components can significantly reduce the calculated value of the irradiated electric field compared to the real-life scenarios. Therefore, to improve the accuracy of the calculation, the antenna is placed above the lossy ground which is formulated by means of Sommerfeld integra approach. The traditional solution of Sommerfeld problem uses Hertz potentials, which cannot be solved analytically without significant approximations.

The EM field generated by a VED was analytically studied extensively beginning with the classical work of Sommerfeld in 1908, and continuing in the work of many researches e.g. [42-46]. The solution of Sommerfeld problem is given in terms of Hertz potentials which are slowly convergent oscillatory integrals.

Fig. 3.1, shows a VED antenna of length L is placed in the air along the z-axis, above a lossy half-space at height h. The resulting field is the superposition of a direct field and earth-reflected field. VED antenna is assumed to satisfy the thin wire approximation, as in [47-49].

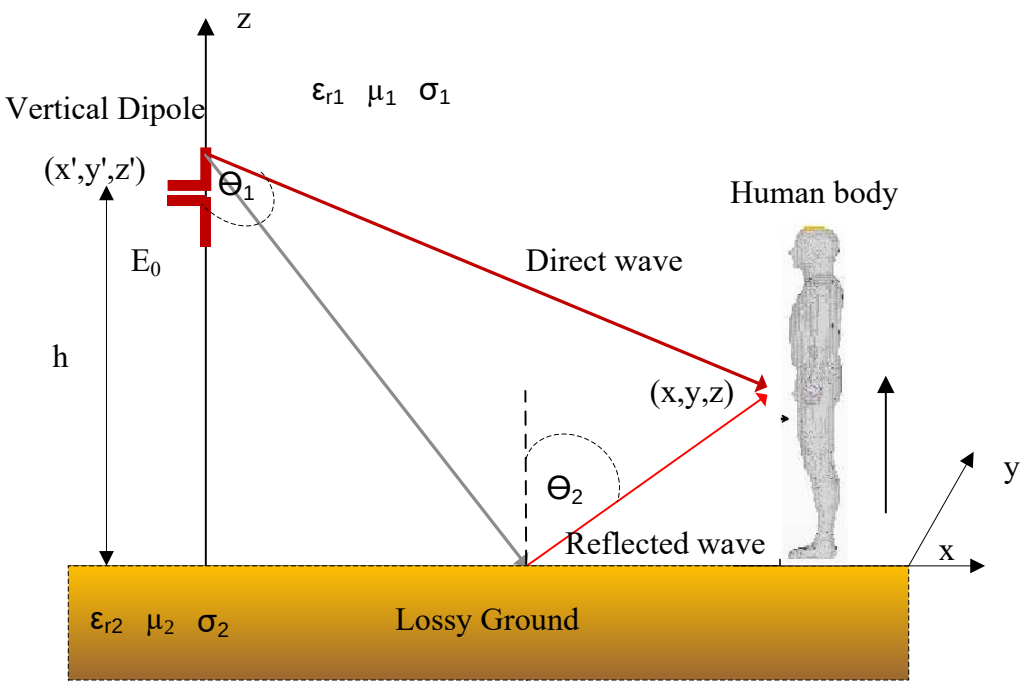

Figure 3.2 VED antenna above a lossy half space at height h

The thin wire approximation requires wire dimensions to satisfy the conditions [26]:

$$a \ll \lambda_0 \tag{3.1}$$

$$a \ll L \tag{3.2}$$

where

- λ_0 is the wavelength of a plane wave in free-space,
- a is the radius of the cross section of the wire, and
- L is wire length.

The antenna parameters depend on the current distribution along the wire, which is obtained as a solution of the Pocklinton integro-differential equation in the frequency domain. This equation is obtained from Maxwell's equations by expressing a time-harmonic electric field by means of a vector magnetic potential and electric scalar potential

$$\vec{E}^{sct} = -\nabla\varphi - j\omega\vec{A} \tag{3.3}$$

where

- $\vec{E}^{sct}$ is scattered electric field,

- φ the electric scalar potential, and
- $\vec{A}$ magnetic vector potential.

By combining (3.3) with the continuity equation for potentials given by.

$$\nabla\vec{A} = -j\omega\mu\varepsilon\varphi \tag{3.4}$$

and by adopting the Thin Wire Approximation (TWA) [48] the electric field in z-axis direction can be witten as:

$$E_z = \frac{1}{j\omega\mu\varepsilon_0}\left[\frac{\partial^2 A_z}{\partial z^2} + k_0^2 A_z\right] \tag{3.5}$$

where

- ω is the angular frequency $\left[\frac{1}{s}\right]$,
- $\mu_0 = 4\pi \times 10^{-7}$ is magnetic permeability $\left[\frac{H}{m}\right]$,
- ε_0=8.854×10^{-12} is the permittivity in free space or air $\left[\frac{F}{m}\right]$, and
- k_0 is air wave number.

The particular solution of the vector wave equation of the vector magnetic potential is

$$A_z = \frac{\mu}{4\pi}\int_{h-\frac{L}{2}}^{h+\frac{L}{2}} I(z')g(z,z')dz' \tag{3.6}$$

where

- $I(z')$ is the unknown axial current along the wire, and
- $g(z,z')$ is total Green function given as

$$g(z,z') = g_0(z,z') + R_{TM}g_i(z,z') \tag{3.7}$$

where

- $g_0(z,z')$ is the free space Green function, and
- $g_i(z,z')$ arises from MIT

$$g_0(z, z') = \frac{e^{-jk_0 R_0}}{R_0} \tag{3.8}$$

$$g_i(z, z') = \frac{e^{-jk_i R_i}}{R_i} \tag{3.9}$$

where

- R_0 denotes the distance from the source to the observation point,
- R_i denotes the distance from the source image to the observation point, and
- R_{TM} is the reflection coefficient for the transverse magnetic polarization.

The current distribution is governed by the Pocklington integro-differential equation which can be determined by applying continuity conditions for tangential to the wire field components on a Perfectly Electric Conducting (PEC) wire surface. The total electric field, composed from an incident and scattered field, respectively, disappears on the PEC wire [26]:

$$E_z^{inc} + E_z^{sct} = 0 \tag{3.10}$$

where

- E_z^{inc} is the tangential to the wire incident field $\left[\frac{V}{m}\right]$, and
- E_z^{sct} is the scattered field.

Now, combining (3.5), (3.6) and (3.10) yields the Pocklington integro-differential equations for the unknown wire current $I(z')$*:*

$$E_z^{inc} = -\frac{j}{\omega 4\pi\varepsilon_0}\left[\frac{\partial^2}{\partial z^2} + k_0^2\right]\int_{h-\frac{L}{2}}^{h+\frac{L}{2}} I(z')g(z, z')dz' \tag{3.11}$$

Provided that current distribution along the wire is known, assumed, or obtained as a solution of (3.11) the radiated field can be evaluated.

$$E_z^{sct} = \frac{1}{j4\pi\omega\varepsilon_0}\left[\frac{\partial^2}{\partial z^2} + k_0^2\right]\int_{h-\frac{L}{2}}^{h+\frac{L}{2}} I(z')g(z, z')dz' \tag{3.12}$$

Next subsection deals with the assessment of the irradiated field for VED antenna using some analytical procedures.

3.2 Incident dosimetry for Vertical Electric Dipole

Incident EMFs are defined as external fields in the absence of – i.e. without interaction with – the human body, animals, or tissue samples. Incident fields couple with the human body and induce EMFs and currents inside the body tissues. The induced fields are the only exposure parameters that can interact with biological processes and, therefore, provide the primary exposure metric [50].

One of the simplest scenarios to assess the human exposure to HF radiation is the human body exposed to the EMF radiated by thin wire antenna. Even with the new technologies coming along a simple human body model exposed to dipole antenna radiation is of interest for quick dosimetry procedures, aiming to get a rapid estimation of the phenomena. EM modelling of the radiation from VED antenna above a lossy half space usually points the problem towards solving rigorous integrals that represent the effect of the media interface. The traditional solution of the classical Sommerfeld problem uses Hertz potentials which cannot be evaluated in a closed form.

Generally, because Sommerfeld type integrals are with infinite limits, they are highly oscillatory, difficult to evaluate numerically [42] require intensive computational resources, and the accurate evaluation of Sommerfeld integral expressions is not a straightforward task.

As mentioned earlier the first step in calculating the electric and magnetic fields generated by wire antennas is to determine the current distribution along the wire. The current distribution along the wire is governed by electric field integral equation (EFIE) for thin wires, known as the Pocklington's integro-differential equation, whose numerical solution is demanding per se in a sense of accuracy, convergence and kernel quasi-singularity [51, 52]. Besides aforementioned analytical and numerical techniques, the problem of quantification of the interaction of EM waves within the exposed human body can also relay on experimental approaches.

As analytical methods offer simplicity, and reduce computational cost they are valuable tool in many applications of EM dosimetry. In the rest of this chapter review of simple analytical techniques for the assessment of VED radiated field is given.

3.2.1 Literature review

This subsection reviews some analytical techniques for the assessment of VEDradiated field. The work of Somerfield on the problem of radiation of VED antenna continued with work of Norton. Norton presented his model for short VED at the surface of the earth in the of 1930s [36]. On Sommerfeld EMF radiated by an infinitesimal VED located on the surface of the planar Earth, Norton introduced the attenuation function, the ground effect, and the frequency dependence of the surface wave.

Norton's formalism starts from the Hertz vector composed of a direct wave, a reflected wave (the sum is also called space wave) and the surface wave [36]. For small angles and short distances, the surface wave term must be used together with direct wave and reflected wave. As the distance increases, the direct wave and reflected wave are sufficient for the full description of the field behaviour.

In 1960s, Wait presented pure analytical model which was an important contribution since field expressions were derived through usage of the complex image theory. The only drawback of the obtained formulas is that they are valid in the quasi-static regime only, that is when the effects of the displacement currents in the air space are negligible [37]. These results were later used in numerous studies.

In the quasi near-field region, the field in the air due to the flow of currents induced in the ground can be described using a MIT. Namely, in this region, the distance from the radiating object is small compared to the wavelength, but large enough compared to the skin depth in the ground [16]. According to MIT, reflection coefficient is given as [16, 53]:

$$R_{MIT} = \frac{\varepsilon_{eff} - \varepsilon_0}{\varepsilon_{eff} + \varepsilon_0} \tag{3.13}$$

$$\varepsilon_{eff} = \varepsilon_r \varepsilon_0 - j\frac{\sigma}{\omega} \tag{3.14}$$

where

- ε_{eff} describes the effective permittivity $\left[\frac{F}{m}\right]$.

Therefore, the reflected and total electric field, respectively:

$$E_{MIT}^{R} = R_{MIT} * E_{MIT}^{Inc} \tag{3.15}$$

$$E_{MIT}^{Tot} = E_{MIT}^{Inc} + E_{MIT}^{R} \tag{3.16}$$

where

- E_{MIT}^{R} describes the reflected electric field component,
- E_{MIT}^{Inc} is a direct electric field component, and
- E_{MIT}^{Tot} is the total electric field.

In order to remove the restrictions for the application of the Norton and Wait models for the field of dipole over imperfectly conducting ground, King formulated a set of equations valid everywhere in the earth and on boundary when the dipole is in either

region, or at depth *d* in the earth. The conditions for applying the model are [38, 39].

$$|k_1^2| \gg k_2^2 \text{ or } |k_1| \geq 3k_2 \tag{3.17}$$

where

- $k_1 = \omega\sqrt{\left[\mu_0\left(\varepsilon_1 - j\frac{\sigma_1}{\omega}\right)\right]}$ is the wave number of lower half space, $z < 0$,
- μ_0 is vacuum permeability, and
- $k_2 = \omega\sqrt{\mu_0\varepsilon_0}$ is the wave numbers of upper half space (air), $z > 0$.

When the radial distance (ρ) is large compared the height (d) of dipole or height z of the observation point, King model uses phase approximations (3.18, 3.19 and 3.20) and amplitude approximations (3.22):

$$\rho^2 \gg (z-d)^2 \; \rho^2 \gg (z+d)^2 \tag{3.18}$$

$$r_1 \sim r_0 - d\cos(\theta) \tag{3.19}$$

$$r_2 \sim r_0 + d\cos(\theta) \tag{3.20}$$

$$r_0 = \sqrt{\rho^2 + z^2} \tag{3.21}$$

$$r_1 \sim r_2 \sim r_0 \tag{3.22}$$

In the beginning of 20th century Kurniawan and Wood presented the method which takes into account the heuristic simplification in calculation of near EMF. Simple closed-form analytical formulas of near fields from free space thin finite length dipole are multiplying with correction factors (c_s or c_{fl}), and the calculations are valid in lossy homogeneous medium [18]. Correction factors to compute the induced near electric field *E* are introduced heuristically:

$$c_s = \left|\frac{k_L}{k_h}\right| = \left[\frac{1}{\sin\left(\frac{|k_L|l_d}{2}\right)}\right] \tag{3.23}$$

$$c_{fl} = \begin{cases} \left|\frac{k_L}{k_h}\right| & \text{for } 0.75 < \left|\frac{k_L}{k_h}\right| < 0.95 \\ e^{-0.002\left|\frac{k_h}{k_L}\right|\frac{\lambda}{\rho}} & \text{for } \left|\frac{k_L}{k_h}\right| < 0.75 \\ 1 & \frac{k_L}{k_h} > 0.95 \end{cases} \tag{3.24}$$

where

- k_L is wavenumber for the insulator (that accounts for the lossy dielectric medium surrounding antenna),
- k_h is the wavenumber of ambient lossy dielectric medium,
- l_d is the dipole length,
- λ is wavelength, and
- ρ is radial distance.

Chaaban, Drissi, and Poljak [19] presented an analytical model for broadband Power line communication (PLC). The mathematical model for EMF calculation is based on integral equitation formulation in frequency domain, and approach assumed spatial current distribution. The PLC line is segmented into an infinite number of elementary dipoles (with positions at the point $M_0\ (0,0,Z_0)$ through which the current $I_{M_0}(s,Z_0)$ flows. Radial to the wire and tangential to the wire electric field components accompanied by an azimuthally component of the magnetic field expressed in terms of axially dependent magnetic vector potential:

$$E_z = -\frac{j\omega}{\beta_0^2}\left(\frac{\partial^2 A_z}{\partial z^2} + \beta_0^2 A_z\right) \tag{3.25}$$

$$E_\rho = -\frac{j\omega}{\beta_0^2}\frac{\partial^2 A_z}{\partial \rho\, \partial z} \tag{3.26}$$

$$H_\varphi = -\frac{1}{\mu_0}\frac{\partial A_z}{\partial \rho} \tag{3.27}$$

$$\overrightarrow{A_z(p)} = \frac{\mu_0}{4\pi}\int_0^L I(p,z)\frac{e^{-\gamma_0 R(z)}}{R(z)}\,dz\overrightarrow{e_z} \tag{3.28}$$

where

- $I(s,z_0)$ is the current distribution along the conductor, and
- $R(z) = \sqrt{\rho^2 + (z-z_0)^2}$ is the distance between the elementary dipole and the observation point M,
- $\gamma_0 = \frac{j\omega}{c} = j\beta_0$ is the propagation constant in free space,
- $\gamma = \frac{j\omega}{v_1} = j\beta_1\ (\gamma a \ll 1)$ is the propagation constant of the PLC,

- c is the speed of light, and

- v_1 is the speed in line.

This model is valid in near and far field and radiated fields are expressed only in terms of current and its derivatives (voltages) at the line ends. By using this model, the computational cost may be reduced. The advantages of their approach are rapid estimation of the phenomena simplicity, and possible reduction of computational cost. Prerequisite is knowing the values of the currents and voltages at the line ends [19].

The components of the time-varying EM field radiated by the line source with uniform current distribution located above a homogeneously dissipative ground were studied by Parise [40]. Total electric field generated in the air space has only one component in the axial direction. This component can be derived by decomposing into the direct field induced by the source current, the ideal reflected field induced by the negative image and a correction term due to the imperfect conductivity of the ground [40]. The advantage of this solution is that it is valid in case displacement currents in both the air and the soil are not negligible, and that requires less computation time than conventional numerical quadrature schemes used to evaluate Sommerfeld integrals. On the other hand the line source needs to have uniform current distribution.

Nazari and Huang introduced a new method which breaks down the intermediate Hertz potential into three terms. The two term of the Hertz potential associated with the Sommerfeld integrals are expressed using hyperbolic functions, and the third term is approximated using Saddle Point Method (SPM) [41]. The disadvantage of SPM method is that is not capable of approximating Sommerfeld integrals since the Sommerfeld pole is close to the saddle point for this problem.

As stated earlier one of the simplest scenarios which can be used to assess human exposure to HF radiation is one where the human body is exposed to the EMF radiated by a thin wire antenna. A simple dipole antenna combined with a simple human body model is often used for quick dosimetry procedures, aiming to get a rapid estimation of the phenomena. The analytical approach to incident field dosimetry of VED is given in Section 3.3 along with the related illustrative results.

3.3 Incident dosimetry – Analytical procedures

Within the thesis framework, the radiated electric field of a finite-length dipole antenna at any point of the upper half-space (as in Fig. 3.1) was obtained using:

- a rigorous numerical approach,
- an approximate numerical approach with an assumed current distribution, and
- an approximate analytical approach.

Usually, the radiated electric field of a dipole antenna of finite length at any point of the upper half-space is calculated numerically. In doing so, the current distribution along the antenna is obtained by numerically solving the Pocklington equation using NEC [20]. The approximation for the solution of the current distribution along the wire segment in NEC can be written as follows

$$I_j(a) = A_j + B_j \sin\left(k\left(s - s_j\right)\right) + C_j \cos\left(k\left(s - s_j\right)\right), |s - s_j| < \frac{\Delta_j}{2} \tag{3.29}$$

where

- s_j is the value of s at the center of segment j,
- Δ_j is the length of the segment,
- A_j, B_j, and C_j are unknown constants.

If the waveform of the current distribution along the wire can be assumed, under certain condition, by analytical expressions, including trigonometric functions as in [18, 19], solving the Pocklington equation can be avoided without significant loss of accuracy. Furthermore, if the field equitation is solved numerically approach is regarded as an approximate numerical approach with an assumed current distribution. On the other hand, if the field equitation is solved analytically approach is referred to as the as approximate analytical approach. The approximations for the antenna current used in this paper are sinusoidal, as in [54, 55] and triangular distribution:

$$I(z') = \frac{\sin\left(k\left(\frac{L}{2} - |z' - h|\right)\right)}{\sin\left(k\frac{L}{2}\right)} \tag{3.30}$$

$$I(z') = \frac{2I_0}{L\left(\frac{L}{2} - |z' - h|\right)} \tag{3.31}$$

where

- I_0 is the maximum value of the current distribution at a feeding point,
- z' is the position of the antenna where distribution is calculated, and
- h is the height of the antenna above the half-space.

For a person standing vertically on the ground, E_z field component is relevant. The corresponding integral expression for E_z can be obtained by combining (3.25) and (3.28). The scattered electric field is given by:

$$E_z^{sct} = \frac{1}{j\omega 4\pi\varepsilon_0}\left(\frac{\partial^2}{\partial z^2} + k_0^2\right) \int_{h-\frac{L}{2}}^{h+\frac{L}{2}} I(z')g(z, z')dz' \tag{3.32}$$

As the first term in right-hand side of (3.32) is rather small in the far field zone, it can be neglected, and expression for the radiated electric field simplifies into:

$$E_z^{sct} = \frac{j}{\omega 4\pi\varepsilon_0} k_0^2 \int_{h-\frac{L}{2}}^{h+\frac{L}{2}} I(z')g(z,z')dz' \tag{3.33}$$

Now, inserting the relation for total Green function yields:

$$E_z^{sct} = \frac{1}{j\omega 4\pi\varepsilon_0} \int_{h-\frac{L}{2}}^{h+\frac{L}{2}} I(z')\left[g_0(z,z') + R_{TM}^F g_i(z,z')\right]dz' = \frac{1}{j\omega 4\pi\varepsilon_0} \int_{h-\frac{L}{2}}^{h+\frac{L}{2}} I(z')\left[\frac{e^{-jk_0R_0}}{r} + R_{TM}^F \frac{e^{-jk_0R_1}}{r1}\right]dz' \tag{3.34}$$

where R_0 and R_1 according to Fig. 3.2 represent the distance from the source to the observation point:

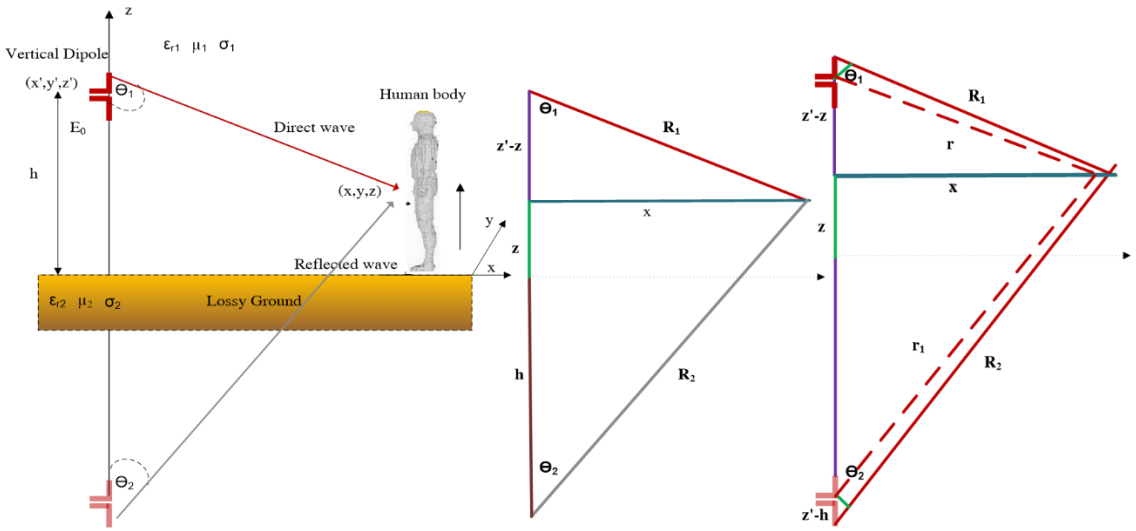

Figure 3.3 Fresnel approximation in far field zone

$$R_1 = r - h\cos(\theta) \tag{3.35}$$

$$R_1 = r_1 + h\cos(\theta_1) \tag{3.36}$$

$$\theta_1 = \frac{\operatorname{acot}(h - z')}{x} \tag{3.37}$$

$$\theta_2 = \frac{\operatorname{acot}(h + z')}{x} \tag{3.38}$$

while r and r_1 represent distances from the center of the antenna to the observation point:

$$r = \sqrt{x^2 + y^2 + (h - z)^2} \tag{3.39}$$

$$r_1 = \sqrt{x^2 + y^2 + (h + z)^2} \tag{3.40}$$

In this manner, distance to the observation point is kept constant thus simplifying the integration, while at the same time phase shift is taken into account rigorously.

Within the framework of the thesis, for approximate numerical approach with assumed current distribution, a procedure for numerical solution of the field integral is developed. Based on assumed sinusoidal and triangular current distribution respectively the corresponding integral expressions for the tangential to the wire field are given by

$$E_z^{sctS} = j\omega 4\pi\varepsilon_0 \left[\frac{\partial^2}{\partial z^2} + k_0^2\right] \int_{h-\frac{L}{2}}^{h+\frac{L}{2}} \frac{\sin\left(k\left(\frac{L}{2} - |z' - h|\right)\right)}{\sin\left(k\frac{L}{2}\right)} \left(g_0(z, z') - \frac{n\cos\theta - \sqrt{n - \sin^2\theta}}{n\cos\theta + \sqrt{n - \sin^2\theta}} g_i(z, z')\right) dz' \tag{3.41}$$

$$E_z^{sctT} = j\omega 4\pi\varepsilon_0 \left[\frac{\partial^2}{\partial z^2} + k_0^2\right] \int_{h-\frac{L}{2}}^{h+\frac{L}{2}} \frac{2I_0}{L\left(\frac{L}{2} - |z' - h|\right)} \left(g_0(z, z') - g_i(z, z')\right) dz' \tag{3.42}$$

When used in proper conditions, approximate numerical approach with assumed current distribution saves time and computer resources since it bypasses solving the Pocklington equation.

Integrating expression (3.34) with the assumption of a triangular current distribution and Fresnel reflection coefficient yields an simple expression for the total electric field at the observation point, while can be for convivence written as follows

$$E_z^{sctT} = \frac{1}{j\omega 4\pi\varepsilon_0} [(T_{11} + T_{12}) + R_{TM}^F T_{21} + T_{22}] \tag{3.43}$$

where T_{11}, T_{12}, T_{21}, and T_{22} are exponential functions of h, L, $cos(\theta)$, and $cos(\theta_1)$, and R_{TM}^F is Fresnel reflection coefficient. The coefficients used in (3.43) are given in Table 3.1.

Table 3.1 Coefficients used in (3.43)

T_{11}	$-\frac{2I_0}{rLk_0^2\cos^2(\theta)} e^{-jk[r-h\cos(\theta)]} \left\{ e^{-jk[(h+\frac{L}{2})\cos(\theta)]} + e^{-jk[(h-\frac{L}{2})\cos(\theta)]} \right\}$
T_{12}	$\frac{4I_0}{rLk_0^2\cos^2(\theta)} e^{-jk[r-h\cos(\theta)]} e^{-jk[h\cos(\theta)]}$
T_{21}	$-\frac{2I_0}{r_1Lk_0^2\cos^2(\theta_1)} e^{-jk[r_1+h\cos(\theta_1)]} \left\{ e^{jk[(h+\frac{L}{2})\cos(\theta_1)]} + e^{jk[(h-\frac{L}{2})\cos(\theta_1)]} \right\}$
T_{22}	$\frac{4I_0}{r_1Lk_0^2\cos^2(\theta_1)} e^{-jk[r_1+h\cos(\theta_1)]} e^{jk[h\cos(\theta_1)]}$
R_{TM}^F	$\frac{n\cos\theta - \sqrt{n-\sin^2\theta}}{n\cos\theta + \sqrt{n-\sin^2\theta}}$

In a similar way, a simple expression for the total electric field at the observation point with the assumption of a sinusoidal current distribution and Fresnel reflection coefficient is obtained. The electrical field can be written in the form

$$E_z^{sctS} = \frac{1}{j\omega 4\pi\varepsilon_0 \sin\frac{k_0 L}{2}} [S_{11} + S_{12} + S_{13} + S_{14} + R_{TM}^F(S_{21} + S_{22} + S_{23} + S_{24})] \quad (3.44)$$

where $S_{11}, S_{12}, S_{13}, S_{14}, S_{21}, S_{22}, S_{23}, S_{24}$ are exponential functions of h, L, $\cos(\theta)$, and $\cos(\theta_1)$ (Table 3.2).

Table 3.2 Coefficients used in (3.44)

S_{11}	$\frac{I_0}{2rk(\cos(\theta)+1)} e^{-jk[r-h\cos(\theta)]} \left\{ e^{-jk[(h+\frac{L}{2})\cos(\theta)]} + e^{-jk[(h-\frac{L}{2})\cos(\theta)]} \right\}$
S_{12}	$-\frac{I_0\cos(\frac{k_0L}{2})}{rk(\cos(\theta)+1)} e^{-jk[r-h\cos(\theta)]} e^{-jk[h\cos(\theta)]}$
S_{13}	$\frac{I_0}{2rk(-\cos(\theta)+1)} e^{-jk[r-h\cos(\theta)]} \left\{ e^{-jk[(h+\frac{L}{2})\cos(\theta)]} + e^{-jk[(h-\frac{L}{2})\cos(\theta)]} \right\}$
S_{14}	$-\frac{I_0\cos(\frac{k_0L}{2})}{rk(-\cos(\theta)+1)} e^{-jk[r-h\cos(\theta)]} e^{-jk[h\cos(\theta)]}$

S_{21}	$\frac{I_0}{2r_1k(\cos(\theta_1)+1)} e^{-jk[r_1+h\cos(\theta_1)]} \left\{ e^{jk[(h+\frac{L}{2})\cos(\theta_1)]} + e^{jk[(h-\frac{L}{2})\cos(\theta_1)]} \right\}$
S_{22}	$-\frac{I_0\cos(\frac{k_0L}{2})}{r_1k(\cos(\theta_1)+1)} e^{-jk[r_1+h\cos(\theta_1)]} e^{jk[h\cos(\theta_1)]}$
S_{23}	$\frac{I_0}{2r_1k(-\cos(\theta_1)+1)} e^{-jk[r_1+h\cos(\theta_1)]} \left\{ e^{jk[(h+\frac{L}{2})\cos(\theta_1)]} + e^{jk[(h-\frac{L}{2})\cos(\theta_1)]} \right\}$
S_{24}	$-\frac{I_0\cos(\frac{k_0L}{2})}{r_1k(-\cos(\theta_1)+1)} e^{-jk[r_1+h\cos(\theta_1)]} e^{jk[h\cos(\theta_1)]}$

3.4 Results for current distribution and irradiated field

In this section results obtained via a rigorous numerical approach, an approximate numerical approach with an assumed current distribution, and an approximate analytical approach are presented. Nominal values of used parameters are shown in Table 3.3.

Table 3.3 Nominal valued of VED and VED environment

Parameter	***Nominal Value***
Physical Length	L=0.01 m
Radius	a=0.1 mm
Operational frequency	f=3 GHz
Height above ground	h=20 m
Relative permittivity of dry, sandy and costal ground	$\varepsilon_r = 10$
Conductivity of dry, sandy and costal ground	$\sigma = 1\ \frac{\mathrm{mS}}{\mathrm{m}}$.
The maximum current applied to the gap in the center of the antenna	I_0 =1 A

Fig. 3.3 shows the current distribution along a vertical dipole antenna above a lossy half-space at a height of h=20 m above the ground. Blue curve shows the current distribution obtained by means of rigorous numerical approach, red by means of

approximate approach with triangular current distribution, and finally, green by using the approximate approach with assumed sinusoidal current distribution along the wire.

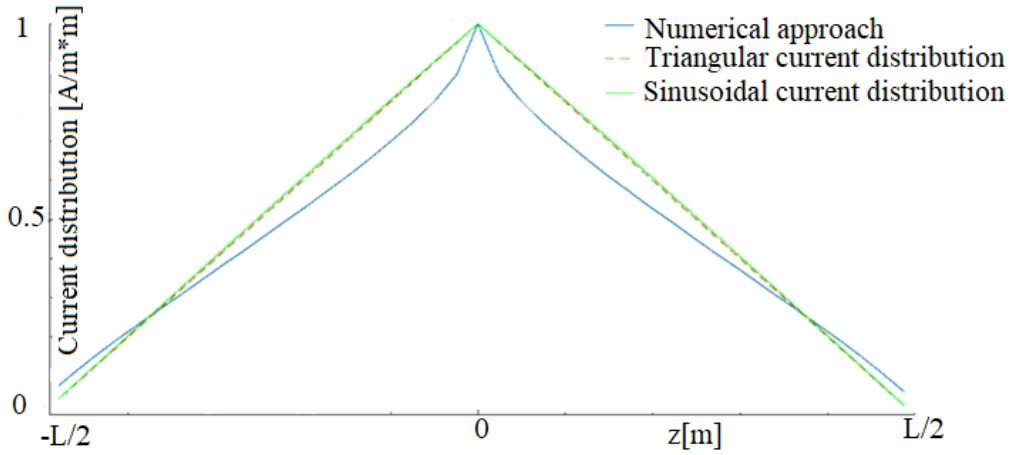

Figure 3.4 Current distribution on a VED above a lossy half-space at h=20m, maximum current in the center of the antenna I_0 =1 A, physical length L=0.01 m, and f=3 GHz

Absolute difference between approximate and actual current distribution is below 11 %, and disappears in narrow bend around the centre of the dipole (where the source is located). The difference between approximate and actual current distribution at the end of VED is below 4 %. The difference in current distribution increases as the current approaches its maximum value (in the canter of the dipole). As the maximum difference is below 11 %, the assumed current distribution (triangular or sinusoidal) is acceptable in this case.

The results for the radiated field obtained using rigorous numerical approach are obtained using NEC [20]. The radiated electric field is calculated in the upper medium from an observation point fixed in a horizontal direction (x=200 m, y=0 m) away from the antenna (which corresponds to a far field zone), while in the vertical direction z changes from 0 m to 1.8 m above ground. Following antenna heights are of interest: 1m, 10 m and 20 m. The absolute value of the electric field radiated in the air versus point location in the z-axis for a fixed distance from the source in an x horizontal direction x = 200 m and at an antenna height of 1 m above are shown in Fig. 3.4, 10 m in Fig. 3.5, and 20 m in Fig. 3.6.

Fig. 3.4 to Fig. 3.6 contain curves obtained via rigorous numerical approach and by using the approximate approach with sinusoidal and triangular current distribution.

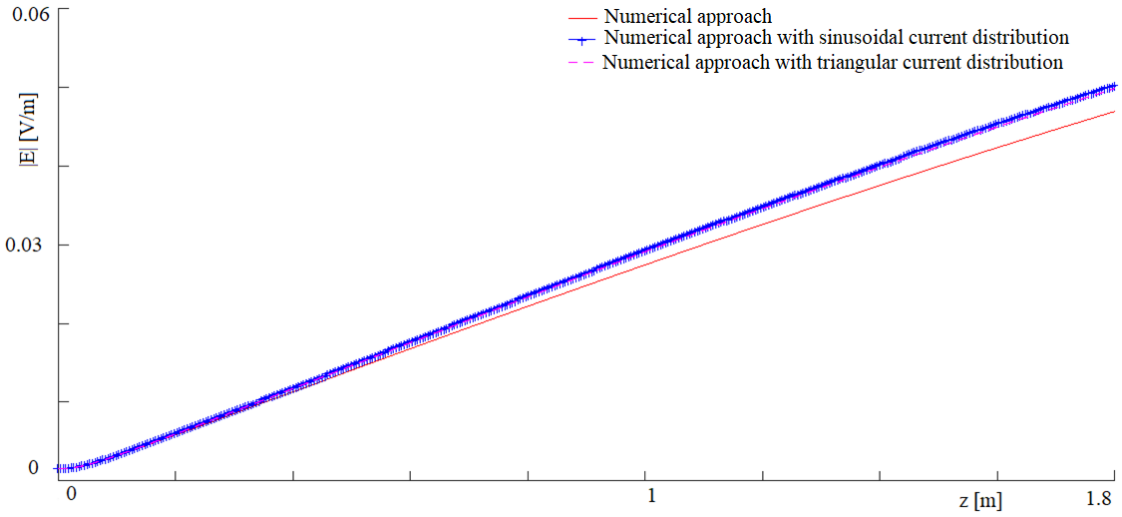

Figure 3.5 The absolute value of the electric field radiated in the air versus point location in the z-axis for a fixed distance from the source in an x horizontal direction x=200 m, frequency f=3 GHz, $\frac{L}{\lambda} = \frac{1}{4}$, and at antenna height h=1 m above ground

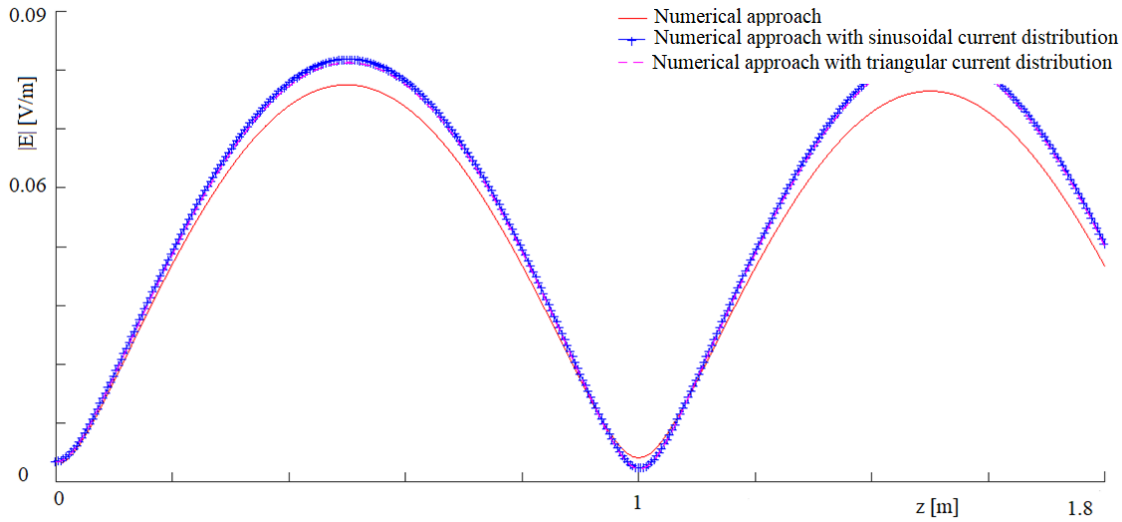

Figure 3.6 The absolute value of the electric field radiated in the air versus point location in the z-axis for a fixed distance from the source in an x horizontal direction x=200 m, frequency f=3 GHz, $\frac{L}{\lambda} = \frac{1}{4}$, and at antenna height h=10 m above ground

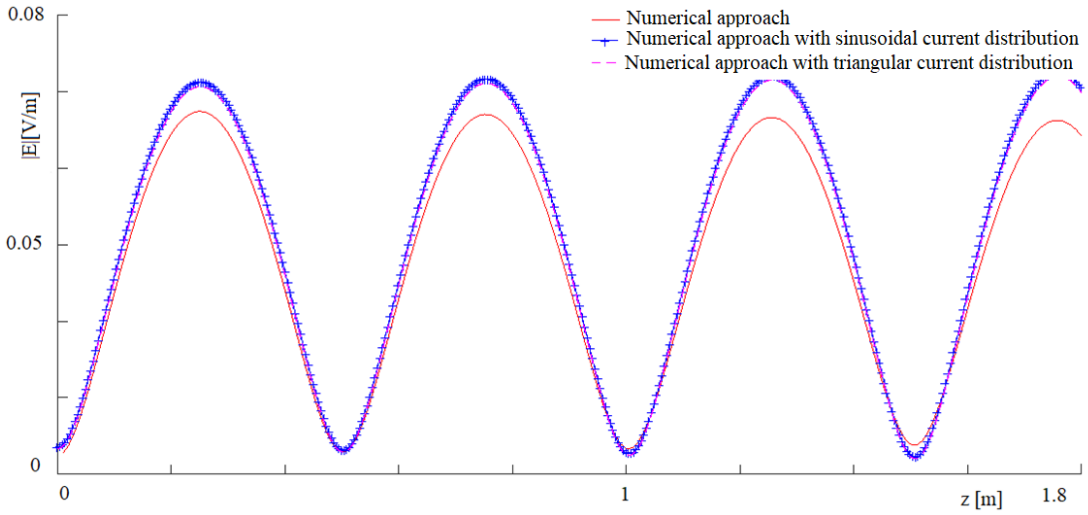

Figure 3.7 The absolute value of the electric field radiated in the air versus point location in the z-axis for a fixed distance from the source in an x horizontal direction x=200 m, frequency f=3 GHz, $\frac{L}{\lambda} = \frac{1}{4}$, and at antenna height h=20 m above ground

It can be observed that the maximum absolute difference between the electric field radiated in the air and at antenna height of 1 m above ground via the rigorous and approximate approaches, respectively is less than 0.4 % (Fig. 3.4). Also, the maximum absolute difference between the electric field radiated in the air at antenna heights of 10 m and 20 m above ground via rigorous and approximate approaches is less than 0.6 % (Fig. 3.5 and Fig. 3.6). Analysing the results for the tangential to the wire electric field component calculated via different approaches it is visible from Fig. 3.4, Fig. 3.5, and Fig. 3.6 that the waveforms obtained by different approaches agree satisfactorily for all height values. Discrepancies appear at the peaks. The number of lobes of electric field increases as h increases. When the height of the antenna above the ground is large enough in relation to the wavelength (in our case at least 10 times) a further increase in height will not affect the change of the radiated electric field.

The impact of ration $\frac{L}{\lambda}$ on irradiated electrical field is shown in Fig. 3.6, Fig. 3.7, and Fig. 3.8. The absolute value of the electric field radiated in the air versus point location in the z-axis for a fixed distance from the source in an x horizontal direction $x = 200$ m and of $\frac{L}{\lambda} = \frac{1}{10}$ is shown in Fig. 3.6, $\frac{L}{\lambda} = \frac{1}{4}$ in Fig. 3.7, and $\frac{L}{\lambda} = \frac{1}{2}$ in Fig. 3.8.

Fig. 3.6 to Fig. 3.8 contain curves obtained via rigorous numerical approach and approximate numerical approach with sinusoidal and triangular current distribution.

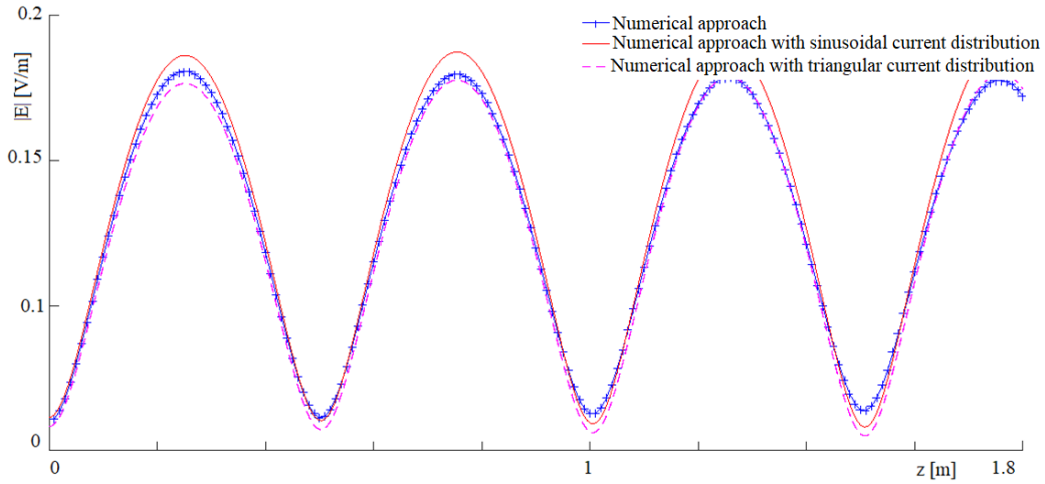

Figure 3.8 The absolute value of the electric field radiated in the air versus point location in the z-axis for a fixed distance from the source in an x horizontal direction x=200 m, frequency f=3 GHz, at antenna height h=20 m above ground, and $\frac{L}{\lambda} = \frac{1}{4}$

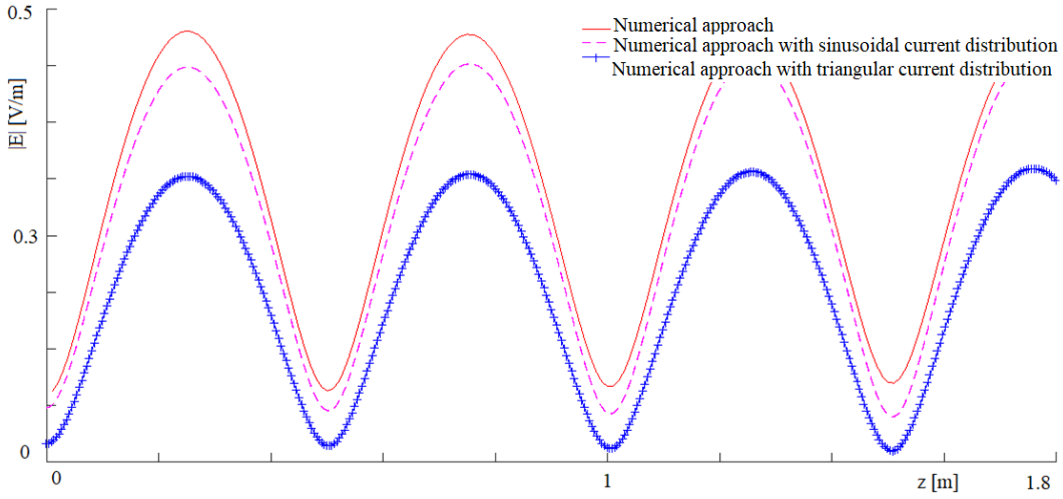

Figure 3.9 The absolute value of the electric field radiated in the air versus point location in the z-axis for a fixed distance from the source in an x horizontal direction x=200 m, frequency f=3 GHz, at antenna height h=20 m above ground, and $\frac{L}{\lambda} = \frac{1}{2}$

The Fig. 3.6 to Fig. 3.8 clearly show that the value of the field increases as the $\frac{L}{\lambda}$ increases. In other words, physically large antennas produce a larger electric field. The maximum value of electric field increases from 0.07 $\frac{\text{V}}{\text{m}}$ to 0.5 $\frac{\text{V}}{\text{m}}$ when $\frac{L}{\lambda}$ increases from 0.1 to 0.5. On the other hand, absolute differences between electric field values of

models with assumed and real current distribution decreases when $\frac{L}{\lambda}$ decreases. In other words when the antenna is electrically small enough these models give the results which differ the most at the peak values, but difference is less than 1 % in this case. As $\frac{L}{\lambda}$ increases the difference also increases.

It should be noted that in all cases the biggest difference between electric field values is observed at the peak values. Also, the values of numerical model with assumed current distribution are smaller because model uses far field approximation (only first term in Pocklington equitation), while rigorous numerical model calculates far field using both terms of integral expression (3.12). This leads to the conclusion that for electrically small antennas ($\frac{L}{\lambda}$ < 0.1) models with assumed and calculated current distribution give similar results. In other words, in such conditions, the model with assumed current distribution gives satisfactory results.

The absolute value of the electric field radiated in the air versus point location in the z-axis for a fixed distance from the source in an x horizontal direction *x* = 200 m and at an antenna height of 10 m above are shown in Fig. 3.9 and Fig. 3.10, and 20 m in Fig. 3.11 and Fig. 3.12.

Fig. 3.9 to Fig. 3.12 contain curves obtained via numerical and analytical approach with sinusoidal and triangular current distribution and obtained via rigorous numerical approach.

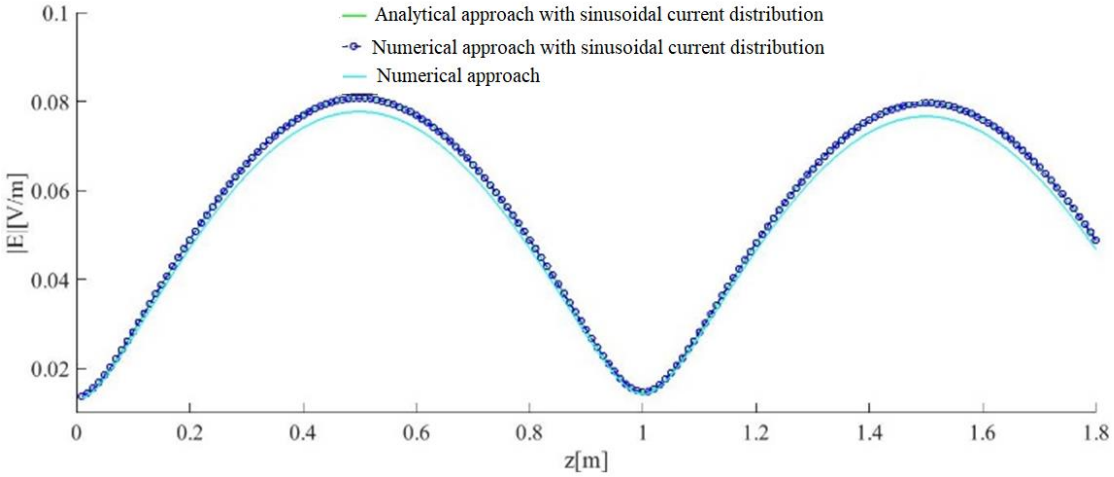

Figure 3.10 The absolute value of the electric field radiated in the air versus point location in the z-axis for a fixed distance from the source in an x horizontal direction x=200 m, f=3 GHz, at antenna height h=10 m above ground, $\frac{L}{\lambda} = \frac{1}{10}$*, and sinusoidal current distribution*

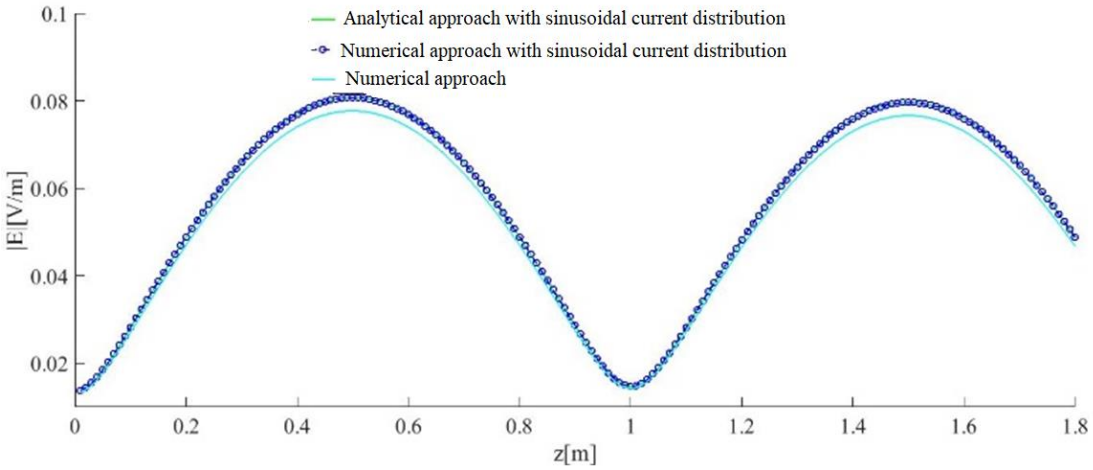

Figure 3.10 The absolute value of the electric field radiated in the air versus point location in the z-axis for a fixed distance from the source in an x horizontal direction x=200 m, f=3 GHZ, at antenna height h=10 m above ground, $\frac{L}{\lambda} = \frac{1}{10}$*, and triangular current distribution*

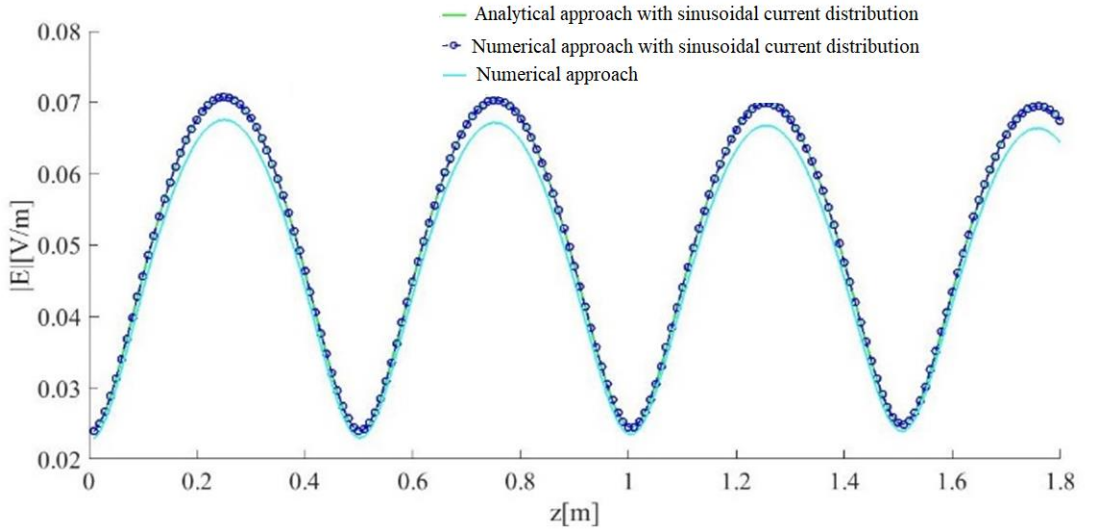

Figure 3.11 The absolute value of the electric field radiated in the air versus point location in the z-axis for a fixed distance from the source in an x horizontal direction x=200 m, f=3 GHz, at antenna height h=20 m above ground, $\frac{L}{\lambda} = \frac{1}{10}$*, and sinusoidal current distribution*

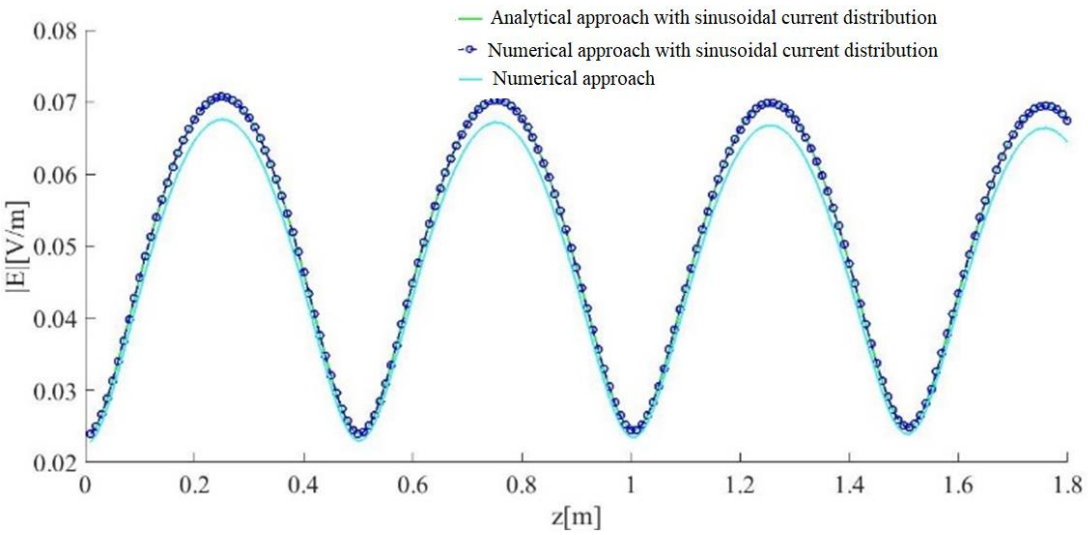

Figure 3.12 The absolute value of the electric field radiated in the air versus point location in the z-axis for a fixed distance from the source in an x horizontal direction x=200 m, f=3 GHZ, at antenna height h=20 m above ground, $\frac{L}{\lambda} = \frac{1}{10}$*, and triangular current distribution*

Previously mentioned lobbying effect is clearly noticeable from Fig. 3.9 to Fig. 3.12. The maximum value of the radiated electric field is the same for heights of 10 m and 20 m and for numerical and analytical approach. Maximal values are higher for analytical and numerical approach when compared to rigorous numerical model.

The difference between field values for analytical and numerical approach with assumed current distribution compared to rigorous numerical approach increases, being maximal at curves maxima. There is no difference in the field values obtained by assuming sinusoidal or triangular current distribution on the antenna. The field waveforms for the analytical and numerical approach totally agree, with the largest difference compared to rigorous numerical approach being noticeable in the region of the maximum.

At height of 10 m and 20 m respectively above the ground, the maximum absolute difference between field radiated in the air by analytical and approximate numerical approach compared to rigorous numerical approach is less than 1 %. Thus, the models based on approximate approach agree satisfactorily with the rigorous numerical model.

The impact of $\frac{L}{\lambda}$ on electrical field is shown in Fig. 3.11 to Fig. 3.16. The absolute value of the field radiated in the air versus point location in the z-axis for a fixed distance from the source in an x horizontal direction *x*=200 m and of $\frac{L}{\lambda} = \frac{1}{10}$ is shown in Fig. 3.11 and Fig. 3.12, $\frac{L}{\lambda} = \frac{1}{4}$ in Fig. 3.13 and Fig 3.14, and $\frac{L}{\lambda} = \frac{1}{2}$ in Fig. 3.15 and Fig 3.16.

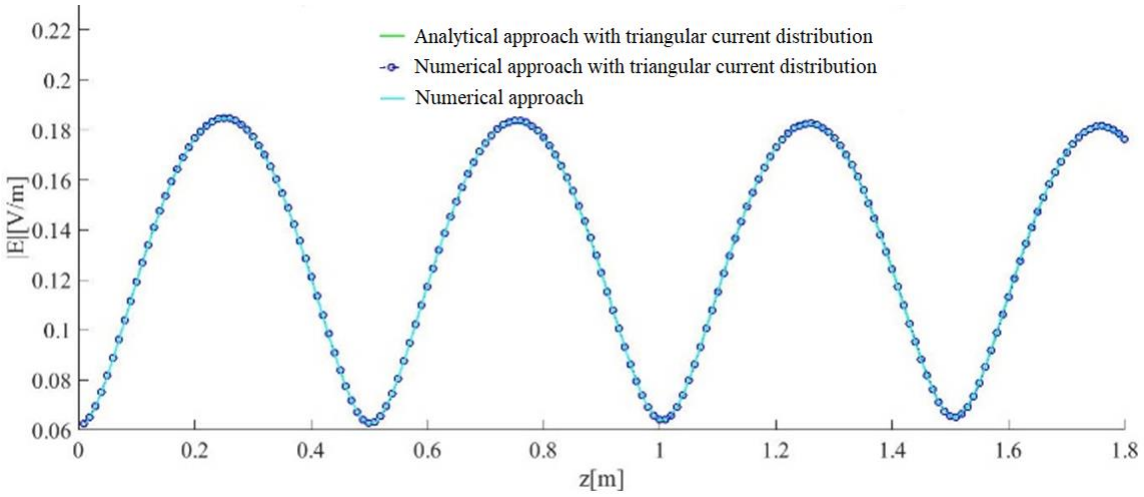

Figure 3.13 The absolute value of the electric field radiated in the air versus point location in the z-axis for a fixed distance from the source in an x horizontal direction x=200 m, f=3 GHz, at antenna height h=20 m above ground, $\frac{L}{\lambda} = \frac{1}{4}$*, and sinusoidal current distribution*

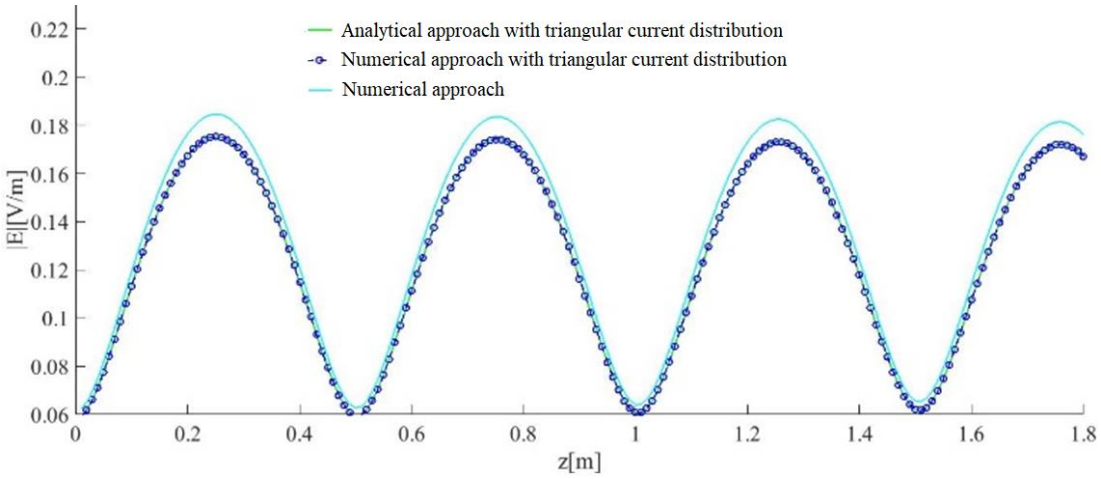

Figure 3.11 The absolute value of the electric field radiated in the air versus point location in the z-axis for a fixed distance from the source in an x horizontal direction x=200 m, f=3 GHz, at antenna height h=20 m above ground, $\frac{L}{\lambda} = \frac{1}{4}$*, and triangular current distribution*

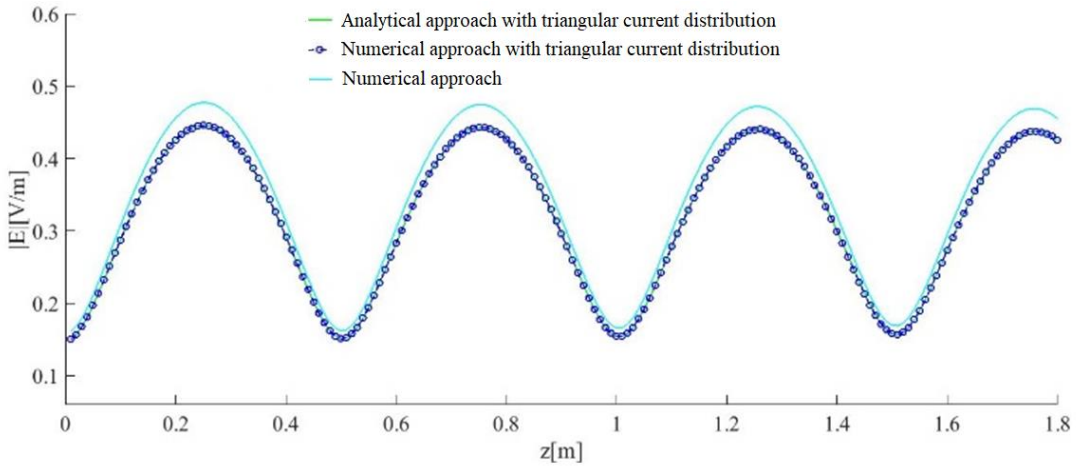

Figure 3.15 The absolute value of the electric field radiated in the air versus point location in the z-axis for a fixed distance from the source in an x horizontal direction x=200 m, f=3 GHz, at antenna height h=20 m above ground, $\frac{L}{\lambda} = \frac{1}{2}$*, and sinusoidal current distribution*

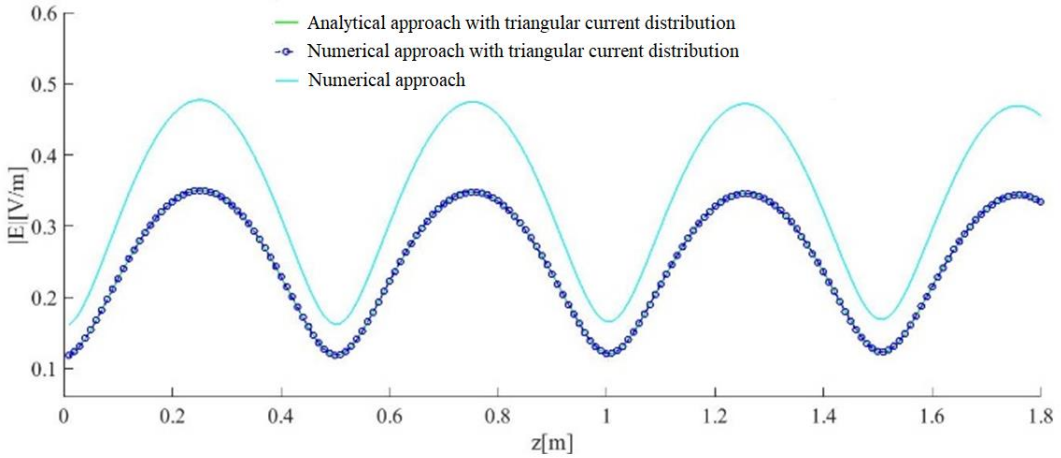

Figure 3.16 The absolute value of the electric field radiated in the air versus point location in the z-axis for a fixed distance from the source in an x horizontal direction x=200 m, f=3 GHz, at antenna height h=20 m above ground, $\frac{L}{\lambda} = \frac{1}{2}$*, and triangular distribution*

Fig. 3.11 to Fig.3.16 clearly show that the field increases as the ratio of physical length and wavelength increase. In other words, physically large antennas generate a larger electric field. The maximum value increases from 0.07 $\frac{\mathrm{V}}{\mathrm{m}}$ to 0.45 $\frac{\mathrm{V}}{\mathrm{m}}$ when $\frac{L}{\lambda}$ increases from $\frac{1}{10}$ to $\frac{1}{2}$ for analytical and numerical model with sinusoidal current distribution,

and from 0.07 $\frac{\mathrm{V}}{\mathrm{m}}$ to 0.35 $\frac{\mathrm{V}}{\mathrm{m}}$ when the $\frac{L}{\lambda}$ increases from $\frac{1}{10}$ to $\frac{1}{2}$ for analytical and numerical model with triangular current distribution. The maximum value increases from 0.065 $\frac{\mathrm{V}}{\mathrm{m}}$ to 0.47 $\frac{\mathrm{V}}{\mathrm{m}}$ when the $\frac{L}{\lambda}$ increases from $\frac{1}{10}$ to $\frac{1}{2}$ for rigorous numerical approach.

As $\frac{L}{\lambda}$ increases, the difference between field values also increases for sinusoidal and triangular current distribution. It should be noted that in all cases the largest difference between field values is observed at the peaks and it is larger for approximate models with triangular current distribution compared to sinusoidal current distribution. The maximum absolute difference between absolute electric field values radiated in the air by approximate numerical approach and analytical approach with assumed current distribution is less than 2 % compared to rigorous numerical approach for $\frac{L}{\lambda} = \frac{1}{10}$.

For electrically middle-sized antennas ($\frac{L}{\lambda} \sim \frac{1}{4}$) the maximum absolute difference between field values radiated in the air by numerical and analytical approach with assumed triangular current distribution is less than 5 % for $\frac{L}{\lambda} = \frac{1}{4}$. Further on, the maximum absolute difference between absolute electric field values radiated in the air by rigorous numerical approach with assumed sinusoidal current distribution is less than 5 % for $\frac{L}{\lambda} = \frac{1}{2}$, and with assumed triangular current distribution is less than 15 % for $\frac{L}{\lambda} = \frac{1}{2}$.

Consequently, for electrically larger antennas the approximation with triangular current distribution should be avoided and more accurate results can be obtained by using the sinusoidal current distribution. This leads to the conclusion that for electrically small antennas ($\frac{L}{\lambda} \leq \frac{1}{10}$) approximate analytical and numerical approach, respectively provides satisfactory results for sinusoidal and triangular current distribution.

Fig. 3.17 to Fig. 3.20 clearly show that the field decreases as the distance from the source increases (from 20 m to 200 m).

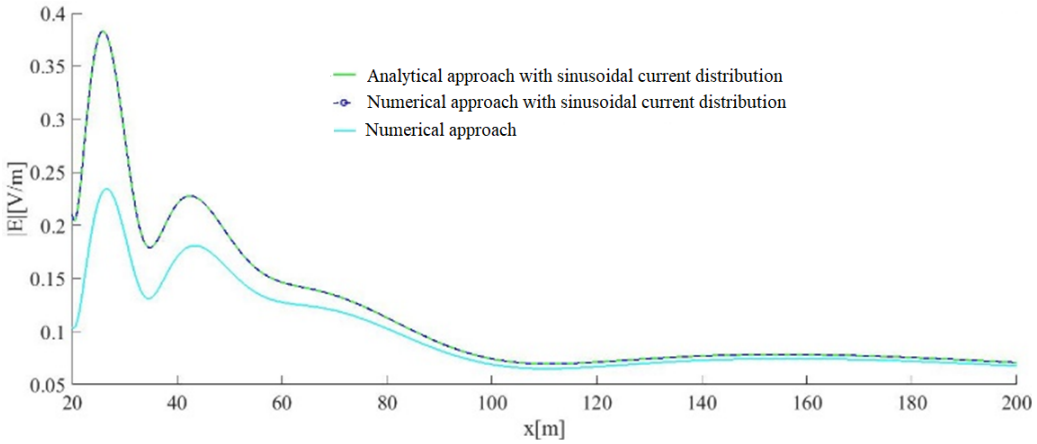

Figure 3.17 The absolute value of the electric field radiated in the air versus point location in the x-axis for a fixed distance in an z vertical direction z=0.25 m, f=3 GHz, at antenna height h=20 m above ground, $\frac{L}{\lambda} = \frac{1}{10}$, and sinusoidal current distribution

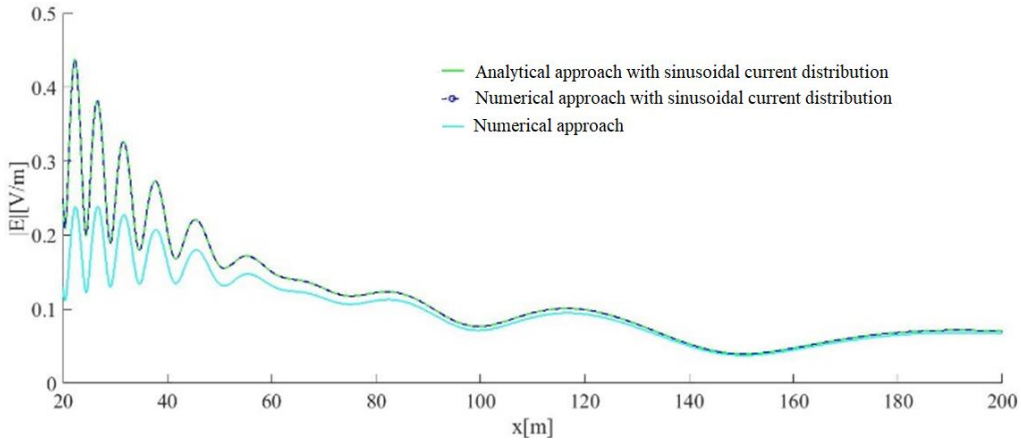

Figure 3.18 The absolute value of the electric field radiated in the air versus point location in the x-axis for a fixed distance in an z vertical direction z=0.75 m, f=3 GHz, at antenna height h=20 m above ground, $\frac{L}{\lambda} = \frac{1}{10}$, and sinusoidal current distribution

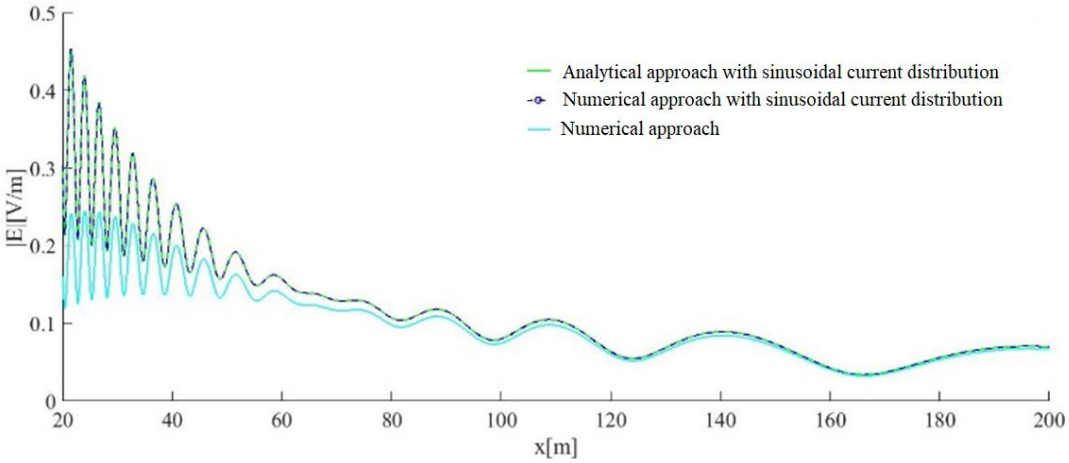

Figure 3.19 The absolute value of the electric field radiated in the air versus point location in the x-axis for a fixed distance in an z vertical direction z=1.25 m, f=3 GHz, at antenna height h=20 m above ground, $\frac{L}{\lambda} = \frac{1}{10}$*, and sinusoidal current distribution*

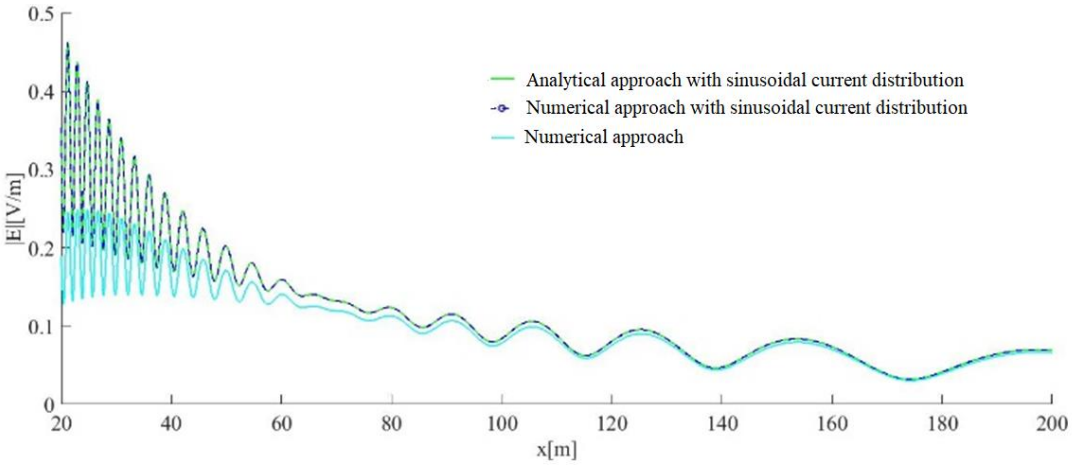

Figure 3.20 The absolute value of the electric field radiated in the air versus point location in the x-axis for a fixed distance in an z vertical direction z=1.75 m, f=3 GHz, at antenna height h=20 m above ground, $\frac{L}{\lambda} = \frac{1}{10}$*, and sinusoidal current distribution*

The maximum value of electric field is 0.46 $\frac{\mathrm{V}}{\mathrm{m}}$ (for approximate numerical and analytical model) and 0.23 $\frac{\mathrm{V}}{\mathrm{m}}$ (for rigorous numerical approach) and it is obtained at point (20 m, 0 m, 1.75 m). The field amplitude approaches the same value as x increases for both models. In all analyzed scenarios, the absolute value of the electric field radiated in the air drops below 0.2 $\frac{\mathrm{V}}{\mathrm{m}}$ when the distance in the horizontal direction

increases to 40 m. When the distance in the horizontal direction is above 60 m these three models agree satisfactorily.

For small distances in the horizontal direction (x<40 m), due to the far field approximation used in proposed model, the significant overestimation of the field values could be observed. The results of rigorous numerical approach obtained from NEC consider the formulations for EMF in near field, meaning that they include the terms $\frac{1}{R^2}$ and $\frac{1}{R^3}$. Our analytical solution is based on far field approximation, and takes only field dependence of term $\frac{1}{R}$, which is his main limitation.

The absolute value of the electric field radiated in the free space versus point location for z = 1.75 m and sinusoidal current distribution is shown in Fig. 3.21.

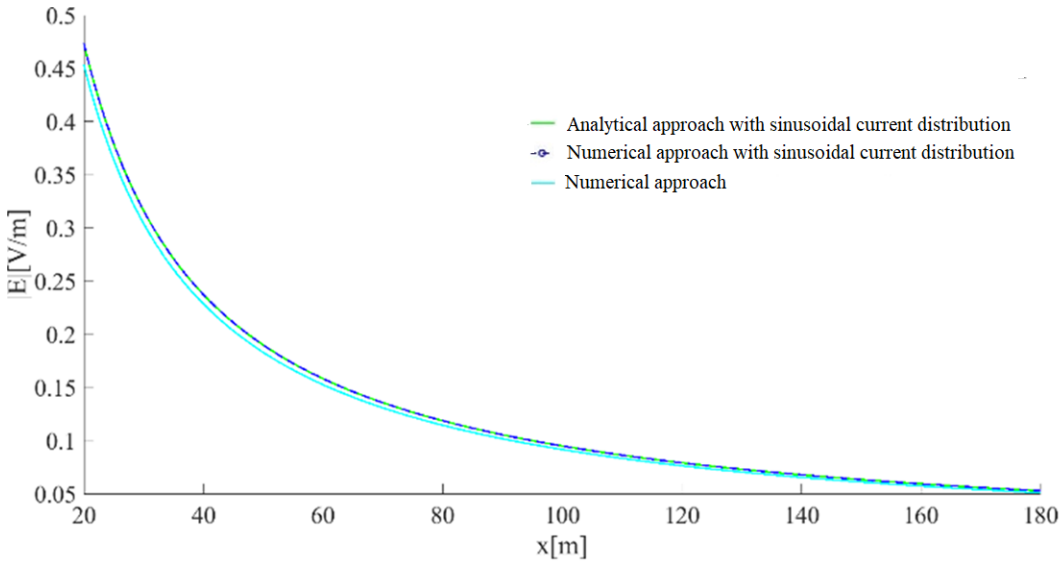

Figure 3.21 The absolute value of the electric field radiated in the free space versus point location in the x-axis for a fixed distance in an z vertical direction z=1.75 m, f=3 GHz, $\frac{L}{\lambda} = \frac{1}{10}$ *and sinusoidal current distribution*

There are no differences between the field values radiated in free space by the approximate numerical approach and the analytical approach with assumed current distribution. And the difference between the mentioned approaches is very small compared to the rigorous numerical approach. In other words, the results of the proposed analytical approach almost completely agree with the results of approximate numerical approach with assumed current distribution and the results of rigorous numerical approach in free space.

Comparing the results between the rigorous formulation and far field approximation in the case of the free space and a lossy media clearly demonstrates that the presence of the lossy ground somehow expands the near field region thus reducing the accuracy of proposed procedure.

The absolute value of the electric field radiated in the air versus point location in the x-axis for a fixed distance in an z vertical direction z=1.75 m and at an antenna height of h=20 m above and frequency f=6 GHz is shown in Fig. 3.22.

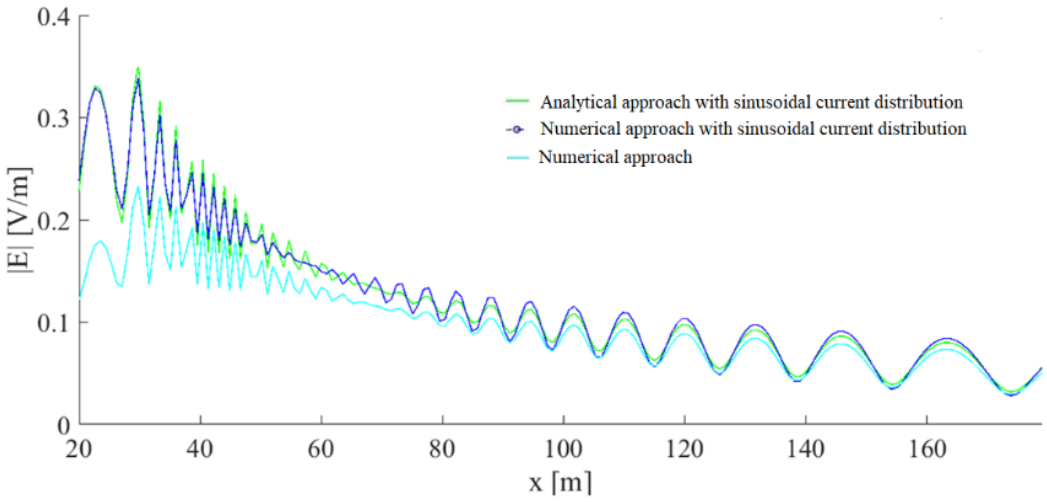

Figure 3.22 The absolute value of the electric field radiated in the free space versus point location in the x-axis for a fixed distance in an z vertical direction z=1.75 m, f=6 GHz, at antenna height h=20 m above ground, $\frac{L}{\lambda} = \frac{1}{10}$*, and sinusoidal current distribution*

There are no differences between the field values obtained by the approximate numerical approach and the analytical approach with assumed current distribution at frequency f=6 GHz compared to f=3 GHz. And the difference between the mentioned approaches is very small compared to the rigorous numerical approach, but higher at f=6 GHz compared to f=3 GHz.

The absolute value of the field radiated in the air versus point location in the x-axis for a fixed distance in an z vertical direction z=1.75 m and at an antenna height of 20 m above and ground conductivity $\sigma = 1\,\frac{\mathrm{mS}}{\mathrm{m}}$ and $\sigma = 1000\,\frac{\mathrm{S}}{\mathrm{m}}$ is shown in Fig. 3.23.

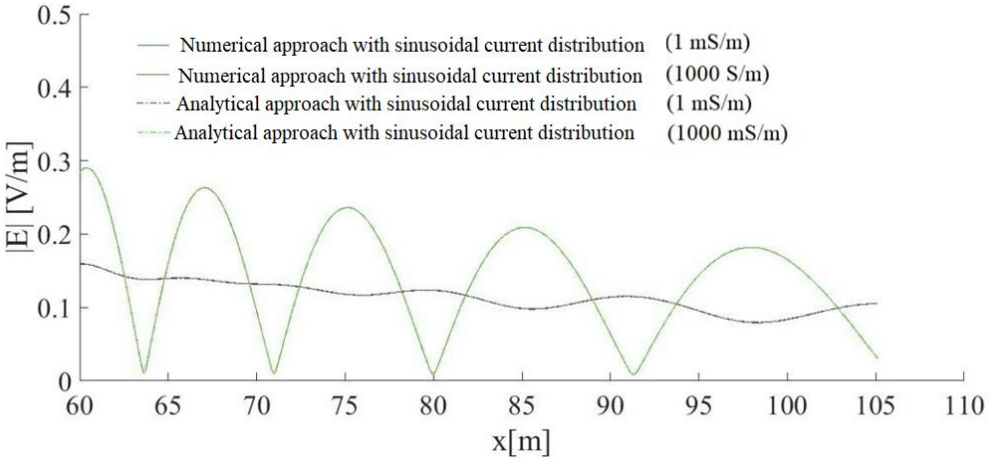

Figure 3.23 The absolute value of the electric field radiated in the free space versus point location in the x-axis for a fixed distance in an z vertical direction z=1.75 m, f=3 GHZ, at antenna height h=20 m above ground, $\frac{L}{\lambda} = \frac{1}{10}$*, and sinusoidal current distribution*

The absolute value of the field radiated in the air versus point location in the x-axis for a fixed distance in an z vertical direction *z*=1.75 m and at an antenna height of *h*=20 m above the ground and relative ground permittivity $\varepsilon_r = 10$ and $\varepsilon_r = 150$ is shown in Fig. 3.24.

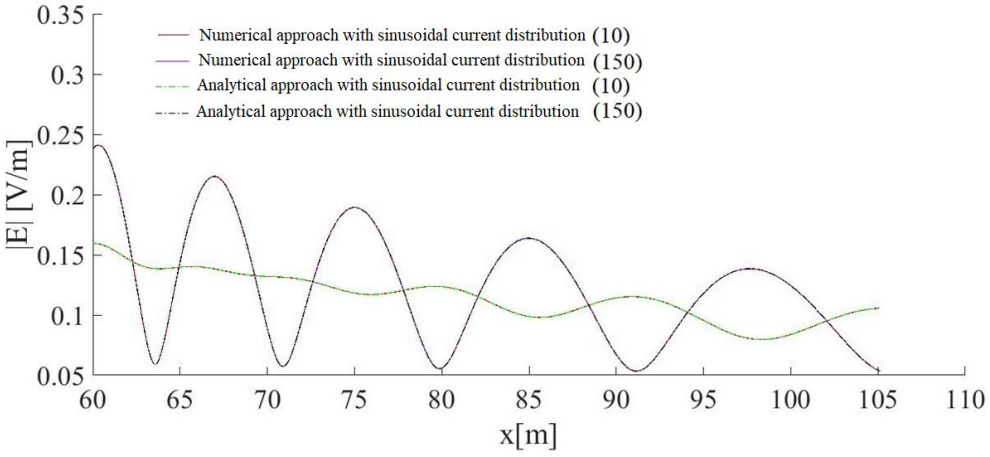

Figure 3.24 The absolute value of the electric field radiated in the free space versus point location in the x-axis for a fixed distance in an z vertical direction z=1.75 m, f=3 GHz, at antenna height h=20 m above ground, $\frac{L}{\lambda} = \frac{1}{10}$*, and sinusoidal current distribution*

There are no differences between the field values obtained by the approximate numerical approach and the analytical approach with assumed current distribution obtained for different electric conductivity and relative ground permittivity.

3.5 Chapter summary

Comparison of the results for the irradiated electric fields obtained for rigorous numerical approach, approximate numerical approach with assumed current distribution and analytical approach for different values of the model parameters, allows to define the conditions in which the approximate approaches can be applied. When used in proper conditions, approximate approaches with assumed current distribution saves time and computer resources as it avoids the solving of the Pocklington equation, and in the case of the analytical approach the field integral. In conclusion, when the height of the antenna above the ground is less than $200 * \lambda$ the results obtained via the approximate analytical and numerical approach agree satisfactorily.

According to the results of the comparison, both models give similar results when the vertical dipole antenna is electrically short ($L \leq \frac{\lambda}{10}$) and when the ratio of the height of the antenna above the ground compared to the wavelength meets the condition $h \geq 10\lambda$. The results obtained on the basis of the previous two approaches are also valid in the near field, which means that they include the terms $\frac{1}{R^2}$ and $\frac{1}{R^3}$.

Note that the analytical solution is based on the far-field approximation and takes only the dependence $\frac{1}{R}$. By comparing the results for all three approaches, an additional limitation is imposed in the form of distance in the horizontal direction $x > 60$ m. For smaller distances in the horizontal direction ($x < 40$ m), due to the far-field approximation used in the proposed analytical model, significant difference in the field values can be observed compered to rigorous and approximate analytical approach with assumed current distribution. Therefore, the presence of lossy soil widens the near-field region, thus limiting the applicability of the proposed procedure.

CHAPTER 4

Internal electromagnetic dosimetry for canonical body models

4.1 Coupling between external and internal fields

Internal dosimetry requires knowledge of the dielectric properties of tissue, tissue geometry and size, tissue orientation and field polarization, field frequency, source configuration, exposure environment, and time-intensity factors [56]. Information about dielectric properties of tissue and its influence on resulting EM filed inside the body are discussed in Section 2.1. Human tissue is multi-layer and fat thickness, tissue curvature, and dimensions of the body, limbs, and head relative to the wavelength all affect the energy distribution. External field intensity and exposure duration are important parameters that determine the total energy absorbed by tissues [56].

It has been shown both theoretically [32], and experimentally [57] that SAR in an exposed person is maximal when the long axis of the body is parallel to the direction of a uniform external electric field. In addition to the frequency dependence of dielectric properties, the strength and spatial distribution of internal fields also vary with frequency [32]. Source configuration depends on source-human body distance, and two configurations appear: far field (there is no interaction or "coupling" between the source and the object) and near field (energy coupling depends on the source shape and size) [56]. Environmental factors affecting EM exposure encompass free space, on a ground plane, near metal reflectors, or in an electrically conductive structure, such as a resonant cavity or waveguide [57].

Having in mind that the induced electric field is the main driver of biological processes that will eventually occur in the human body as a result of exposure to EM radiation, establishing a mathematical relationship between incident and induced electric field is the next step in EM dosimetry procedure. Induced electric field inside the body has the same direction as the external field but is reduced in strength.

Geometrical complexity and inhomogeneous nature make the mathematical representation of the human body rather challenging. In the early beginning of dosimetric calculations models such as spheres, prolate spheroids, block models (cubical mathematical cells arranged in a shape like a human body), have been used to assess the absorbed energy during plane wave irradiation [32]. The relationship between human height and the wavelength at the resonance frequency is originally derived on prolate spheroid or a homogeneous block model [8].

Canonical body models are used by different authors, such as a cylinder [25, 48, 58-60] or a parallelepiped [61, 62]. These planar models do not represent humans with high level of uncertanity, but provide some basic understanding of energy-absorption properties. When a plane wave is incident on a planar electrically lossy object, the wave transmitted into the object attenuates as it travels and transfers energy to the object. The more lossy the object, the more rapidly the wave attenuates.

High resolution, to order of a millimeter or finer, and detailed numerical human models can be used today due to the aid of powerfull computers. Some realistic human body models are used in [63-70]. However, these models have a rather high computational cost, while simplified ones are computationally much less expensive, but fail to ensure accurate results in most scenarios [26].

Analytical methods of EM dosimetry are usually applied to simplified human body models. Some theoretical dosimetry basics, with short literature review and general aspects in numerical and experimental internal EM dosimetry are also covered.

4.2 Theoretical dosimetry basics

Generally, EM dosimetry relies on analytical, numerical or experimental techniques. Analytical methods can be used in canonical models. Numerical dosimetry makes use of computational techniques on digital computers to handle realistic body models, while experimental dosimetry uses instrumentation and measurements to directly measure the dosimetric quantities.

Although, early research in this field proposed the use of current density in tissue, or an internal electric field, a mass-normalized rate of energy absorption was introduced in the late 1960s. The first organization that adopted SAR as the fundamental dosimetry parameter for the RF exposure safety standard was the American National Standards Institute (ANSI) [56].

HF dosimetry uses SAR in the frequency region of 100 kHz to 6 GHz. Above this transition frequency APD is used [3]. SAR is defined as the rate of energy absorbed by or dissipated in human body unit mass:

$$\mathrm{SAR} = \frac{\mathrm{d}}{\mathrm{dt}}\frac{\mathrm{dW}}{\mathrm{dm}} = \frac{\mathrm{d}}{\mathrm{dt}}\frac{\mathrm{dW}}{\rho \mathrm{dV}} = \mathrm{C}\frac{\mathrm{dT}}{\mathrm{dt}} \tag{4.1}$$

Also, in terms of internal field we have

$$\mathrm{SAR} = \frac{\sigma|\mathrm{E}|^2}{2\rho} = \frac{\mathrm{J}^2}{\sigma\rho} \tag{4.2}$$

where

- W is absorbed energy [J],
- m is the mass of the tissue [kg],
- J is induced current density in tissue [$\frac{\mathrm{A}}{\mathrm{m}^2}$],
- ρ describes the mass density of human tissue [$\frac{\mathrm{gr}}{\mathrm{cm}^3}$],
- σ represents the tissue conductivity,
- $\mathrm{E}_{\mathrm{rms}}$ the root mean square of the electric field strength,
- C is the specific heat capacity of tissue [$\frac{\mathrm{J}}{\mathrm{kgK}}$],
- T is the temperature [℃], and
- t denotes time [s].

Furthmore, two metrics are most often determined: $\mathrm{SAR}_{\mathrm{WB}}$ and local SAR. $\mathrm{SAR}_{\mathrm{WB}}$ is defined as the total EM power absorbed by a body divided by its mass, and it is one value that represents the magnitude of spatially averaged SAR throughout an exposed biological object [56]. $\mathrm{SAR}_{\mathrm{WB}}$ is given by:

$$\mathrm{SAR}_{\mathrm{WB}} = \frac{1}{\mathrm{V}} \int_{\mathrm{V}} \mathrm{SAR}_{\mathrm{surf}} \mathrm{dV} \tag{4.3}$$

where

- V is the volume of the human body [m^3], and
- $\mathrm{SAR}_{\mathrm{surf}}$ is the surface SAR value assumed to decrease exponentially through the human body, as follows

$$\mathrm{SAR}_{\mathrm{surf}} = \mathrm{SAR}_0 \mathrm{e}^{-\frac{2\mathrm{x}}{\delta}} \tag{4.4}$$

where

- SAR_0 is the intensity of SAR at the surface as a function of depth x [$\frac{\mathrm{W}}{\mathrm{kg}}$],
- x is depth, and
- δ is the is the penetration depth.

Local SAR is defined as SAR averaged over any cube inside the body with a tissue mass of 1 g ($\mathrm{SAR}_{1\mathrm{g}}$) or 10 g ($\mathrm{SAR}_{10\mathrm{g}}$). The distribution of the local SAR values can be directly calculated from the electric field distribution [71].

$$SAR = \frac{\sigma|E|^2}{\rho_m} \tag{4.5}$$

SAR_{10g} is obtained by averaging the maximum SAR of the points within the 10 g volume and this calculation is performed until it covers the whole sample volume. The same principle is applied for computing the SAR within the 1 g volume covering the whole volume. The SAR (10 g or 1 g) value may be subsequently calculated considering the contribution of the smaller cube and the contribution of the cubical shell around it each with a predefined weighting coefficient using (4.5) [71]:

$$SAR_{10g} \text{or } SAR_{1g} = \frac{\sum_{v1} SAR_i m_i + \sum_{v2-v1} SAR_j m_j}{\sum_{v1} m_i + \sum_{v2-v1} m_j} \tag{4.6}$$

where

- $m_i = \rho_i \Delta V$ is the mass of 10 g cell or 1 g cell,
- $m_j = P_j \Delta V \frac{10-V1}{V2-V1}$ for 10 g cell and $m_j = P_j \Delta V \frac{1-V1}{V2-V1}$,
- index i refers to the lattice cells inside the inner cube, and
- index j to those around it.

Evaluation of the maximum local SAR is particularly important when a part of the human body is exposed to EM radiation from nearby sources. An example of such a scenario, is the estimation of SAR distribution throughout a human head during the use of cellular telephones. Both SAR types are averaged during a certain period of time.

According to ICNIRP for frequencies below 6 GHz and above 100 kHz, SAR should be used, while for frequencies in the range 6 GHz to 300 GHz APD should be used as the BR for the human exposure to EMFs.

APD is defined at the body surface, averaged over the tissue area of interest, *A* [72].

$$S_{ab} = \frac{1}{2A} \iint_A \Re(\vec{S}) d\vec{s} \tag{4.7}$$

where

- $\vec{S} = \vec{E} x \vec{H}^*$ is the Poynting vector yields a direction of the electromagnetic wave propagation, and
- $d\vec{s}$ is variable vector normal to the integral area *A*.

APD for the general public should be restricted to 20 $\frac{W}{m^2}$, averaged over 6 min and over a 4 cm^2 area. In addition to SAR and APD the metric TPD to the skin surface or epithelial power density is defined as [55]

$$\mathrm{TPD}(x, y) = \frac{1}{2}\int \sigma(r)|E(r)|^2 dz \quad (4.8)$$

where

- $|E(r)|$ is the peak value of the electric field at position r,
- σ is the conductivity of human tissue, and
- r is the direction perpendicular to the human body surface.

TPD corresponds to integrated SAR over the depth direction. In the far-field region, wave propagation is spherical in nature and TPD decays as $\frac{1}{r^2}$, where r is the distance from the antenna. In guidelines and standard SAR_{10g} and Incident Power Density (IPD) are considered as metrics, but TPD at the surface is also evaluated in [55]. Therefore, depending of operational frequency different internal dosimetric quantity are used.

4.2.1 Literature review

SAR distributions is usually determined from measurements in human phantoms, in animal tissues, but primarily from calculations. For SAR calculation different simple and complex human body models are used e.g. [21,62,73]. Some experimental techniques that are commonly used to determine SAR distribution are presented in [56, 74].

Study [8] proposes an equation for estimating SAR_{WB} in human body models (NORMAN, NAOMI and BAFB) for plane wave exposure at whole-body resonance frequency. The finite-difference time-domain (FDTD) method is used to calculate the EM power absorbed in these models. The dominant factors influencing the resonance frequency of the human body models are investigated for plane wave exposures. According to results of this study, the uncertainty of the SAR_{WB} estimated with the proposed equation is approximately 10 %, which is mainly attributed to the electrical constants of tissue, including the inhomogeneity of the human body model. The variability of the SAR_{WB} due to the body shape was found to be 30 % for humans of the same age.

SAR_{WB} in simplified parallelepiped model due to radiation of RFID anti-theft antenna gate system (13.56 MHz) is analysed in [62]. The SAR_{WB} is calculated for the two cases: human being is in the center of the antenna gate system, and human standing beside the gate. The obtained SAR_{WB} values are found to be below the ICNIRP exposure limits.

Authors from [21] propose an estimation of SAR_{WB} for far field exposure of an isolated human body in the frequency range of 10 MHz to 200 MHz. Human body is modelled as a lossy homogenous cylindrical antenna. Equations for the total induced axial current and the SAR_{WB} based on a rigorous treatment of cylindrical antenna theory are derived. The

expression for the total induced axial current is derived based on the thin-wire approximation. The calculated SAR_{WB} is in excellent agreement with the FDTD results in chosen frequency range. The calculated axial current for higher frequencies becomes less accurate, which further results in divergence of calculated SAR_{WB} values from the FDTD results for frequencies above 150 MHz.

An analytical method for calculation of the EM absorption in human tissue based on the wave matrix method is proposed in [73]. The method is applied to determine the electrical field and SAR in a planar multi-layer structure exposed to a linearly polarized plane wave in the frequency band between 0.1 GHz and 10 GHz. The results of the proposed analytical method are validated by comparing them to the outcome of a full wave solver using the finite integration technique (FIT). According to the results SAR_{WB} reaches its peak at 3 GHz in the skin and the muscle tissue, and for $f > 3$ GHz high SAR_{WB} values are only present in the skin layer.

In the international guidelines for human protection, used metric to prevent excessive surface temperature elevation at frequencies up to 3 GHz or 10 GHz is SAR. IEEE-Std C95.1-2019 and ICNIRP-RF Guidelines – 2020 have merged towards 6 GHz as transition frequency from specific absorption rate (SAR) to IPD - pertaining to free space, and APD - pertaining to the skin surface [55].

The results for the induced field and the APD at the surface of planar multi-layer model of the human tissue obtained by means of analytical/numerical approach are given in [75]. The multi-layer model is exposed to radiation of dipole antenna, and the influence of multi-layer domain is taken into account via Fresnel plane wave reflection/transmission approximation. Numerical procedures are based on Galerkin-Bubnov Indirect Boundary Element Method (GB-IBEM). In 2-layer model (composed of skin and muscle) the field values obtained using analytical and numerical approach agree satisfactory. Further on, APD decreases as antenna moves away from interface. If the distance between the tissues and the antenna is fixed, then a slow increase of APD with frequency is observed. In 3-layer model (composed of skin, fat and muscle) the field values obtained using analytical and numerical approach agree satisfactory. APD behavior is the same as in the 2-layer model.

Since the IPD is a reference level, effectiveness of a new metric, TPD at the skin, for the estimation of steady-state skin temperature elevation above the transition frequency (3 GHz or 10 GHz) was discussed in [76]. Authors concluded that the TPD provides an excellent estimate of skin temperature elevation through the millimetre wave band (30 GHz to 300 GHz) and a reasonable and conservative estimate down to 10 GHz.

The results of analytical and numerical modelling of the impact of antenna/human body interactions on the TPD, using a skin-equivalent model are presented in [77]. Results from this study demonstrate that the presence of the body in the vicinity of a source results in

an increase in the average TPD. The variations are higher for wet skin (up to 98.25 %) and for children (up to 103.3 %). These results suggest that the exact distribution of TPD cannot be retrieved from measurements of the IPD in free space in absence of the body.

The results for the transmitted field, volume power density (VPD) and TPD in flat human tissue model exposed to the radiation of dipole antenna are presented in the study [55]. Human tissue is represented by muscle properties and a frequency of interest were $f = 6\,\text{GHz}$, $f = 10\,\text{GHz}$, $f = 30\,\text{GHz}$, and $f = 60\,\text{GHz}$. The influence of two-media interface is taken into account via the Fresnel plane wave reflection/transmission approximation. Numerical procedures pertain to GB-IBEM. VPD practically vanishes for shorter wires. TPD penetrates faster through the tissue for higher frequencies and rapidly goes to saturation, as well.

4.3 Approach to internal electromagnetic dosimetry

4.3.1 Experimental and numerical approach

Experimental and numerical dosimetry techniques can be used to assess internal fields for different sources and geometries. Numerical dosimetric approach usually uses phantoms (physical or computational) which simulate the human body or its parts.

Physical model, made from different organic and non-organic materials, represents the electrical properties of various human tissues. The most challenging task in designing physical phantoms are the uncertainty of the electrical properties measured by commercially available systems, temperature change and water evaporation [78]. Some examples of already design and used physical phantoms can be found in [79, 80].

First computational phantoms were based upon mathematical expressions representing sample analytical models [32]. Later, more realistic replication of human anatomy was created by dividing human body model into small voxels (volume pixel). A voxel is a small volume element or cube of a desired tissue and with dimensions of a few millimetres on each side. A whole-human body human voxel model can consist of many million voxels. Each voxel is given appropriate dielectric properties according to which organ it belongs.

The first phantom, called NORMAN, was created in 1997 and consisted of 37 kinds of tissues with accuracy up to 2 mm [81]. Later, in 2005, the same authors created first female phantom, NAOMI [82], and in 2007 three boys and two girls' children. Voxel models of whole-human body humans in various postures and of children, foetuses, and embryos have been developed by several laboratories [68, 83, 84].

Intrinsic disadvantage of voxel models is that they are usually based on the anatomy of a single man or woman, and they do not contain any spatial information at scales smaller than their native resolution and that they cannot be easily deformed to adopt different postures [85].

These problems can be overcome by adopting a Computer Aided Design (CAD) approach, as in [86], to develop models in which the organ and tissue boundaries are represented by parametric surfaces.

Over the years, experimental phantoms have been developed to understand coupling of EM fields to models of the biological systems. Although these models were relatively crude representations of the size and shape of the human body in beginning, experimental results show that calculations of the average SAR agree reasonably well with empirical values [32]. While most of these models do an excellent job of modelling the external shape of the exposed bodies, detailed modelling of the internal heterogeneities of the human body is very difficult and has been attempted only on a very limited scale and in a relatively crude manner. Simple homogeneous models have, therefore, been used more often [87].

Studies show that analytical models in EM dosimetry can provide the satisfying level of accuracy under some conditions which makes them attractive to use. Besides simplicity and possibility for closed form solution, these models yield relatively precise results for electric field magnitude and SAR in regions of the human body with isotropic electrical behavior and when exposed area is approximately plane [73]. Generally, analytical models provide rapid estimation of the phenomena in an engineering sense.

4.3.2 Analytical approach to internal electromagnetic dosimetry

Analytical dosimetry approaches in internal EM dosimetry are usually related to some particularly simplified geometries, such as the planar models, spheres, the cylinders, the spheroids and the ellipsoids, in free space or over an infinite, perfectly conducting ground plane.

The early work in theoretical dosimetry consisted of the calculation of energy absorbed in planar [88], spherical [89], and cylindrical [90] models of humans. These models were chosen, because they were the simplest to treat mathematically. Later on, block models composed of cubical cells arranged to simulate the human body [91] and prolate spheroidal models were introduced. The analysis of the prolate spheroidal models was extended to ellipsoidal models and more work was done on cylindrical models. Models of irregular shape were also analysed [92].

Generally, each of these techniques provides useful information over a limited range of

parameters, for example, over a limited range in frequency. However, despite the limitations of each specialized method, the composite of information obtained from these various techniques has provided a very valuable picture of EM dosimetry.

Two representations of the human body interesting for analytical internal dosimetry approach are considered in this study: simple parallelepiped model of the human body and cylindrical human body model. The values of SAR_{WB} values obtained by both models are compared.

4.3.1.1 Parallelepiped human body model

SAR is defined as the mass averaged rate of energy absorption in tissue (4.11)

$$\mathrm{SAR} = \frac{\mathrm{dP}}{\mathrm{dm}} = \frac{\mathrm{dP}}{\rho \mathrm{dV}} \tag{4.9}$$

In HF EM fields can be quantify using power density Q_{EM}

$$\mathrm{Q_{EM}} = \sigma |\mathrm{E_0}|^2 \tag{4.10}$$

where E_0 stands for effective electric field value. Power density is directly related to SAR

$$\mathrm{Q_{EM}} = \rho \mathrm{SAR} \tag{4.11}$$

Since the left sides of (4.10) and (4.11) are the same, the right sides should be to

$$\mathrm{SAR} = \frac{\sigma}{2\rho} |\mathrm{E_0}|^2 \tag{4.12}$$

Now at any point in the human tissue SAR is proportional to internal electric field [62, 26]:

$$\mathrm{SAR} = \frac{\sigma}{2\rho} |\Gamma_{\mathrm{tr}}|^2 |\mathrm{E_0}|^2 \tag{4.13}$$

$$\Gamma_{\mathrm{tr}}^{\mathrm{MIT}} = \frac{2\mathrm{n}}{\mathrm{n}+1} \tag{4.14}$$

where

- σ is electric conductivity of tissue,
- ρ is density of the biological tissue,
- $\mathrm{E_0}$ is the peak value of the field at the surface of the parallelepiped, and

- Γ_{tr}^{MIT} [53, 52, 16] is the transmission coefficient arising from the MIT, and
- n is the refraction index

According to Fig. 4.1 parallelepiped human body model with height of *H*, depth of *D*, and width of *W* is placed at position $(x, 0, 0)$ and exposed to radiation of VED antenna at height *h* above the ground.

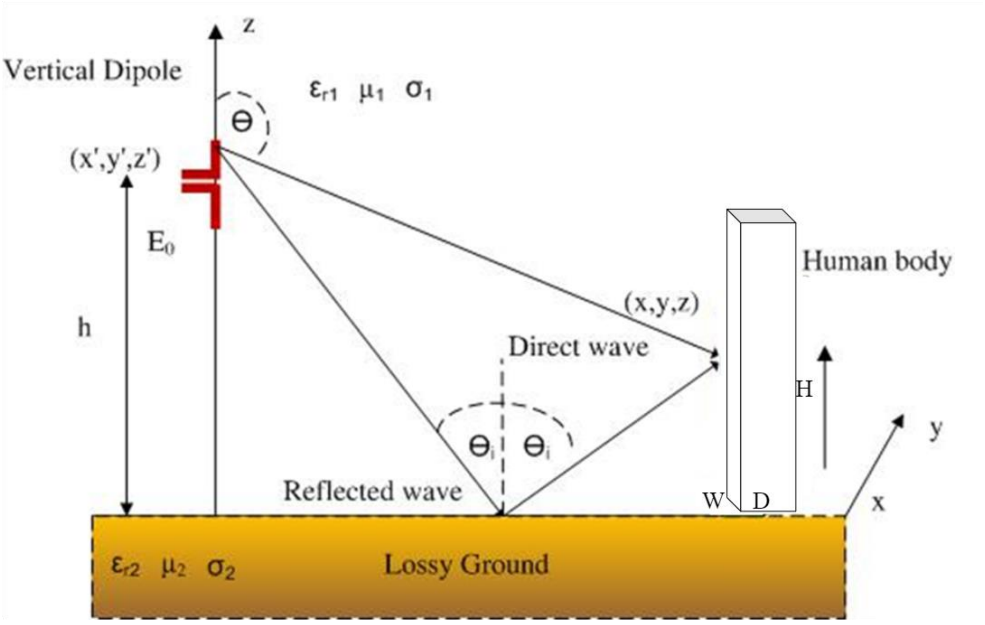

Figure 4.1 Parallelepiped human body model with height of H, depth of D, and width of W is placed at position $(x, 0, 0)$

SAR_{WB} depends on SAR value on body surface and body dimensions, and for parallelepiped body model is given by expression [26, 62]:

$$SAR_{WB} = \frac{1}{HD}\int_H \int_D SAR_{surf}\, dydy \tag{4.15}$$

where for illuminated by the plane wave, approximation formula for SAR_{surf}

$$SAR_{surf} = SAR_0 e^{-\frac{2x}{\delta}} \tag{4.16}$$

SAR_0 is calculated using (4.13), and skin depth is given by:

$$\delta = \sqrt{\frac{2}{\omega\mu\sigma}} \tag{4.17}$$

Inserting (4.16) in (4.15), and using (4.13)

$$\mathrm{SAR_{WB}} = \frac{\delta}{2D}\mathrm{SAR_0} = \frac{\sigma}{2\rho}|\Gamma_{tr}|^2|E_0|^2\left(1 - e^{-\frac{2D}{\delta}}\right) \quad (4.18)$$

For the purposes of the thesis model dimensions are $H = 180$ cm, $W = 40$ cm, and $D = 20$ cm as in [62]. Conductivity may significantly vary in different body compartments, and increases considerably and non-linearly with frequency. The average conductivity of parallelepiped human body is $0.1\ \frac{S}{m}$, as in [8]. Tissue density is considered constant on all frequencies, and the used value is $1010\ \frac{kg}{m^3}$. When internal electric field is known, $\mathrm{SAR_{WB}}$ can be easily computed using (4.18).

4.3.1.2 Cylindrical human body model

The human body is represented by a homogenous cylinder, that comprises muscle tissue, which is the predominant tissue in the human body. Length of the cylinder is $L = 1.8$ m and corresponds to the height of the body, and radius $a = 20$ cm, and assumed to be vertically positioned on ground and exposed to HF field (Fig. 4.2).

The cylindrical human body model represents a standing posture with arms in contact with sides. It was assumed that a time-harmonic vertically polarized plane wave induces a rotationally symmetric current density inside the equivalent cylindrical monopole antenna representing a grounded human body ($Z_c = 0$).

The average value of the conductivity of the human skin is frequency dependent:

$$\sigma_\omega^* = \sigma + j\omega\varepsilon_0\varepsilon_r \quad (4.19)$$

where

- σ_ω^* is complex conductivity,
- σ is conductivity,
- ε_r is relative permittivity,
- ε_0 is the permittivity of free space, and
- ω is the angular frequency.

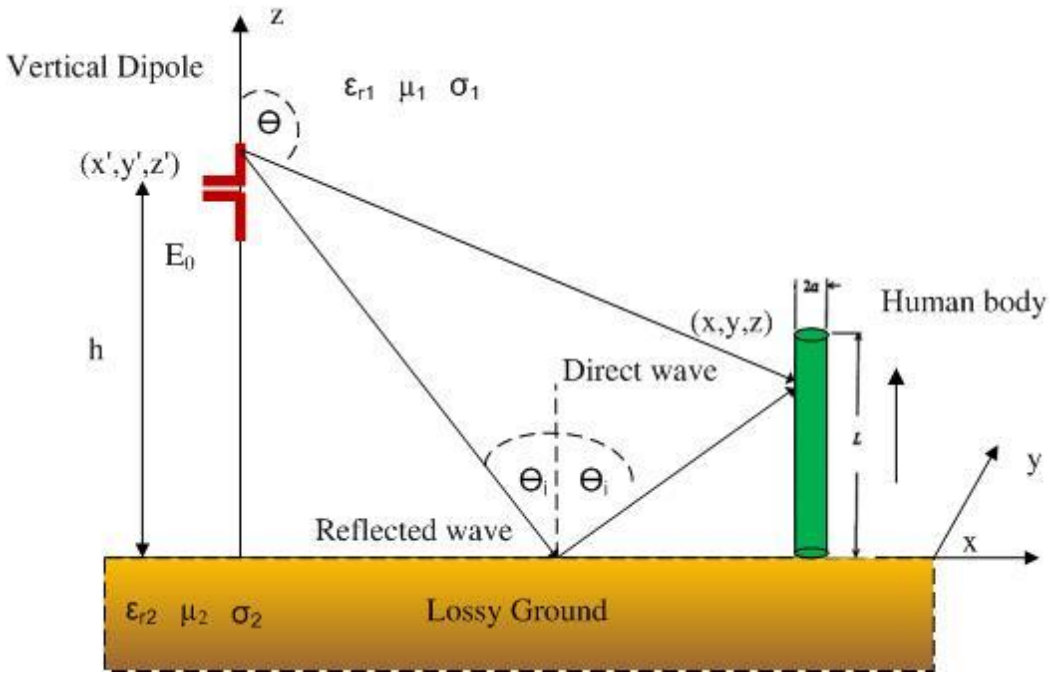

Figure 4.2 Cylindrical human body model with length L and radius a

The BCs for the tangential to the wire electric field components can be written as [93]

$$E_z^{inc} + E_z^{sct} = I(z)Z_c(z) \tag{4.19}$$

where

- E_z^{inc} is the excitation function in the form of incident field,
- E_z^{sct} is the scattered field due to the presence of the imperfectly conducting cylinder,
- $I(z)$ is induced axial current, and
- $Z_c(z)$ is the impedance per unit length of the finitely conductive cylinder.

The expression for the SAR_{WB} of the equivalent cylindrical monopole antenna is provided based on the three-term approach [59] (4.21), (4.22) and (4.23)

$$SAR_{WB} = \frac{1}{V}\int_V SARdV = CI_1I_2 \tag{4.20}$$

$$\frac{\sigma k^2}{4\rho La^4\pi^3(\sigma^2+\omega^2\varepsilon^2)} \frac{1}{\left|J_1\left(j^{-\frac{1}{2}}ka\right)\right|^2} = C \tag{4.21}$$

$$\int_0^a |J_0\left(j^{-\frac{1}{2}}k\zeta\right)|^2 \, d\zeta = I_1 \tag{4.22}$$

$$\int_0^L |I_z(z)|^2 dz = I_2 \tag{4.23}$$

The approximate analytic expression for the total induced axial current inside the equivalent cylindrical monopole antenna of height *L*, radius *a*, and complex conductivity

$$I_z(z) = V_0^e v(z) + U_0 u(z) \tag{4.24}$$

where

$$V_0^e = -\frac{I_{sc}(0)(2Z_A Z_L)}{2Z_A + Z_L} \tag{4.25}$$

$$U_0 = \frac{E_0}{k} \tag{4.26}$$

$$v(z) = \frac{j2\pi k}{\varsigma_0 \gamma \psi_{dR} \cos(\gamma h)} \left[\sin\big(\gamma(h - |z|)\big) + T_u(\cos\gamma z - \cos\gamma h) + T_D\left(\frac{\cos kz}{2} - \frac{\cos kh}{2}\right)\right] \tag{4.27}$$

$$u(z) = \frac{j4\pi}{\varsigma_0}\left[H_U(\cos\gamma z - \cos\gamma h) + H_D\left(\frac{\cos kz}{2} - \frac{\cos kh}{2}\right)\right] \tag{4.28}$$

where

- E_0 is the incident electric field at the surface of the cylinder,
- k is the free space wave number,
- $Z_A = \frac{1}{2v(0)}$ is the driving point impedance of the same cylinder when driven in base $[\Omega]$,
- Z_L is the load impedance at the base of the cylinder,
- $I_{sc}(0) = U_0 u(0)$ is the current at the base when there is no load, and
- Z_0 is the free space impedance.

The expressions of the frequency dependent coefficients are given in Appendix A, which involve integrals that are solved numerically. The imperfectly conducting nature of the equivalent cylindrical antenna was characterized by the complex propagation constant γ, which was defined as

$$\gamma = k\sqrt{1 - j\frac{4\pi z^i}{kZ_0\psi_{dR}}} \tag{4.29}$$

where

- z^i is the surface impedance per unit length of the cylinder

$$z^i = \frac{\kappa}{2\pi a \sigma_\omega^*} \frac{J_0(\kappa a)}{J_1(\kappa a)} = r^i + jx^i \tag{4.30}$$

$$\kappa = \sqrt{-j\omega\mu_0\varepsilon_0 \left(\frac{\sigma_\omega^*}{\varepsilon_0} - j\omega - \frac{4\pi z^i}{\mu_0 \psi_{dR}}\right)} \tag{4.31}$$

where

- J_0 is zero-order Bessel functions,
- J_1 is first-order Bessel functions, and
- μ_0 is the permeability of free space.

Bessel function of the zero order first kind, and first order first kind are illustrated in Fig. 29.

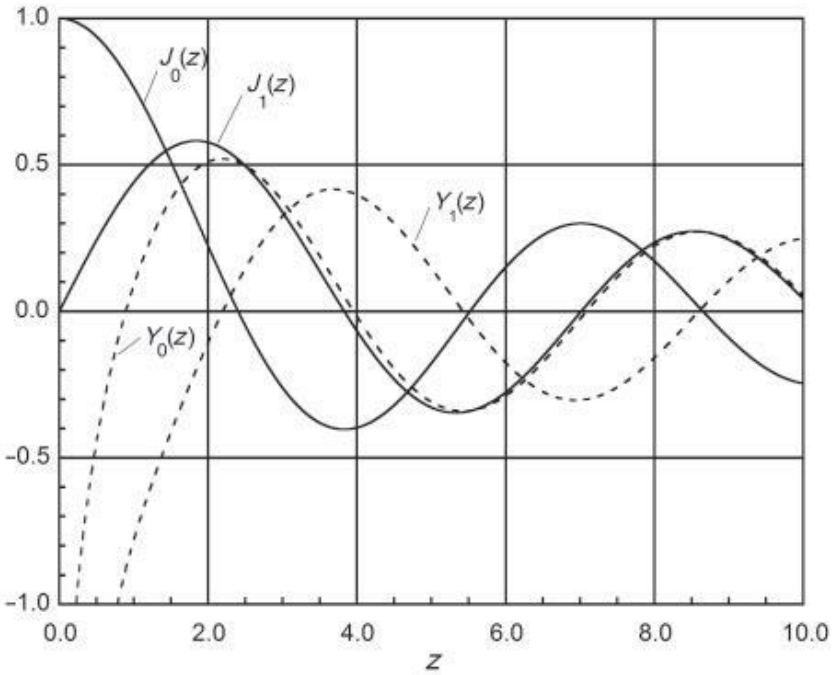

Figure 4.3 Bessel functions of the first and second kind [94]

When calculating induced current one sets $\gamma = k$, and then calculates z^i, ψ_{dR}, and updates γ for new iteration. When calculating $I_z(z)$ according to (4.24), it is considered that human is barefoot ($V_0^e = 0$). Knowing $I_z(z)$, integral I_2 can be calculateed according (4.23), and then SAR_{WB} according to (4.20).

4.4 Internal dosimetry – Analytical procedure

Based on the (4.18) and (4.20), and the already described source of EM waves (Section 3.3), in this section $\mathrm{SAR_{WB}}$ values calculated for parallelepiped and cylindrical human body models are compared. The changes of $\mathrm{SAR_{WB}}$ when the human body models change location in x-axis ($20 \leq x \leq 200$) are considered. These changes are studied in 4 points in vertical z direction which correspond to electric field maximums $z = 0.25$ m, $z = 0.75$ m, $z = 1.25$ m, and $z = 1.75$ m. The body properties are given in Table 4.1, and nominal valued of EMI source are as in Table 3.3.

Table 4.1 Human body properties

Parameter	***Nominal Value***
Parallelepiped human body dimensions	$H = 180$ cm, $W = 40$ cm, $D = 20$ cm
The average conductivity of human body	$\sigma = 0.1 \frac{\mathrm{S}}{\mathrm{m}}$
Tissue density	$\rho = 1010 \frac{\mathrm{kg}}{\mathrm{m^3}}$.
Cylindrical human body dimensions	$L = 180$ cm, $a = 20$ cm

Fig. 4.4 to Fig. 4.7 show $\mathrm{SAR_{WB}}$ versus point location in the x-axis for a fixed distance in z vertical direction corresponding to field maxima z=0.25 m, z=0.75 m, z=1.25 m, and z=1.75 m, frequency $f = 3$ GHz and at antenna height of h=20 m above ground. $\mathrm{SAR_{WB}}$ is calculated using previously obtained values of the incident field, presented in Section 3.3.

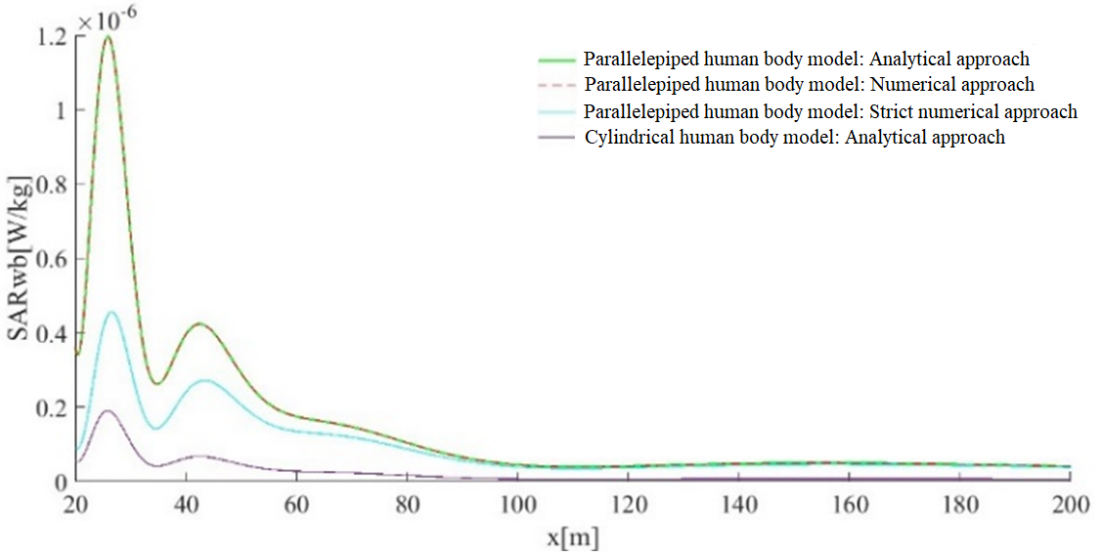

Figure 4.4 SAR_{WB} versus point location in the x-axis for a fixed distance from the source in an z vertical direction z=0.25 m, f=3 GHz, h=20 m and sinusoidal current distribution

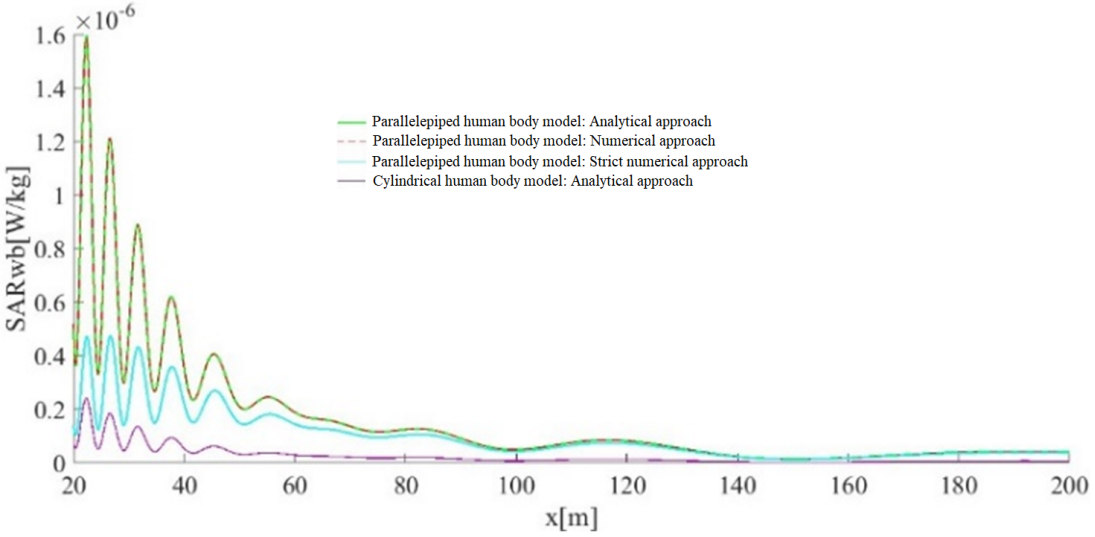

Figure 4.5 SAR_{WB} versus point location in the x-axis for a fixed distance from the source in an z vertical direction z=0.75 m, f=3 GHz, h=20 m and sinusoidal current distribution

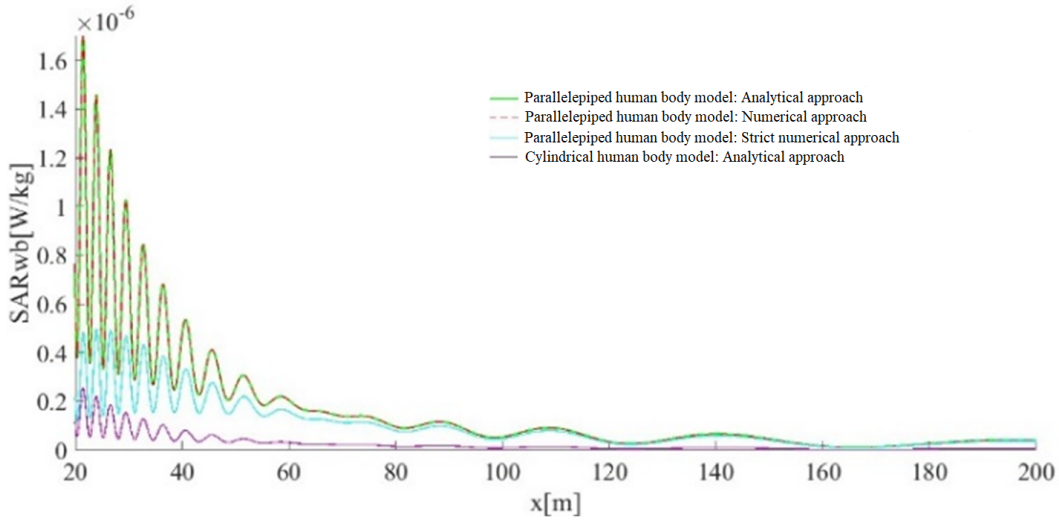

Figure 4.6 SAR_{WB} versus point location in the x-axis for a fixed distance from the source in an z vertical direction z=1.25 m, f=3 GHz, h=20 m and sinusoidal current distribution

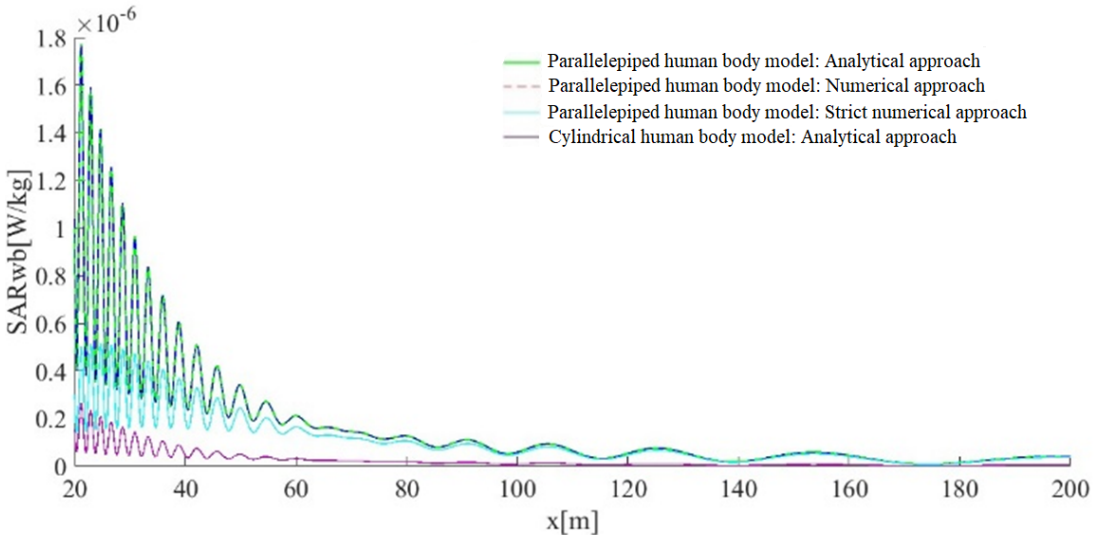

Figure 4.7 SAR_{WB} versus point location in the x-axis for a fixed distance from the source in an z vertical direction z=1.75 m, f=3 GHz, h=20 m and sinusoidal current distribution

Spatial distributions for SAR_{WB} follows a similar pattern as the corresponding electric field distributions, presented in Section 3.3. According to the [3], the maximum value of SAR_{WB} should not exceed 0.4 $\frac{W}{kg}$ for workers and 0.08 $\frac{W}{kg}$ for the general public. According to Fig. 4.4 to Fig. 4.7 the SAR_{WB} is bellow limits defined by ICNIRP in all analyzed cases.

Maximum value of $\mathrm{SAR_{WB}}$ is obtained using the approximate analytical and numerical models in parallelepiped human body model and it is obtained at point around 26 m from source in x direction, and is less than 1.2 $10^{-6}\frac{\mathrm{W}}{\mathrm{kg}}$. In case of rigorous numerical model (obtained in NEC), the maximum is less than $0.46 \cdot 10^{-6}\frac{\mathrm{W}}{\mathrm{kg}}$, and in cylindrical human body model the maximum of $\mathrm{SAR_{WB}}$ obtained in this point is less than 0.2 $10^{-6}\frac{\mathrm{W}}{\mathrm{kg}}$. Overestimation of the SAR value in the analytical model compared to the rigorous model does not introduce the danger of undetected excessive exposure of the body to field radiation. Whereas, underestimation introduces risks for undetected excessive exposure of the body to field radiation, which should be avoided.

This difference between $\mathrm{SAR_{WB}}$ obtained using parallelepiped and cylindrical body models, falls below 10 % at 80 m and reaches the value less than 1 % at 200 m from source antenna in x horizontal direction. Generally, positioning of human body model far away from source antenna allows simpler human body modelling. Therefore, the simplified body models may be used in the far field zone.

As already stated, below $f = 6$ GHz, EMFs penetrate deep into human tissue, and the used dosimetrie quantity is SAR. Above $f = 6$ GHz, EMFs are absorbed at the surface, and the APD specified over different areas is used. Also, area-averaged TPD at skin surface as a metric for the estimation of surface temperature elevation above the transition frequency is discussed [76].

Bearing this in mind, the calculation of an internal electric field, SAR and TPD has been performed at frequencies $f = 3$ GHz, $f = 6$ GHz, and $f = 9$ GHz respectively. Calculated values where compared for analytical and numerical approach with sinusoidal current distribution.

Furthermore, SAR and TPD are calculated by using the proposed closed form expressions for the corresponding irradiated electrical field assuming the sinusoidal current distribution along a vertical dipole antenna, placed above lossy half space and parallelepiped human body model. Results are compared to the more rigorous approach using the near field Green function (reduced kernel) and numerical integration for the incident field calculation.

Note that, TPD is obtained by evaluating the integral (4.8) and for geometry shown in Fig. 4.1 it follows

$$\mathrm{TPD(x)} = \frac{1}{2}\int_0^{\mathrm{x}} \rho \mathrm{SAR}\, \mathrm{dx} = \frac{\sigma\delta}{2}|\Gamma_{\mathrm{tr}}|^2|\mathrm{E}_0|^2\left(1 - \mathrm{e}^{-\frac{2\mathrm{x}}{\delta}}\right) \tag{4.32}$$

Relative permittivity and specific conductivity values of the human body for different frequencies are given in Table 4.2, and nominal valued of EMI source are as in Table 3.1. The body is approximately represented by muscle tissue properties [29].

Table 4.2 Electric properties of the human body [29]

Frequency [GHz]	***Permittivity***	***Conductivity [$\frac{S}{m}$]***
3	52.1	2.14
6	48.2	5.2
9	44.1	9.19

First the absolute value of incident field at the surface of the human body and at transition frequency $f = 6$ GHz is analysed. The incident electric field for the distances of $x = 60$ m to $x = 100$ m from the antenna and a fixed height $z = 1.65$ m above ground, are calculated and shown in Fig. 4.8.

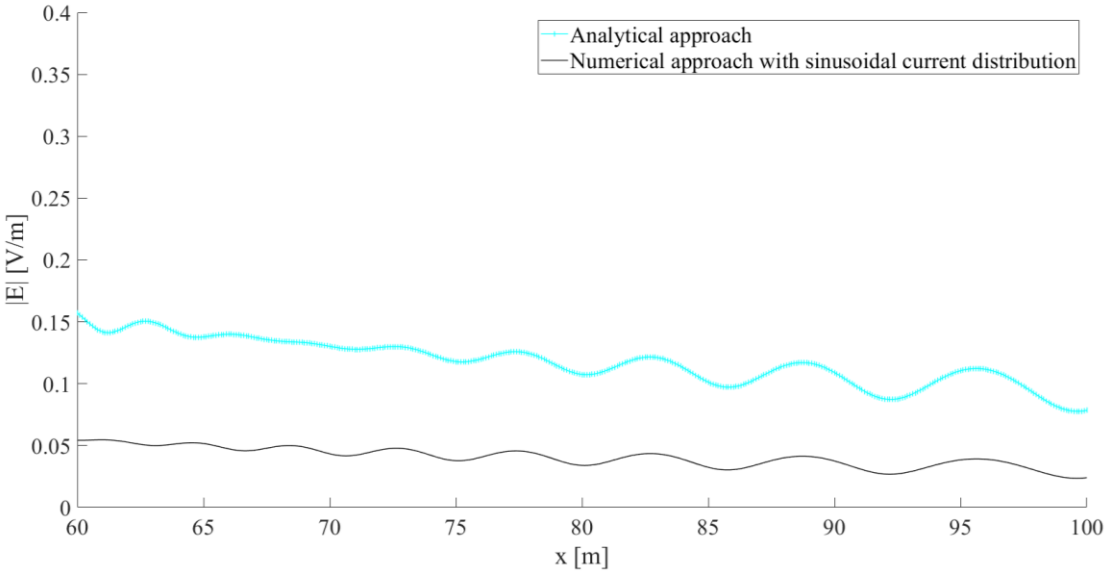

Figure 4.8 The absolute value of the electric field versus point location in the x-axis for the frequency f=6 GHz

The maximum value of the irradiated field obtained for an analytical approach is 0.16 $\frac{\mathrm{V}}{\mathrm{m}}$ and for an approximate numerical approach with an assumed current distribution is 0.06 $\frac{\mathrm{V}}{\mathrm{m}}$. The highest values of the field are obtained around $x = 60$ m, a point close to the antenna. The phase deviation of these two models decreases as *x* increases, showing better

model agreement at points on the *x*-axis that are farther from the antenna. Thus, further analysis is carried out for the body placed at distance of $x = 60$ m from the antenna.

Next, the electric field induced inside the human body has been calculated for the frequencies of $f = 3$ GHz, $f = 6$ GHz and $f = 9$ GHz, respectively and results are shown in Fig. 4.9, Fig. 4.10, and Fig. 4.11, respectively. Since field values inside human tissue drop rapidly, the diagrams for are presented depth of 20 mm.

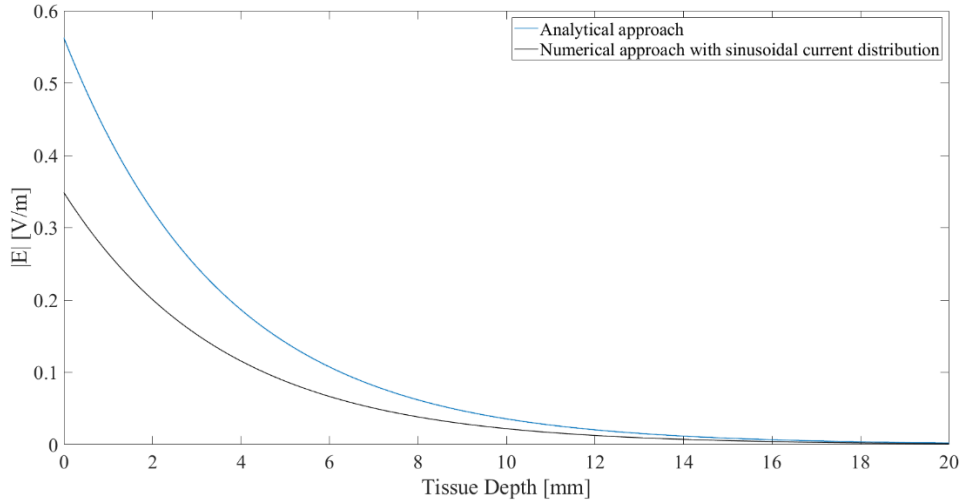

Figure 4.9 The absolute value of the electric field versus tissue depth for a fixed distance from the source in a z vertical direction z=1.65 m, h=20 m, f=3 GHz, $\frac{L}{\lambda} = \frac{1}{10}$*, and sinusoidal current distribution*

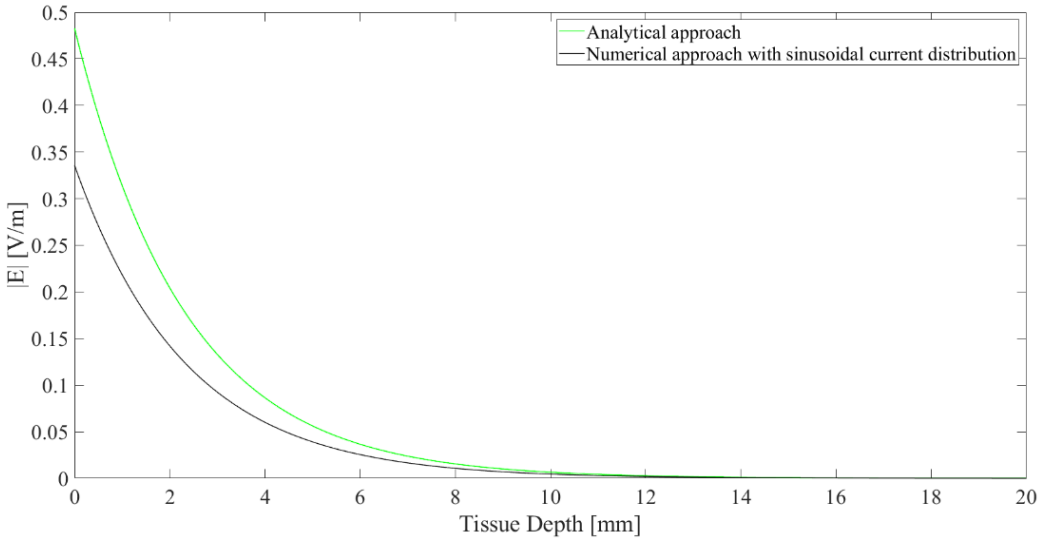

Figure 4.10 The absolute value of the electric field versus tissue depth for a fixed distance from the source in a z vertical direction z=1.65 m, h=20 m, f=6 GHz, $\frac{L}{\lambda} = \frac{1}{10}$*, and sinusoidal current distribution*

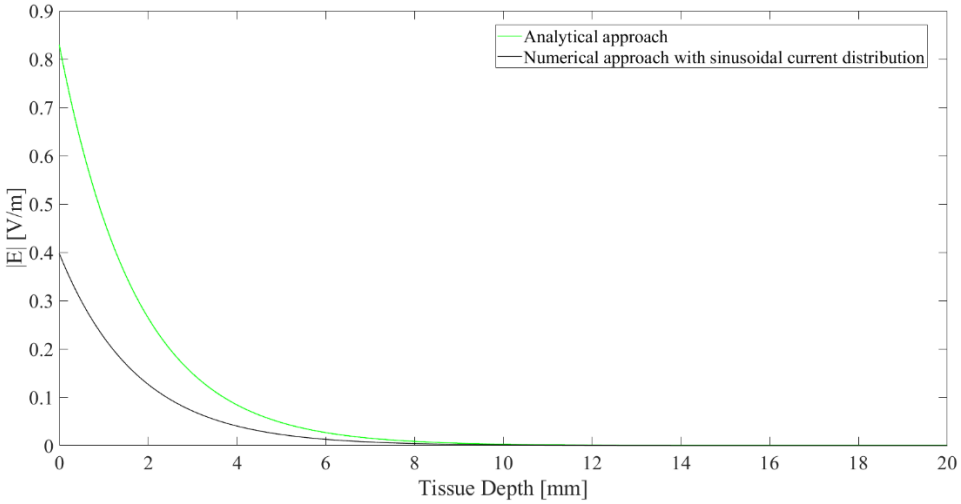

Figure 4.11 The absolute value of the electric field versus tissue depth for a fixed distance from the source in a z vertical direction z=1.65 m, h=20 m, f=9 GHz, $\frac{L}{\lambda} = \frac{1}{10}$*, and sinusoidal current distribution*

As expected the internal field decreases exponentially with tissue depth. Based on the Fig. 4.9 to Fig. 4.11, it can be concluded that the absolute value of the transmitted field dies off more rapidly for the higher frequency. Thus, the penetration depth is smaller for the higher frequencies. The results obtained via different approaches agree satisfactorily.

Fig. 4.12 to Fig. 4.14 show SAR versus tissue depth for frequencies of $f = 3$ GHz, $f = 6$ GHz and $f = 9$ GHz, respectively. SAR is calculated using previously obtained values of an incident electric field.

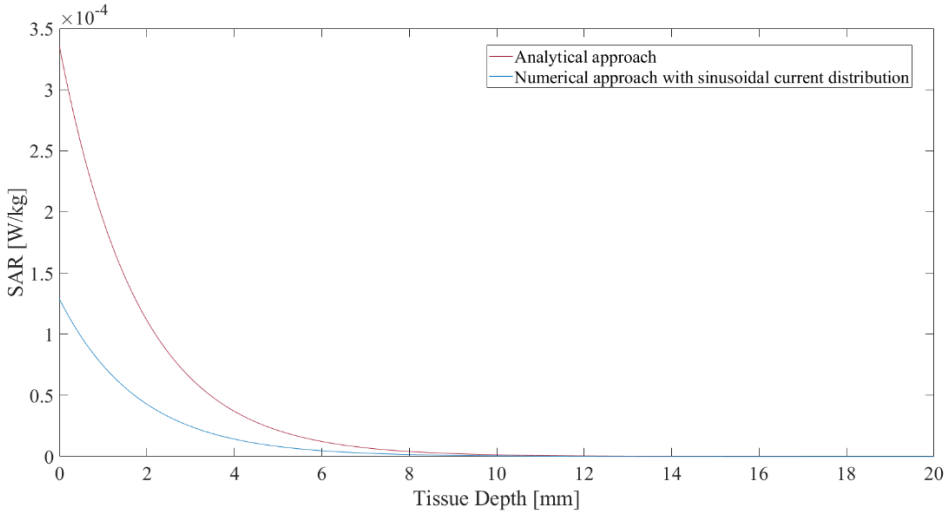

Figure 4.12 SAR versus point location in the x-axis for a fixed distance from the source in an z vertical direction z=1.65 m, h=20 m, f=3 GHz, $\frac{L}{\lambda} = \frac{1}{10}$*, and sinusoidal current distribution*

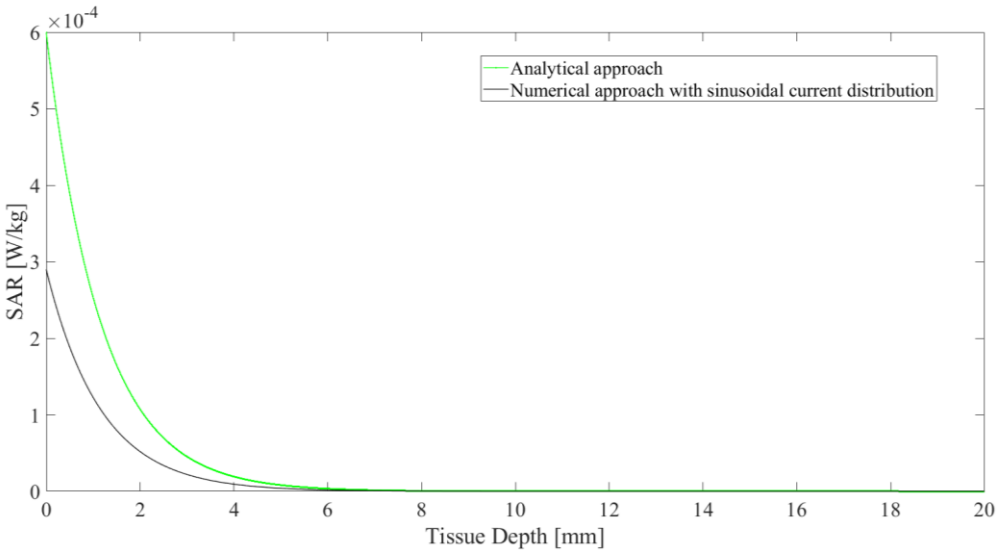

Figure 4.13 SAR versus point location in the x-axis for a fixed distance from the source in an z vertical direction z=1.65 m, h=20 m, f=6 GHz, $\frac{L}{\lambda} = \frac{1}{10}$, and sinusoidal current distribution

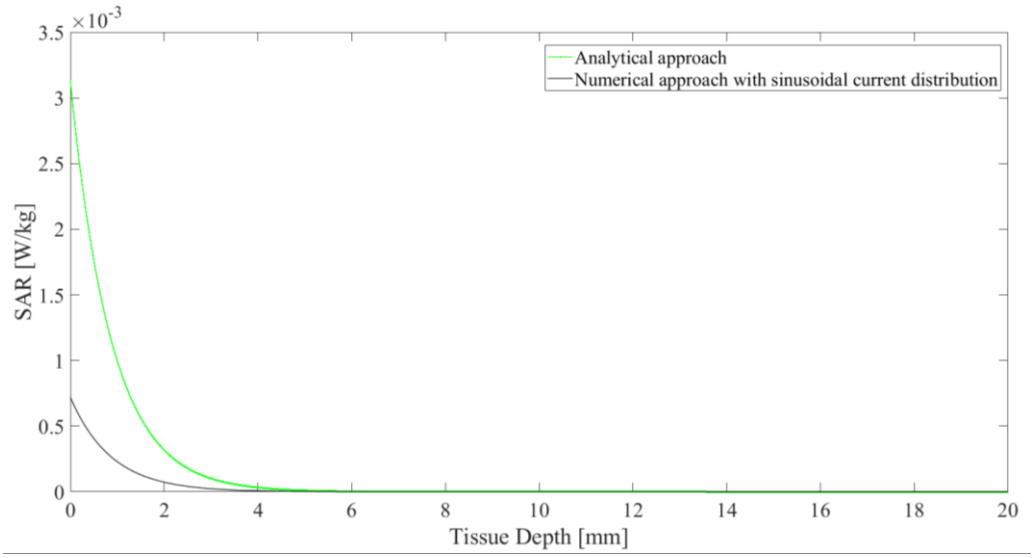

Figure 4.14 SAR versus point location in the x-axis for a fixed distance from the source in an z vertical direction z=1.65 m, h=20 m, f=9 GHz, $\frac{L}{\lambda} = \frac{1}{10}$, and sinusoidal current distribution

Spatial distributions for SAR follow the similar pattern as the corresponding electric field distributions as expected.

Fig. 4.15 to Fig. 4.17 show TPD versus tissue depth for three frequencies: $f = 3$ GHz, $f = 6$ GHz and $f = 9$ GHz. TPD is calculated using previously obtained values of the incident electric field and SAR according to equation (4.32).

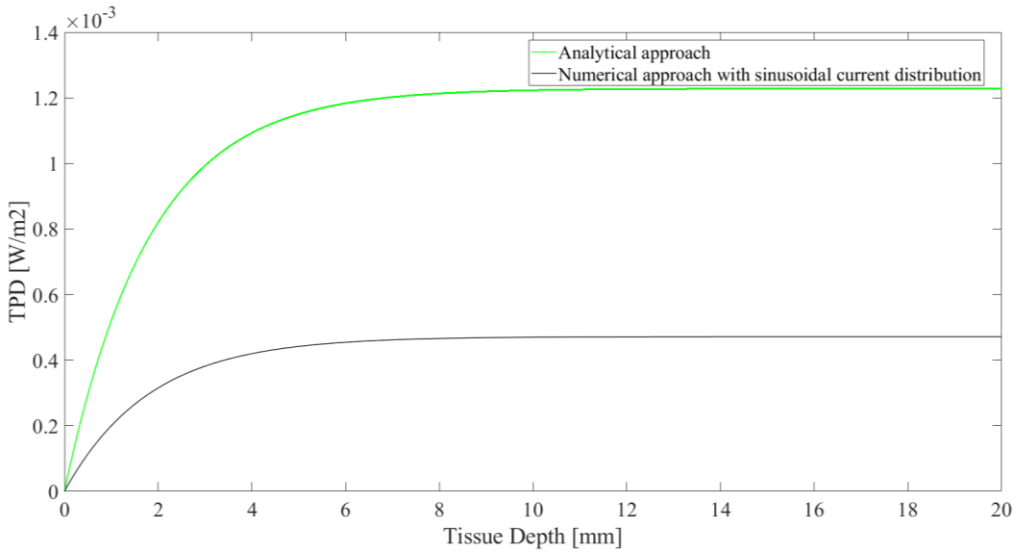

Figure 4.15 TPD versus tissue depth for a fixed distance from the source in a z vertical direction z=1.65 m, h=20 m, f=3 GHz, $\frac{L}{\lambda} = \frac{1}{10}$, and sinusoidal current distribution

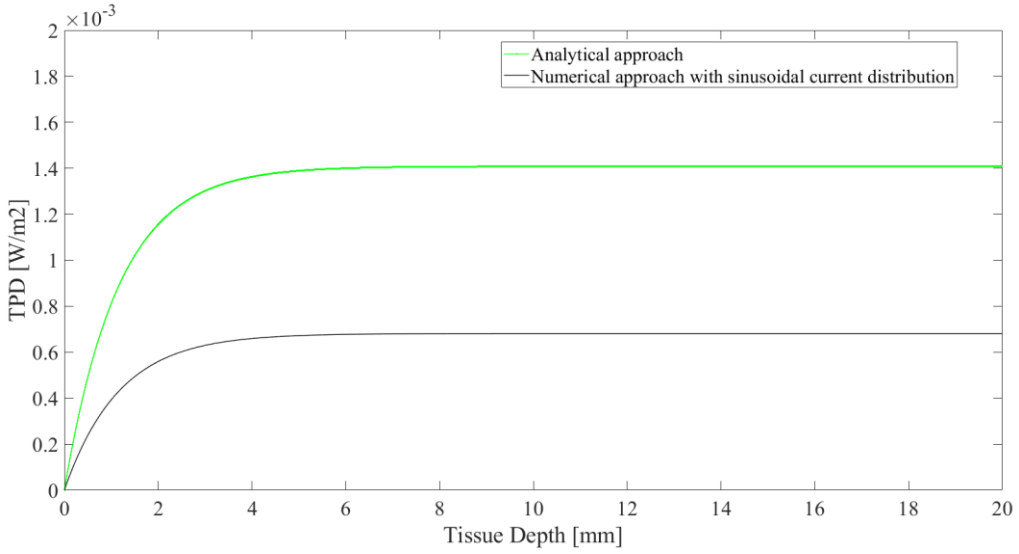

Figure 4.16 TPD versus tissue depth for a fixed distance from the source in a z vertical direction z=1.65 m, h=20 m, f=6 GHz, $\frac{L}{\lambda} = \frac{1}{10}$, and sinusoidal current distribution

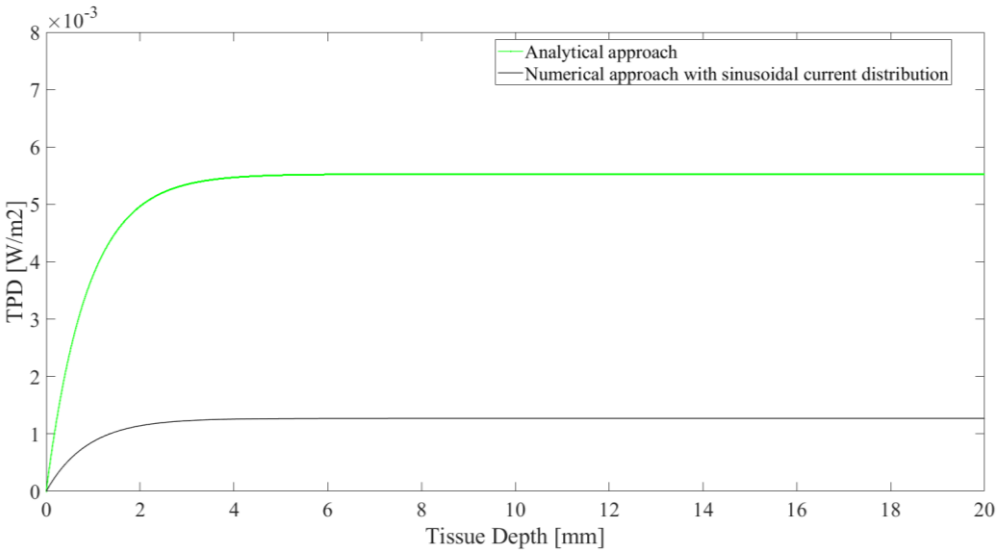

Figure 4.17 TPD versus tissue depth for a fixed distance from the source in a z vertical direction z=1.65 m, h=20 m, f=9 GHz, $\frac{L}{\lambda} = \frac{1}{10}$, and sinusoidal current distribution

Fig. 4.15 to Fig. 4.17 show the difference in the calculated TPD values for analytical model with far field approximation and numerical model observed for a change of frequency from $f = 3$ GHz to $f = 9$ GHz. TPD values increase rapidly and reaches a maximum value at a certain tissue depth that remains constant regardless of further depth increase. The maximum value corresponds to final accumulated EM energy in human body.

The difference between the observed models grows with increasing frequency, so it is at a maximum of $f = 9$ GHz and a minimum of $f = 3$ GHz. With increasing frequency, TPD reaches its maximum (constant value) faster, that is, energy accumulates closer to the surface of human tissue (skin effect). Compared to the SAR values it could be seen that for the simple homogeneous model of the human body, values obtained by two approaches correspond to each other since the TPD reaches the maximum as the SAR drops to the zero. Thus, both quantities could be used on frequencies above the 6 GHz since they provide the same information and insight in the induced field and power distribution

Finally, Fig. 4.18 and Fig. 4.19 show the $\mathrm{SAR_{WB}}$ and total TPD versus location of the human body in the x-axis direction at frequency $f = 6$ GHz. The total TPD corresponds to TPD value obtained for a tissue depth of 20 cm.

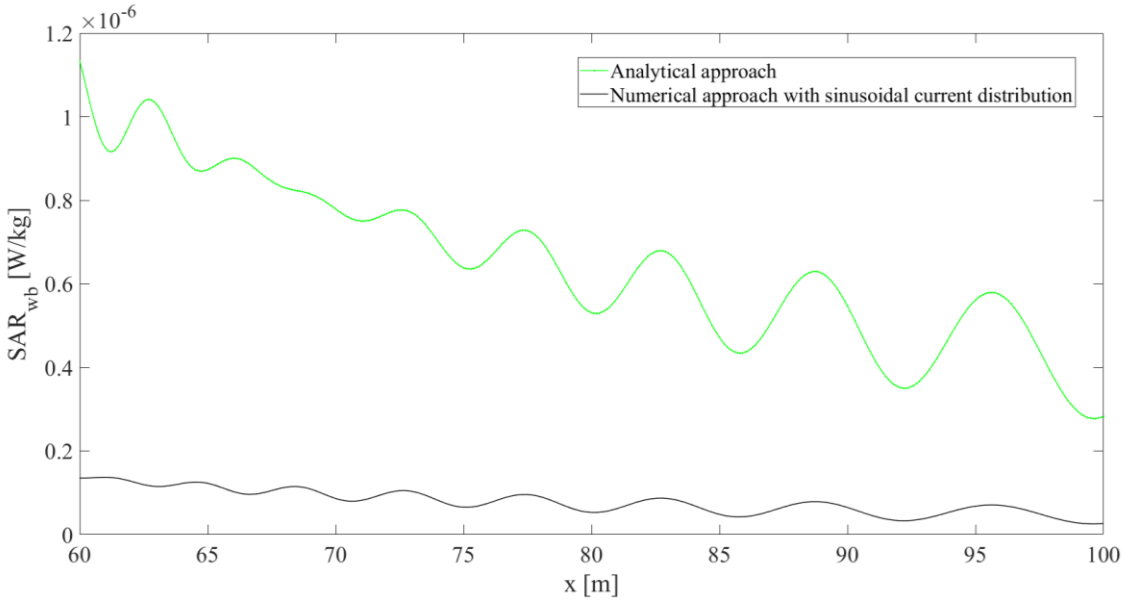

Figure 4.18 SAR_{WB} versus point location in the x-axis for a fixed distance from the source in an z vertical direction z=1.65 m, f=6 GHz, h=20 m, $\frac{L}{\lambda} = \frac{1}{10}$, and sinusoidal current distribution

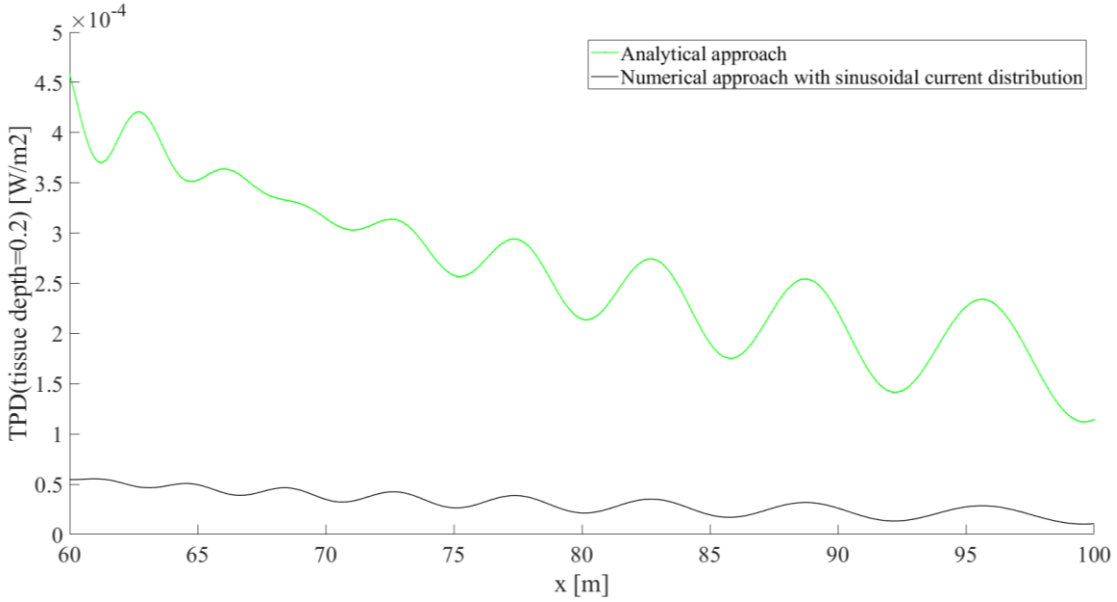

Figure 4.19 TPD_{tot} versus point location in the x-axis for a fixed distance from the source in an z vertical direction z=1.65 m, f=6 GHz, h=20 m, $\frac{L}{\lambda} = \frac{1}{10}$, and sinusoidal current distribution

Spatial distributions for total TPD follows a similar pattern as SAR_{WB} distributions, and the difference between SAR_{WB} values and total TPD values obtained by both models are similar. The proposed analytical model can be used when the dosimetric quantity, that is, the frequency, changes.

4.5 Chapter Summary

Analytical approaches in internal EM dosimetry deal with canonical geometries, such as the planar models, spheres, the cylinders, the spheroids and the ellipsoids, in free space or over an infinite, perfectly conducting ground plane. In this thesis SAR_{WB} is computed by using a simple parallelepiped and cylindrical human body models. Both SAR_{WB} values are below limits defined by ICNIRP in all analyzed cases. Maximum value of SAR_{WB} obtained for approximate analytical and numerical models in parallelepiped is less than $1.6\ 10^{-6}\frac{W}{kg}$. EM dosimetry in parallelepiped human body model is considered as mathematically simpler compared to cylindrical human body model. The small differences in SAR_{WB} values imply that the proposed approaches are useful in getting rapid estimation of the phenomenon in average sense, without significant loss of accuracy.

Furthermore, straightforward calculation of the induced electric field, SAR and TPD values are performed in simple parallelepiped human body model for transition frequency [3], and frequencies that are 50 % away from it.

Undertaken analysis shows that, the absolute values of the field, SAR and TPD within the tissue decrease faster with frequency increase and thus penetrates less into the human body. The results obtained via different approaches agree satisfactorily, thus verifying the proposed simple analytical method. This finding is very interesting since the analytical approach is less demanding in terms of computational cost and could be of interest for more complex antenna configurations arising from various realistic scenarios.

Bearing in mind that the electric field and SAR values obtained by means of analytical approach is higher than the ones corresponding to the results obtained via more rigorous numerical modelling it can be concluded that such an overestimation is acceptable for the health risk assessment. Namely, if the overestimated values do not exceed exposure limits it is ensured that the values stemming from realistic scenarios from either computation or measurement will stay within the proposed limits.

CHAPTER 5

Thermal dosimetry procedures for canonical tissue representation

5.1 Modelling of the heat transfer phenomena in biological tissue

The normal body core temperature is around 37 ℃. This body temperature is the result of equilibrium between heat production and heat loss. If the body temperature stretches so far from normal temperature, death will occur. The temperature nearly 27 ℃ and below and nearly 42 ℃ and above are critical, so the body temperature should be maintained around 37 ℃.

By the definition, the occurrence of storing a larger amount of energy than the thermoregulatory capacity of the human body, is referred to as the thermal effect [48]. Further on, the main effect of exposure to HF fields is heating. The rise of local temperature in tissue may be a consequence of oscillations in the molecules caused by absorbed EM energy [95]. Better understanding of process that actually happens in biological tissues as a result of EM interaction is needed to obtain the increase of tissue temperature and to conclude if the radiation effects are hazard for humans or not. To obtain the desired temperature increase in HF frequency range, it is important to know the time of exposure.

There are numerous models that can be used to describe the process of heat exchange, but the model proposed by Pennes' is widely used, because of its simplicity and acceptable accuracy if no large thermally significant blood vessels are close to the analysed heated region [96]. The PBHE was established by conducting a sequence of experiments measuring temperatures of tissue and arterial blood in the resting human forearm [96, 97]. The equation includes a special term that describes the heat exchange between blood flow and solid tissues. The blood temperature is assumed to be constant arterial blood temperature. A generalized form of the PBHE can be written as [98]:

$$\rho_t c_t \frac{\partial T(\mathbf{X},t)}{\partial t} = \nabla\lambda(\mathbf{X})\nabla[T(\mathbf{X},t)] + \rho_b c_b \omega_b(\mathbf{X})[T_a - T(\mathbf{X},t)] + Q_m(\mathbf{X},t) + Q_r(\mathbf{X},t), \mathbf{X}\epsilon\Omega \tag{5.1}$$

where

- ρ_t is tissue density $\left[\frac{kg}{m^3}\right]$,

- c_t is the specific heat of tissue $\left[\frac{J}{kg°C}\right]$,
- $T(\mathbf{X}, t)$ is the tissue temperature [°C],
- t is the time [s],
- $\lambda(\mathbf{X})$ is the space dependent thermal conductivity $\left[\frac{W}{m°C}\right]$,
- $\mathbf{X}$ contains the Cartesian coordinates x, y and z,
- ρ_b is the density of blood $[\frac{kg}{m^3}]$,
- c_b is the specific heat of blood $[\frac{J}{kg°C}]$,
- $\omega_b(\mathbf{X})$ is the space dependent blood perfusion $[\frac{m^3}{s \cdot kg}]$,
- T_a is the arterial temperature [°C],
- Q_m is the power produced by metabolic process $\left[\frac{W}{m^3}\right]$,
- Q_r is the power deposition of external sources $\left[\frac{W}{m^3}\right]$, and
- Ω is the analyzed spatial domain.

According to (5.1) PBHE describes the energy balance between conductive heat transfer per tissue volume unit ($\nabla\lambda(\mathbf{X})\nabla[T(\mathbf{X}, t)]$), heat loss due to perfusion ($\rho_b c_b \omega_b(\mathbf{X})[T_a - T(\mathbf{X}, t)]$), metabolism ($Q_m(\mathbf{X}, t)$) and energy absorption due to external sources ($Q_r(\mathbf{X}, t)$). In EM studies, external source is usually EM source, and external heat is the result of EM radiation. PBHE derivation is given in the Appendix B.

PBHE was used in numerous studies to predict temperature changes in biological tissue [22, 96, 99-107]. Thermal tissue parameters (blood perfusion rate, the metabolic rate and the thermal conductivity) are assumed to be time and temperature independent. Having in mind above mentioned, the PBHE usually has the following form [95, 96]:

$$\underbrace{\nabla(\lambda\nabla T)}_{\text{heat flux}} + \underbrace{W_b c_b (T_a - T)}_{\text{perfusion rate}} + \underbrace{Q_m}_{\text{metabolism}} + \underbrace{Q_{EM}}_{\text{EM energy}} = \rho_t c_t \frac{\partial T}{\partial t} \tag{5.2}$$

where

- W_b is the volumetric perfusion rate $\left[\frac{1}{s}\right]$, and

- Q_{EM} is the EM power deposition $\left[\frac{W}{m^3}\right]$.

Q_{EM} represents the resistive heat generated by the EM source and is expressed as [95]:

$$Q_{EM} = \frac{\sigma}{2}|E|^2 \tag{5.3}$$

where

- σ is the electric conductivity of the tissue, and
- E is the maximal value of the electric field induced inside the human body.

Dissipated power density Q_{EM} is directly related to SAR, as follows [48]:

$$Q_{EM} = \rho SAR \tag{5.4}$$

For simplicity thermal tissue parameters are assumed to be constant in most of the studies, yet some studies analyse the effects of thermal tissue parameters on temperature change [22, 103, 108-110]. In [111] the effects of thermal conductivity, ambient temperature and blood temperature on steady-state temperature distribution in 2D model of the human eye was numerically analysed. Effects of the thermal conductivity, the blood perfusion, the metabolic heat generation, and the coefficient of heat transfer on the temperature distribution are analysed in [108, 103]. Authors from [112] shown that the gradient of the temperature variation ($\nabla[T(\mathbf{X}, t)]$) decreases with blood perfusion (ω_b) increase. Further on, changes in metabolic heat generation (Q_m) elevates the inner tissue temperature magnitudes but maintains an almost constant slope in the temperature flow path to the boundary regardless the metabolic rate [112]. The effect of thermal conductivity (λ) has the significant and more remarkable effects in temperature variation in living tissue compared to other thermal parameters [113].

To reach PBHE solution the BCs at the interface between tissue types with different electrical and dielectric properties, including the human body and ambient air, needs to be define. Generally, BCs belong to one of three types: BCs of first type (5.5), BCs of second type (5.6) and BCs of third type - convection (5.6).

$$T|_{surface} = T_0 \text{ or } T|_{surface} = f(\mathbf{X}, t) \tag{5.5}$$

$$-\lambda \frac{\partial T}{\partial n}|_{surface} = q_0'' \tag{5.6}$$

$$-\lambda \frac{\partial T}{\partial n}|_{surface} = h(T|_{surface} - T_\infty) \tag{5.7}$$

where

- T_0 is a prescribed constant temperature,
- $T|_{surface} = f(\mathbf{X}, t)$ is the prescribed surface temperature distribution that is, in general, a function of position and time,
- n is the unit outward normal to the surface,
- q_0'' is a prescribed constant heat flux $[\frac{W}{m^2}]$,
- h is the convection coefficient, and
- T_∞ denotes the temperature of the air.

Special case in which $T|_{surface} = 0$ is denoted as homogenous BC of the first type, the special case of zero heat flux at the boundary is called the homogeneous BC of the second type (perfectly insulated or adiabatic surface), and special case of T_∞ is called the homogeneous BC of the third type.

Heat flux is directed to the internal normal, and the minus sign is introduced in (5.7) to make the heat flow a positive quantity in the positive coordinate direction (opposite of the temperature gradient). A positive value corresponds to a heat source, and negative value represent a heat sink (Fig. 46).

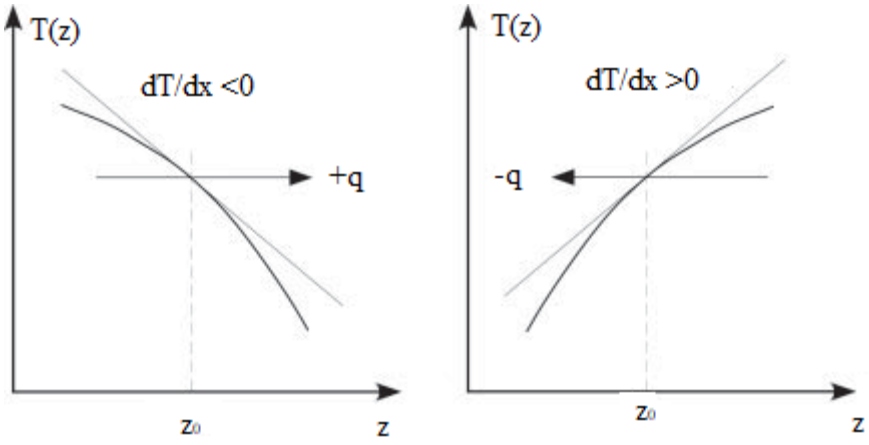

Figure 5.1 Heat flux [94]

The expression $h(T|_{surface} - T_\infty)$ describes convective heat transfer with the surrounding environment. The value of h depends on the geometry and the ambient flow conditions. Heat transfer coefficient varies with the type of flow (laminar, transition, turbulent, etc.), the geometry of the body and flow passage area, the physical properties of the fluid, the average surface and fluid temperatures, and many other parameters. As a result, there is a wide difference in the range of values of the heat transfer coefficient for various

applications. This ambient dependence phenomenon in thermal distribution of biological body produces a distinguishable elevation in skin temperature [112], and the higher the coefficient of heat transfer, the lower the temperature near the boundary of the body.

Fig. 5.2 illustrates BCs for a 1-D plane wall over the domain $0 \leq x \leq \mathrm{L}$. Initially the slab is at a temperature $T = \mathrm{F(x)}$ (BCs of first type) and for times $t > 0$ the boundary surface at $\mathrm{x} = 0$ is exposed to an incident heat flux, while the boundary at $x = \mathrm{L}$ dissipates heat by convection with a heat transfer coefficient h into a zero-temperature fluid ($T_\infty = 0$).

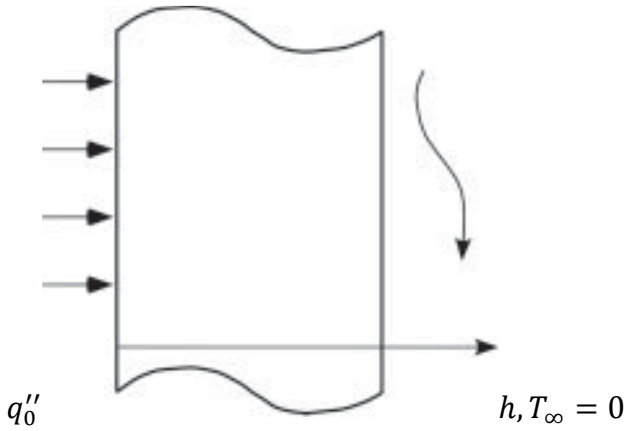

Figure 5.2 Example for BCs formulation for 1-D plane wall [112]

When exposed to external heat sources, the body it reacts with metabolic processes, trying to maintain a stable temperature state. This transition process is called a transient process. After a certain time, a stationary temperature state occurs. In other words, the temperature is constant in respect to time. According to previous mentioned, heat transfer problems are often classified as steady-state and transient (Fig. 5.3).

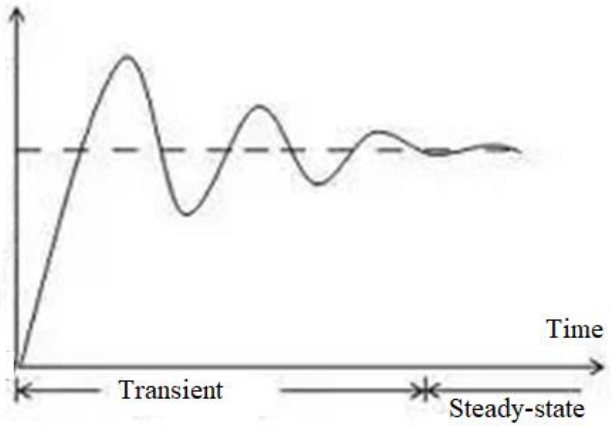

Figure 5.3 Transient vs Steady-state response

The term stationary implies no change with time at any point within the medium, while transient implies variation with time or time dependence. Most heat transfer problems

encountered in practice are transient in nature, but are usually analyzed under some assumed steady-state conditions since stationary processes are easier to analyze. For steady-state solution, PBHE has the form [114]

$$\underbrace{\nabla(\lambda\nabla T)}_{\text{heat flux}} + \underbrace{W_b c_b (T_a - T)}_{\text{perfusion rate}} + \underbrace{Q_m}_{\text{metabolism}} + \underbrace{\rho SAR}_{\text{EM energy}} = 0 \tag{5.8}$$

Analysis of thermal response of biological materials, such as human skin, due to EM radiation is very important not only for understanding of biological processes but also for many clinical applications such as cancer therapy, hyperthermia and cryopreservation [98]. Many authors solve the PBHE assuming steady-state conditions [102, 112, 115-117]. Others authors describe the transient temperature response of tissue for the whole-time domain starting from transient periodic oscillation to the final steady periodic oscillation [100, 118, 119]. In the rest of this section, different approaches to solving for PBHE are presented.

5.2 Solving the Pennes' Bio-Heat transfer equation

As is the case with EM dosimetry, the PBHE can be solved both analytically and numerically. Traditionally, numerical methods are used when analytical solutions are not available, but if both analytical and numerical solutions can be obtained for the same issue, the analytical one is often preferred [9]. Although analytical solutions fail when dealing with complex geometries or nonlinearities, they provide the tools for numerical code testing and also for performing a valuable sensitivity analysis (SA) of the parameters involved in a problem [120].

On the other hand, analytical solution od PBHE requires adoption of appropriate assumptions. Depending on the relative magnitudes of the heat transfer rates in different directions and the desired level of accuracy, heat transfer problems are classified as one-dimensional, two-dimensional, or three-dimensional [121]. In the most general case, heat transfer through a medium is three-dimensional, but for simplicity one-dimensional problems are covered in literature. A heat transfer problem is said to be one-dimensional if the temperature in the medium changes in only one direction and therefore heat is transferred in one direction, and temperature variations and thus heat transfer in other directions are negligible or zero.

The exact solution of one-dimensional PBHE has been given for single-layer model [99, 120, 122, 123], 2-layer model [124], and 3-layer model [98, 102, 110, 125]. To obtain analytical solution most of these studies are considering steady-state or assume a constant heating at skin surface. Pure analytical methods, among others, include the Laplace transform method [100, 102], a method based on Modified PBHE (MPBH) [101], a method based on Bessel functions [108, 112], and SoV [94].

If it is very difficult, or even impossible, to obtain analytical solutions of the PBHE, numerical solutions are attempted. The use of numerical methods is computationally demanding, especially for some complex cases with three-dimensional domains or variable thermophysical properties [9]. Some of the numerical approaches used to solve PBHE include the BEM, the FEM [104, 126], the FDM [127], and MC [9]. Hybrid analytical-numerical methods for PBHE using the methodology of Variational Iteration Method (VIM) are mentioned in [109, 128].

In addition to the mentioned dosimetric methods, it should be emphasized that the beginnings of research in the field of thermal dosimetry are related to experimental dosimetry. Experimental investigations of temperature rise produced in parts of the human body during heat to microwaves of 10 cm and 94 cm wavelength are described in [129]. In [130] cutaneous thresholds for thermal pain were measured in 10 human subjects during 3-s exposures at 94 GHz, and corresponded to an increase in surface temperature of ≈ 9.9°C. Thresholds for thermal damage to the cornea was studied in [131] and the threshold value correspond to temperature increases of about 20 °C at irradiation frequencies, of 35 GHz to 94 GHz, and exposure duration of 1-5 s. Study [132] reports measurements of the skin surface temperature elevations during localized irradiation (94 GHz) of three species: rat (irradiated on lower abdomen), rhesus monkey (posterior forelimb), and human (posterior forearm), and concludes that variable blood flow model, reflecting a dynamic thermoregulatory response, may be more suited to describing skin surface temperature response under long-duration MMW irradiation.

The basic idea behind numerical, hybrid and analytical approaches is presented in the rest of this chapter. First, short description for numerical and hybrid approaches is given, followed by detailed explanation of some of the analytical methods.

5.2.1 Numerical methods in thermal dosimetry

Numerical techniques are applicable to almost all scientific engineering problems, but the main drawbacks are related to the approximation limitation within the model itself, space and time discretization [133]. The application of classical numerical methods (FEM, FDM, and BEM) for solving Pennes' equation is explained below.

The finite element formulation of steady-state PBHE starts by multiplying (5.8) by a set of weighting functions and integrating over the domain, after some work, a suitable expression for the FEM implementation is [134]:

$$\iiint_{\Omega} \lambda \nabla T \cdot \nabla W_j d\Omega + \iiint_{\Omega} W_b T W_j d\Omega + \iiint_{\partial\Omega} h_s T W_j dS = \iiint_{\Omega} (W_b T_a + Q_m + Q_{EM}) W_j d\Omega + \iiint_{\partial\Omega} h_s T_{air} W_j dS \quad (5.9)$$

where

– W_j is the weighting function.

FEM is widely used because it can compute complex shapes well, such as the human head [134, 135] or eye [136], but the main disadvantage of the method is that it requires domain discretization which may give rise to high computational cost.

FDM can be applied to EM problems with different boundary shapes, different kinds of BCs, and regions containing a number of different materials. Method is based on the approximation of the function derivatives using the finite differences, that is, a differential equation is replaced by a finite difference equation [133]. In case of (5.8) second order temperature derivative is replaced as in (5.10)

$$\nabla^2 u = \frac{\partial^2 u}{\partial x^2} + \frac{\partial^2 u}{\partial y^2} \approx \frac{u_{i+1,j} + u_{i-1,j} - 2u_{i,j}}{h^2} + \frac{u_{i,j+1} + u_{i,j-1} - 2u_{i,j}}{h^2} \tag{5.10}$$

where

- $\nabla^2 u$ at node (i, j) is replaced by an algebraic finite-difference operation of the function at adjacent nodes.

It was reported that FDM is more efficient than the FEM by a factor of 2 in computer storage for calculating the propagation constants and fields of a dielectric wave guide [137]. If the region contains different materials and complex shapes, the FDM application becomes more complicated. If the field contains rapid changes of gradient, the accuracy declines. In these cases, the FEM is preferred.

BEM involves the discretization of the domain boundary into elements, which is an important advantage of this method [133]. BEM algorithm for PBHE is given with integral equation [138]

$$B(\xi)T(\xi) + \int_\Gamma T^*(\xi, x) q(x) d\Gamma = \int_\Gamma q^*(\xi, x) T(x) d\Gamma + \int_\Omega [Q - gT(x)] T^*(\xi, x) d\Omega \tag{5.11}$$

where

- ξ is the observation point,
- $B(\xi) \epsilon (0, 1]$,
- $T^*(\xi, x)$ is the fundamental solution,
- $q(x) = -\lambda \frac{\partial T(x)}{\partial n}$ is the heat flux, and

- $q^*(\xi, x) = -\lambda \frac{\partial T^*(\xi,x)}{\partial n}$ is the heat flux resulting from the fundamental solution.

Some illustrative numerical examples of BEM implementation are given in [48, 49, 138, 139]. BEM requires a more complex formulation and related numerical implementation as it is computationally more expensive then FDM and FEM [140].

Based on the above-mentioned, numerical methods are an excellent tool for solving bio-heat transfer problems, but their general applicability requires a special care to handle the complicated geometry and properties of the biological bodies. Trying to integrate the advantages of numerical and analytical approaches some studies suggest hybrid methods, such as VIM.

5.2.2 Hybrid methods in thermal dosimetry

VIM application starts from a dimensionless relation for the evaluation of temperature in the tissue ((5.12) and (5.13)), together with associated BCs ((5.14)).

$$x' = \frac{x}{L}, t' = \frac{t}{t*}, \theta = \frac{T - T_0}{T_a - T_0} \tag{5.12}$$

$$\frac{\partial \theta}{\partial t} = \lambda \frac{\partial}{\partial x}\left(\frac{\partial}{\partial x}\right) + \alpha(1 - \theta) + Q_1 + Q_2 \tag{5.13}$$

$$\theta(x, 0) = x, \theta(0, t) = 0, \theta(L, t) = 0 \tag{5.14}$$

In this sense, the nonlinear partial differential equation (PDE) is observed in which $L\theta(x, t)$ is linear operators, $N\theta(x, t)$ is a nonlinear operator and $g(x, t)$ is inhomogeneous term.

$$L\theta(x, t) + N\theta(x, t) = g(x, t) \tag{5.15}$$

By using the correlation function, successive approximations are established by determining the Lagranian multiplier by variational theory. Applying VIM to relation (5.15), i.e. constructing a correlation function in the x direction, the iteration formula in the x direction is determined, and using initial conditions, the desired number of iterations of the solution can be determined to the desired levels of accuracy [128].

Even computationally less demanding compared to pure numerical method, in some practical situations simple and fast solution for temperature distribution may be required. Therefore, the focus of the next subsection is on analytical methods, and they are described in more detail.

5.2.3 Analytical methods in thermal dosimetry

Analytic solutions of bio-heat transfer equations are difficult to obtain in general, due to process complexity, and in many equations only numerical methods are applicable. However, as already stated, analytic solutions are of important not only because they can accurately reflect the actual physical feature of equations but they are valuable tool in verification the corresponding results of numerical calculation. In vivo measurements are certainly impossible.

Various techniques have been proposed to obtain analytical solutions of the PBHE. The one-dimensional heat transport equation has been solved in [141] using the Fourier transform for a semi-infinite plane, and the effects of thermal convection due to blood flow and transfer of heat from the tissue surface into space on the steady-state temperature distribution in the tissue is analyzed. In [9] Green's function method is used to obtained several closed form analytical solutions to the bio-heat transfer problems with stationary or transient heating on skin surface or inside biological bodies. By using the Laplace transform, the analytical solution of the PBHE with surface sinusoidal heating condition is found in [100]. Investigation of the analytical solution of the temperature elevation for parametric analysis in one-dimensional human model started in [102], and continued in [115] with one-dimensional 3-layer (skin, fat and muscle) and one-layer (skin only) models. Obtained analytical solution can provide insights of thermal behaviour of living tissues and it useful to easily and accurately study the thermal behaviour of the biological system [101].

The computational procedure has been applied to study the exposure of a 3-layer model composed by skin, subcutaneous adipose tissue (SAT) and muscle, both at 100 GHz and 1 THz in [22]. A temperature-based technique for the evaluation of safety compliance is proposed in [27]. Authors from [142] concluded that dielectric properties of adipose tissue in multilayer plane model do not impact on temperature elevation at frequencies over 30 GHz. A revision of the 1-D problem described in [141] along with a comprehensive mathematical derivation of analytical solution, and extension to irradiation of multiple electromagnetic heating pulses is offered in [107]. A simple, analytical method is proposed to determine the temperature increase in human tissue based on the wave matrix method in [73].

The basic idea behind some of aforementioned analytical approaches along with their advantages and disadvantages is presented in the rest of this section.

The Laplace transform (L) of function $f(t)$ denoted by $F(s)$, s being the complex variable is defined as:

$$\mathrm{F(s)} = \bar{\mathrm{f}}(\mathrm{s}) = \mathrm{L\{f(t); s\}} = \int_0^\infty \mathrm{e}^{-\mathrm{st}}\mathrm{f(t)dt; t} \in \mathrm{R}^+ \tag{5.16}$$

Inverse Laplace transform (L^{-1}) of $F(s)$ is defined as:

$$f(t) = \{F(s); t\} = \frac{1}{2\pi i}\int_{\gamma-i\infty}^{\gamma+i\infty} e^{st}F(s)ds; t \in R^{+}, \gamma = R(s) \tag{5.17}$$

where

- s is the Laplace transform variable, and
- γ is a positive number

Temperature elevations at a steady-state for the one-dimensional single-layer and one-dimensional 3-layer human tissue models obtained via Laplace transform method were offered in [100] and in [102] respectively:

$$T(x) = T_a + \frac{q_0}{\sqrt{4\lambda W_b c_b}}\left[e^{-\sqrt{\frac{W_b c_b}{\lambda}}}\operatorname{erfc} x\left(\frac{x}{\sqrt{4\alpha t}} - \sqrt{\frac{W_b c_b}{\rho_t c_t}t}\right) - e^{-\sqrt{\frac{W_b c_b}{\lambda}}}\operatorname{erfc}\left(\frac{x}{\sqrt{4\alpha t}} + \sqrt{\frac{W_b c_b}{\rho_t c_t}t}\right)\right] \tag{5.18}$$

$$T_n(z) = T_n(0)\cosh\sqrt{\frac{b_n}{\lambda_n}}z + T_n'(0)\frac{1}{\sqrt{\frac{b_n}{\lambda_n}}}\sinh\sqrt{\frac{b_n}{\lambda_n}}z + \left(T_b + \frac{A_n}{b_n}\right)\left(1 - \cosh\sqrt{\frac{b_n}{\lambda_n}}z\right) + S_n(z) \tag{5.19}$$

where

- q_0 is constant heat flux on the skin surface,
- erfc is the complementary error function,
- $\alpha = \frac{\lambda}{\rho_t c_t}$ dimensionless variables
- $T_n(0)$ denotes temperature in tissue n and z=0,
- b_n is the term associated with blood flow,
- $T_n'^{(0)} = \left.\frac{\partial T_n(z)}{\partial z}\right|_{z=0}$, and
- $S_n(z)$ denotes the term related to the plane wave exposure.

Although the application of the Laplace transform for the removal of the partial derivative is a relatively straightforward matter, the inversion of the transformed solution generally is rather involved unless the inversion is available in the standard Laplace transform tables.

Bessel functions under certain conditions, describe the PBHE solution. In [108] the Bessel functions, described the PBHE solution for one-dimensional cylindrical living tissues $(\mathrm{r}, \theta, \mathrm{z})$ in the steady-state:

$$T(\mathrm{r}) = \mathrm{T}_\infty + (\mathrm{T}_\mathrm{a} - \mathrm{T}_\infty)\left(1 + \frac{\mathrm{Q}_\mathrm{m}^*}{\mathrm{w}_\mathrm{b}^*}\right)\left[1 - \frac{\mathrm{J}_0\left(\sqrt{\mathrm{w}_\mathrm{b}^*}\frac{\mathrm{r}}{\mathrm{R}}\right)}{\mathrm{J}_0\left(\sqrt{\mathrm{w}_\mathrm{b}^*}\right) + \frac{\sqrt{\mathrm{w}_\mathrm{b}^*}}{\mathrm{h}^*}\mathrm{J}_1\left(\sqrt{\mathrm{w}_\mathrm{b}^*}\right)}\right] \tag{5.20}$$

where

- $\mathrm{Q}_\mathrm{m}^* = \frac{\mathrm{QR}^2}{\lambda(\mathrm{T}_\mathrm{a} - \mathrm{T}_\infty)}$,
- $\mathrm{w}_\mathrm{b}^* = \frac{\mathrm{W}_\mathrm{b}\mathrm{c}_\mathrm{b}\mathrm{R}^2}{\lambda}$,
- $\mathrm{h}^* = \frac{\mathrm{hR}}{\lambda}$,
- J_0 is the Bessel function of the zero order first kind, and
- J_1 is the Bessel function of the first order first kind.

Since Bessel functions can be computed using approximated polynomials, this solution may be difficult to perform some parametric study, and simpler analytical solution would be also favoured.

The SoV method has been widely used in the solution of heat conduction problems and it is suitable for homogeneous PDE, or multi-dimensional steady-state heat conduction PDE with no generation and if only one of the BCs is nonhomogeneous [94]. Problems involving more than one nonhomogeneous BC can be split up into simpler problems using the principle of superposition. To apply the solution structure theorem and the SoV method, the BCs must be linear, homogeneous, separable, and with constant coefficients [10].

Pennes' Bio-heat equitation can be solved analytically for all homogeneous layer in one-dimensional multi-layer models, by exploiting the classical theory of ordinary differential equations. Inside each layer, steady-state temperature elevation is given by the superposition of the solution related to the homogeneous linear equation and the particular solutions. In order to determine the values of constant in solution related to the homogeneous linear equation in each biological layer (for a total of *2N* values), the resulting solution must be forced to satisfy the proper BCs (constant variation method). The method of constant variation is very suitable for linear systems, while it is more difficult to apply this approach to non-linear systems [24]. Further on, mathematic simplicity of this methods enables parametric analysis, and one example is reported in

[22]. On the other hand, this solution is suitable for steady-state temperature elevation.

Prediction of heat transport has long been carried out by both analytical and numerical methods. Although analytical solutions fail when dealing with complex geometries or nonlinearities, they provide the tools for numerical code testing and also for performing a proper sensitivity analysis of the parameters involved in a problem. To simplify the mathematical model, some assumptions must be made, such as: the skin tissue is homogeneous and isotropic, the skin tissue properties are independent of skin temperature, heat generated by metabolism is constant, blood perfusion rate is uniform spatially and temporally and independent of tissue temperature, and arterial blood temperature is constant. In most of the existing analytical studies, the solutions to the bio-heat transfer problem are available for the cases with one dimensional geometry, steady-state, and constant heating.

Even if the solution method is the author's choice, the application of some methods requires the fulfilment of certain conditions, and the choice of method itself depends on the chosen human body model and thermal properties of the exposed body model. Next section deals with to the description of the analytical approach for solving PBHE used in our study.

5.3 Thermal dosimetry - Analytical procedure

In the framework of thermal dosimetry the stationary one-dimensional PBHE in biological tissues is considered. This approach does not take into account dependence. The simplicity of the mathematical expression facilitates parametric analysis [102] and provides relatively simple analysis in multi-layer tissue modelling [22]. The case of a single-layer and 3-layer human body model is considered and depicted in Fig. 49 and Fig. 50, respectively.

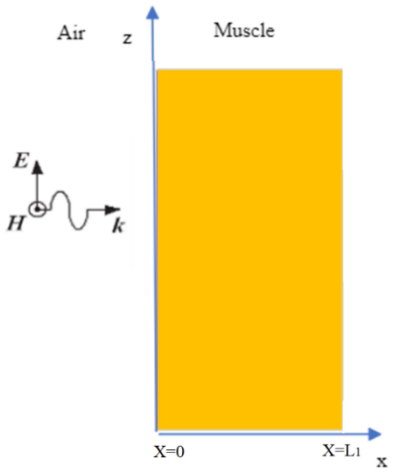

Figure 5.4 Geometry of the single-layer problem

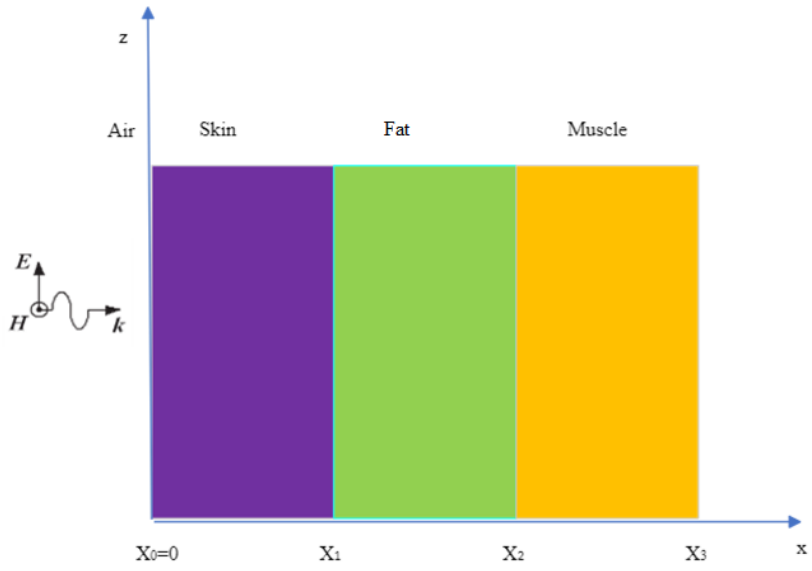

Figure 5.5 Geometry of the 3-layer human body model

The both models are derived under the assumption that the tissues inside human body are homogeneous and isotropic, that the properties of the tissues are independent of the skin temperature, that the heat generated by metabolism is constant, that the blood perfusion rate is uniform spatially and temporally and independent of the tissue temperature, and that arterial blood temperature is constant. The human body is assumed to be at a constant initial temperature until the start-up of the EM exposure process. In rest of this chapter, for models shown on Fig. 49 and Fig. 50, the mathematical details are presented.

Our goal is to analytically solve the PBHE in single-layer human body model (with muscle tissue characteristics), and in a planar 3-layer human body model (composed of skin-fat-muscle tissue). The solution of PBHE variant used in the thesis is encompasses three steps

- reduce the number of parameters in the parametric analysis, by observing the state before exposure to the EM field (described by the constant temperature in all tissues for single-layer and 3-layer model), and then
- introduce a new variable related to the temperature change in the stationary state in relation to the state before exposure to the EM field, instead of observing the final temperature in the stationary state.

Now starting from one-dimensional steady-state PBHE [143]

$$\lambda\frac{\left(\partial^2 \mathrm{T(x)}\right)}{\partial \mathrm{x}^2} + \mathrm{h_b}\left(\mathrm{T_b} - \mathrm{T(x)}\right) + \mathrm{Q_m} + \mathrm{SAR(x)}\rho = 0 \tag{5.21}$$

we assume that the basic temperature of human body before EM exposure was T_a (constant in all parallelepiped human body model and for single-layer and 3-layer geometry). Temperature change due to EM exposure is:

$$u(x) = T(x) - T_a \tag{5.22}$$

where

- $T(x)$ is a steady-state temperature in human body and it is function of depth.

Inserting $T(x) = u(x) + T_a$ in (5.21), one obtains the following set of relations: (5.26).

$$\lambda \frac{\partial^2}{(\partial x^2)} (u(x) + T_a) - h_b\big(u(x)\big) + Q_m + SAR(x)\rho = 0 \tag{5.23}$$

$$\frac{\partial^2 u(x)}{\partial x^2} - \frac{h_b}{\lambda}\, u(x) = -\left[\frac{\rho SAR(x) + Q_m}{\lambda}\right] \tag{5.24}$$

$$-\left[\frac{\rho SAR(x) + Q_m}{\lambda}\right] = f(x) \tag{5.25}$$

$$u''(x) - \frac{h_b}{\lambda} u(x) = f(x) \tag{5.26}$$

The resulting modified equation (5.26) describing the heat transfer in tissue can be solved analytically for single-layer geometry and 3-layer geometry using the classical theory of ordinary differential equations. The temperature elevation is described by the superposition of the solution of the homogeneous linear equation and the solution of the particular linear equation (within each tissue layer)

$$u(x,t) = u_H(x,t) + u_P(x,t) \tag{5.27}$$

where

- $u(x,t)$ is the temperature elevation presented by the nonhomogeneous bio-heat problem,
- $u_H(x,t)$ is the general solution of the corresponding homogeneous equation, and
- $u_P(x,t)$ represents the particular solutions of the corresponding nonhomogeneous equation.

The general solution of homogeneous differential equation is given in the form:

$$u_{Hi}(x) = A_i e^{-\sqrt{\frac{h_{bi}}{\lambda_i}}x} + B_i e^{\sqrt{\frac{h_{bi}}{\lambda_i}}x},\ i=1,2,3 \tag{5.28}$$

The value of the constants in the (5.28) in each tissue layer in human body can be determined using appropriate BCs at the boundaries between two layers. This method is

called the variation of constants and is very suitable for linear systems, while it is more difficult to apply this approach to non-linear systems [24].

To solve the Pennes' equation analytically, power density from external heat source related to the absorbed part of EM energy irradiated from VED antenna, is assumed to either be constant, or exponentially decreasing with the tissue depth. Since *f(x)* (from (5.25) and (5.26)) depends of SAR(x) and some constants, and SAR(x) is known, *f(x)* is further assumed to be constant or exponential decaying function, which further implies

$$u_{PM1}(x) = \text{Const} \tag{5.29}$$

$$u_{PM2}(x) = Ce^{-2x} + D \tag{5.30}$$

As (5.29) and (5.20) must also satisfy (5.26) it follows:

$$u_{PM1i}(x) = \frac{\rho_i SARi_{max}}{h_{bi}} + \frac{Q_{mi}}{h_{bi}} \tag{5.31}$$

$$u_{PM2i}(x) = -\left(\frac{\rho_i SAR_{imax}}{4\lambda_i - h_{bi}}\right) e^{-2x} + \frac{Q_{mi}}{h_{bi}} \tag{5.32}$$

The total solutions for temperature elevation and resulting steady-state temperature with assumed constant EM power density throughout the tissues in human body are given by:

$$u_{M1i}(x) = A_{M1i} e^{-\sqrt{\frac{h_{bi}}{\lambda_i}}x} + B_{M1i} e^{\sqrt{\frac{h_{bi}}{\lambda_i}}x} + \frac{\rho_i SAR_{maxi}(x) + Q_{mi}}{h_{bi}}, i = 1,2,3 \tag{5.33}$$

$$T_{M1i}(x) = A_{M1i} e^{-\sqrt{\frac{h_{bi}}{\lambda_i}}x} + B_{M1i} e^{\sqrt{\frac{h_{bi}}{\lambda_i}}x} + \frac{\rho_i SAR_{maxi}(x) + Q_{mi}}{h_{bi}} + T_a, \quad i=1,2,3 \tag{5.34}$$

The total solution for the temperature elevation and resulting steady-state temperature with assumed EM power density that exponentially decays with the tissue depth are given by:

$$u_{M2i}(x) = A_{M2i} e^{-\sqrt{\frac{h_{bi}}{\lambda_i}}x} + B_{M2i} e^{\sqrt{\frac{h_{bi}}{\lambda_i}}x} - \left(\frac{\rho_i SAR_{imax}}{4\lambda_i - h_{bi}}\right) e^{-2x} + \frac{Q_{mi}}{h_{bi}}, \quad i=1,2,3 \tag{5.35}$$

$$T_{M2i}(x) = A_{M2i}e^{-\sqrt{\frac{h_{bi}}{\lambda_i}}x} + B_{M2i}e^{\sqrt{\frac{h_{bi}}{\lambda_i}}x} - \left(\frac{\rho_i SAR_{imax}}{4\lambda_i - h_{bi}}\right)e^{-2x} + \frac{Q_{mi}}{h_{bi}} + T_a \quad (5.36)$$

i=1,2,3

where

- ρ is the density of muscle tissue for single-layer geometry,
- $\rho_i, i = 1,2,3$ is the density for skin, fat and muscle for 3-layer geometry,
- $SAR_i, i = 1,2,3$ is the maximum SAR at the surface of skin, fat and muscle tissue for 3-layer geometry,
- $Q_{mi}, i = 1,2,3$ is the metabolic heat generated in skin, fat and muscle tissue for 3-layer geometry, and
- $h_{bi}, i = 1,2,3$ is blood perfusion in skin, fat and muscle tissue for 3-layer geometry.

Maximum SAR value at surface of skin, fat and muscle tissue are:

$$SAR_1(X_0 = 0) = SAR_{MAX} \quad (5.37a)$$

$$SAR_2(X_1 = d_1) = SAR_{MAX}e^{-2d_1} \quad (5.37b)$$

$$SAR_3(X_2 = d_2) = SAR_{MAX}e^{-2d_1}e^{-2d_2} \quad (5.37c)$$

Constants A_i and B_i for single-layer and for 3-layer geometry, can be defined by prescribing BCs:

BC: Air-Skin ($x_0 = 0$)

$$-\lambda_1 \frac{\partial T_i}{\partial x}(x_0 = 0) = h(T_i(x_0 = 0) - T_{air}) \quad (5.38)$$

BC: Skin-SAT and SAT-Muscle ($x_1 = d_1, x_2 = d_2$)

$$\lambda_{i-1}\frac{\partial T_{i-1}}{\partial x}(x_i^-) = \lambda_i \frac{\partial T_i}{\partial x}(x_i^+) \quad (5.39)$$

$$T_i(x_i^-) = T_i(x_i^+) \quad (5.40)$$

BC 4: At penetration depth

$$T_3(x_3 = d_3 = L_1) = T_a \tag{5.41}$$

The total solution for steady-state temperature with assumed constant EM power density throughout the tissues in human body

$$T_{M1}(x) = A_{M1} e^{-\sqrt{\frac{h_b}{\lambda}}x} + B_{M1} e^{\sqrt{\frac{h_b}{\lambda}}x} + \frac{\rho\ SAR_{max(x)} + Q_m}{h_b} + T_a \tag{5.42}$$

$$A_{M1} = \left(- \frac{-\frac{h}{\lambda}(s_1 + T_a - T_{air}) + s_4 \left(s_1 e^{\sqrt{\frac{h_b}{\lambda}}L_1} \right)}{\left\{ s_3 - s_4 e^{2\sqrt{\frac{h_b}{\lambda}}L_1} \right\}} e^{2\sqrt{\frac{h_b}{\lambda}}L_1} - \frac{\rho\ SAR_{max} + Q_m}{h_b} e^{\sqrt{\frac{h_b}{\lambda}}L_1} \right) \tag{5.43}$$

$$B_{M1} = \frac{-\frac{h}{\lambda}(s_1 + T_a - T_{air}) + s_4 \left(s_1 e^{\sqrt{\frac{h_b}{\lambda}}L_1} \right)}{\left\{ s_3 - s_4 e^{2\sqrt{\frac{h_b}{\lambda}}L_1} \right\}} \tag{5.44}$$

Details of the mathematical procedure used to obtain the solution for the steady-state temperature in single-layer human body with assumed constant EM power density throughout the tissues are given in Appendix C.

The total solution for the steady-state temperature with assumed EM power density that exponentially decays with the tissue depth is given by following relation:

$$T_{M2}(x) = A_{M2} e^{-\sqrt{\frac{h_b}{\lambda}}x} + B_{M2} e^{\sqrt{\frac{h_b}{\lambda}}x} - \left(\frac{\rho\ SAR_{max}}{4\lambda - h_b} \right) e^{-2x} + \frac{Q_m}{h_b} \tag{5.45}$$

$$A_{M2} = - \frac{-\frac{h}{\lambda}\left(-s_2 + \frac{Q_m}{h_b} + T_a - T_{air} \right) - 2s_2 - s_4 \left\{ s_2 e^{-2L_1} e^{\sqrt{\frac{h_b}{\lambda}}L_1} - \frac{Q_m}{h_b} e^{\sqrt{\frac{h_b}{\lambda}}L_1} \right\}}{\left\{ s_3 - s_4 e^{2\sqrt{\frac{h_b}{\lambda}}L_1} \right\}} e^{2\sqrt{\frac{h_b}{\lambda}}L_1} + s_2 e^{-2L_1} e^{\sqrt{\frac{h_b}{\lambda}}L_1} - \frac{Q_m}{h_b} e^{\sqrt{\frac{h_b}{\lambda}}L_1} \tag{5.46}$$

$$B_{M1} = \frac{-\frac{h}{\lambda}\left(-s_2 + \frac{Q_m}{h_b} + T_a - T_{air}\right) - 2s_2 - s_4\left\{ s_2 e^{-2L_1}\sqrt{\frac{h_b}{\lambda}} e^{\sqrt{\frac{h_b}{\lambda}}L_1} - \frac{Q_m}{h_b} e^{\sqrt{\frac{h_b}{\lambda}}L_1} \right\}}{\left\{ s_3 - s_4\, e^{2\sqrt{\frac{h_b}{\lambda}}L_1} \right\}} \tag{5.47}$$

where coefficients

- $s_1 = \frac{\rho SAR_{max} + Q_m}{h_b}$
- $s_2 = \frac{\rho\ SAR_{max}}{(4\lambda_1 - h_{b1})}$
- $s_3 = \left(\sqrt{\frac{h_b}{\lambda}} + \frac{h}{\lambda}\right)$, and
- $s_4 = \left(\frac{h}{\lambda} - \sqrt{\frac{h_b}{\lambda}}\right)$.

Further mathematical details are available in Appendix D. The resulting solutions for steady-state temperature after EM exposure in skin, fat and muscle tissue with assumed constant EM power density throughout skin, fat and muscle respectively are:

$$T_1(x) = A_1 e^{-\sqrt{\frac{h_{b1}}{\lambda_1}}x} + B_1 e^{\sqrt{\frac{h_{b2}}{\lambda_1}}x} + \frac{\rho_1 SAR_{max1} + Q_{m1}}{h_{b1}} + T_a, \quad X_0 \le x \le X_1 \tag{5.50}$$

$$T_2(x) = A_2\, e^{-\sqrt{\frac{h_{b2}}{\lambda_2}}x} + B_2\, e^{\sqrt{\frac{h_{b2}}{\lambda_2}}x} + \frac{\rho_2 SAR_{max2} + Q_{m2}}{h_{b2}} + T_a, \quad X_1 \le x \le X_2 \tag{5.51}$$

$$T_3(x) = A_3 e^{-\sqrt{\frac{h_{b3}}{\lambda_3}}x} + B_3\, e^{\sqrt{\frac{h_{b3}}{\lambda_3}}x} + \frac{\rho_3 SAR_{max3} + Q_{m3}}{h_{b3}} + T_a,\ X_2 \le x \le X_3 \tag{5.52}$$

The coefficients used in (5.50), (5.51), and (5.52) are given in Table 5.1.

Table 5.1 Coefficients used in (5.50), (5.51), and (5.52)

A_1	$0.5e^{\sqrt{\frac{h_{b1}}{\lambda_1}}d_1}\{a_{11}\, B_3 + a_{12}\}$
B_1	$0.5e^{-\sqrt{\frac{h_{b1}}{\lambda_1}}d_1}\{b_{11}B_3 + b_{12}\}$

A_2	$0.5e^{\sqrt{\frac{h_{b2}}{\lambda_2}}d_2}[a_{21}B_3 + a_{22}]$
B_2	$0.5e^{-\sqrt{\frac{h_{b2}}{\lambda_2}}d_2}[b_{21}B_3 + b_{22}\,]$
A_3	$-B_3\, e^{2l_{31}} - s_3 e^{l_{31}}$
B_3	$\frac{-a_{12}0.5e^{\sqrt{\frac{h_{b1}}{\lambda_1}}d_1} + 0.5c_1b_{12}e^{-\sqrt{\frac{h_{b1}}{\lambda_1}}d_1} + c_2(s_1+T_a-T_{air})}{\left(0.5a_{11}e^{\sqrt{\frac{h_{b1}}{\lambda_1}}d_1} - 0.5b_{11}c_1e^{-\sqrt{\frac{h_{b1}}{\lambda_1}}d_1}\right)}$
a_{11}	$\left[0.5a_{21}\left(1+\sqrt{\frac{\lambda_1 h_{b2}}{\lambda_2 h_{b1}}}\right)e^{\sqrt{\frac{h_{b2}}{\lambda_2}}d_2}e^{-\sqrt{\frac{h_{b2}}{\lambda_2}}d_1} + 0.5b_{21}\left(1-\sqrt{\frac{\lambda_1 h_{b2}}{\lambda_2 h_{b1}}}\right)e^{-\sqrt{\frac{h_{b2}}{\lambda_2}}d_2}e^{\sqrt{\frac{h_{b2}}{\lambda_2}}d_1}\right]$
a_{12}	$0.5a_{22}\left(1+\sqrt{\frac{\lambda_1 h_{b2}}{\lambda_2 h_{b1}}}\right)e^{\sqrt{\frac{h_{b2}}{\lambda_2}}d_2}e^{-\sqrt{\frac{h_{b2}}{\lambda_2}}d_1} + 0.5b_{22}\left(1-\sqrt{\frac{\lambda_1 h_{b2}}{\lambda_2 h_{b1}}}\right)e^{-\sqrt{\frac{h_{b2}}{\lambda_2}}d_2}e^{\sqrt{\frac{h_{b2}}{\lambda_2}}d_1} + \frac{\rho_2 SAR_{max2}+Q_{m2}}{h_{b2}} - \frac{\rho_1 SAR_{max1}+Q_{m1}}{h_{b1}}$
b_{11}	$\left[0.5a_{21}\left(1-\sqrt{\frac{\lambda_1 h_{b2}}{\lambda_2 h_{b1}}}\right)e^{\sqrt{\frac{h_{b2}}{\lambda_2}}d_2}e^{-\sqrt{\frac{h_{b2}}{\lambda_2}}d_1} + 0.5b_{21}\left(1+\sqrt{\frac{\lambda_1 h_{b2}}{\lambda_2 h_{b1}}}\right)e^{-\sqrt{\frac{h_{b2}}{\lambda_2}}d_2}e^{\sqrt{\frac{h_{b2}}{\lambda_2}}d_1}\right]$
b_{12}	$0.5a_{22}\left(1-\sqrt{\frac{\lambda_1 h_{b2}}{\lambda_2 h_{b1}}}\right)e^{\sqrt{\frac{h_{b2}}{\lambda_2}}d_2}e^{-\sqrt{\frac{h_{b2}}{\lambda_2}}d_1} + 0.5b_{22}\left(1+\sqrt{\frac{\lambda_1 h_{b2}}{\lambda_2 h_{b1}}}\right)e^{-\sqrt{\frac{h_{b2}}{\lambda_2}}d_2}e^{\sqrt{\frac{h_{b2}}{\lambda_2}}d_1} + \frac{\rho_2 SAR_{max2}+Q_{m2}}{h_{b2}} - \frac{\rho_1 SAR_{max1}+Q_{m1}}{h_{b1}}$
a_{21}	$\left(1-\sqrt{\frac{\lambda_2 h_{b3}}{\lambda_3 h_{b2}}}\right)e^{\sqrt{\frac{h_{b3}}{\lambda_3}}d_2} - e^{2l_{31}}\left(1+\sqrt{\frac{\lambda_2 h_{b3}}{\lambda_3 h_{b2}}}\right)e^{-\sqrt{\frac{h_{b3}}{\lambda_3}}d_2}$
a_{22}	$-s_3\left(1+\sqrt{\frac{\lambda_2 h_{b3}}{\lambda_3 h_{b2}}}\right)e^{-\sqrt{\frac{h_{b3}}{\lambda_3}}d_2}e^{l_{31}} + \frac{\rho_3 SAR_{max3}+Q_{m3}}{h_{b3}} - \frac{\rho_2 SAR_{max2}+Q_{m2}}{h_{b2}}$
b_{21}	$\left[\left(1+\sqrt{\frac{\lambda_2 h_{b3}}{\lambda_3 h_{b2}}}\right)e^{\sqrt{\frac{h_{b3}}{\lambda_3}}d_2} - \left(1-\sqrt{\frac{\lambda_2 h_{b3}}{\lambda_3 h_{b2}}}\right)e^{-\sqrt{\frac{h_{b3}}{\lambda_3}}d_2}\, e^{2l_{31}}\right]$
b_{22}	$-s_3 e^{l_{31}}\left(1-\sqrt{\frac{\lambda_2 h_{b3}}{\lambda_3 h_{b2}}}\right)e^{-\sqrt{\frac{h_{b3}}{\lambda_3}}d_2} + \frac{\rho_3 SAR_{max3}+Q_{m3}}{h_{b3}} - \frac{\rho_2 SAR_{max2}+Q_{m2}}{h_{b2}}$

l_{31}	$\sqrt{\frac{h_{b3}}{\lambda_3}}L_1$
s_1	$\frac{\rho_1 SAR_{max1} + Q_{m1}}{h_{b1}}$
s_2	$\frac{\rho_2 SAR_{max2} + Q_{m2}}{h_{b2}}$
s_3	$\frac{\rho_3 SAR_{max3} + Q_{m3}}{h_{b3}}$
c_1	$\frac{\sqrt{\lambda_1 h_{b1}} + h}{\sqrt{\lambda_1 h_{b1}} - h}$
c_2	$\frac{h}{\sqrt{\lambda_1 h_{b1}} - h}$

The resulting solutions for steady-state temperature after EM exposure in skin, fat and muscle tissue with assumed EM power density that exponentially decays with the tissue depth are:

$$T_1(x) = A_{M21}e^{-\sqrt{\frac{h_b}{\lambda_1}}x} + B_{M21}e^{\sqrt{\frac{h_b}{\lambda_1}}x} - \left(\frac{\rho_1 SAR_{1max}}{4\lambda_1 - h_{b1}}\right)e^{-2x} + \frac{Q_{m1}}{h_{b1}} + T_a, \quad X_0 \le x \le X_1 \tag{5.53}$$

$$T_2(x) = A_{M22}\, e^{-\sqrt{\frac{h_b}{\lambda_2}}x} + B_{M22}\, e^{\sqrt{\frac{h_b}{\lambda_2}}x} - \left(\frac{\rho_2 SAR_{2max}}{4\lambda_2 - h_{b2}}\right)e^{-2x} + \frac{Q_{m2}}{h_{b2}} + T_a, \quad X_1 \le x \le X_2 \tag{5.54}$$

$$T_3(x) = A_{M23}e^{-\sqrt{\frac{h_b}{\lambda_3}}x} + B_{M23}\, e^{\sqrt{\frac{h_b}{\lambda_3}}x} - \left(\frac{\rho_3 SAR_{3max}}{4\lambda_3 - h_{b3}}\right)e^{-2x} + \frac{Q_{m3}}{h_{b3}} + T_a, \; X_2 \le x \le X_3 \tag{5.55}$$

The coefficients used in (5.53), (5.54), and (5.55) are given in Table 5.2.

Table 5.2 Coefficients used in (5.53), (5.54), and (5.55)

A_1	$0.5e^{\sqrt{\frac{h_{b1}}{\lambda_1}}d_1}\{a_{11}\,B_3 + a_{12}\}$
B_1	$0.5e^{-\sqrt{\frac{h_{b1}}{\lambda_1}}d_1}\{b_{11}B_3 + b_{12}\}$
A_2	$0.5e^{\sqrt{\frac{h_{b2}}{\lambda_2}}d_2}[a_{21}B_3 + a_{22}]$
B_2	$0.5e^{-\sqrt{\frac{h_{b2}}{\lambda_2}}d_2}[b_{21}B_3 + b_{22}\,]$
A_3	$-B_3\,e^{2l_{31}} + \,s_3e^{l_{31}}e^{-2L_1} - \frac{Q_{m3}}{h_{b3}}e^{l_{31}}$
B_3	$\frac{-a_{12}0.5e^{\sqrt{\frac{h_{b1}}{\lambda_1}}d_1} + 0.5c_1b_{12}e^{-\sqrt{\frac{h_{b1}}{\lambda_1}}d_1} + c_2\left(-s_1 + \frac{Q_{m1}}{h_{b1}} + T_a - T_{air}\right) + \frac{2\lambda_1c_2s_1}{h}}{\left(0.5a_{11}e^{\sqrt{\frac{h_{b1}}{\lambda_1}}d_1} - 0.5b_{11}c_1e^{-\sqrt{\frac{h_{b1}}{\lambda_1}}d_1}\right)}$
a_{11}	$\left[b_{21}0.5\left(1 - \sqrt{\frac{\lambda_1h_{b2}}{\lambda_2h_{b1}}}\right)e^{-\sqrt{\frac{h_{b2}}{\lambda_2}}d_2}e^{-\sqrt{\frac{h_{b2}}{\lambda_2}}d_1} + \,a_{21}0.5\left(1 + \sqrt{\frac{\lambda_1h_{b2}}{\lambda_2h_{b1}}}\right)e^{\sqrt{\frac{h_{b2}}{\lambda_2}}d_2}e^{-\sqrt{\frac{h_{b2}}{\lambda_2}}d_1}\right]$
a_{12}	$a_{22}0.5\left(1 + \sqrt{\frac{\lambda_1h_{b2}}{\lambda_2h_{b1}}}\right)e^{\sqrt{\frac{h_{b2}}{\lambda_2}}d_2}e^{-\sqrt{\frac{h_{b2}}{\lambda_2}}d_1} + b_{22}0.5\left(1 - \sqrt{\frac{\lambda_1h_{b2}}{\lambda_2h_{b1}}}\right)e^{-\sqrt{\frac{h_{b2}}{\lambda_2}}d_2}e^{-\sqrt{\frac{h_{b2}}{\lambda_2}}d_1} - s_2e^{-2d_1} + \frac{Q_{m2}}{h_{b2}} + s_1e^{-2d_1} - \frac{Q_{m1}}{h_{b1}} - 2\frac{\lambda_2}{\lambda_1}\sqrt{\frac{\lambda_1}{h_{b1}}}s_2e^{-2d_1} + 2\frac{\lambda_2}{\lambda_1}\sqrt{\frac{\lambda_1}{h_{b1}}}s_1e^{-2d_1}$
b_{11}	$\left[b_{21}0.5e^{-\sqrt{\frac{h_{b2}}{\lambda_2}}d_2}\left(1 + \sqrt{\frac{\lambda_1h_{b2}}{\lambda_2h_{b1}}}\right)e^{-\sqrt{\frac{h_{b2}}{\lambda_2}}d_1} + \,0.5e^{\sqrt{\frac{h_{b2}}{\lambda_2}}d_2}\left(1 - \sqrt{\frac{\lambda_1h_{b2}}{\lambda_2h_{b1}}}\right)e^{-\sqrt{\frac{h_{b2}}{\lambda_2}}d_1}a_{21}\right]$

b_{12}	$0.5e^{\sqrt{\frac{h_{b2}}{\lambda_2}}d_2}\left(1-\sqrt{\frac{\lambda_1 h_{b2}}{\lambda_2 h_{b1}}}\right)e^{-\sqrt{\frac{h_{b2}}{\lambda_2}}d_1}a_{22}+0.5e^{-\sqrt{\frac{h_{b2}}{\lambda_2}}d_2}\left(1+\sqrt{\frac{\lambda_1 h_{b2}}{\lambda_2 h_{b1}}}\right)e^{-\sqrt{\frac{h_{b2}}{\lambda_2}}d_1}b_{22}-s_2e^{-2d_1}+\frac{Q_{m2}}{h_{b2}}+s_1e^{-2d_1}-\frac{Q_{m1}}{h_{b1}}+2\frac{\lambda_2}{\lambda_1}\sqrt{\frac{\lambda_1}{h_{b1}}}s_2e^{-2d_1}-2\frac{\lambda_2}{\lambda_1}\sqrt{\frac{\lambda_1}{h_{b1}}}s_1e^{-2d_1}$
a_{21}	$\left[\left(1-\sqrt{\frac{\lambda_2 h_{b3}}{\lambda_3 h_{b2}}}\right)e^{\sqrt{\frac{h_{b3}}{\lambda_3}}d_2}-\left(1+\sqrt{\frac{\lambda_2 h_{b3}}{\lambda_3 h_{b2}}}\right)e^{2l_{31}}e^{-\sqrt{\frac{h_{b3}}{\lambda_3}}d_2}\right]$
a_{22}	$+s_3\left(1+\sqrt{\frac{\lambda_2 h_{b3}}{\lambda_3 h_{b2}}}\right)e^{l_{31}}e^{-2L_1}e^{-\sqrt{\frac{h_{b3}}{\lambda_3}}d_2}-\left(1+\sqrt{\frac{\lambda_2 h_{b3}}{\lambda_3 h_{b2}}}\right)\frac{Q_{m3}}{h_{b3}}e^{l_{31}}e^{-\sqrt{\frac{h_{b3}}{\lambda_3}}d_2}-s_3e^{-2d_2}+\frac{Q_{m3}}{h_{b3}}+s_2e^{-2d_2}-\frac{Q_{m2}}{h_{b2}}-2\frac{\lambda_3}{\lambda_2}\sqrt{\frac{\lambda_2}{h_{b2}}}s_3e^{-2d_2}+2\frac{\lambda_3}{\lambda_2}\sqrt{\frac{\lambda_2}{h_{b2}}}s_2e^{-2d_2}$
b_{21}	$\left(1+\sqrt{\frac{\lambda_2 h_{b3}}{\lambda_3 h_{b2}}}\right)e^{\sqrt{\frac{h_{b3}}{\lambda_3}}d_2}-\left(1-\sqrt{\frac{\lambda_2 h_{b3}}{\lambda_3 h_{b2}}}\right)e^{2l_{31}}e^{-\sqrt{\frac{h_{b3}}{\lambda_3}}d_2}$
b_{22}	$s_3\left(1-\sqrt{\frac{\lambda_2 h_{b3}}{\lambda_3 h_{b2}}}\right)e^{l_{31}}e^{-2L_1}e^{-\sqrt{\frac{h_{b3}}{\lambda_3}}d_2}-\frac{Q_{m3}e^{l_{31}}}{h_{b3}\left(1-\sqrt{\frac{\lambda_2 h_{b3}}{\lambda_3 h_{b2}}}\right)}e^{-\sqrt{\frac{h_{b3}}{\lambda_3}}d_2}-s_3e^{-2d_2}+\frac{Q_{m3}}{h_{b3}}+s_2e^{-2d_2}-\frac{Q_{m2}}{h_{b2}}+2\frac{\lambda_3}{\lambda_2}\sqrt{\frac{\lambda_2}{h_{b2}}}s_3e^{-2d_2}-2\frac{\lambda_3}{\lambda_2}\sqrt{\frac{\lambda_2}{h_{b2}}}s_2e^{-2d_2}$
l_{31}	$\sqrt{\frac{h_{b3}}{\lambda_3}}L_1$
s_1	$\frac{\rho_1 SAR_{1max}}{4\lambda_1-h_{b1}}$
s_2	$\frac{\rho_2 SAR_{2max}}{4\lambda_2-h_{b2}}$
s_3	$\frac{\rho_3 SAR_{3max}}{4\lambda_3-h_{b3}}$
c_1	$\frac{\sqrt{\lambda_1 h_{b1}}+h}{\sqrt{\lambda_1 h_{b1}}-h}$
c_2	$\frac{h}{\sqrt{\lambda_1 h_{b1}}-h}$

Details of the mathematical procedure used to obtain the solution for the steady-state temperature in 3-layer human body and the proposed approaches is described in Appendix E and Appendix F.

5.4 Results for temperature increase in tissue

Figure 5.6 shows the comparation between tissue temperature vs tissue depth obtained via steady-state with constant EM power density and steady-state with EM power density that decays exponentially with tissue depth, when maximum external heat is generated by external EM source and in single-layer muscle tissue. Nominal values for thermal parameters are given in Table 5.3.

Table 5.3 The nominal values for the thermal parameters

Thermal parameters	**Nominal values**
Thermal conductivity: $\lambda\ [W/m°C]$	0.49
Blood perfusion rate: $W_b\ [Wkg/sm^3]$	2100
Arterial blood temperature: T_a [°C]	37
Power produced by metabolic process: $Q_m[W/m^3]$	300
Convection coefficient: $h[W/m^2°C]$	7
Temperature of the air: T_{air}[°C]	25

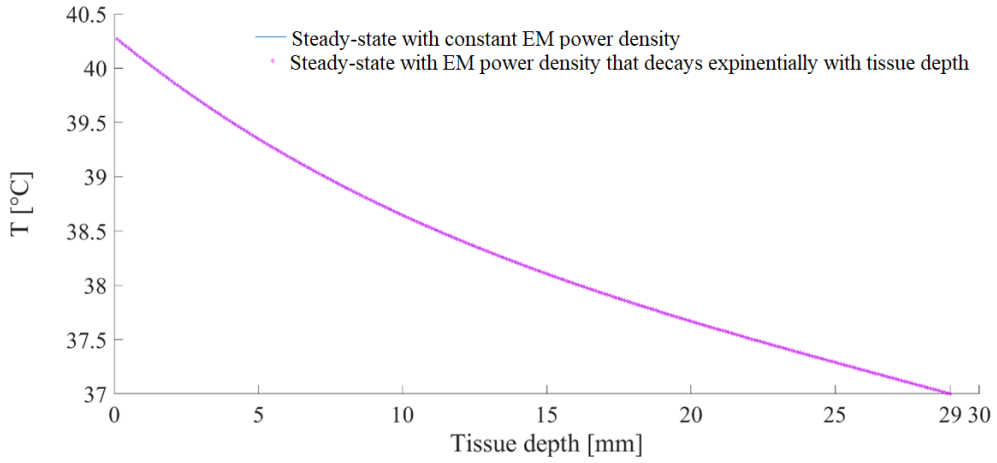

Figure 5.6 Tissue temperature vs tissue depth in single-layer tissue model for $\lambda = 0.49, W_b = 2100, T_a = 37, Q_m = 300, h = 7,$ *and* $T_{air} = 25$

The maximum SAR_{max} applied on the surface of muscle tissue is $1.4024 \cdot 10^{-6} \frac{W}{kg}$. According to Fig. 5.6, the highest temperature increase occurs at the surface of tissue (maximum obtained temperature at skin surface is 40.25 °C. Note that the same conclusion is highlighted in [144, 118]. The discrepancies between the results obtained via different approaches for the case of single-layer is negligible (< 0.01 %).

In Fig. 5.7, the family of curves illustrates tissue temperature vs tissue depth in single-layer tissue model for different values of power produced by metabolic process. Changes are 50 % around typical value given in Table 5.3.

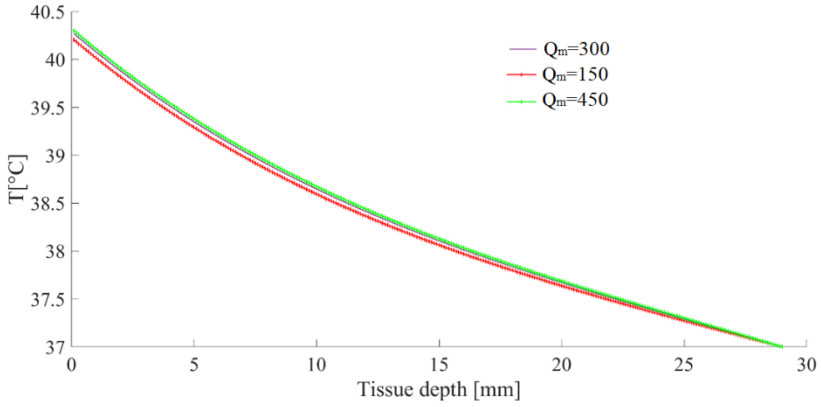

Figure 5.7 Tissue temperature vs tissue depth in single-layer tissue model for different values of power produced by metabolic process, $\lambda = 0.49$, $W_b = 2100$, $T_a = 37$, $h = 7$, *and* $T_{air} = 25$

Fig. 5.7 shows that skin surface temperature increases with metabolic heat, while slope in the temperature flow path to the boundary remains almost constant. The effect of blood perfusion rate on the temperature distribution vs tissue depth in single-layer tissue model is illustrated in Fig. 5.8.

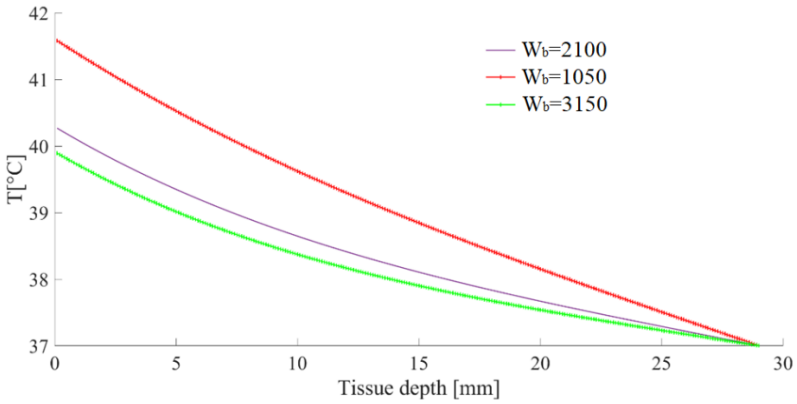

Figure 5.8 Tissue temperature vs tissue depth in single-layer tissue model for different blood perfusion rate, $\lambda = 0.49$, $T_a = 37$, $Q_m = 300$, $h = 7$, *and* $T_{air} = 25$

The curves indicate that the gradient of the temperature variation decreases as blood perfusion increases. The simulation results presented in Fig. 5.9 shows the tissue temperature vs tissue depth in single-layer tissue model for different tissue thermal conductivities.

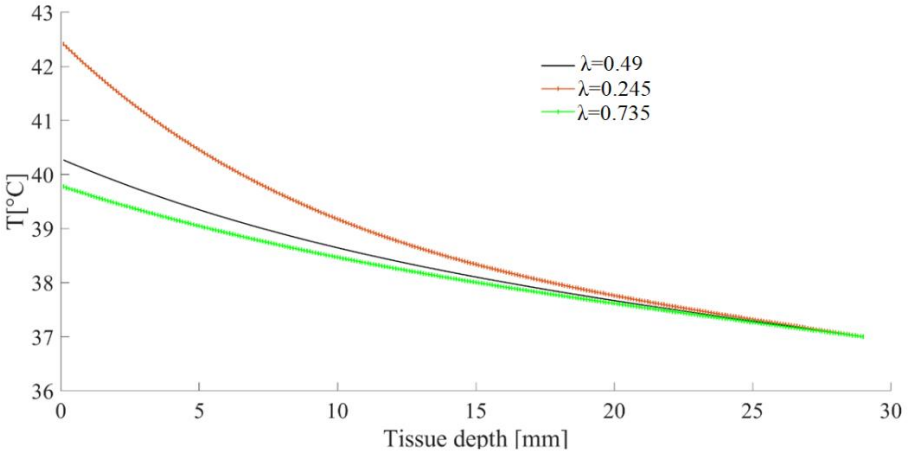

Figure 5.9 Tissue temperature vs tissue depth in single-layer tissue model for different tissue thermal conductivities, $W_b = 2100$, $T_a = 37$, $Q_m = 300$, $h = 7$, *and* $T_{air} = 25$

Curves of temperature elevation on the body surface decreases monotonically with increasing blood perfusion rate and thermal conductivity. Fig. 5.10 and 5.11 show the influence of the surrounding environment expressed through heat exchange coefficient and ambient temperature on tissue temperature vs tissue depth in single-layer tissue model.

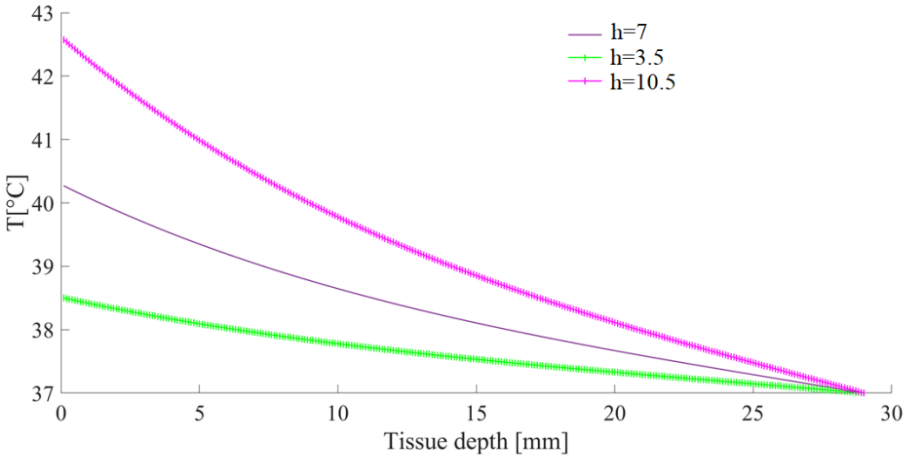

Figure 5.10 Tissue temperature vs tissue depth in single-layer tissue model for different heat exchange coefficient, $\lambda = 0.49$, $W_b = 2100$, $T_a = 37$, $Q_m = 300$, *and* $T_{air} = 25$

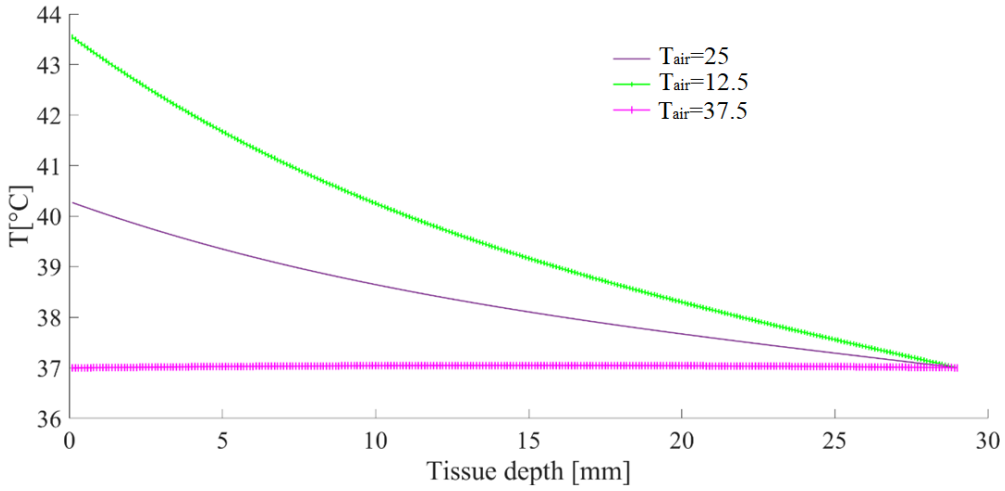

Figure 5.11 Tissue temperature vs tissue depth in single-layer tissue model for different ambient temperature, $\lambda = 0.49$, $W_b = 2100$, $T_a = 37$, $Q_m = 300$, *and* $h = 7$

Based on Fig. 5.10 the higher the outer coefficient of heat transfer *h*, the higher the temperature near body surface. On the other hand, the higher value of ambient temperature, significantly decreases the temperature near the body surface (Fig. 5.11).

Figure 5.12 shows the tissue temperature vs tissue depth obtained for various analytical approaches and proposed analytical approach with assumed constant EM power density and EM power density that exponentially decays with the tissue depth. The results of our models are compared to eight other analytical approaches described in [9, 22, 25, 100, 104, 112, 113, 145]. The comparation is done using nominal parameters presented in Table 5.4.

In the study [25] the stochastic model of bio-heat transfer equitation for the assessment of the temperature distribution in the biological tissue is presented. Study [145] solves transient PBHE using numerical technique based on Haar wavelets. A one-dimensional steady-state bio-heat transfer model of temperature distribution in cylindrical living tissue using numerical approximation technique the Galerkin Finite element method is discussed in [113]. A study [22] deals with the thermal response due to plane wave illuminating the human tissue composed of N biological layers, where the solution method arises from classical theory of differential equations, and pertaining to the steady-state. In [104] FEM is used to analyze 1D bio-heat transfer in human tissue. A simplified one-dimensional bio-heat transfer model of the spherical living tissues in the steady-state has been set up for application in heat transfer studies based on the Pennes' bio-heat transfer equation and its corresponding analytical solution by using Bessel's functions is derived [112]. In [100]

the analytical method used to solve the transient Pennes' equation is the Laplace method. Our results are obtained for the special case with constant heat flux. A closed form analytical solution to the generalized 1-D Pennes equation is described in [9].

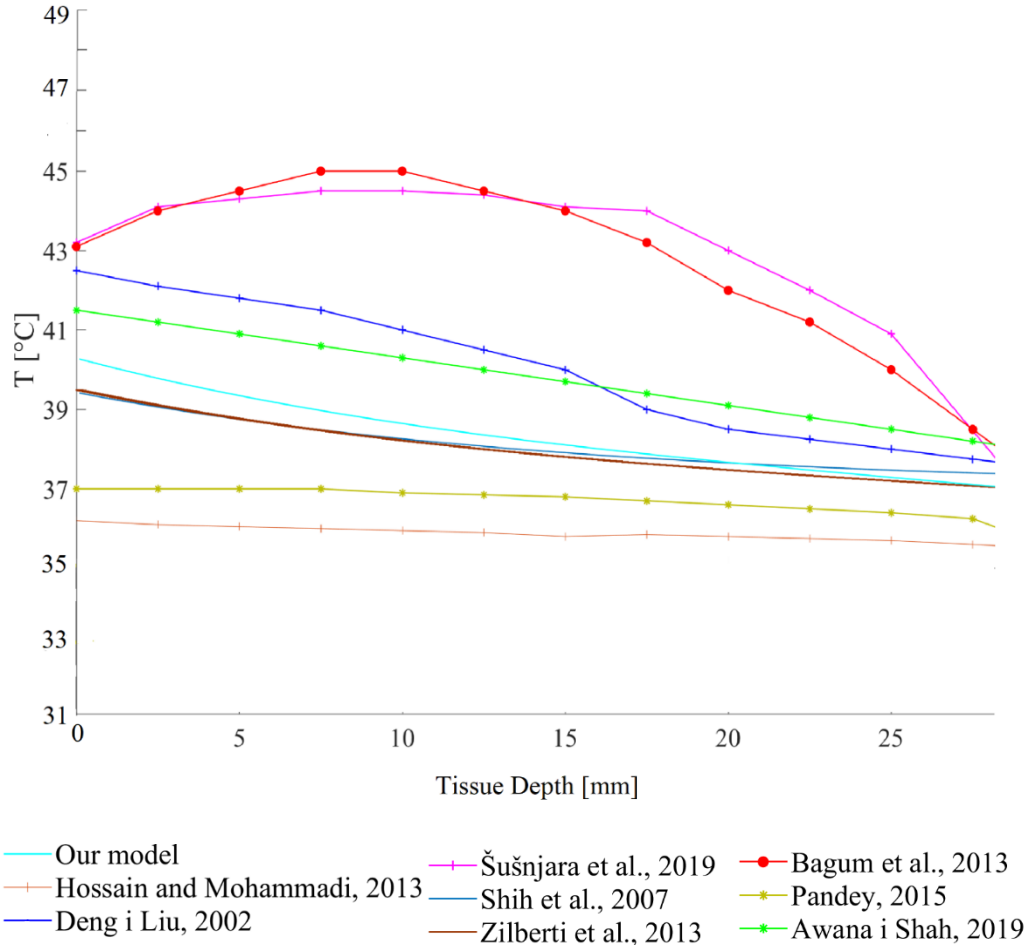

Figure 5.12 Tissue temperature vs tissue depth in single-layer tissue model: comparation with other analytical methods for $\lambda = 0.49$, $W_b = 2100$, $T_a = 37$, $Q_m = 300$, $h = 7$, *and* $T_{air} = 25$

Table 5.4 The values for the thermal parameters

Nominal values of thermal parameters	λ [$W/m°C$]	W_b [Wkg/sm^3]	T_a [°C]	Q_m [W/m^3]	h [$W/m^2°C$]	T_{air} [°C]	t [s]
Our model	0.49	2100	37	300	7	25	-
Šušnjara et al., 2019	0.5	2100	37	33800	10	25	-

Awana i Shah, 2019	0.5	2000	37	420	-	-	0.6
Pandey, 2015	0.48	11550	37	1085	10.023	25	-
Zilberti et al. 2013	0.49	2100	37	300	7	25	-
Bagum et al., 2013	0.5	2100	37	33800	10	25	-
Hossain and Mohammadi, 2013	0.48	11550	37	1085	8.77	25	-
Shih et al., 2007	0.49	2100	37	300	7	25	1800
Deng i Liu, 2002	0.5	2100	37	33800	10	25	0

Fig. 5.12 shows that significantly higher values of temperature are obtained in studies [9, 25, 104]. Based on Table 5.4 these studies used the nominal value of metabolic heat significantly higher ($Q_m = 33800\ W/m^3$) compared to [22, 100, 145] which results in similar temperature values regardless of tissue depth (difference is less than 1 ℃). This confirms that changes in metabolic heat generation elevates the inner tissue temperature magnitudes.

Furthermore, significantly smaller values of obtained temperature, as in [112, 113] according to Table 5.4 are caused by a significantly higher blood perfusion (> 5 times higher) compared to other studies, and a higher coefficient of heat exchange at the boundary between the tissue and the environment.

On the basis of the previous analysis, Figure 5.12 and Table 5.4, a clear conclusion is imposed that the results of our models agree satisfactorily with the models of other authors described in [9, 22, 25, 100, 104, 113, 145]. Maximal difference is below 50 %.

Figure 5.13 shows the tissue temperature vs tissue depth obtained for our 3-layered models with assumed constant EM power density and EM power density that exponentially decays with the tissue depth, and the ones obtained in [115, 143, 146, 147]. The comparation is carried out using nominal parameters presented in Table 5.5.

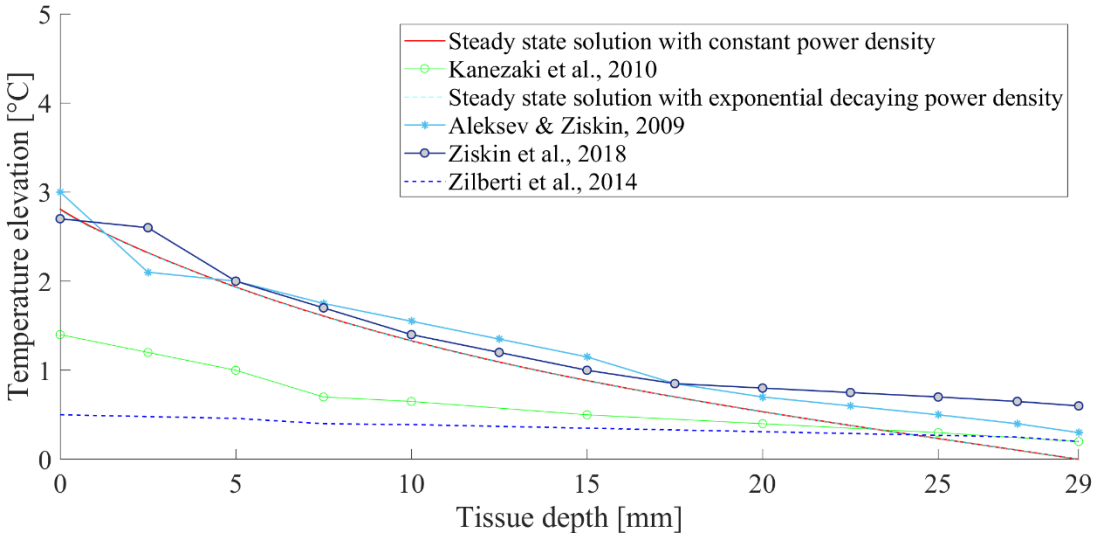

Figure 5.13 Tissue temperature elevation vs tissue depth in 3-layer tissue model: comparation with other analytical methods, $\lambda_{skin} = 0.42$, $\lambda_{FAT} = 0.25$, $\lambda_{muscle} = 0.50$, $d_{skin} = 1$, $d_{FAT} = 2$, *and* $d_{muscle} = 26$

Table 5.5 The values for the thermal parameters in 3-layer models

Nominal values of thermal parameters	Our models	Alekseev & Ziskin, 2009	Kanezaki et al., 2010	Zilberti et al., 2014	Ziskin et al., 2018
$\lambda_{skin}, \lambda_{fat}, \lambda_{muscle}$ $[W/m°C]$	0.42, 0.25, 0.50	(0.32+0.32, 0.16, 0.32	0.42, 0.25, 0.50	0.37, 0.21, 0.49	(0.32+0.32), 0.18, 0.43
$d_{skin}, d_{fat}, d_{muscle}$ $[mm]$	1, 2, 26	(0.1+1.5), 8, ∞	1, 3.5, 55.5	1, 3.5, ∞	(1.2+0.05), 4, ∞
h_b $[Wkg/sm^3]$	9100, 1700, 2700	2469600, 7585.2, 940212	9100, 1700, 2700	7441, 1903, 2691	2469600, 529200, 940212,
T_a[°C]	37	36.8	32	-	37

Q_{mskin}, Q_{mfat}, Q_{muscle} $[W/m^3]$	1620, 300, 480	0, 0, 0	1620, 300, 480	-	0, 0, 0
$h[Wkg/°Cm^2]$	7	-	7	7	8.48
T_{air}[°C]	25	22	23.6	-	22
ρ_{skin}, ρ_{fat}, ρ_{muscle} $[kg/m^3]$	1100, 920, 1040	(1622+ 1540), 633, 1222	1100, 920, 1040	-	(1622+ 1540), 633, 1222
$SAR_0[W/kg]$	$0.14 \cdot 10^{-7}$	-	-	-	-
Power Density $[W/m^2]$	-	200	50	10	2080
f [GHz]	3	42	60	1000	42.5
t[s]	-	-	-	92	-

*SAR= (Incident) Power Density/ ρ_{skin}

In [146] authors tested 4 tissue models consisting of 1 to 4-layers and applied the one-dimensional steady-state hybrid bio-heat equation (HBHE) which incorporates a blood flow dependent effective thermal conductivity. In [115] an analytical solution for a bio-heat equation is derived by using the Laplace transform for the one-dimensional 3-layer (skin, fat and muscle) and single-layer (skin) models due to millimeter-wave exposure. The investigation of the effect of relevant physical parameters on transient temperature elevation induced in human tissues (3-layer model) by EM waves in the terahertz (THz) band was is reported in [143]. A series of modeling studies is undertaken using the 3-layer and 4-layer models exposed to mm waves in [147]. The analysis is based on an IPD of 200 W/m^2 at 42 GHz. Sensitivity analysis for model parameters in the 4-layer model, assuming 10 % variations in the thickness and blood flow of different tissue layers is performed, as well.

It is clearly noticeable that the wave form of our approaches and the approaches described in [115, 143, 146, 147] is the same. Deeper in the tissue, further from the radiation source,

the difference in temperature elevation decreases. Our models describe tissue temperature under the condition of maximum SAR on the surface of the human body, so they give the upper limit is the temperature change in stationary conditions. Further on, they are mathematically simple and agree well with the models already implemented in practice. More appreciable differences in the temperature elevation, primarily on the multi-layered tissue surface, may arise due to the large number of parameters in the PBHE. This makes the process of comparison rather challenging. Furthermore, different studies use different frequencies and power of the EM sources. This highlights the importance of parametric analysis in thermal dosimetry, which is presented in Chapter 6.

Although our analytical solutions cannot be applied to cases with complex geometries they will provide useful tools for testing of numerical codes and/or more complicated approaches, and for performing SA of the parameters involved in a problem. Although simplified, analysis using this equation can still provide valuable information for some practical bio-heat transfer problems.

Yet many engineering applications are affected by a relatively large amount of uncertainty in the input data, such as model coefficients, forcing terms, BCs, and geometry [148]. In this case, to obtain a reliable temperature prediction, one has to include uncertainty quantification (UQ) due to the uncertainty in the input data.

The values of thermal parameters often exhibit variation around their average, and it has been shown by several experiments and numerical simulations that physiological responses such as blood perfusion and metabolism in living tissues are temperature-dependent [103]. For this reason, the next section presents the stochastic model of the bio-heat transfer equation to assess the temperature distribution in the biological tissue with the aim to incorporate the uncertainties in the tissue thermal parameters aiming to quantify the uncertainty in the output temperature.

5.5 Chapter summary

The experimental measurements of the body thermal response due to EM radiation is not possible in healthy humans. The problem of determining the temperature distribution in the human body is addressed using analytical method. The analytical solutions have important significance in the study of bio-heat transfer because they reflect actual physical feature of the equations and can be used as standards to verify the corresponding numerical results and as a proof to the reasonability of in-vitro mode analysis.

The steady-state temperature distribution in the single-layer and 3-layered parallelepiped human body, exposed to an incident time harmonic electromagnetic (EM) field, is governed by the stationary form of the PBHE. This equation is supplemented by the Robin BC.

The steady-state temperature distribution in the 3-layered parallelepiped human body, exposed to an incident time harmonic electromagnetic (EM) field, is governed by the stationary form of the PBHE [126]. This equation is supplemented by the Robin BC. The obtained solution is compared to other analytical methods presented in analysed literature. The obtained solution gives overestimation of steady-state temperature due to EM radiation compared to other analytical methods.

Proposed models describe tissue temperature under the condition of maximum SAR on the surface of the human body, so they give the upper limit is the temperature change in stationary conditions. The obtained solution gives overestimation of steady-state temperature due to EM radiation compared to other analytical methods. The obtained solution is also compared to other analytical methods presented in analysed literature, but the large number of parameters in the PBHE, makes the comparation challenging.

This highlights the importance of parametric analysis in thermal dosimetry in terms oof stochastic modelling and sensitivity analysis. Large differences in the temperature elevation in different studies appear as a result of the large number of parameters configured in the PBHE equation (and the fact that in some studies they are assumed to be constan and in other they change with tissue depth) but also due to the different approaches used to EM source to modelling.

CHAPTER 6

Stochastic modelling in thermal dosimetry

6.1 Stochastic modelling in computational electromagnetics

In computational electromagnetics (CEM) the uncertainties of the input parameters including the uncertainties in the description of the human body, such as the nature of tissues or the morphology of the human body, or in the description of EM source, lead in the uncertainties in the assessment of the related EM and/or thermal response. These problems could be overcome and a reliable prediction of output can be obtained by quantification of uncertainty in the input data. Using combinations of well-established deterministic EM models with certain stochastic methods to quantify the uncertainty of model input parameters is a new area in EM thermal dosimetry called stochastic dosimetry (Fig. 6.1) [114].

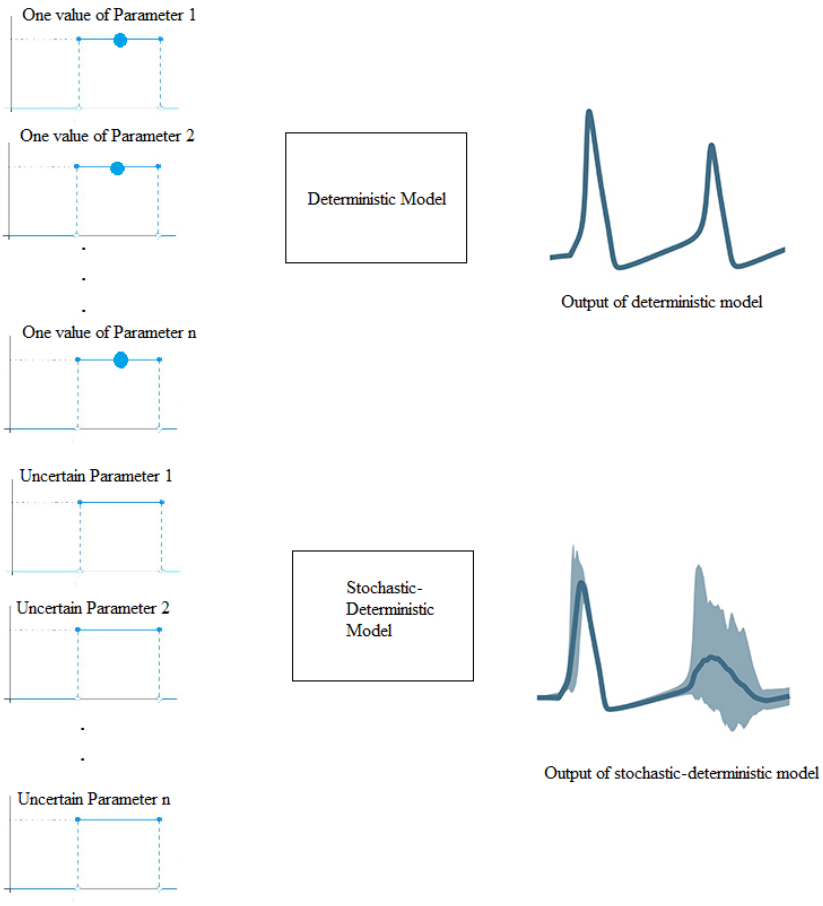

Figure 6.1 Deterministic vs Stochastic-Deterministic Model [140]

In the past two decades, there have been some efforts to provide the means to include the thermal parameter variability into the model and propagate it to the output value of interest. The effects of the variability of thermal parameters on the heating of surface tissues exposed to a plane millimetre/submillimetre wave is discussed in [143]. According to the results of the study, the variability of the temperature increase in the skin depends mainly on the electrical/dielectric properties, while in the subcutaneous fat tissue temperature increase depends mainly on the thickness of the skin.

The authors in [149] examined how the variability of brain and eye morphology and tissue properties affect the estimation of SAR induced in a homogeneous human brain exposed to the HF EM field. Once the deterministic modeling via BEM and BEM/FEM, respectively is carried out a stochastic post-processing of the obtained numerical results can be performed via SC technique by simply choosing one or more random variables depending on the problem of interest. Authors concluded that SC is shown to be robust and efficient technique providing a satisfactory convergence rate.

A stochastic approach to the estimation of temperature increase in human head tissues due to exposure to HF EM field is reported in [150]. The work is based on combining a deterministic heterogeneous model of the human head with a stochastic method. The thermal parameters of the three head tissues are modelled as RVs to observe the influence of the input uncertainty on the temperature rise. Volumetric blood perfusion rate and thermal conductivity of scalp, skull, and brain tissue are modelled as RVs with a uniform distribution. Uncertainty propagation (UP) from input random parameters to the output of interest is performed using SC. The presented results provide an insight into the behaviour of the model output with respect to parameter variations and enable the ranking of the input parameters from those with the greatest to those with the least impact.

The stochastic model of the bio-heat transfer equation for the assessment of temperature distribution in biological tissue from the point of view of biomedical applications of EM fields is presented in [25]. The authors highlight the importance of stochastic bio-heat transfer in the planning and modelling of biomedical applications of EM fields such as EM hyperthermia procedures used in the treatment of certain types of cancer. The presented approach accounts for uncertainties in the tissue thermal parameters aiming to quantify the uncertainty in the output temperature.

In [151] electric field induced in the three-compartment head model exposed to HF plane wave obtained using the hybrid FEM/BEM approach is coupled with the SC technique. The conductivity and relative permittivity of the scalp, skull and brain tissue, respectively, are modelled as random variables (RVs) with uniform distribution. The analysis shows that the highest impact pertains to scalp permittivity, while skull conductivity impact can be considered rather negligible. The results obtained using the three-compartment head model confirm that both brain permittivity and conductivity are the parameters most significantly influencing the variance of the induced field inside the brain.

SC method is combined with TPD in a 2-layered planar tissue model (skin-fat and skin-muscle) exposed to a plane wave incidence at 10, 30 and 90 GHz in [152]. Tissues' permittivities and conductivities are modelled as uniformly distributed RVs. It is proved that SC method is suitable for UQ of TPD when tissue electromagnetic properties exhibit random nature. Further on, skin conductivity becomes the most influential parameter as observation points are moved deeper into the tissue and by increasing the frequency. There is an exception for skin-muscle configuration at 10 GHz where skin permittivity has stronger impact than skin conductivity.

In conclusion, this review of papers in the area of stochastic dosimetry indicates the importance of the exact knowledge of thermal parameters of body tissues and sources of EM radiation. By taking into account their random nature and propagating it to the output we can increase our knowledge about the underlying physical processes and quantify their impact on reliability of numerical predictions of the induced electric field and related quantities.

6.2 An outline of Stochastic Collocation method for uncertainty propagation

The models used in EM and thermal dosimetry are computationally very demanding as they tend to describe complex physical phenomena and environments. Further on, values of the various model parameters can vary considerably due to difference in size and/or morphology of the models [126]. The usual practice in the EM engineering is to use average values of input parameters thus leading to a rough representation of a phenomenon.

However, the uncertainty present in input parameters can be quantified by using the statistical/ stochastic tools and propagated to the output value of interest via suitable UP method. UQ of the unknown stochastic output of the model is preceded by two steps: the UQ of input parameters and UP of uncertainties present in the model inputs to the output of interest.

The UQ of input parameters implies modelling the input parameters as RVs and/or random processes. Random input variable is denoted as *X*, or in the case of more than one random input parameters (*d*), a vector of random input parameters is formed:

$$\mathrm{X} = [\mathrm{X}_1, \mathrm{X}_2, \dots, \mathrm{X}_\mathrm{d}] \tag{6.1}$$

In practice RVs representing the input parameters are not standardized in general, and vector of random input parameters *X* has to be transformed into a set of reduced variables [153]. Depending on the marginal distribution of each input variable $X_k (k = 1, .., d)$, the

associated reduced variable may be standard normal: $\xi \sim N(0,1)$, standard uniform: $\xi \sim U(0,1)$ or some other variable with standard distribution. The resulting vector of input parameters is denoted by:

$$\boldsymbol{\xi} = [\xi_1, \xi_2, \dots, \xi_d] \tag{6.2}$$

UP refers to the choice and implementation of the stochastic method that is capable of solving the stochastic model [114], by propagating uncertainties from the input parameters to the output. Given the known deterministic model M, we seek to represent the output Y is a function of input RVs. Different methods exist and they can be classified in several ways. The general classification is into the statistical and non-statistical methods. Traditional methods for uncertainty propagation are easy to implement as they rely upon statistical approaches, e.g. brute force Monte Carlo (MC) sampling [151]. The basic principle of non-statistical methods is the representation of the unknown stochastic solution as a polynomial in the stochastic space of input parameters [151].

Traditional UP methods relaying upon the statistical approaches such as MC sampling, could be applied. The advantages of applying the MC method lies in the simplicity of its implementation [151], robustness and accuracy [25]. But despite the fact that the sample size does not depend on random dimension, it needs to be very high [> 100000] [114, 140], and the convergence rate is slow [114]. MC based methods are out of the scope of this work, and complete definition with thorough discussion can be found elsewhere, e.g. [154, 155].

Various non-statistical techniques available in the literature aim to represent the unknown stochastic solution as a polynomial in the stochastic space of input parameters. The two spectral discretization-based technique, named the generalized polynomial chaos (gPC) and SC method emerged as the most promising substitutes for MC.

According to the gPC theory the output variable *Y* is approximated by a polynomial expansion [156]

$$Y(\xi) \approx \hat{Y}(\xi) = \sum_{i=0}^{P} Y_i \varphi_i(\xi) \tag{6.3}$$

where

- $\boldsymbol{\xi} = \left[\xi^{(1)}, \xi^{(2)}, \dots, \xi^{(d)}\right]$ is d input vector,
- Y_i are unknown expansion coefficients to be solved,
- φ_i is a suitable multivariate basis of polynomial functions, and
- P is order of truncated expansion.

In practice the value of *P* depends on the total polynomial degree *p* and number of input random variables *d* [156]:

$$P + 1 = \binom{d + p}{p} = \frac{(p+d)!}{p!d!} \tag{6.4}$$

The polynomial expansion is an analytical relationship between the output Y and the random input parameters $\boldsymbol{\xi} = \left[\xi^{(1)}, \xi^{(2)}, \ldots, \xi^{(d)}\right]$ thus providing a sort of a surrogate for the original deterministic model. With P large enough the polynomial representation is quite accurate and the statistical information can be obtained. Since gPC is intrusive[1] in nature it will requires the change of governing equations which can be challenging when they take complicated forms [151].

The second non-statistical approach relies on the SC techniques. The non-intrusive nature of SC enables the use of previously validated deterministic models as black boxes in stochastic computations [114]. The expansion coefficients for the SC are actually the deterministic outputs of the considered model, calculated at N_{sc} predetermined input points also called the collocation points. Similarly, to the gPC theory, the fundamental principle of SC lies in the polynomial approximation of the considered output Y for d dimensional stochastic space [156].

$$\widehat{Y}(\boldsymbol{\xi}) = \sum_{k=1}^{N} L_k(\xi) Y^k \tag{6.5}$$

where

- $L_k(\boldsymbol{\xi})$ is basis function,
- Y^k is the output realization for the k-th input point, and
- N is the total number of deterministic simulations needed to construct the surrogate model of output.

The advantage of the SC method is its simplicity, strong mathematical background, and the polynomial representation of stochastic output. Although the total number of samples required for stochastic analysis is lower than in case of MC, the SC method suffers from the "curse of the dimensionality" for large number of input RVs.

Stochastic mean, variance, standard deviation, skewness, and kurtosis are given as follow [156]:

$$\mu\left(\widehat{Y}\right) = \sum_{k=1}^{N} Y^k w_k \tag{6.6}$$

[1] The intrusiveness implies a more demanding implementation since new codes need to be developed, while the non-intrusive methods enable the use of previously validated deterministic models as black boxes in stochastic computations.

$$\mathrm{Var}\left(\hat{Y}\right) = \sum_{k=1}^{N} \left(Y^k\right)^2 w_k - \mu^2 \tag{6.7}$$

$$\mathrm{Std}\left(\hat{Y}\right) = \sqrt{\mathrm{Var}\left(\hat{Y}\right)} \tag{6.8}$$

$$\mathrm{skew}\left(\hat{Y}\right) \approx \frac{\sum_{k=1}^{N} (Y^k)^3 w_k - 3\mu(\hat{Y})\mathrm{Var}(\hat{Y}) - \left(\mu(\hat{Y})\right)^3}{(\mathrm{Std}(\hat{Y}))^2 \mathrm{Var}(\hat{Y})} \tag{6.9}$$

$$\mathrm{kurt}\left(\hat{Y}\right) \approx \frac{\sum_{k=1}^{N} (Y^k)^4 w_k - 4\mu(\hat{Y})\mathrm{skew}(\hat{Y})(\mathrm{Std}(\hat{Y}))^2 \mathrm{Var}(\hat{Y}) - 6\left(\mu(\hat{Y})\right)^2 \left(\mathrm{Var}(\hat{Y})\right) - \mu^4}{(\mathrm{Var}(\hat{Y}))^4} \tag{6.10}$$

where

- w_k is the weight of *k-th* input point precomputed according to the chosen Gauss-Legendre quadrature and uniform distributions.

The standard deviation is important for the crude estimation of confidence intervals. Therefore, the confidence intervals (CI) used in this thesis is for 95 % level of confidence:

$$\mathrm{CI} = \mathrm{Mean}(T) \pm 2 * \mathrm{Std}(T) \tag{6.11}$$

Confidence intervals play an important role in the comparison with RLs and BRs defined by ICNIRP and IEEE since they define the range in which the output value is expected with a certain level of confidence. In SC two important questions are questions pertaining to the choice of basis function and collocation points. It is worth mentioning that, although Lagrange polynomials are mostly used for the polynomial representation of the stochastic output, other types of basis functions are also possible [114]. Lagrange polynomials have the character of locally global basis functions, while piecewise linear basis functions are used when it is important to capture discontinuous issues in stochastic solutions.

The choice of the collocation points is essential part of any collocation-based method. The aim of SC method is to approximate following integral as accurate as possible:

$$w_i = \int_{\Gamma} L_k(\boldsymbol{\xi}) p(\boldsymbol{\xi}) d\boldsymbol{\xi} \tag{6.12}$$

where

- $p(\boldsymbol{\xi})$ is joint probability density function of input RVs.

The weights w_i are computed numerically. When stochastic dimension space is one-dimensional ($d = 1$) the point selection is straightforward. There are numerous numerical studies proposing wide range of quadrature rules to deal with the 1-dimensional integral evaluation and the optimal choice is Gauss quadrature [156].

The most natural approach to multi-dimensional integration is the tensor product of 1-dimensional quadrature rules which leads to relatively simple generalization of integration properties from one-dimensional to d-dimensional case [156]. The multivariate basis functions $L_k(\boldsymbol{\xi})$ are also formed by means of a tensor product of a univariate basis functions in each dimension:

$$\mathrm{L_k}(\boldsymbol{\xi}) = \mathrm{l}\left(\xi_1^{(\mathrm{i})}\right) \otimes \mathrm{l}\left(\xi_2^{(\mathrm{i})}\right) \otimes \ \ldots \otimes \mathrm{l}\left(\xi_{\mathrm{d}}^{(\mathrm{i})}\right) \tag{6.13}$$

The total number of simulation points is thus:

$$\mathrm{N_{SC}} = \prod_{\mathrm{k}=1}^{\mathrm{d}} \mathrm{m_k} \tag{6.14}$$

In most of the applications the number of collocation points in each dimension is equal, thus

$$\mathrm{N_{SC}} = (\mathrm{m_k})^{\mathrm{d}} \tag{6.15}$$

Obviously, the number of simulation points grows exponentially with the number of input RVs, therefore the tensor product is mostly used at lower dimensions. The generally accepted limitation is $d \leq 5$ [157]. The idea behind the sparse grids is to alleviate the problem of a "curse of dimensionality" present in the tensor product by using a sparse instead of a tensorized grid of points. The classical sparse-grid approach applied to the construction of multi-variate basis function $L_i(\boldsymbol{\xi})$ can be expressed in the following way [157]:

$$\begin{aligned} \mathrm{L_k}(\boldsymbol{\xi}) = \sum_{\mathrm{q}+1 \leq |\vec{\mathrm{h}}| \leq \mathrm{q}+\mathrm{d}} (-1)^{\mathrm{q}+\mathrm{d}-|\vec{\mathrm{h}}|} \begin{pmatrix} \mathrm{d}-1 \\ \mathrm{q}+\mathrm{d}-|\vec{\mathrm{h}}| \end{pmatrix} \\ \left(\mathrm{l}\left(\xi_1^{(\mathrm{i})}, \mathrm{h}_1\right) \otimes \ \ldots \otimes \mathrm{l}\left(\xi_{\mathrm{d}}^{(\mathrm{i})}, \mathrm{h}_{\mathrm{d}}\right)\right) \end{aligned} \tag{6.16}$$

where

- q is a sparseness parameter or the sparseness level, and
- h denotes the depth coordinate for each dimension: $\mathrm{k} = 1, \ldots, \mathrm{d}$.

The dependence of the total number of simulation points of the sparse grid products on the dimension is much weaker than in case of tensor product with the reduction from

$NSC = (m_k)^d$ to approximately $N_{SC-SG} = \frac{(2*m_k)^d}{d!}$ simulation points. The sparse grid approximation is accurate for $d > 5$.

6.3 Sensitivity Analysis

The definition of the sensitivity analysis is the one describing it as the study of how the uncertainty in the output of a mathematical model or system (numerical or otherwise) can be apportioned to different sources of uncertainty in its inputs [158]. The ideal approach would be to run both uncertainty quantification and SA in the same stochastic framework, usually UQ preceding the SA, thus minimizing the computational burden as much as possible. Two approaches of SA are described as part of this work, the so-called OAT and ANOVA.

OAT approach is based on changing the input parameter one at a time while the others are kept at some nominal value. The sensitivity is estimated by monitoring the changes in the output which can be done in different ways, e.g. partial derivatives or linear regression. It the sensitivity is assessed by monitoring the change in the variance of the output after computing the variance for *d* univariate cases, then the impact factor of each input parameter is given by [140]

$$\mathrm{I_i} = \frac{\mathrm{V_i(Y)}}{\mathrm{V(Y)}} \tag{6.17}$$

where

- $\mathbf{X} = [\mathrm{X_1}, \mathrm{X_2}, \dots, \mathrm{X_k}, \dots \mathrm{X_d}] \rightarrow \mathrm{Var(Y|\mathbf{X})} = \mathrm{V(Y)}$
- $\mathbf{X} = [\mathrm{X_i}] \rightarrow \mathrm{Var(Y|\mathbf{X})} = \mathrm{Var(Y|X_i)} = \mathrm{V_i(Y)}$

Although in this way any change observed in the output is unambiguously prescribed to the single variable changed, the approach does not fully explore the input space, since it does not take into account the simultaneous variation of input variables. The OAT approach cannot detect the presence of interactions between input variables.

The ANOVA is based on variance decomposition within the probabilistic framework. The total variance of a model output is decomposed into terms depending on the input factors and their mutual interactions [158]:

$$\mathrm{V(Y)} = \sum_k \mathrm{V_k} + \sum_k \sum_{j>k} \mathrm{V_{kj}} + \cdots + \mathrm{V_{12\dots d}} \tag{6.18}$$

where

- $V(Y)$ is the output variance when $\mathbf{X} = [X_1, X_2, \dots, X_k, \dots X_d]$,
- $V_k = V(f_k(X_k)) = V_{X_k}[E_{X_{\sim k}}(Y|X_k)]$,
- $V_{ij} = V\left(f_{ij}(X_i, X_j)\right)$

Using the terms define above (6.18) becomes

$$V\left(f_{ij}(X_i, X_j)\right) = V_{X_i X_j}[E_{X_{\sim ij}}(Y|X_i, X_j)] - V_{X_i}[E_{X_{\sim i}}(Y|X_i)] \\ - -V_{X_i}[E_{X_{\sim j}}(Y|X_{ij})] \tag{6.19}$$

Normalizing the above expression by total variance *V(Y)* the sensitivity indices are obtained:

$$1 = \sum_k S_k + \sum_k \sum_{j>k} S_{kj} + \cdots + S_{12\dots d} \tag{6.20}$$

In SA, based on a variance decomposition, the variance of a model is decomposed into terms depending on the input factors and their mutual interactions, allows the computation of sensitivity indices of first and high order [25].

The first order indices measure the effect of only the *i-th* random input variable, without any interaction with other RVs, is given by the following expression:

$$S_i = \frac{V_{x_i}\left[E_{x_{\sim i}}(Y|X_i)\right]}{V(Y)}, i = 1, \dots, d \tag{6.21}$$

where

- $E_{x_{\sim i}}(Y|X_i)$ is the conditional expectation for the output temperature

Namely, there are $d - 1$ such expectations: the i-th input parameter is kept at its constant value while the expected temperature is computed for $(d - 1)$-dimensional stochastic model. Thee tilde sign "$\sim$" stands for "all except". After the computation of $(d - 1)$ conditional expectations, their variance is computed, i.e., $V_{X_k}(\cdot)$. The $V(E)$ stands for the electric field variance in d-dimensional case (total variance).

The second and high order sensitivity indices, S_{ij} and $S_{12,\dots d}$ give the information about the effect that the interaction of two, ore more random input variables has w.r.t. to the output. The computational burden may become very prohibitive when all groups of sensitivity indices needs to be computed, therefore, very often only first order sensitivity index is computed. In order to still obtain the information about the potential significant interactions between the variables, a total effect sensitivity index is defined as:

$$S_{T_i} = \frac{E_{x_{\sim i}}\left[V_{x_i}(Y|X_{\sim i})\right]}{V(Y)} = 1 - \frac{V_{x_i}\left[E_{x_{\sim i}}(Y|X_{\sim i})\right]}{V(Y)} \tag{6.22}$$

Thus, SA methodology is incorporated into the framework of SC method straightforwardly, without the need of additional simulations.

6.4 Results in Stochastic-Deterministic Modelling

6.4.1 Results for Single-layer tissue

The approach in this thesis aims to incorporate the uncertainties in the tissue thermal parameters aiming to quantify the uncertainty in the output temperature. First, six RVs are considered in single-layer human body model $(\lambda, W_b, T_a, Q_m, h, T_{air})$. The thermal parameters are modelled as RVs with uniform distribution in the range of ± 20% from their nominal values which are given in the Table 5.3.

The tissue depth is considered to be $L = 0.29\,cm$. The full-tensor SCM results in 729 deterministic simulations. The results for mean and variance of temperature distribution are compared to the results obtained in [25]. Fig. 6.2 and Fig. 6.3 show the mean and the standard deviation of steady-state temperature obtained in single layer model.

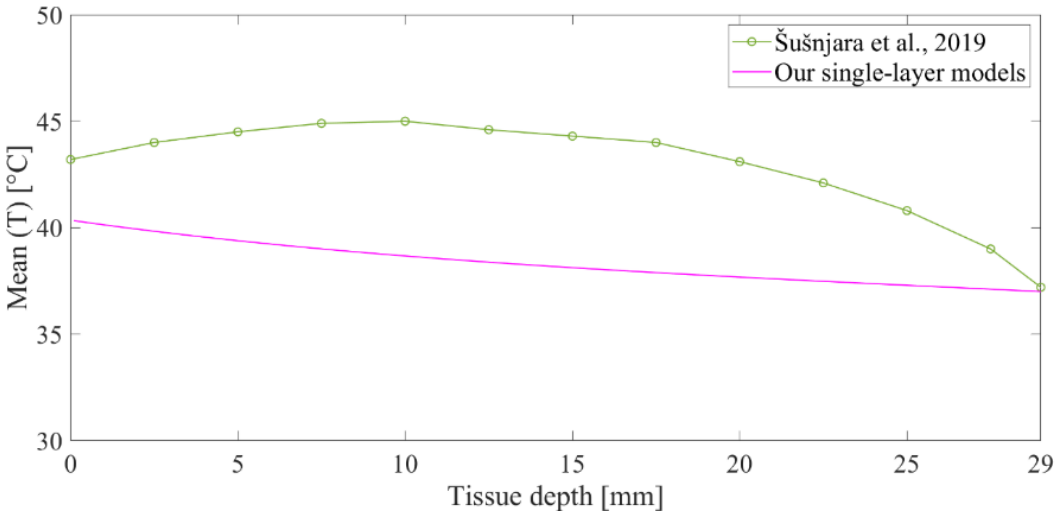

Figure 6.2 The mean of the temperature distribution for $\lambda = 0.49$, $W_b = 2100$, $T_a = 37$, $Q_m = 300$, $h = 7$, *and* $T_{air} = 25$

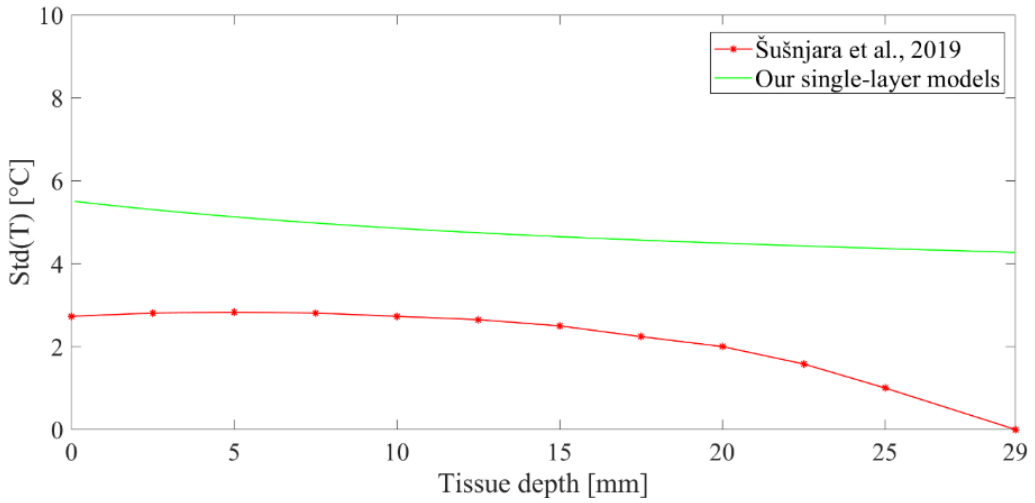

Figure 6.3 The standard deviation of the temperature distribution for $\lambda = 0.49$, $W_b = 2100$, $T_a = 37$, $Q_m = 300$, $h = 7$, *and* $T_{air} = 25$

As mentioned earlier significantly higher values of mean temperature obtained in [25] are related to the significantly higher nominal value of metabolic heat ($Q_m = 33800\ W/m^3$). Higher values of metabolic heat generation (Q_m) elevates the inner tissue temperature magnitudes but maintains an almost constant slope in the temperature flow path to the boundary regardless the metabolic rate.

The crude estimation of the confidence intervals (CI) given as the mean value ± 1 standard deviation is shown in Fig. 6.4 (pink and green our single layer models).

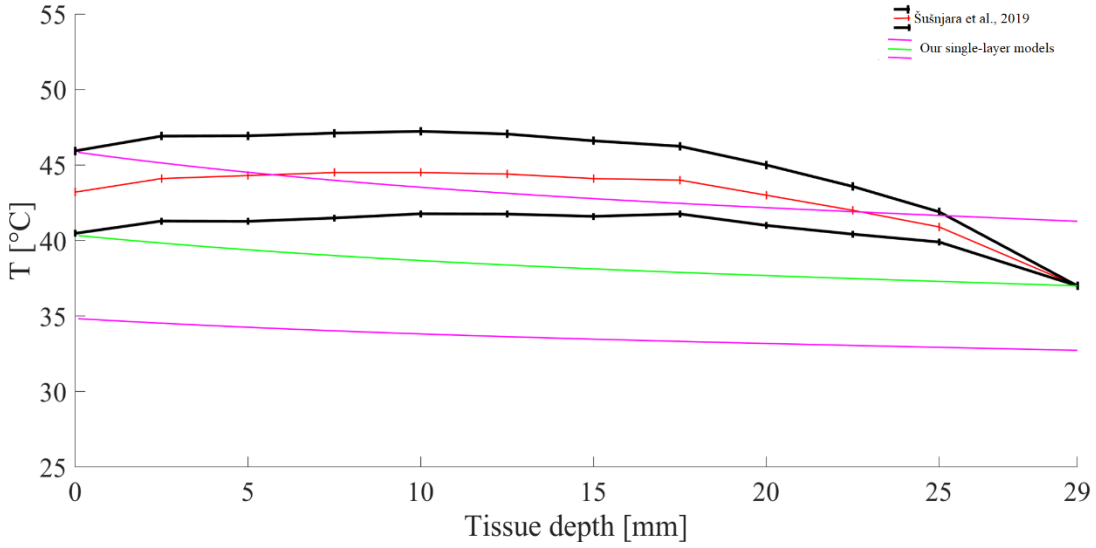

Figure 6.4 The confidence interval (CI) given as the mean temperature $\mp$ *standard deviation of the temperature for* $\lambda = 0.49$, $W_b = 2100$, $T_a = 37$, $Q_m = 300$, $h = 7$, *and* $T_{air} = 25$

The maximal deviation is 15 % from the mean value. Since input parameter variation is 20 %, as in [25], and CI is wider, our model should be used for smaller input parameter variation.

The influence of the variation in the input variables on the output temperature distribution is computed by using earlier mentioned Sobol indices. The first and total order sensitivity indices are shown in Fig. 6.5. The first order sensitivity indices give the information about the impact of certain input parameter while all possible interactions of a certain parameters with other parameters are included in the total effect indices.

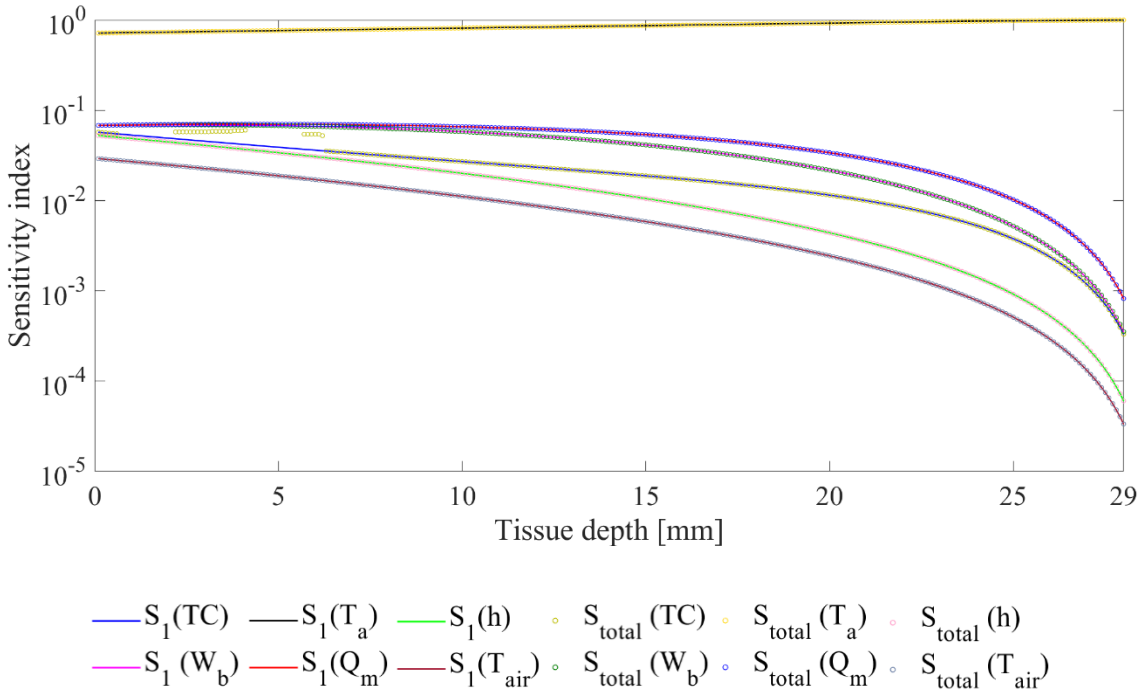

Figure 6.5 The sensitivity indices of first (solid line) and total order (star marker) for each random input parameter

The results presented in Fig. 6.5 demonstrate the overwhelming impact of arterial temperature over the whole domain, and confirmed the results presented in [25]. The average temperature and the maximum temperature are mostly affected by the variation of the arterial blood temperature. Considering its overall influence, this thermal parameter has the major effect on temperature distribution. Other thermal parameters exhibit small impact, as stated in [25]. The influence of arterial blood temperature has homogenous trend. Other parameters exhibit nonhomogeneous influence. The values of total and first order indices are almost the same for each parameter (except for thermal conductivity near tissue surface), thus proving that none of the mutual interactions has a significant impact on the temperature distribution.

6.4.2 Results for 3-layer tissue model

As stated earlier, there is considerable variation in the individual depth-temperature distributions [96]. Variation of output temperature distribution may be the result of possible differences in individual size and age (morphology), or the general variability of permittivity and conductivity, due to difference in age or sex [149]. Earlier dielectric measurements of skin conducted in vivo reported that the considerable variability of the measured data with the body site can be attributed to the variability in skin layer thickness [159]. The results in [6] also reveal that the skin surface temperature elevation may be correlated with the blood perfusion rates in the deeper layers as well as the thickness of the skin tissues.

The special contribution of this study is analysis of the effects of thermal conductivity and tissue thickness in our 3-layer models on resulting temperature in steady-state. Thermal conductivity and tissue thickness are modeled as RVs with uniform probability distribution (Table 6.1). The mean values used in this paper are taken from [102], with muscle depth being smaller because of limitation of penetration depth.

Table 6.1 Parameters modeled as input RVs

Thermal parameter	d_{skin} $[mm]$	d_{SAT} $[mm]$	d_{muscle} $[mm]$	λ_{skin} $[W/m°C]$	λ_{SAT} $[W/m°C]$	λ_{muscle} $[W/m°C]$
Initial value	1	2	26	0.42	0.25	0.50
Distribution of RV U [min, max]	U [0.8, 1.2]	U [1.6 + 2.4]	U [20.8, 31.2]	U [0.336,0.504]	U [0.2,0.3]	U [0.4,0.6]

The full-tensor SCM resulted in 729 deterministic simulations for 3 collocation points, 15625 deterministic simulations for 5 collocation points, and 117649 for 7 collation points. The results for the mean, variance, and standard deviation of temperature distribution are shown in Fig. 6.6, Fig. 6.7, and Fig. 6.8.

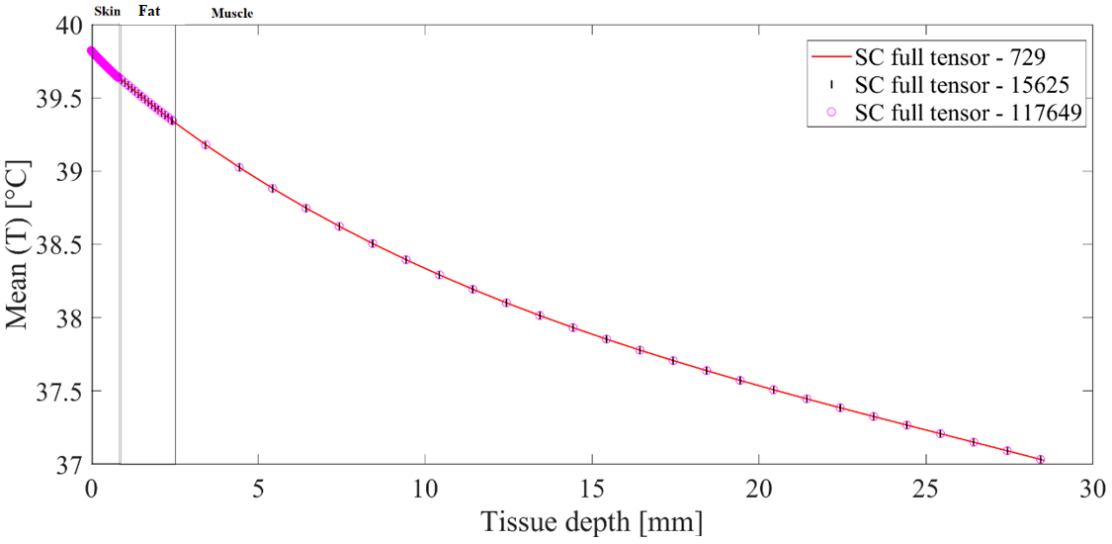

Figure 6.6 The mean of the temperature distribution for $\lambda_{skin} = 0.42$, $\lambda_{FAT} = 0.25$, $\lambda_{muscle} = 0.50$, $d_{skin} = 1$, $d_{FAT} = 2$, *and* $d_{muscle} = 26$

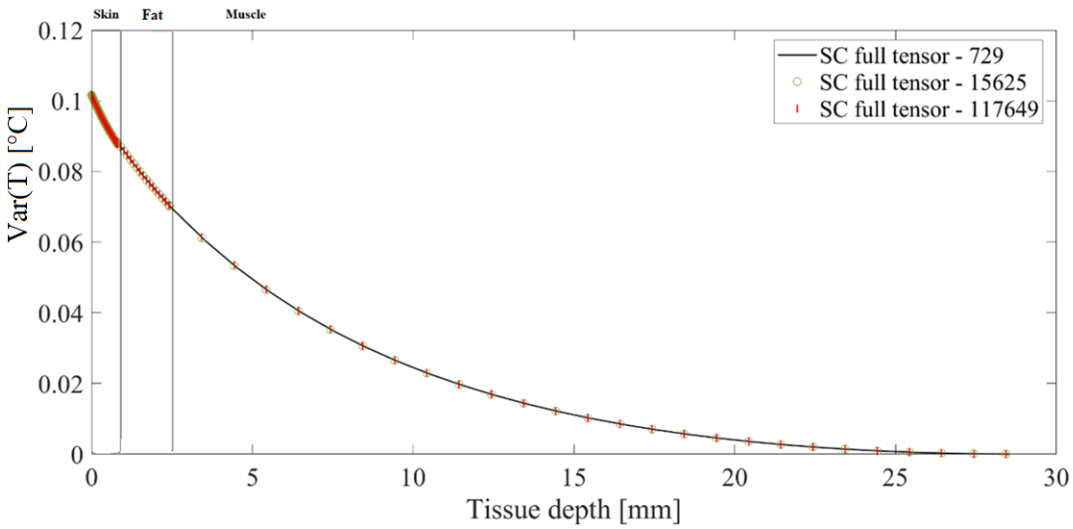

Figure 6.7 The variance deviation of the temperature distribution for $\lambda_{skin} = 0.42$, $\lambda_{FAT} = 0.25$, $\lambda_{muscle} = 0.50$, $d_{skin} = 1$, $d_{FAT} = 2$, *and* $d_{muscle} = 26$

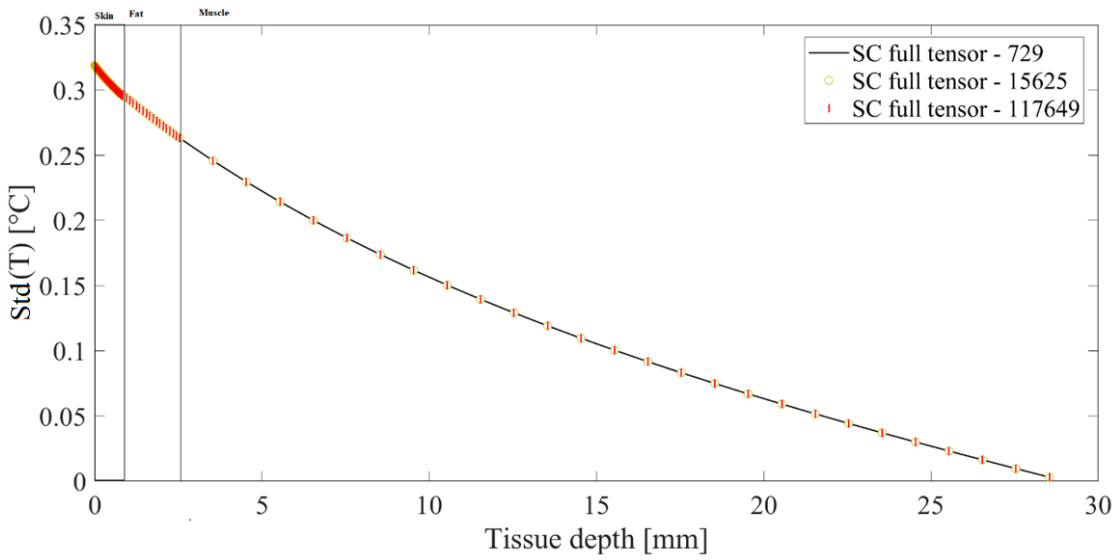

Figure 6.8 The standard deviation of the temperature distribution for $\lambda_{skin} = 0.42$, $\lambda_{FAT} = 0.25$, $\lambda_{muscle} = 0.50$, $d_{skin} = 1$, $d_{FAT} = 2$, *and* $d_{muscle} = 26$

The obtained results for mean, variance, and standard deviation of temperature distribution show good convergence. Furthermore 20% variation of input RVs results in less than 10 % change of output temperature distribution.

The crude estimation of the confidence intervals (CI) given as the mean value ± 2 standard deviation or mean value ± 3 standard deviation are shown in Fig. 6.9 and Fig. 6.10. It is useful to mention that the confidence interval is most often shown as two or three standard deviations. Namely, double standard deviation means a precision of 95.5 %, and triple standard deviation means a precision of 99,7 % [160].

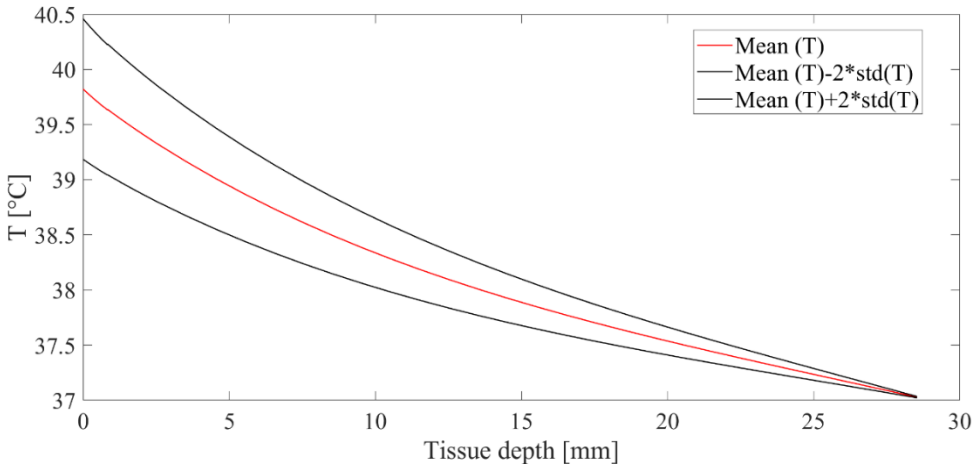

Figure 6.9 The confidence interval (CI) given as the mean temperature ∓ 2 *standard deviation of the temperature for* $\lambda_{skin} = 0.42$, $\lambda_{FAT} = 0.25$, $\lambda_{muscle} = 0.50$, $d_{skin} = 1$, $d_{FAT} = 2$, *and* $d_{muscle} = 26$

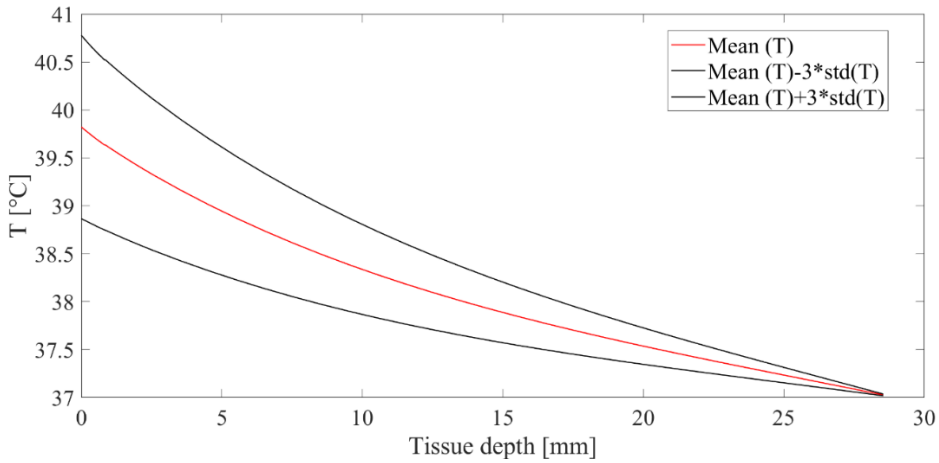

Figure 6.10 The confidence interval (CI) given as the mean temperature ∓ 3 *standard deviation of the temperature for* $\lambda_{skin} = 0.42$, $\lambda_{FAT} = 0.25$, $\lambda_{muscle} = 0.50$, $d_{skin} = 1$, $d_{FAT} = 2$, *and* $d_{muscle} = 26$

The influence of the variation in the input variables on the output temperature distribution is computed by using OAT and Sobol indices. The variance of the temperature in the 3-layer tissue is calculated for six univariate cases by using 3, 5, 9, and 17 collocation points obtained from Gauss-Legendre quadrature rule. The standard deviation is calculated as the square root of the variance.

Fig. 6.11 to Fig. 6.16 contain the information about the convergence of SC methods in computation of temperature standard deviation and OAT sensitivity analysis for 6 univariate cases, i.e., when only one input parameter is random at a time (skin depth, SAT depth, muscle depth, skin thermal conductivity, SAT thermal conductivity, muscle thermal conductivity).

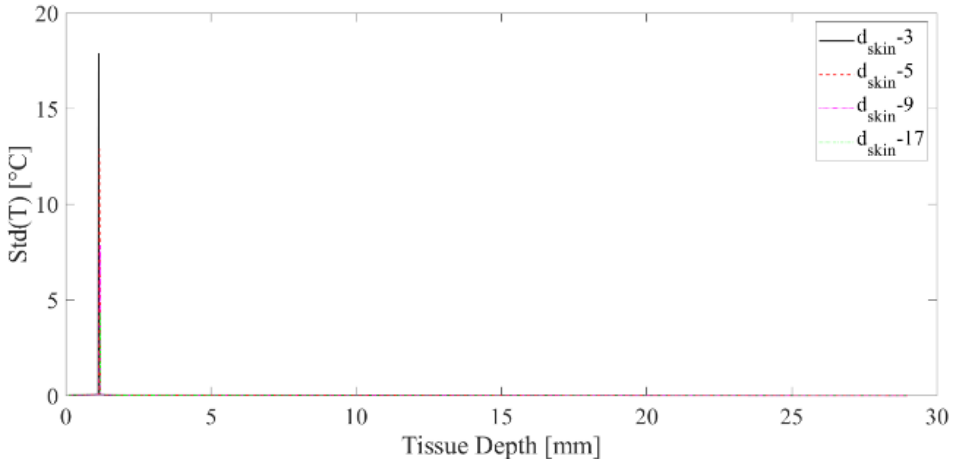

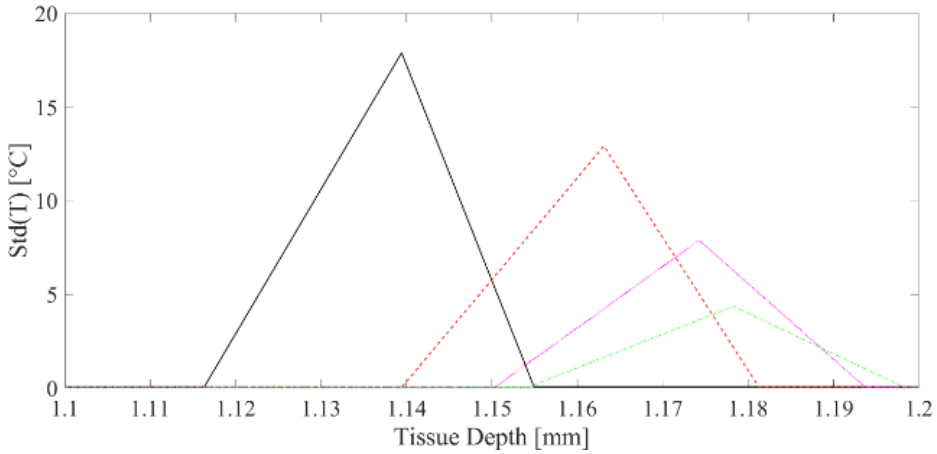

Figure 6.11 Convergence of SC methods in computation of standard deviation of temperature when only skin depth is RV at a time for $\lambda_{skin} = 0.42$, $\lambda_{FAT} = 0.25$, $\lambda_{muscle} = 0.50$, $d_{skin} = 1$, $d_{FAT} = 2$, *and* $d_{muscle} = 26$

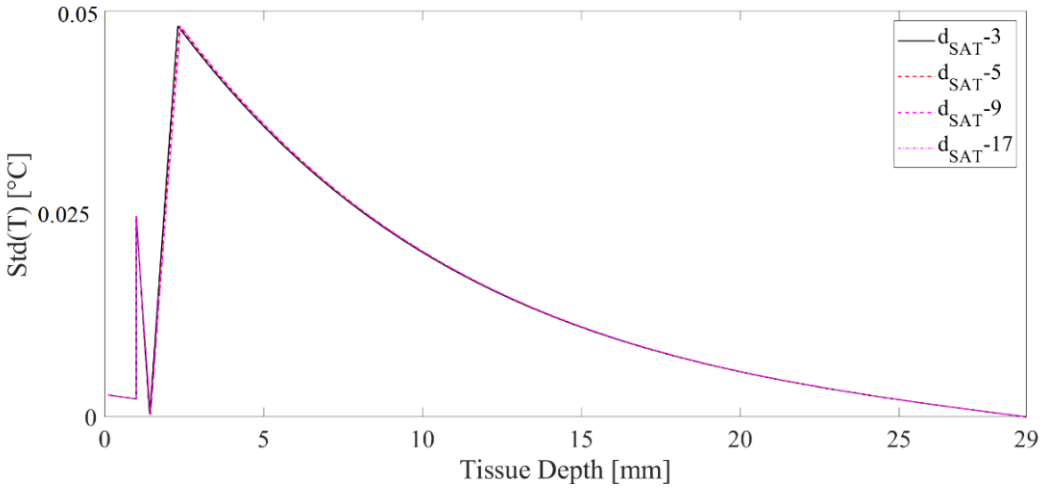

Figure 6.12 Convergence of SC methods in computation of standard deviation of temperature when only SAT depth is RV at a time for $\lambda_{skin} = 0.42$, $\lambda_{FAT} = 0.25$, $\lambda_{muscle} = 0.50$, $d_{skin} = 1$, $d_{FAT} = 2$, *and* $d_{muscle} = 26$

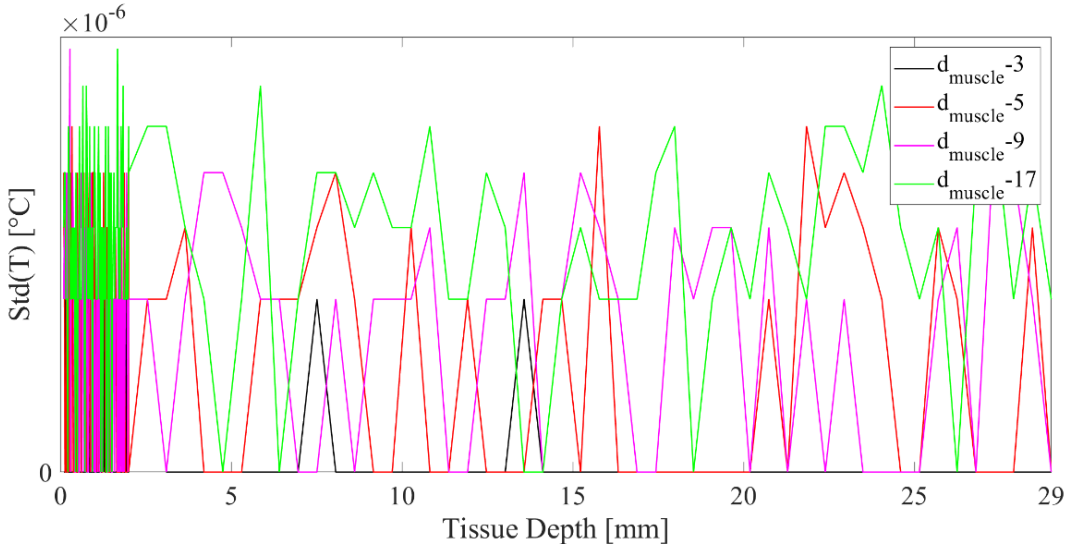

Figure 6.13 Convergence of SC methods in computation of standard deviation of temperature when only muscle depth is RV at a time for $\lambda_{skin} = 0.42$, $\lambda_{FAT} = 0.25$, $\lambda_{muscle} = 0.50$, $d_{skin} = 1$, $d_{FAT} = 2$, *and* $d_{muscle} = 26$

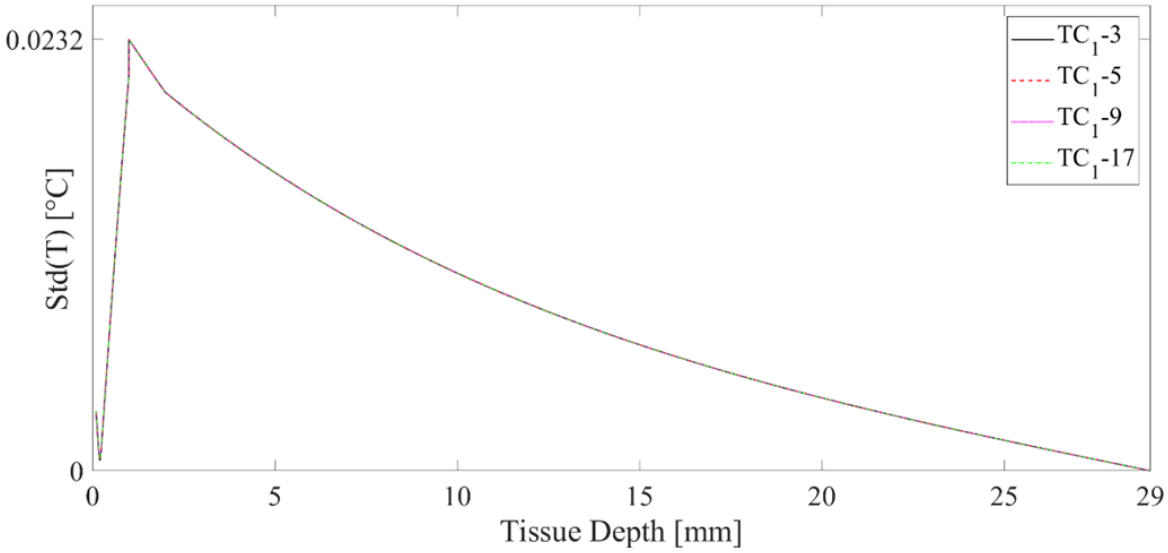

Figure 6.14 Convergence of SC methods in computation of standard deviation of temperature when only skin thermal conductivity is RV at a time for $\lambda_{skin} = 0.42$, $\lambda_{FAT} = 0.25$, $\lambda_{muscle} = 0.50$, $d_{skin} = 1$, $d_{FAT} = 2$, *and* $d_{muscle} = 26$

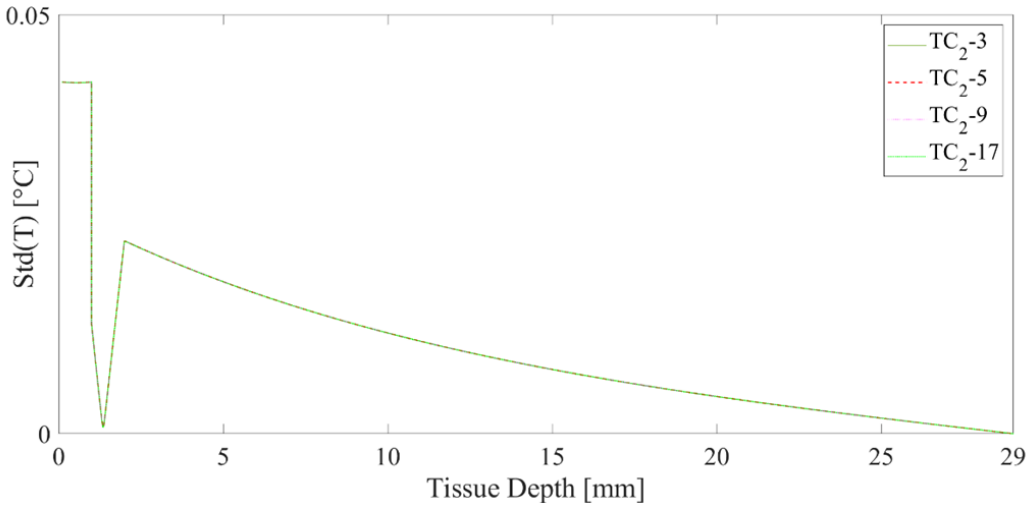

Figure 6.15 Convergence of SC methods in computation of standard deviation of temperature when only SAT thermal conductivity is RV at a time for $\lambda_{skin} = 0.42$, $\lambda_{FAT} = 0.25$, $\lambda_{muscle} = 0.50$, $d_{skin} = 1$, $d_{FAT} = 2$, *and* $d_{muscle} = 26$

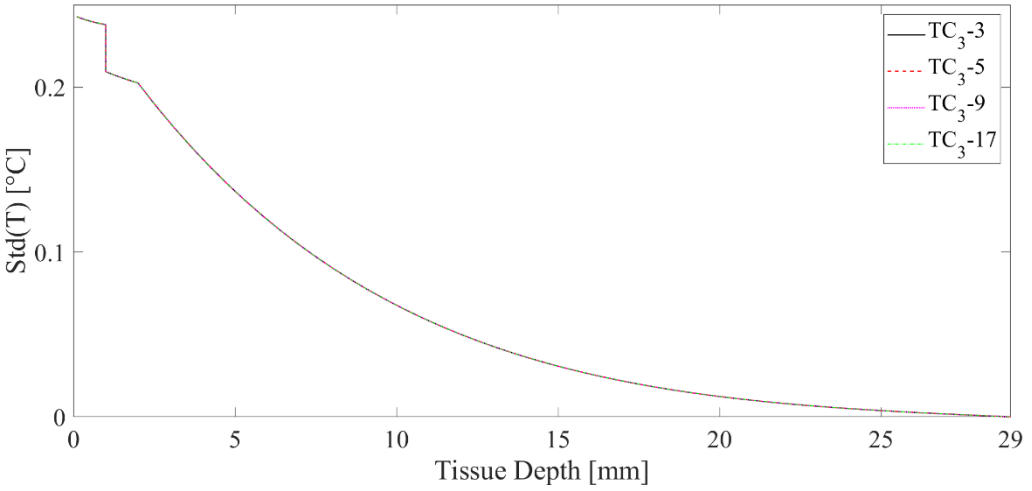

Figure 6.16 Convergence of SC methods in computation of standard deviation of temperature when only muscle thermal conductivity is RV at a time for $\lambda_{skin} = 0.42$, $\lambda_{FAT} = 0.25$, $\lambda_{muscle} = 0.50$, $d_{skin} = 1$, $d_{FAT} = 2$, *and* $d_{muscle} = 26$

SC method exhibits problems with convergence when computing the standard deviation of the temperature. Convergence is not accomplished for chosen number of collocation points when only skin depth is RV and when muscle depth is RV. To improve the convergence, number of collocation points should be further increased. Based on Fig. 6.11 to Fig. 16 the variation of these input parameters do not have any effect on the convergence of the total standard deviation, i.e., the standard deviation of 6-dimensional

stochastic model. Beforementioned points the problem toward ANOVA analysis. The first and total order sensitivity indices are shown in Fig. 6.17.

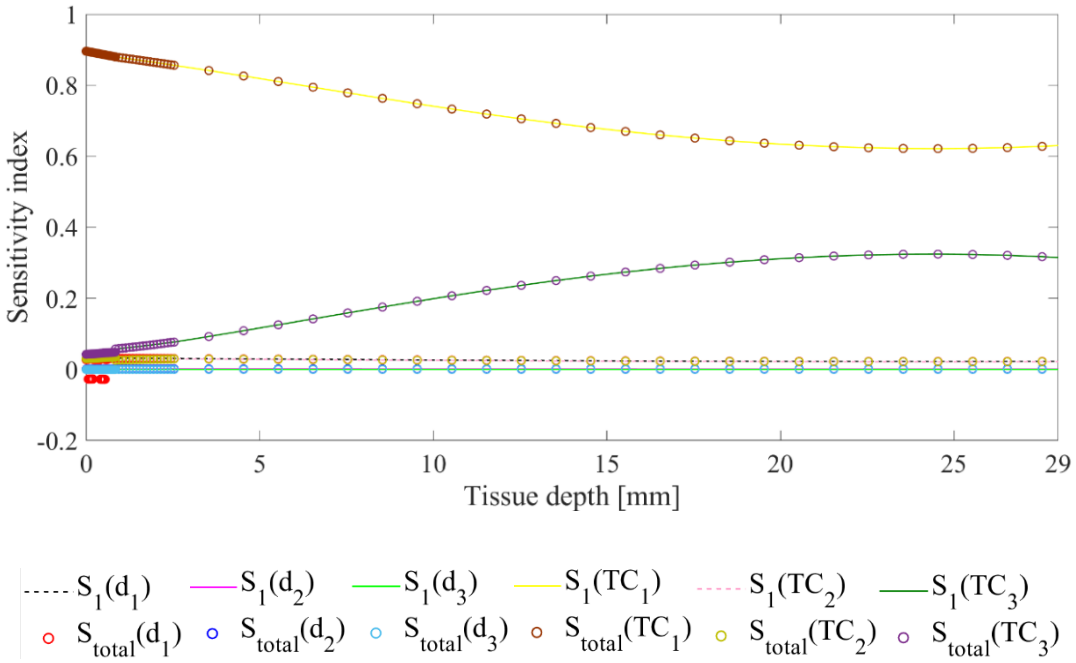

Figure 6.17 The sensitivity indices of first (solid line) and total order (circle marker) for each random input parameter

In 3-layer human body model composed of skin, fat and muscle, the variance of temperature is mostly affected by the variation of the skin thermal conductivity. Considering its overall influence, this thermal parameter has the major effect on temperature distribution. In skin and fat tissues other parameter exhibit small influence. Furthermore, the thermal conductivity of muscle has significant influence on temperature distribution in muscle tissue. The influence of the remaining parameters is negligible. These parameters, along with arterial blood temperature mostly describe the heat exchange between the human body (single-layer and 3-layer) and the environment.

The values of total and first order indices are almost the same for each parameter (except for thermal conductivity near tissue surface), thus proving that none of the mutual interactions has a significant impact on the temperature distribution.

Based on UQ in thermal dosimetry with a 95 % level of precision the largest variability in output temperature does not exceed 130% of its expectation in 3-layer tissue. However, if the level of precision is increased to 99.7% variability in output temperature does not exceed 180% of expected value in 3-layer tissue. Furthermore, sensitivity analysis reveals that one input parameter (skin thermal conductivity) bears significant impact on the output CI width while other five parameters can be neglected.

6.5 Chapter Summary

Presented approach provides an insight into the behaviour of the model output with respect to input parameters variation. The analysis of the influence of thermal parameters on temperature distribution is given in this chapter. The existing thermal models are combined with the state of the art SC. Sensitivity analysis of the individual thermal parameters confirmed previous findings: arterial blood temperature has the most significant influence on general steady-state temperature distribution.

SC method exhibits problems with convergence when computing the standard deviation of the temperature. Convergence is not accomplished for chosen number of collocation points when only skin depth is RV and when muscle depth is RV. To improve the convergence, number of collocation points should be further increased. The variation of these input parameters do not have any effect on the convergence of the total standard deviation, i.e., the standard deviation of 6-dimensional stochastic model. Beforementioned points the problem toward ANOVA analysis. The values of total and first order indices are almost the same for each parameter (except for thermal conductivity near tissue surface), thus proving that none of the mutual interactions has a significant impact on the temperature distribution.

Based on UQ in thermal dosimetry with a 95 % level of precision the largest variability in output temperature does not exceed 130% of its expectation in 3-layer tissue. However, if the level of precision is increased to 99.7% variability in output temperature does not exceed 180% of expected value in 3-layer tissue. Furthermore, sensitivity analysis reveals that one input parameter (skin thermal conductivity) bears significant impact on the output CI width while other five parameters can be neglected. Considering the fact that in vivo measurements are impossible, and that the models overestimate temperature elevation, they can be used for quick and efficient assessments of the phenomenon.

The important contribution of our study is the analysis of the influence of thermal tissue depth and thermal tissue conductivity on temperature distribution is 3-layer human body models. The variance of temperature is mostly affected by the variation of the skin thermal conductivity. Considering its overall influence, this thermal parameter has the major effect on temperature distribution. In skin and fat tissues other parameter exhibit small influence. Furthermore, the thermal conductivity of muscle has significant influence on temperature distribution in muscle tissue. The influence of the remaining parameters is negligible. These parameters, along with arterial blood temperature describe the heat exchange between the human body (single-layer and three layer) and the environment.

CHAPTER 7

Concluding Remarks

A simplified analytical deterministic-stochastic model for rapid assessment of thermal response of the human body due to exposure to external fields is developed in this thesis. The model consists of a vertical electric dipole (VED) placed at a height *h* above the real ground and a human body modelled in the form of a parallelepiped or cylinder. Plane wave exposure is assumed, and complete dosimetric procedure includes 3 steps: incident field dosimetry, internal field dosimetry and thermal dosimetry.

Within the incident field dosimetry, the electric field irradiated by finite-length dipole antenna at any point of the upper half-space is obtained, using a rigorous numerical approach, an approximate numerical approach with an assumed current distribution, and an analytical approach. Three approaches give similar results when the vertical dipole antenna is electrically short ($L \leq \frac{\lambda}{10}$) and when the ratio of the height of the antenna above the ground and wavelength satisfies $h \geq 10\lambda$. Furthermore, when the distance in the horizontal direction is above 60 m these three models agree satisfactorily. The results obtained using a rigorous numerical approach, an approximate numerical approach with an assumed current distribution are also valid in the near field, and analytical solution is based on the far-field approximation.

Approximate approaches with assumed current distribution saves time and computer resources as it avoids the solving of the Pocklington equation, and in the case of the analytical approach the field integral.

Furthermore, an efficient deterministic model for internal field dosimetry, based on calculation of SAR_{WB} in a parallelepiped or cylindrical human body model is proposed. The difference between the SAR_{WB} obtained in parallelepiped and cylindrical human body models in the x horizontal direction is less than 10 % at 80 m away from source VED antenna.

The developed model provides the implementation of internal dosimetry without the use of very demanding realistic, anatomically based, models of the human body. Bearing in mind that the electric field and SAR values obtained by means of analytical approach are higher than the ones corresponding to the results obtained via more rigorous numerical modeling it can be concluded that such an overestimation is acceptable for the health risk assessment. Namely, if the overestimated values do not exceed exposure limits it is ensured that the values stemming from realistic scenarios from either computation or

measurement will stay within the proposed limits. A parallelepiped human body model can further simplify the internal dosimetry and consequently save computational cost, specifically if thermal dosimetry is of interest.

Within the framework of the thesis, a new stochastic-deterministic model for thermal dosimetry based on a multi-layer planar representation of the human body is developed. The deterministic part is based on a simplified one-dimensional single-layer and 3-layer Pennes' Bio-Heat transfer Equotion (PBHE) in biological tissues. The SAR determined in the previous step in the parallelepiped human body model is used as the input EM quantity, i.e. as heat surface density. To solve the PBHE analytically, power density from external heat source related to the absorbed EM energy irradiated from VED antenna, is assumed to either be constant, or exponentially decreasing with the tissue depth.

Proposed models describe tissue temperature under the condition of maximum SAR on the surface of the human body, so they give the upper limit of the temperature change in stationary conditions. The obtained solution gives overestimation of steady-state temperature due to EM radiation compared to other analytical methods. The obtained solution is also compared to other analytical methods presented in analysed literature, but the large number of parameters in the PBHE, makes the comparation challenging. This highlights the importance of parametric analysis in thermal dosimetry.

The impossibility of in-vivo measurement of thermal parameters is the cause of uncertainties in the set of input parameters. In the framework of stochastic modelling of the thermal response of the human body, the influence of uncertainty in the set of input parameters on the resulting temperature elevation in steady-state, in terms of the output quantity of interest, is quantified using the stochastic collocation method. The input random variables are thermal conductivity and tissue thickness of each layer (skin, fat, muscle), and the confidence interval of the temperature elevation is obtained, which extends the usability of the deterministic model. Finally, in the stochastic part of the thermal dosimetry, a sensitivity analysis is performed, thus providing the assessment of the influence of each of the input parameters and their mutual influence on the output value of interest.

UQ results in thermal dosimetry show that the largest variability in output temperature does not exceed 130% of its expectation in 3-layer tissue (95 % level of precision). However, if the level of precision is increased to 99.7% variability in output temperature does not exceed 180% of expected value in 3-layer tissue. Furthermore, SA analysis reveals that skin thermal conductivity bears significant impact on the output CI width while other five parameters can be neglected.

The application of analytical procedures provides fast and complete dosimetry for realistic scenarios in terms of exposure to high frequency radiation from specific antenna systems. By applying stochastic modelling of the body's thermal response, it is possible to estimate

the uncertainty of temperature rise due to the uncertainty of input parameters (thermal conductivity, thickness of tissue layers) that cannot be determined by in vivo measurement.

References

[1] E.G. Kivrak, et al., "Effects of electromagnetic fields exposure on the antioxidant defense system," *Journal of Microscopy and Ultrastructure*, vol. 5, pp. 167–176, 2017.

[2] M. Bonato, et al. "Stochastic Dosimetry Assessment of the Human RF-EMF Exposure to 3D Beamforming Antennas in indoor 5G Networks," *Appl. Sci*., vol. 11, pp. 1751, 2021.

[3] ICNIRP, "Guidelines for Limiting Exposure to Electromagnetic Fields (100 kHz to 300 GHz)," *Health Physics*, vol. 118, no 5, pp. 483–524, 2020.

[4] W. H. Bailey et al., „Synopsis of IEEE std C95. 1TM-2019 'IEEE standard for safety levels with respect to human exposure to electric, magnetic, and electromagnetic fields, 0 Hz to 300 GHz," *IEEE Access*, vol. 7, pp. 171346–171356, 2019.

[5] Y. Imam-Fulani, et al., "5G Frequency Standardization, Technologies, Channel Models, and Network Deployment: Advances, Challenges, and Future Directions," *Sustainability*, vol. 15, no. 6, pp. 1-71, 2023.

[6] K. Li, et al., "Parameter variation effects on millimeter wave dosimetry based on precise skin thickness in real rats," *Scientific Reports*, vol. 13, 17397, 2023.

[7] S. Kodera, A. Hirata, D., Funahashi, S., Watanabe, K., Jokela, K., R.J. Croft, „Temperature Rise for Brief Radio-Frequency Exposure Below 6 GHz," *IEEE Access*, vol. 6, pp. 65737-65746, 2018.

[8] Hirata, et al., "Estimation of Whole-Body Average SAR in Human Models Due to Plane-Wave Exposure at Resonance Frequency," *IEEE Transactions on Electromagnetic Compatibility*, vol. 52(1), pp. 41-48, 2010.

[9] Z.S. Deng, J. Liu, "Monte carlo method to solve multidimensional bioheat transfer problem," *Numer. Heat Transfer*, vol. 42, pp. 543–567, 2002.

[10] J. Fan, L. Wang, „Analytical theory of bioheat transport," *Journal of applied physics*, vol. 109, 2011.

[11] D. Poljak, R. Lucic, V. Doric, S. Antonijevic, „Frequency domain boundary element versus time domain finite element model for the transient analysis of horizontal grounding electrode," *Engineering Analysis with Boundary Elements*, vol. 35, 2011.

[12] B.M. Kibret, „The Human Body Antenna: Characteristics and its Application," PhD thesis, College of Engineering and Science, Victoria University, Melburne, AU, 2016.

[13] A. Sommerfeld, „On the propagation of waves in wireless telegraphy, " *Ann. Phys*., vol. 28; pp. 665–736, 1909.

[14] D.H. Gultekin, P.H. Siegel, „Absorption of 5G Radiation in Brain Tissue as a Function of Frequency, Power and Time," *IEEE Access*, vol.8, pp. 115593- 115612, 2020.

[15] A. Miller, A.J. Poggio, G.J. Burke, E.S. Selden, „Analysis of Wire Antenna in the Presence of a Conducting Half Space: Part I: The Vertical Antenna in Free Space," *Canadian Journal of Physics*, vol. 50, pp. 879–888, 1972.

[16] M. Galić, D. Poljak, V. Dorić, „Simple analytical models for the calculation of the electric field radiated by the base station antenna," *Engineering modelling*, vol. 31, no. 1-2, pp. 31-42, 2018.

[17] D. Poljak, I. Carev, Z.N. Sesnic, "A Multidisciplinary View to the Human Exposure to Electromagnetic Fields – A Note on Multiphysics, Engineering, Biochemical and Legal Aspects," in International Conference on Software, Telecommunications and Computer Networks, Sept 26– 28 , Bol, Croatia, 2024.

[18] T. Kurniawan, A.W. Wood, R.L. McIntosh, "Simplified Analysis of Near Electromagnetic Fields from a Dipole in Lossy Dielectric," *IEEE Transactions on Dielectrics and Electrical Insulation, v*ol. 17, no. 6; pp. 1943- 1949, 2010.
[19] M. Chaaban. et al., "Analytical model for electromagnetic radiation by bare-wire structures," *Progress In Electromagnetics Research*, vol. 45, pp. 395-413, 2012.
[20] G.J. Burke, „Present Capabilities and New Developments in Antenna Modellng with the Numerical El ectromagnetics Code NEC," in *1988 Tactical Comnunications Conference For*t, Wayne, Indiana, May 3-5, 2005.
[21] Kibret, A.K. Teshome, D.T.H. Lai, „Human Body as Antenna and Its Effect on Human Body Communications," *Progress In Electromagnetics Research,* vol. 148, pp.193-207, 2014.
[22] L. Zilberti, et al., "A model to analyze the skin heating produced by millimeter and submillimeter electromagnetic waves," in *2013 International Conference on Electromagnetics in Advanced Applications (ICEAA)*, Turin, Italy, Sept. 09-13, 2013.
[23] J. Okajima, S. Maruyama, H. Takedo, and A. Komiya, "Dimensionless solutions and general characteristics of bioheat transfer during thermal therapy," *International Journal of Thermal Biology*, vol. 34, no. 8, 2009.
[24] W.I Newman, M. Efroimsky, „ The method of variation of constants and multiple time scales in orbital mechanics," *Chaos: An Interdisciplinary Journal of Nonlinear Science,* vol. 13, pp. 476-485, 2003.
[25] A. Šušnjara, et al.,"Stochastic Sensitivity Analysis of Bioheat Transfer Equation," in *URSI EM Theory Symposium,* San Diego, CA, May 27-31, 2019.
[26] D. Poljak, M. Cvetković, "Human Interaction with Electromanetic Fields," Computational Models in Dosimetry, St. Louis, Missouri: Elsevier, Academic Press, 2019.
[27] T. Wu, et al., "The Human body and Millimetre-Wave Wireless Communication Systems: Interactions and Implications," in *IEEE International Conference on Communications,* London, UK, June 08-12, 2015.
[28] R. Pethig, D.B. Kell, "The Passive electrical properties of biological systems: their significance in physiology, biophysics, and biotechnology," *Phys. Med. Biol.,* vol. 32,1987.
[29] C. Gabriel, S. Gabriel, E. Corthout, "The Dielectric Properties of Biological Tissues: I. Literature Survey," *Physics in Medicine and Biology*, 1996.
[30] H.P. Schwan, "Electrical properties of tissues and cell suspensions," *Advanced Phys. Med. Biol.*, vol. 5, pp. 147–209, 1957.
[31] H.P. Schwan, K.R. Foster, "Microwave dielectric properties of tissue. Some comments on the rotational mobility of tissue water," *Biophysical Journal*, vol. 17, 1977.
[32] C.H. Durney, et al., Radiofrequency Radiation Dosimetry Handbook, Second Edition Report SARTR-78-22., Helotes, TX., USA, Country, 1986.
[33] Z.C. Hardiman, "Electromagnetic Radiation and Human Health: A Review of Sources and Effects," *EMR & Human Health*, 2005.
[34] D. Poljak, et al., „On the use of the boundary element analysis in bioelectromagnetics," *Engineering Analysis with Boundary Elements,* vol. 49, pp.2-14, 2014.
[35] P. Vecchia, „Exposure of humans to electromagnetic fields. Standards and regulations," *Ann Ist Super Sanità*, vol. 43, no. 3, pp. 260-267, 2007.
[36] K.A. Norton, "The propagation of radio waves over the surface of the Earth and upper atmosphere — PART 1," *Proceeding of the institute of radio engineers,* vol. 24, no. 2, 1936.

[37] J.R. Wait, K.P. Spied, "On the image representation of the quasi-static fields of a line current source above the ground," *Canadian Journal of Physics*, vol. 47, pp. 2731, 1969.
[38] R.W.P. King, "Electromagnetic field of a vertical dipole over an imperfectly conducting half-space," *Radio Science*, vol. 25, no 2, pp. 149-160, 1990.
[39] R.W.P. King, "The Electromagnetic Field of a Vertical Electric Dipole over the Earth or Sea," *IEEE Transaction on antennas and propagation*, vol. 42, no 3, pp. 382-389, 1994.
[40] M. Parise, "On the Electromagnetic Field of an Overhead Line Current Source," *Electronics*, vol. 9, pp. 1-12, 2020.
[41] M.E. Nazari, W. Huang, „Asymptotic solution for the electromagnetic scattering of a vertical dipole over plasmonic and non-plasmonic half-spaces," *IET Microwave Antennas Propagation*, vol. 15, pp. 704–717, 2021.
[42] P. Perhami, M. Mitra, „Analysis of arbitrarily shaped wire antennas radiating over a lossy half-space," Electromagnetics laboratory department of electrical engineering engineering experiment station university of Illinois at Urbana, Illinois, 1980.
[43] D. Poljak, R. Sesnic, D. Čavka, K.El.K. Drissi, „On the analysis of vertical straight thin wire above a lossy ground: Analytical versus numerical solution," in *International Symposium on Electromagnetic Compatibility - EMC EUROPE*, Rome, Italy, Sept. 17-21, 2012.
[44] S. Bourgiotis, et al., "Radiation of a Vertical Dipole over Flat and Lossy Ground using the Spectral Domain Approach: Comparison of Stationary Phase Method Analytical Solution with Numerical Integration Results," *Electron. Electr. Eng.*, vol. 21, pp. 38–41, 2015.
[45] Chrysostomou, S: Bourgiotis, S. Sautbekov, K. Ioannidi, „Radiation of a Vertical Dipole Antenna over Flat and Lossy Ground: Accurate Electromagnetic Field Calculation using the Spectral Domain Approach along with Redefined Integral Representations and corresponding Novel Analytical Solution," *Elektronika ir Elektrotechnika*, vol. 22, no. 2, 2016.
[46] K.A. Michalski, H.I. Lin, „On the far-zone electromagnetic field of a vertical Hertzian dipole over an imperfectly conducting half-space with extensions to plasmonics," *Radio Science*, vol. 52, pp. 798–810, 2017.
[47] D. Poljak, C. Y. Tham, A. McCowen, „Transient Response of Nonlinearly Loaded Wires in a Two Media Configuration," *IEEE transactions on electromagnetic compatibility*, vol. 46, no. 1, 2004A.
[48] D. Poljak, N. Kovač, „A Simplified Electromagnetic-thermal Analysis of Human Exposure to Radiation from Base Station Antennas," *ATKAAF*, vol. 45, no. 1-2, 2004B.
[49] D. Poljak, C.A. Brebbia, „Indirect Galerkin–Bubnov boundary element method for solving integral equations in electromagnetics," *Engineering Analysis with Boundary Elements*, vol. 28, 2004C.
[50] S. Kuhn, „EMF Risk Assessment: Exposure Assessment and Compliance Testing in Complex Environments," PhD thesis, Swiss Federal Institute of Technology, Zurich, Switzerland, 2009.
[51] M. Ferna´ndez Pantoja, A.G. Yarovoy, A.R. Bretones, „Time domain analysis of thin-wire antennas over lossy ground using the reflection-coefficient approximation," *Radio Science*, vol. 44, pp. 1-14, 2009.

[52] D. Poljak, N. Kovač, „Time domain modeling of a thin wire in a two-media configuration featuring a simplified reflection/transmission coefficient approach,“ *Engineering Analysis with Boundary Elements*, vol. 33, 2009.

[53] A. Šušnjara, M. Cvetković, D. Poljak, S. Lallechere, K. El Khamlichi Drissi, “Stochastic Thermal Dosimetry for Homogenous Human Brain Model”, in *Uncertainty Modelling for Engineering Applications (UMEMA 2017)*, Torino, Italy, Nov. 23-24, 2017.

[54] A. Šarolić, D. Senić, Z. Živković, „Radiation Pattern of a Vertical Dipole over Sea and Setup for Measuring thereof,“ *Automatika,* vol. 53, pp. 56-68, 2012.

[55] D. Poljak, A. Šušnjara, A. Džolić., „Assessment of Transmitted Power Density due to Radiation from Dipole Antenna of Finite Length : Part I: Theoretical background and current distribution,“ in *International Conference on Software, Telecommunications and Computer Networks (SoftCOM)*, Split, Croatia, Sept. 23-25, 2021.

[56] C.K. Chou, et al., “Radio Frequency Electromagnetic Exposure: Tutorial Review on Experimental Dosimetry,” *Bioelectromagnetic*, vol. 17, pp. 195-208, 1996.

[57] O.P. Gandhi, E.L. Hunt, J.A. D’Andrea, “Deposition of electromagnetic energy in animals and in models of man with and without grounding and reflector effects,” *Radio Sci.,* vol. 12, no. 63, pp. 39-47, 1977.

[58] D. Poljak, S. Šesnić, M. Birkić, D. Kosor, „Towards the model for the assessment of the current density induced in the human body due to the electric field irradiated from the rod struck by lightning,“ in *15th International Conference on Software, Telecommunications and Computer Networks*, Split, Croatia, Sept. 27-29, 2007.

[59] Kibret, A.K. Teshome, D.T.H. Lai, „Cylindrical Antenna Theory for the Analysis of Whole-Body Averaged Specific Absorption Rate,“ *IEEE Transactions on Antennas and Propagation*, vol. 63, pp. 5224-5229, 2015.

[60] M. Andriychuk, T. Nazarovets, „Evaluation of the em field exposure in the range of 4g frequencies in the laboratory environment,“ *Computer design systems. Theory and practice,* vol. 5, no. 1, 2023.

[61] R.W.P. King, “Electromagnetic field generated in model of human head by simplified telephone transceiver,” *Radio Science,* vol. 30, no 1, pp. 267-281, 1995.

[62] Zulim, et al., „Assessment of SAR in the human body exposed to an RFID loop antenna,“ in *20th International Conference on Software, Telecommunications and Computer Networks*, Split, Croatia, Sept. 11-13, 2012.

[63] Gonzalez, A. Peratta, D. Poljak, „Induced Currents in the human body resulting from the proximity to surfaces at fixed potentials,“ in *15th International Conference on Software, Telecommunications and Computer Networks*, Split, Croatia, Sept. 27-29, 2007.

[64] J.F. Bakker, M.M. Paulides, A. Christ, N. Kuster, G.C. van Rhoon, „Assessment of induced SAR in children exposed to electromagnetic plane waves between 10 MHz and 5.6 GHz,“ *Physics in medicine and biology*, vol. 55, pp. 3115-3130, 2010.

[65] F. Niedermayr, „Human thermoregulation model of RF-EMF interaction,“ Ph.D. dissertation, Institute of Health Care Engineering with European Testing Institute, Graz, 2012.

[66] D. Poljak, R. Šesnić, M. Cvetković, S. Lallechere, K.El.K. Drissi, „On the analysis of vertical straight thin wire above a lossy ground: Analytical versus numerical solution,“ in *24th International Conference on Software, Telecommunications and Computer Networks (SoftCOM)*, Split, Croatia, Sept. 22-24, 2016.

[67] M. Cvetković, S. Lalléchère, K. El.K. Drissi, P. Bonnet, D. Poljak, „Stochastic Sensitivity in Homogeneous Electromagnetic-Thermal Dosimetry Model of Human Brain,“ *Aces journal*, vol. 31, no. 6, 2016.

[68] T. Nagaoka et al., „Development of realistic high-resolution whole-body voxel models of Japanese adult males and females of average height and weight, and application of models to radio-frequency electromagnetic field dosimetry,“ *Phys. Med. Biol.*, vol. 49, no. 1, pp. 1-15, 2004.

[69] J. Chakarothai, K. Wake, K. Fujii, “Dosimetry of Various Human Bodies Exposed to Microwave Broadband Electromagnetic Pulses,” *Front. Public Health*, vol. 9, 2021.

[70] M.S. Morelli, S. Gallucci, B. Siervo, V. Hartwig, V., “Numerical Analysis of Electromagnetic Field Exposure from 5G Mobile Communications at 28 GHZ in Adults and Children Users for Real-World Exposure Scenarios,“ *Int. J. Environ. Res. Public Health*, vol. 18, 2021.

[71] S. Khalatbari, D. Sardari, A.A. Mirzaee, and H. A. Sadafi, „Calculating SAR in Two Models of the Human Head Exposed to Mobile Phones Radiations at 900 and 1800MHz,“ Progress In Electromagnetics Research Symposium 2006, Cambridge, USA, March 26-29, 2006.

[72] M. Cvetković, D. Poljak, A.L. Kapetanović, „On the Applicability of Numerical Quadrature for Double Surface Integrals at 5G Frequencies,“ *Journal of communications software and systems*, vol. 18, no. 1, 2022.

[73] J. Grund, “Planar Multilayer Model of Human Tissue Exposed to a Plane Electromagnetic Wave,” *IEEE Journal of electromagnetics, RF, and microwaves in medicine and biology*, vol. 5, pp. 305-312, 2021.

[74] T. Hikage, Y. Kawamura and T. Nojima, "Whole-body averaged SAR measurement method using cylindrical scanning of external electromagnetic fields," *2009 International Symposium on Electromagnetic Compatibility - EMC Europe*, Athens, Greece, 2009, pp. 1-4.

[75] D. Poljak, A. Šušnjara, A. Fišić, “Assessment of Transmitted Power Density in the Planar Multilayer Tissue Model due to Radiation from Dipole Antenna,” *Journal of communications software and systems*, vol. 19, no. 1, 2023.

[76] D. Funahashi, et al., „Area-Averaged Transmitted Power Density at Skin Surface as Metric to Estimate Surface Temperature Elevation,“ *IEEE Access*, vol. 6, pp. 77665-77674, 2018.

[77] M. Ziane, R. Sauleau, M. Zhadovov, „Antenna/Body Coupling in the Near-Field at 60 GHz: Impact on the Absorbed Power Density,“ *Appl. Sci.*, vol. 10, pp. 1-16, 2020.

[78] K. Fukunaga, S. Watanabe, Y. Yamanaka, “Dielectric properties of tissue-equivalent liquids and their effects on specific absorption rate”, *IEEE Trans. EMC*, vol.46, no.1, pp.126-129, 2004.

[79] R.G. Olsen, „Preliminary studies: far-field microwave dosimetric measurements of a full-scale model of man,“ *J Microw Power*, vol. 14, no. 4, pp. 383-388, 1979.

[80] R.G. Olsen, T.A. Griner, „Outdoor measurement of SAR in a full-sized human model exposed to 29.9 MHz in the near field,“ *Bioelectromagnetics*, vol. 10, no. 2, pp.161-171, 1989.

[81] R.L. McIntosh, S. Iskra, V. Anderson, „Significant RF-EMF and thermal levels observed in a computational model of a person with a tibial plate for grounded 40 MHz exposure,“ *Bioelectromagnetics*, vol. 35, no. 4, pp. 284-295, 2014.

[82] P. Dimbylow, „Resonance behaviour of whole-body averaged specific energy absorption rate (SAR) in the female voxel model, NAOMI,“ *Phys. Med. Biol.*, vol. 50, no. 17, pp. 4053-4063, 2005.

[83] C.M. Furse, O.P. Gandhi, „Calculation of electric fields and currents induced in a millimeter-resolution human model at 60 Hz using the FDTD method," *Bioelectromagnetics*, vol. 19, no. 5, pp. 293-299, 1998.
[84] C. Lee et al., „Whole-body voxel phantoms of paediatric patients--UF Series B," *Phys. Med. Biol*., vol. 51, no. 18, pp. 4649-4661, 2006.
[85] M. Zankl, et al., "Computational phantoms, ICRP/ICRU, and further developments," *Ann. ICRP*., vol. 47, no 3-4, pp. 35-44, 2018.
[86] A. Christ, et al., "The Virtual Family--development of surface-based anatomical models of two adults and two children for dosimetric simulations," *Phys. Med. Biol.*, vol. 55, no. 2, pp. 23-38, 2010.
[87] O.P. Gandi, et al., "Millimeter-resolution MRI-based models of the Human Body for Electromagnetic Dosimetry from ELF to Microwave Frequencies, Voxel Phantom Development ", In Proc. Of the International Workshop At: National Radiological Protection Board (NRPB), Project: Implantable Antennas (medical, geophysical, plasma applications), 1995.
[88] H.P. Schwan, K. Li, "Hazards due to total body irradiation," *Proc. IRE*, vol. 44, pp. 1572-1561, 1956.
[89] J.C. Lin, A.W. Guy and G.H. Kraft, "Microwave selective brain heating," *J. Microwave Power*, vol. 8, pp. 275-286, 1973.
[90] H.S. Ho, A.W. Guy, R.A. Sigelmann, J. F. Lehmann, "Microwave heating of simulated human limbs by aperture source," *IEEE Trans. Microwave Theory Tech*., vol. MTT-19, pp. 224.231, 1971.
[91] K.M. Chen, B.S. Guru, "Internal EM field and absorbed power density in human torsos induced by 1-500-MHz EM waves," *IEEE Trans. Microwave Theory Tech*., vol. MTT-25, pp. 746-755, 1977.
[92] C.H. Durney, "Electromagnetic Dosimetry for Models of Humans and Animals: A Review of Theoretical and Numerical Techniques," *Proceedings of IEEE,* vol. 68, no. 1, 1980.
[93] D. Poljak, Y.F. Rashed, "The boundary element modelling of the human body exposed to the ELF electromagnetic fields," *Engineering Analysis with Boundary Elements*, vol. 26, pp. 871–875, 2002.
[94] D.W. Hahn, M.N. Ozisik, „Heat Confuction," Third Edition, Published by John Wiley & Sons, Inc., Hoboken, New Jersey, 2012.
[95] J. Kaur, S.A. Khan, "Numerical analysis of heat transfer of in multilayered skin tissue exposed to 5G mobile communication frequencies," *Journal of Thermal Engineering*, vol. 7, no 2, pp. 103-116, 2021.
[96] H.H. Pennes, "Analysis of tissue and Arterial Blood Temperatures in the Resting Human Forearm," *Journal of Applied Physiology*, vol. 1, pp. 93-122, 1948.
[97] H.-W. Huang, T.-L- Horng, „Chapter 1 - Bioheat Transfer and Thermal Heating for Tumor Treatment," Heat Transfer and Fluid Flow in Biological Processes (Chap. 1), S.M. Becker & A.V. Kuznetsov (Eds.), pp. 1-42, 2015.
[98] Z.-S. Deng, J. Liu, "Analytical Solutions to 3-D Bioheat Transfer Problems with or without Phase Change," *Heat Transfer Phenomena and Applications*, 2012.
[99] K. Murase, „An integral-transform approach to the bioheat transfer problems in magnetic hyperthermia," Department of Medical Physics and Engineering, Division of Medical Technology and Science, Faculty of Health Science, Graduate School of Medicine, Osaka University 1-7 Yamadaoka, Suita, Osaka 565-0871, Japan.
[100] T.C. Shih, et al., "Analytical analysis of the Pennes bioheat transfer equation with sinusoidal heat flux condition on skin surface," *Med. Eng. Phys.*, vol. 29, pp. 946–953, 2007.

[101] A. Lakhssassi, et al., "Modifed pennes' equation modelling bio-heat transfer in living tissues: analytical and numerical analysis," *Natural Science*, vol. 2, pp. 1-12, 2010.
[102] S. Kanezaki, A. Watanabe, A. Hirata, H. Shirai, "Theoretical analysis of the layer structure dependence of temperature elevation on skin surface due to millimeter-wave exposure," Technical Report IEICE Japan, EMCJ2008–20, pp. 77–82, 2008.
[103] A. Kengne, A. Lakhssassi, R. Vaillancourt, „Temperature Distributions for Regional Hypothermia Based on Nonlinear Bioheat Equation of Pennes Type: Dermis and Subcutaneous Tissues," *Applied Mathematics*, vol. 3, pp. 217-224, 2012.
[104] N. Bagum, A. Shaha, M. Ahmed, C.A.A. Rashed, „Finite Element Analysis of One Dimensional Bio-Heat Transfer in Human Tissue," *IOSR Journal of Engineering (IOSRJEN)*, vol. 3, no. 6, 2013.
[105] A. Šušnjara, M. Cvetković, D. Poljak, S. Lallechere, K.E.K. Drissi, „Stochastic Thermal Dosimetry for Homogenous Human Brain Model," *UMEMA 2017*, Uncertainty Modeling for Engineering Applications, 1-2.
[106] A. Šušnjara, M. Cvetković, H. Dodig, D. Poljak, „Numerical analysis of a three-compartment head model subjected to variation of input parameters,"*BIOEM*, 2018, pp. 605-610.
[107] H. Wang, W.A. Burgei, H. Zhou, „Analytical solution of one-dimensional Pennes' bioheat equation," *Open Physics*, vol. 18, pp. 1084-1092, 2020.
[108] K. Yue, X. Zhang, F. Yu, „An Analytic Solution of One-dimensional Steady-state Pennes' Bioheat Transfer Equation in Cylindrical Coordinates," *J. of Thermal Science*, vol. 13, no.3, 2004.
[109] A.F. Elsayed, O.A. Beg, „New computational approaches for biophysical heat transfer in tissue under ultrasonic waves: the variational iteration and Chebyshev spectral simulations," *Journal of Mechanics in Medicine and Biology*, vol. 14, no. 3, 2014.
[110] D.C. Shrestha, S. Acharya, D.B. Gurung, „Modeling on Metabolic Rate and Thermoregulation in Three Layered Human Skin during Carpentering, Swimming and Marathon," *Applied Mathematics*, , vol. 11, pp. 753-770, 2020.
[111] M. Cvetković, „pPorast temperature u glavi čovjeka uslijed GSM zračenja, "Graduate work, FESB, Split, Croatia, 2006.
[112] S. Hossain, "One-dimensional Steady-state Analysis of Bioheat Transfer Equation: Tumour Parameters Assessment for Medical Diagnosis Application," Department of Electrical and Computer Engineering, Ryerson University Toronto, ON, M5B 2K3, Canada, 2013.
[113] H.R. Pandey „A One- Dimensional Bio-Heat Transfer Equation with Galerkin FEM in Cylindrical Living Tissue," *Journal of Advanced College of Engineering and Management*, vol. 1, 2015.
[114] D. Poljak, et al., „Stochastic Collocation Applications in Computational Electromagnetics," *Mathematical Problems in Engineering*, vol. 2018, 2018.
[115] S. Kanezaki, A. Hirata, S. Watanable, H. Shirai, "Parameter variation effects on temperature elevation in a steady-state, one-dimensional thermal model for millimeter wave exposure of one- and three-layer human tissue," *Physics in medicine and biology*, vol. 55, pp. 4647–4659, 2010.
[116] E. Kengne, A. Lakhssassi, R. Vaillancourt, „Temperature Distributions for Regional Hypothermia Based on Nonlinear Bioheat Equation of Pennes Type: Dermis and Sub-cutaneous Tissues," *Applied Mathematics*, vol. 3, pp. 217-224, 2012.
[117] K.R. Foster, M.C. Ziskin, S.I. Alekseev, „ Tissue models for RF exposure evaluation at frequencies above 6 GHz: Tissue Models for RF Exposure Evaluation above 6 GHz," *Bioelectromagnetics*, vol. 39, no. 3, 2018.

[118] M.A. Ezzat, N.S. AlSowayan, Z.I.A. Al-Muhiameed, S.M. Ezzat, „Fractional modelling of Pennes' bioheat transfer equation," *Heat and Mass Transfer*, vol. 50, no. 7, 2014.
[119] K.-C. Liu, F.-J. Tu, „Numerical solution of a bioheat transfer problem with transient blood temperature," *International Journal of Computational Methods*, vol. 16, no. 04, 2019.
[120] M.A. Giordano, G. Gutierrez, C. Rinaldi, „Fundamental solutions to the bioheat equation and their application to magnetic fluid hyperthermia," *International Journal of Hyperthermia*, vol. 26, no. 5, pp. 475-484, 2010.
[121] S.M. Becker, „Analytical Bioheat Transfer: Solution Development of the Pennes' Model," Heat Transfer and Fluid Flow in Biological Processes (Chap. 4), S.M. Becker & A.V. Kuznetsov (Eds.), pp. 77-124, 2015.
[122] W. Shen, J. Zhang, „Modeling and Numerical Simulation of Bioheat Transfer and Biomechanics in Soft Tissue," *Mathematical and Computer Modelling*, vol. 41, pp. 1251-1265, 2005.
[123] H. G. Bagaria, D.T. Johnson, „Transient solution to the bioheat equation and optimization for magnetic fluid hyperthermia treatment," *International Journal of Hyperthermia*, vol. 21, no. 1, pp. 57-75, 2005.
[124] D.A. Hodson, G. Eason, and J.C. Barbenel, "Modeling Transient Heat Transfer Through the Skin and Superficial Tissues—1: Surface Insulation," *ASME J. Biomech. Eng*., vol. 108, no. 2, pp. 183–188, 1986.
[125] M. Cvetković, D. Poljak, A.L. Kapetanović, „On the Use of Compound and Extracted Models in Thermal Dosimetry Assessment," *Mathematical Problems in Engineering*, vol. 2020, no. 1, 2020.
[126] M. Cvetković, D. Poljak, „Effects of Electromagnetic Polarization in Homogeneous Electromagnetic-Thermal Dosimetry Model of Human Brain," in *2015 23rd International Conference on Software, Telecommunications and Computer Networks (SoftCOM)*, Split, Croatia, Sept. 16-18, 2015.
[127] H.M. Patil, R. Maniyeri, "Finite difference method based analysis of bio-heat transfer in human breast cyst," *Thermal Science and Engineering Progress*, vol. 10, pp. 42-47, 2019.
[128] A.T. Cole, R.O. Olayiwola, "Variational Iteration Method for Solving Partial Differential Equation Arising from Modeling Heat Transfer in Human Tooth," *International Journal of Sciences: Basic and Applied Research* (IJSBAR), vol. 46, no. 2, pp. 1-7, 2019.
[129] H.F.A Cook, „Comparison of dielectric behavior of pure water and human blood at microwave frequencies," *Br. J. Appl. Phys.*, vol. 3, pp. 249-255, 1952.
[130] T.J. Walters, D.W. Blick, L.R. Johnson, A.R. Eleanor, K.R. Foster, „Non-ionizing radiation protection: summary of research," *Health Physics*, vol. 78, no. 3, pp. 259-267, 2000.
[131] K.R. Foster, J.A.D. Andrea, S. Chalfin, D.J. Hatcher, „ Thermal modeling of millimeter wave damage to the primate cornea at 35 GHz AND 94 GHz," *Health Physics*, vol. 84, no. 6, 2003.
[132] D. Nelson, et al., „Inter-species extrapolation of skin heating resulting from millimeter wave irradiation: Modeling and experimental results," *Health Physics*, vol. 84, no. 5, pp. 608-15, 2003.
[133] D. Poljak, „Introduction to Numerical Methods in Electromagnetics," Advanced Modeling in Computational Electromagnetic Compatibility (Chap. 3), D. Poljak (Eds.), John Wiley & Sons, Inc, 2007A.

[134] M. Cvetković, D. Poljak, A. Hirata „The electromagnetic-thermal dosimetry for the homogeneous human brain model,“ *Engineering Analysis with Boundary Elements*, vol. 63, pp. 61-73, 2016.
[135] M.A. Khanday, V.P. Saxena, „Finite Element Approach for the Study of Thermoregulation in Human Head Exposed to Cold Environment,“ in *AIP Conf. Proc.*, vol. 1146, 2009.
[136] M. Aijaz, M.A. Khanday, „Variational finite element approach to estimate the heat distribution in multi-layered human eye,“ *Finite Elements*, vol. 106, no. 2, pp. 93-104.
[137] E. Schweig, W.B. Brdidges, "Computer Analysis of Dielectric Waveguides, A Finite Difference Method," *IEEE Trans. Microwave Theory and Techniques*, vol. 32, no. 5, pp. 531 -541, 1984.
[138] J. Drozdek, E. Majchrzak, “Numerical solution of bioheat transfer equation by means of the dual reciprocity BEM,” S*cientific Research of the Institute of Mathematics and Computer Science*, vol. 6, no. 1, pp. 47-56, 2007.
[139] Peratta, C.G. Gonzalez, D. Poljak, „Current Density Induced in the Human Body due to Power Distributions Lines using the Boundary Element Method,“ *Journal of communications software and systems*, vol. 3, no. 1, 2007.
[140] A. Šušnjara, „Application of Stochastic Collocation Method and Sensitivity Analysis to Bioelectromagnetics Models,“ PhD thesis, University of Split, Faculty of Electrical Engineering, Mechanical Engineering and Naval Architecture, Split, Croatia, 2021.
[141] K.R. Foster, H.N. Kritikos, H.P. Schwan, „Effect of surface cooling and blood flow on the microwave heating of tissue,“ *IEEE Trans. Biomed. Eng.*, vol. 25, no. 3, pp. 313–319, 1978.
[142] K. Sasaki, M. Mizuno, K. Wake, and S. Watanabe, “Monte Carlo simulations of skin exposure to electromagnetic field from 10 GHz to 1 THz,” *Phys. Med. Biol*., vol. 62, no. 17, pp. 6993–7010, 2017.
[143] L. Zilberti et al., „Parametric Analysis of Transient Skin Heating Induced byTerahertz Radiation,“ *Bioelectromagnetics*, vol. 35, pp. 314-323, 2014.
[144] S. Karaa, J. Zhang, F. Yang, „numerical study of a 3D bioheat transfer problem with different spatial heating,“ *Mathematics and Computers in Simulation*, vol. 68, pp. 375–388, 2005.
[145] Awana, F.A. Shah, „An efficient haar wavelet collocation method for solving Pennes' bioheat transfer model,“ *Acta Universitatis Apulensis*, vol. 60, pp. 75-89, 2019.
[146] S.I. Alekseev and M.C. Ziskin, „Influence of blood flow and millimeter wave exposure on skin temperature in different thermal models,“ *Bioelectromagnetic*, vol. 30, no. 1, pp. 52–58, 2009.
[147] M.C. Ziskin, S. I. Alekseev,K.R. Foster, and Q. Balzano, „Tissue Modelsfor RF Exposure Evaluation at Frequencies above 6 GHz,“ *Bioelectromagnetics*, vol. 39, no. 3, pp. 1-17, 2018.
[148] I. Babuška, F. Nobile, R. Tempone, „A Stochastic Collocation Method for Elliptic Partial Differential Equations with Random Input Data,“ *siam Review*, vol. 52, no. 2, pp. 317-355, 2010.
[149] D. Poljak, et al., “Deterministic-stochastic boundary element modeling of the brain and eye exposed to high-frequency radiation,” *Int. J. Comp. Meth. and Exp. Meas*., vol. 5, no. 3, pp. 250–259, 2017.
[150] A. Šušnjara, M. Cvetković, H. Dodig, D. Poljak, “Stochastic Thermal Dosimetry for the Three Compartment Head Model”, in *26th International Conference on Software, Telecommunications and Computer Networks (SoftCOM 2018)*, Split, Croatia, Sept.13-15, 2018.

[151] A. Šušnjara, et al. (2020), "Stochastic dosimetry of a three compartment head model," *Engineering Analysis with Boundary Elements*, vol. 117, pp. 332–345, 2020.
[152] A. Šušnjara, D. Poljak, M. Galić (2023), "An Efficient Stochastic Modeling of Transmitted Power Density in Two-layered Planar Tissue Exposed to Incident Plane Wave," in *8th International Conference on Smart and Sustainable Technologies*, Split/Bol, Croatia, June 20-23, 2023.
[153] A. Sudret, „Polynomial Chaos Expansions and Stochastic Finite Element Methods," Risk and Reliability in Geotechnical Engineering (Chap. 6), K.-K. Phoon & J. Ching (Eds.), pp. 265-300, CRC Press, Zurich, 2014.
[154] I.M. Sobol, A Primer for the Monte Carlo Method, Boca Raton, Florida, USA: CRC Press, Inc., 1994.
[155] M.H. Kalos, P.A. Whitlock, The Monte Carlo Methods, Hoboken, NJ: Wiley, 2008.
[156] A. Xiu, „Fast numerical methods for stochastic computations: a review," *Communications in Computational Physics*, vol.5, no. 2–4, pp.242–272, 2009.
[157] L. Mathelin, M.Y. Hussaini, "A Stochastic Collocation Algorithm of Uncertainty Analyis," NASA Center for AeroSpace Information, Hanover, 2003.
[158] A. Saltelli, M. Ratto, T. Andres, F. Campologno, F. Cariboni, D. Gatelli, M. Saisana and S. Tarantola, Global Sensitivity Analysis: The Primer, West Susex, England: John Wiley & Sons, Ltd, 2008.
[159] G. Sacco, S. Pisa, M. Zhadobov, "Age-dependence of electromagnetic power and heat deposition in near-surface tissues in emerging 5G bands," *Sci Rep*, vol. 11, 3983, 2021.
[160] C. Andrade, „Understanding the Difference Between Standard Deviation and Standard Error of the Mean, and Knowing When to Use Which*," Indian Journal of Psychological Medicine,* vol. 42, no. 4, pp. 409-410, 2020.

APPENDIX A

Whole-body averaged SAR for cylindrical body model:

$$SAR_{WB} = \frac{1}{V}\int_V SAR dV \tag{A.1}$$

where

$$SAR_{WB} = \frac{\sigma \mathrm{k}^2}{4\rho L a^4 \pi^3 (\sigma^2+\omega^2\varepsilon^2)} \frac{1}{\left|J_1(j^{-1/2}ka)\right|^2} \int_0^a \left|J_0(j^{-1/2}k\zeta\right|^2 d\zeta \int_0^L |I_z(z)|^2 dz \tag{A.2}$$

$$\frac{\sigma \mathrm{k}^2}{4\rho L a^4 \pi^3 (\sigma^2+\omega^2\varepsilon^2)} \frac{1}{\left|J_1(j^{-1/2}ka)\right|^2} = C \tag{A.3}$$

$$\int_0^a \left|J_0(j^{-1/2}k\zeta\right|^2 d\zeta = I_1 \tag{A.4}$$

$$\int_0^L |I_z(z)|^2 dz = I_2 \tag{A.5}$$

$$SAR_{WB} = \mathrm{C} I_1 I_2 \tag{A.6}$$

Since current distribution in cylindrical human body model depends of Bessel function, axial current should have a form similar to (7), where:

$$I(z) = C_1 cos\gamma z + C_2 sin\gamma z \tag{A.7}$$

$$\gamma^2 = k^2\left(1 - \frac{j4\pi Z_c(\zeta)}{kZ_c\Psi_{dR}}\right) \tag{A.8}$$

where k is the free space wave number, Z_c=120π is the free space impedance and $Z_c(\zeta)$ is the HF region, the impedance per unit length is given by

$$k = \omega\sqrt{\mu_0\varepsilon_0} \tag{A.9}$$

$$Z_c(\zeta) = \frac{k}{2\mathrm{a}\pi\sigma} \frac{J_0(j^{-1/2}k\zeta)}{J_1(j^{-1/2}ka)} \tag{A.10}$$

$$\Psi_{dR} = csc\gamma(h-|z|)\int_{-h}^{h} sin\gamma(h-|z'|)\left[\frac{coskR}{R} - \frac{coskR_h}{R_h}\right]dz' \tag{A.11}$$

Appendix B

Heat conduction through a medium is described by Fourier law:

$$\vec{q} = -\lambda \nabla T \tag{B.1}$$

The heat through surface element dS in differential dt is:

$$\mathrm{Q} = \int_t \int_S \vec{q} d\vec{S} dt - \int_t \int_S \lambda \nabla T d\vec{S} dt \tag{B.2}$$

Now, Gauss divergence theorem yields

$$\mathrm{Q} = -\int_t \int_S \lambda \nabla T d\vec{S} dt = -\int_t \int_S \nabla \cdot (\lambda \nabla T) d\mathrm{V} dt \tag{B.3}$$

The differential of total heat delivered into a volume V, due to internal and external heat sources in time differential dt, is given by

$$dQ_{tot} = dQ_{int} + dQ_{ext} \tag{B.4}$$

where the differential of internal and external heat sources are as follows

$$dQ_{int} = Q_i dV dt \tag{B.5}$$

$$dQ_{ext} = \nabla \cdot (\lambda \nabla T) d\mathrm{V} dt \tag{B.6}$$

Now, returning (5) and (6) in (4) and combining previous equations

$$\rho C \frac{\partial T}{\partial t} dV dt = Q_i dV dt + \nabla \cdot (\lambda \nabla T) d\mathrm{V} dt \tag{B.7}$$

Taking spatial and temporal integration yields

$$\rho C \int_t \int_S \frac{\partial T}{\partial t} d\mathrm{V} dt = \int_t \int_S Q_i d\mathrm{V} dt + \int_t \int_S \nabla \cdot (\lambda \nabla T) d\mathrm{V} dt \tag{B.8}$$

Rearranging the integral expression Fourier heat conduction equation is obtained

$$\rho C \frac{\partial T}{\partial t} = Q_i + \nabla \cdot (\lambda \nabla T) \tag{B.9}$$

For source-free areas Fourier heat conduction equation becomes Laplace equation.

In an external forced flow, the rate of heat transfer is approximately proportional to the difference between the surface temperature T_s, and the temperature of the free stream fluid T_e. Therefore, the heat flux density q can be expressed as

$$\mathrm{q}_s = -\lambda \frac{\partial T}{\partial n} = h_c (T_s - T_a) \tag{B.10}$$

Volume blood perfusion of tissue Q_b can be expressed as

$$Q_b = W_b C_{pb}(T_a - T) \tag{B.11}$$

Finally, the space-time bioheat transfer equation can be written in the form

$$\nabla \cdot (\lambda \nabla T) + W_b C_{pb}(T_a - T) + Q_m + Q_{ext} = \rho C \frac{\partial T}{\partial t} \tag{B.12}$$

APPENDIX C

For single-layer geometry and model M_1, according to (1), (2) results in (3)

$$-\lambda_1 \frac{\partial T_i}{\partial x}(x_1 = 0) = h(T_i(x_1 = 0) - T_{air}) \tag{C.1}$$

$$-\lambda \frac{\partial}{\partial x}(A\, e^{-\sqrt{\frac{h_b}{\lambda}}x} + B\, e^{\sqrt{\frac{h_b}{\lambda}}x} + \frac{\rho\, SAR_{max}+Q_m}{h_b} + T_a)(x = 0) = h\Bigg(A\, e^{-\sqrt{\frac{h_b}{\lambda}}x} + B\, e^{\sqrt{\frac{h_b}{\lambda}}x} + \frac{\rho\, SAR_{\max}+Q_m}{h_b} + T_a(x = 0) - T_{air}\Bigg) \tag{C.2}$$

$$\left(\frac{h}{\lambda} - \sqrt{\frac{h_b}{\lambda}}\right)A + \left(\frac{h}{\lambda} + \sqrt{\frac{h_b}{\lambda}}\right)B = -\frac{h}{\lambda}\left(\frac{\rho\, SAR_{\max}+Q_m}{h_b} + T_a - T_{air}\right) \tag{C.3}$$

Using (4), we obtained (5)

$$T_3(x_4 = d_3 = L_1) = T_a \tag{C.4}$$

$$A = -B\, e^{2\sqrt{\frac{h_b}{\lambda}}L_1} - \frac{\rho\, SAR_{max}+Q_m}{h_b} e^{\sqrt{\frac{h_b}{\lambda}}L_1} \tag{C.5}$$

After minor mathematical manipulation, the value of constant B is obtained. With known B, (5) is used to calculate A.

$$A = -\frac{-\frac{h}{\lambda}(s_1 + T_a - T_{air}) + s_4\left(s_1\, e^{\sqrt{\frac{h_b}{\lambda}}L_1}\right)}{\left\{s_3 - s_4\, e^{2\sqrt{\frac{h_b}{\lambda}}L_1}\right\}} e^{2\sqrt{\frac{h_b}{\lambda}}L_1} - \frac{\rho\, SAR_{max}+Q_m}{h_b} e^{\sqrt{\frac{h_b}{\lambda}}L_1} \tag{C.6}$$

$$B = \frac{-\frac{h}{\lambda}(s_1 + T_a - T_{air}) + s_4\left(s_1\, e^{\sqrt{\frac{h_b}{\lambda}}L_1}\right)}{\left\{s_3 - s_4\, e^{2\sqrt{\frac{h_b}{\lambda}}L_1}\right\}} \tag{C.7}$$

$$s_1 = \frac{\rho SAR_{max}+Q_m}{h_b}, s_2 = \frac{\rho\, SAR_{max}}{(4\lambda_1 - h_{b1})}, s_3 = \left(\sqrt{\frac{h_b}{\lambda}} + \frac{h}{\lambda}\right),\ s_4 = \left(\frac{h}{\lambda} - \sqrt{\frac{h_b}{\lambda}}\right) \tag{C.8}$$

APPENDIX D

For single-layer geometry and model M_2, according to (1), (2) results in (3)

$$-\lambda_1 \frac{\partial T_i}{\partial x}(x_1 = 0) = h(T_i(x_1 = 0) - T_{air}) \tag{D.1}$$

$$-\lambda \frac{\partial}{\partial x}(A\, e^{-\sqrt{\frac{h_b}{\lambda}}x} + B\, e^{\sqrt{\frac{h_b}{\lambda}}x} - \left(\frac{\rho SAR_{max}}{4\lambda - h_b}\right) e^{-2x} + \frac{Q_m}{h_b} + T_a)(x = 0) = h\left(A\, e^{-\sqrt{\frac{h_b}{\lambda}}x} + B\, e^{\sqrt{\frac{h_b}{\lambda}}x} - \left(\frac{\rho SAR_{max}}{4\lambda - h_b}\right) e^{-2x} + \frac{Q_m}{h_b} + T_a(x = 0) - T_{air}\right) \tag{D.2}$$

$$-\sqrt{\frac{h_b}{\lambda}}(A - B) + 2\left(\frac{\rho SAR_{max}}{4\lambda - h_b}\right) = -\frac{h}{\lambda}\left(A + B - \left(\frac{\rho SAR_{max}}{4\lambda - h_b}\right) + \frac{Q_m}{h_b} + T_a - T_{air}\right) \tag{D.3}$$

Using (4), we obtained (5)

$$T_3(x_4 = d_3 = L_1) = T_a \tag{D.4}$$

$$A = -\frac{\left(\frac{h}{\lambda} + \sqrt{\frac{h_b}{\lambda}}\right)}{\left(\frac{h}{\lambda} - \sqrt{\frac{h_b}{\lambda}}\right)} B - \frac{h}{\lambda\left(\frac{h}{\lambda} - \sqrt{\frac{h_b}{\lambda}}\right)}\left(-\frac{\rho SAR_{max}}{4\lambda - h_b} + \frac{Q_m}{h_b} + T_a - T_{air}\right) - 2\left(\frac{\rho SAR_{max}}{4\lambda - h_b}\right) \tag{D.5}$$

After minor mathematical manipulation, the value of constant B is obtained. With known B, (5) is used to calculate A.

$$A = -\frac{-\frac{h}{\lambda}\left(-s_2 + \frac{Q_m}{h_b} + T_a - T_{air}\right) - 2s_2 - s_4 \left\{ s_2\, e^{-2L_1} e^{\sqrt{\frac{h_b}{\lambda}}L_1} - \frac{Q_m}{h_b} e^{\sqrt{\frac{h_b}{\lambda}}L_1} \right\}}{\left\{ s_3 - s_4\, e^{2\sqrt{\frac{h_b}{\lambda}}L_1} \right\}} e^{2\sqrt{\frac{h_b}{\lambda}}L_1} + s_2\, e^{-2L_1} e^{\sqrt{\frac{h_b}{\lambda}}L_1} - \frac{Q_m}{h_b} e^{\sqrt{\frac{h_b}{\lambda}}L_1} \tag{D.6}$$

$$B = \frac{-\frac{h}{\lambda}\left(-s_2 + \frac{Q_m}{h_b} + T_a - T_{air}\right) - 2s_2 - s_4 \left\{ s_2\, e^{-2L_1} e^{\sqrt{\frac{h_b}{\lambda}}L_1} - \frac{Q_m}{h_b} e^{\sqrt{\frac{h_b}{\lambda}}L_1} \right\}}{\left\{ s_3 - s_4\, e^{2\sqrt{\frac{h_b}{\lambda}}L_1} \right\}} \tag{D.7}$$

$$s_1 = \frac{\rho SAR_{max} + Q_m}{h_b}, s_2 = \frac{\rho\, SAR_{max}}{(4\lambda_1 - h_{b1})}, s_3 = \left(\sqrt{\frac{h_b}{\lambda}} + \frac{h}{\lambda}\right),\ s_4 = \left(\frac{h}{\lambda} - \sqrt{\frac{h_b}{\lambda}}\right) \tag{D.8}$$

APPENDIX E

For 3-layer geometry and model M_1, starting from (1), the relationship between A_3 and B_3 is obtained

$$T_3(x_3 = d_3 = L_1) = T_a \tag{E.1}$$

$$A_3 = -B_3\, e^{2l_{31}} - s_3 e^{l_{31}} \tag{E.2}$$

On the boundary fat-muscle:

$$A_2\, e^{-\sqrt{\frac{h_{b2}}{\lambda_2}}d_2} + B_2\, e^{\sqrt{\frac{h_{b2}}{\lambda_2}}d_2} = A_3 e^{-\sqrt{\frac{h_{b3}}{\lambda_3}}d_2} + B_3\, e^{\sqrt{\frac{h_{b3}}{\lambda_3}}d_2} + \frac{\rho_3 SAR_{max3}+Q_{m3}}{h_{b3}} - \frac{\rho_2 SAR_{max2}+Q_{m2}}{h_{b2}} \tag{E.3}$$

$$-A_2\, e^{-\sqrt{\frac{h_{b2}}{\lambda_2}}d_2} + B_2\, e^{\sqrt{\frac{h_{b2}}{\lambda_2}}d_2} = -A_3\sqrt{\frac{\lambda_2 h_{b3}}{\lambda_3 h_{b2}}}\, e^{-\sqrt{\frac{h_{b3}}{\lambda_3}}d_2} + \sqrt{\frac{\lambda_2 h_{b3}}{\lambda_3 h_{b2}}}\, B_3\, e^{\sqrt{\frac{h_{b3}}{\lambda_3}}d_2} \tag{E.4}$$

On the boundary skin-fat:

$$A_1 e^{-\sqrt{\frac{h_{b1}}{\lambda_1}}d_1} + B_1 e^{\sqrt{\frac{h_{b1}}{\lambda_1}}d_1} = A_2\, e^{-\sqrt{\frac{h_{b2}}{\lambda_2}}d_1} + B_2\, e^{\sqrt{\frac{h_{b2}}{\lambda_2}}d_1} + \left\{ \frac{\rho_2 SAR_{max2}+Q_{m2}}{h_{b2}} - \frac{\rho_1 SAR_{max1}+Q_{m1}}{h_{b1}} \right\} \tag{E.5}$$

$$-A_1\, e^{-\sqrt{\frac{h_{b1}}{\lambda_1}}d_1} + B_1\, e^{\sqrt{\frac{h_{b1}}{\lambda_1}}d_1} = -A_1\sqrt{\frac{\lambda_1 h_{b2}}{\lambda_2 h_{b1}}}\, e^{-\sqrt{\frac{h_{b2}}{\lambda_2}}d_1} + B_3\sqrt{\frac{\lambda_1 h_{b2}}{\lambda_2 h_{b1}}}\, e^{\sqrt{\frac{h_{b3}}{\lambda_3}}d_2} \tag{E.6}$$

On air-skin interface

$$A_1 = \frac{\sqrt{\lambda_1 h_{b1}}+h}{\sqrt{\lambda_1 h_{b1}}-h} B_1 + \frac{h}{\sqrt{\lambda_1 h_{b1}}-h}(s_1 + T_a - T_{air}) \tag{E.7}$$

$$A_1 = c_1 B_1 + c_2(s_1 + T_a - T_{air}) \tag{E.8}$$

Adding and subtracting (3) and (4) will yield to equations (9) and (10) in which A_2 and B_2 are expressed through A_3 and B_3

$$A_2 = 0.5 e^{\sqrt{\frac{h_{b2}}{\lambda_2}}d_2}\left[\left(1+\sqrt{\frac{\lambda_2 h_{b3}}{\lambda_3 h_{b2}}}\right) e^{-\sqrt{\frac{h_{b3}}{\lambda_3}}d_2} A_3 + B_3\left(1-\sqrt{\frac{\lambda_2 h_{b3}}{\lambda_3 h_{b2}}}\right) e^{\sqrt{\frac{h_{b3}}{\lambda_3}}d_2} + \left\{ \frac{\rho_3 SAR_{max3}+Q_{m3}}{h_{b3}} - \frac{\rho_2 SAR_{max2}+Q_{m2}}{h_{b2}} \right\}\right] \tag{E.9}$$

$$B_2 = 0.5e^{-\sqrt{\frac{h_{b2}}{\lambda_2}}d_2}\left[A_3\left(1-\sqrt{\frac{\lambda_2 h_{b3}}{\lambda_3 h_{b2}}}\right)e^{-\sqrt{\frac{h_{b3}}{\lambda_3}}d_2} + B_3\left(1+\sqrt{\frac{\lambda_2 h_{b3}}{\lambda_3 h_{b2}}}\right)e^{\sqrt{\frac{h_{b3}}{\lambda_3}}d_2} + \left\{\frac{\rho_3 SAR_{max3}+Q_{m3}}{h_{b3}} - \frac{\rho_2 SAR_{max2}+Q_{m2}}{h_{b2}}\right\}\right] \quad \text{(E.10)}$$

Inserting (2) in (9) and (10), (11) and (12) are obtained. (11) and (12) can be written as (13) and (14)

$$A_2 = 0.5e^{\sqrt{\frac{h_{b2}}{\lambda_2}}d_2}\left\{\left[\left(1-\sqrt{\frac{\lambda_2 h_{b3}}{\lambda_3 h_{b2}}}\right)e^{\sqrt{\frac{h_{b3}}{\lambda_3}}d_2} - e^{2l_{31}}\left(1+\sqrt{\frac{\lambda_2 h_{b3}}{\lambda_3 h_{b2}}}\right)e^{-\sqrt{\frac{h_{b3}}{\lambda_3}}d_2}\right]B_3 - s_3\left(1+\sqrt{\frac{\lambda_2 h_{b3}}{\lambda_3 h_{b2}}}\right)e^{-\sqrt{\frac{h_{b3}}{\lambda_3}}d_2}e^{l_{31}} + \frac{\rho_3 SAR_{max3}+Q_{m3}}{h_{b3}} - \frac{\rho_2 SAR_{max2}+Q_{m2}}{h_{b2}}\right\} \quad \text{(E.11)}$$

$$B_2 = 0.5e^{-\sqrt{\frac{h_{b2}}{\lambda_2}}d_2}\left\{\left[\left(1+\sqrt{\frac{\lambda_2 h_{b3}}{\lambda_3 h_{b2}}}\right)e^{\sqrt{\frac{h_{b3}}{\lambda_3}}d_2} - \left(1-\sqrt{\frac{\lambda_2 h_{b3}}{\lambda_3 h_{b2}}}\right)e^{-\sqrt{\frac{h_{b3}}{\lambda_3}}d_2}e^{2l_{31}}\right]B_3 - s_3 e^{l_{31}}\left(1-\sqrt{\frac{\lambda_2 h_{b3}}{\lambda_3 h_{b2}}}\right)e^{-\sqrt{\frac{h_{b3}}{\lambda_3}}d_2} + \frac{\rho_3 SAR_{max3}+Q_{m3}}{h_{b3}} - \frac{\rho_2 SAR_{max2}+Q_{m2}}{h_{b2}}\right\} \quad \text{(E.12)}$$

$$A_2 = 0.5e^{\sqrt{\frac{h_{b2}}{\lambda_2}}d_2}[a_{21}B_3 + a_{22}] \quad \text{(E.13)}$$

$$B_2 = 0.5e^{-\sqrt{\frac{h_{b2}}{\lambda_2}}d_2}[b_{21}B_3 + b_{22}] \quad \text{(E.14)}$$

Adding and subtracting (5) and (6) will yield to equations (15) and (16) in which A_1 and B_1 are expressed through A_2 and B_2

$$A_1 = 0.5e^{\sqrt{\frac{h_{b1}}{\lambda_1}}d_1}\left[\left(1+\sqrt{\frac{\lambda_1 h_{b2}}{\lambda_2 h_{b1}}}\right)A_2\, e^{-\sqrt{\frac{h_{b2}}{\lambda_2}}d_1} + \left(1-\sqrt{\frac{\lambda_1 h_{b2}}{\lambda_2 h_{b1}}}\right)B_2\, e^{\sqrt{\frac{h_{b2}}{\lambda_2}}d_1} + \frac{\rho_2 SAR_{max2}+Q_{m2}}{h_{b2}} - \frac{\rho_1 SAR_{max1}+Q_{m1}}{h_{b1}}\right] \quad \text{(E.15)}$$

$$B_1 = 0.5e^{-\sqrt{\frac{h_{b1}}{\lambda_1}}d_1}\left[\left(1-\sqrt{\frac{\lambda_1 h_{b2}}{\lambda_2 h_{b1}}}\right)A_2\, e^{-\sqrt{\frac{h_{b2}}{\lambda_2}}d_1} + \left(1+\sqrt{\frac{\lambda_1 h_{b2}}{\lambda_2 h_{b1}}}\right)B_2\, e^{\sqrt{\frac{h_{b2}}{\lambda_2}}d_1} + \frac{\rho_2 SAR_{max2}+Q_{m2}}{h_{b2}} - \frac{\rho_1 SAR_{max1}+Q_{m1}}{h_{b1}}\right] \quad \text{(E.16)}$$

Inserting (13) and (14) in (15) and (16), (17) and (18) are obtained, and (19) and (20) express A_1 and B_1 through B_3. (19) and (20) can be written as (21) and (22)

$$A_1 = 0.5e^{\sqrt{\frac{h_{b1}}{\lambda_1}}d_1}\left[\left(1+\sqrt{\frac{\lambda_1 h_{b2}}{\lambda_2 h_{b1}}}\right)\left(0.5e^{\sqrt{\frac{h_{b2}}{\lambda_2}}d_2}a_{21}B_3 + \right.\right. \quad \text{(E.17)}$$

$$a_{22}0.5e^{\sqrt{\frac{h_{b2}}{\lambda_2}}d_2}\Big)\, e^{-\sqrt{\frac{h_{b2}}{\lambda_2}}d_1} + \left(1-\sqrt{\frac{\lambda_1 h_{b2}}{\lambda_2 h_{b1}}}\right)\left(0.5e^{-\sqrt{\frac{h_{b2}}{\lambda_2}}d_2}b_{21}B_3 + 0.5e^{-\sqrt{\frac{h_{b2}}{\lambda_2}}d_2}b_{22}\right) e^{\sqrt{\frac{h_{b2}}{\lambda_2}}d_1} + \frac{\rho_2 SAR_{max2}+Q_{m2}}{h_{b2}} - \frac{\rho_1 SAR_{max1}+Q_{m1}}{h_{b1}}\Bigg]$$

$$B_1 = 0.5e^{-\sqrt{\frac{h_{b1}}{\lambda_1}}d_1}\Bigg[\left(1-\sqrt{\frac{\lambda_1 h_{b2}}{\lambda_2 h_{b1}}}\right)\left(0.5e^{\sqrt{\frac{h_{b2}}{\lambda_2}}d_2}a_{21}B_3 + a_{22}0.5e^{\sqrt{\frac{h_{b2}}{\lambda_2}}d_2}\Big)\, e^{-\sqrt{\frac{h_{b2}}{\lambda_2}}d_1} + \left(1+\sqrt{\frac{\lambda_1 h_{b2}}{\lambda_2 h_{b1}}}\right)\left(0.5e^{-\sqrt{\frac{h_{b2}}{\lambda_2}}d_2}b_{21}B_3 + 0.5e^{-\sqrt{\frac{h_{b2}}{\lambda_2}}d_2}b_{22}\right) e^{\sqrt{\frac{h_{b2}}{\lambda_2}}d_1} + \frac{\rho_2 SAR_{max2}+Q_{m2}}{h_{b2}} - \frac{\rho_1 SAR_{max1}+Q_{m1}}{h_{b1}}\Bigg] \quad \text{(E.18)}$$

$$A_1 = 0.5e^{\sqrt{\frac{h_{b1}}{\lambda_1}}d_1}\Bigg\{\Bigg[0.5a_{21}\left(1+\sqrt{\frac{\lambda_1 h_{b2}}{\lambda_2 h_{b1}}}\right)e^{\sqrt{\frac{h_{b2}}{\lambda_2}}d_2}e^{-\sqrt{\frac{h_{b2}}{\lambda_2}}d_1} + 0.5b_{21}\left(1-\sqrt{\frac{\lambda_1 h_{b2}}{\lambda_2 h_{b1}}}\right)e^{-\sqrt{\frac{h_{b2}}{\lambda_2}}d_2}e^{\sqrt{\frac{h_{b2}}{\lambda_2}}d_1}\Bigg]B_3 + 0.5a_{22}\left(1+\sqrt{\frac{\lambda_1 h_{b2}}{\lambda_2 h_{b1}}}\right)e^{\sqrt{\frac{h_{b2}}{\lambda_2}}d_2}e^{-\sqrt{\frac{h_{b2}}{\lambda_2}}d_1} + 0.5b_{22}\left(1-\sqrt{\frac{\lambda_1 h_{b2}}{\lambda_2 h_{b1}}}\right)e^{-\sqrt{\frac{h_{b2}}{\lambda_2}}d_2}e^{\sqrt{\frac{h_{b2}}{\lambda_2}}d_1} + \frac{\rho_2 SAR_{max2}+Q_{m2}}{h_{b2}} - \frac{\rho_1 SAR_{max1}+Q_{m1}}{h_{b1}}\Bigg\} \quad \text{(E.19)}$$

$$B_1 = 0.5e^{-\sqrt{\frac{h_{b1}}{\lambda_1}}d_1}\Bigg\{\Bigg[0.5a_{21}\left(1-\sqrt{\frac{\lambda_1 h_{b2}}{\lambda_2 h_{b1}}}\right)e^{\sqrt{\frac{h_{b2}}{\lambda_2}}d_2}e^{-\sqrt{\frac{h_{b2}}{\lambda_2}}d_1} + 0.5b_{21}\left(1+\sqrt{\frac{\lambda_1 h_{b2}}{\lambda_2 h_{b1}}}\right)e^{-\sqrt{\frac{h_{b2}}{\lambda_2}}d_2}e^{\sqrt{\frac{h_{b2}}{\lambda_2}}d_1}\Bigg]B_3 + 0.5a_{22}\left(1-\sqrt{\frac{\lambda_1 h_{b2}}{\lambda_2 h_{b1}}}\right)e^{\sqrt{\frac{h_{b2}}{\lambda_2}}d_2}e^{-\sqrt{\frac{h_{b2}}{\lambda_2}}d_1} + 0.5b_{22}\left(1+\sqrt{\frac{\lambda_1 h_{b2}}{\lambda_2 h_{b1}}}\right)e^{-\sqrt{\frac{h_{b2}}{\lambda_2}}d_2}e^{\sqrt{\frac{h_{b2}}{\lambda_2}}d_1} + \frac{\rho_2 SAR_{max2}+Q_{m2}}{h_{b2}} - \frac{\rho_1 SAR_{max1}+Q_{m1}}{h_{b1}}\Bigg\} \quad \text{(E.20)}$$

$$A_1 = 0.5e^{\sqrt{\frac{h_{b1}}{\lambda_1}}d_1}\{a_{11}\,B_3 + a_{12}\} \quad \text{(E.21)}$$

$$B_1 = 0.5e^{-\sqrt{\frac{h_{b1}}{\lambda_1}}d_1}\{b_{11}B_3 + b_{12}\} \quad \text{(E.22)}$$

Using (8) B_3 is obtained. With B_3 known $A_3, A_2, B_2, A_1, and\ B_1$ can be obtained using (2), (13), (14), (21) and (22)

$$B_3 = \frac{-a_{12}0.5e^{\sqrt{\frac{h_{b1}}{\lambda_1}}d_1} + 0.5c_1 b_{12}e^{-\sqrt{\frac{h_{b1}}{\lambda_1}}d_1} + c_2(\,s_1 + T_a - T_{air})}{\left(0.5a_{11}e^{\sqrt{\frac{h_{b1}}{\lambda_1}}d_1} - 0.5b_{11}c_1 e^{-\sqrt{\frac{h_{b1}}{\lambda_1}}d_1}\right)} \quad \text{(E.23)}$$

APPENDIX F

For 3-layer geometry and model M_2, starting from (1), the relationship between A_3 and B_3 is obtained

$$T_3(x_3 = d_3 = L_1) = T_a \tag{F.1}$$

$$\begin{aligned} A_3 &= -B_3\, e^{2\sqrt{\frac{h_b}{\lambda_3}}L_1} + \left(\frac{\rho_3 SAR_{3max}}{4\lambda_3 - h_{b3}}\right) e^{\sqrt{\frac{h_b}{\lambda_3}}L_1} e^{-2L_1} - \frac{Q_{m3}}{h_{b3}} e^{\sqrt{\frac{h_b}{\lambda_3}}L_1} \\ &= -B_3\, e^{2l_{31}} + s_3 e^{l_{31}} e^{-2L_1} - \frac{Q_{m3}}{h_{b3}} e^{l_{31}} \end{aligned} \tag{F.2}$$

On the boundary fat-muscle:

$$\begin{aligned} A_2\, e^{-\sqrt{\frac{h_{b2}}{\lambda_2}}d_2} + B_2\, e^{\sqrt{\frac{h_{b2}}{\lambda_2}}d_2} = A_3 e^{-\sqrt{\frac{h_{b3}}{\lambda_3}}d_2} + B_3\, e^{\sqrt{\frac{h_{b3}}{\lambda_3}}d_2} - s_3 e^{-2d_2} + \frac{Q_{m3}}{h_{b3}} + \\ s_2 e^{-2d_2} - \frac{Q_{m2}}{h_{b2}} \end{aligned} \tag{F.3}$$

$$\begin{aligned} -A_2\, e^{-\sqrt{\frac{h_{b2}}{\lambda_2}}d_2} + B_2\, e^{\sqrt{\frac{h_{b2}}{\lambda_2}}d_2} = -\sqrt{\frac{\lambda_3 h_{b3}}{\lambda_2 h_{b2}}} A_3 e^{-\sqrt{\frac{h_{b3}}{\lambda_3}}d_2} + \sqrt{\frac{\lambda_3 h_{b3}}{\lambda_2 h_{b2}}} B_3\, e^{\sqrt{\frac{h_{b3}}{\lambda_3}}d_2} + \\ 2\frac{\lambda_3}{\lambda_2}\sqrt{\frac{\lambda_2}{h_{b2}}} s_3 e^{-2d_2} - 2\frac{\lambda_3}{\lambda_2}\sqrt{\frac{\lambda_2}{h_{b2}}} s_2 e^{-2d_2} \end{aligned} \tag{F.4}$$

On the boundary skin-fat:

$$\begin{aligned} A_1 e^{-\sqrt{\frac{h_{b1}}{\lambda_1}}d_1} + B_1 e^{\sqrt{\frac{h_{b1}}{\lambda_1}}d_1} \\ = A_2\, e^{-\sqrt{\frac{h_{b2}}{\lambda_2}}d_1} + B_2\, e^{\sqrt{\frac{h_{b2}}{\lambda_2}}d_1} - s_2 e^{-2d_1} + \frac{Q_{m2}}{h_{b2}} + s_1 e^{-2d_1} - \frac{Q_{m1}}{h_{b1}} \end{aligned} \tag{F.5}$$

$$\begin{aligned} -A_1\, e^{-\sqrt{\frac{h_{b1}}{\lambda_1}}d_1} + B_1\, e^{\sqrt{\frac{h_{b1}}{\lambda_1}}d_1} = \left[-\sqrt{\frac{\lambda_2 h_{b2}}{\lambda_1 h_{b1}}} A_2 e^{-\sqrt{\frac{h_{b2}}{\lambda_2}}d_1} + \sqrt{\frac{\lambda_2 h_{b2}}{\lambda_1 h_{b1}}} B_2\, e^{\sqrt{\frac{h_{b2}}{\lambda_2}}d_1} + \right. \\ \left. 2\frac{\lambda_2}{\lambda_1}\sqrt{\frac{\lambda_1}{h_{b1}}} s_2 e^{-2d_1} \right] - 2\frac{\lambda_2}{\lambda_1}\sqrt{\frac{\lambda_1}{h_{b1}}} s_1 e^{-2d_1} \end{aligned} \tag{F.6}$$

On air-skin interface

$$\begin{aligned} A_1 = \frac{\sqrt{\lambda_1 h_{b1}} + h}{\sqrt{\lambda_1 h_{b1}} - h} B_1 + \frac{h}{\sqrt{\lambda_1 h_{b1}} - h}\left[-\left(\frac{\rho_1 SAR_{1max}}{4\lambda_1 - h_{b1}}\right) + \frac{Q_{m1}}{h_{b1}} + T_a - T_{air})\right] \\ + \frac{2\lambda_1 c_2 s_1}{h} \end{aligned} \tag{F.7}$$

$$A_1 = c_1 B_1 + c_2\left(-s_1 + \frac{Q_{m1}}{h_{b1}} + T_a - T_{air}\right) + \frac{2\lambda_1 c_2 s_1}{h} \tag{F.8}$$

Adding and subtracting (3) and (4) will yield to equations (9) and (10) in which A_2 and B_2 are expressed through A_3 and B_3

$$\begin{aligned} A_2 = 0.5e^{\sqrt{\frac{h_{b2}}{\lambda_2}}d_2}\Bigg\{ & A_3\left(1+\sqrt{\frac{\lambda_2 h_{b3}}{\lambda_3 h_{b2}}}\right)e^{-\sqrt{\frac{h_{b3}}{\lambda_3}}d_2} + B_3\left(1-\sqrt{\frac{\lambda_2 h_{b3}}{\lambda_3 h_{b2}}}\right)e^{\sqrt{\frac{h_{b3}}{\lambda_3}}d_2} \\ & - s_3 e^{-2d_2} + \frac{Q_{m3}}{h_{b3}} + s_2 e^{-2d_2} - \frac{Q_{m2}}{h_{b2}} - 2\frac{\lambda_3}{\lambda_2}\sqrt{\frac{\lambda_2}{h_{b2}}}s_3 e^{-2d_2} \\ & + 2\frac{\lambda_3}{\lambda_2}\sqrt{\frac{\lambda_2}{h_{b2}}}s_2 e^{-2d_2}\Bigg\} \end{aligned} \tag{F.9}$$

$$\begin{aligned} B_2 = 0.5e^{-\sqrt{\frac{h_{b2}}{\lambda_2}}d_2}\Bigg\{ & A_3\left(1-\sqrt{\frac{\lambda_2 h_{b3}}{\lambda_3 h_{b2}}}\right)e^{-\sqrt{\frac{h_{b3}}{\lambda_3}}d_2} + B_3\left(1+\sqrt{\frac{\lambda_2 h_{b3}}{\lambda_3 h_{b2}}}\right)e^{\sqrt{\frac{h_{b3}}{\lambda_3}}d_2} \\ & - s_3 e^{-2d_2} + \frac{Q_{m3}}{h_{b3}} + s_2 e^{-2d_2} - \frac{Q_{m2}}{h_{b2}} + 2\frac{\lambda_3}{\lambda_2}\sqrt{\frac{\lambda_2}{h_{b2}}}s_3 e^{-2d_2} \\ & - 2\frac{\lambda_3}{\lambda_2}\sqrt{\frac{\lambda_2}{h_{b2}}}s_2 e^{-2d_2}\Bigg\} \end{aligned} \tag{F.10}$$

Inserting (2) in (9) and (10), (11) and (12) are obtained. (11) and (12) can be written as (13) and (14)

$$\begin{aligned} A_2 = 0.5e^{\sqrt{\frac{h_{b2}}{\lambda_2}}d_2}\Bigg\{ & B_3\left[\left(1-\sqrt{\frac{\lambda_2 h_{b3}}{\lambda_3 h_{b2}}}\right)e^{\sqrt{\frac{h_{b3}}{\lambda_3}}d_2} - \left(1+\sqrt{\frac{\lambda_2 h_{b3}}{\lambda_3 h_{b2}}}\right)e^{2l_{31}}e^{-\sqrt{\frac{h_{b3}}{\lambda_3}}d_2}\right] + \\ & s_3\left(1+\sqrt{\frac{\lambda_2 h_{b3}}{\lambda_3 h_{b2}}}\right)e^{l_{31}}e^{-2L_1}e^{-\sqrt{\frac{h_{b3}}{\lambda_3}}d_2} - \left(1+\sqrt{\frac{\lambda_2 h_{b3}}{\lambda_3 h_{b2}}}\right)\frac{Q_{m3}}{h_{b3}}e^{l_{31}}e^{-\sqrt{\frac{h_{b3}}{\lambda_3}}d_2} - s_3 e^{-2d_2} + \\ & \frac{Q_{m3}}{h_{b3}} + s_2 e^{-2d_2} - \frac{Q_{m2}}{h_{b2}} - 2\frac{\lambda_3}{\lambda_2}\sqrt{\frac{\lambda_2}{h_{b2}}}s_3 e^{-2d_2} + 2\frac{\lambda_3}{\lambda_2}\sqrt{\frac{\lambda_2}{h_{b2}}}s_2 e^{-2d_2}\Bigg\} \end{aligned} \tag{F.11}$$

$$B_2 = 0.5e^{-\sqrt{\frac{h_{b2}}{\lambda_2}}d_2}\left\{B_3\left[\left(1+\sqrt{\frac{\lambda_2 h_{b3}}{\lambda_3 h_{b2}}}\right)e^{\sqrt{\frac{h_{b3}}{\lambda_3}}d_2} - (1-\sqrt{\frac{\lambda_2 h_{b3}}{\lambda_3 h_{b2}}})e^{2l_{31}}e^{-\sqrt{\frac{h_{b3}}{\lambda_3}}d_2}\right]\right.$$
$$+ s_3(1-\sqrt{\frac{\lambda_2 h_{b3}}{\lambda_3 h_{b2}}})e^{l_{31}}e^{-2L_1}e^{-\sqrt{\frac{h_{b3}}{\lambda_3}}d_2}$$
$$-\frac{Q_{m3}}{h_{b3}}(1-\sqrt{\frac{\lambda_2 h_{b3}}{\lambda_3 h_{b2}}})e^{l_{31}}e^{-\sqrt{\frac{h_{b3}}{\lambda_3}}d_2} + -s_3e^{-2d_2} + \frac{Q_{m3}}{h_{b3}} + s_2e^{-2d_2}$$
$$\left.-\frac{Q_{m2}}{h_{b2}} + 2\frac{\lambda_3}{\lambda_2}\sqrt{\frac{\lambda_2}{h_{b2}}}s_3e^{-2d_2} - 2\frac{\lambda_3}{\lambda_2}\sqrt{\frac{\lambda_2}{h_{b2}}}s_2e^{-2d_2}\right\} \quad \text{(F.12)}$$

$$A_2 = 0.5e^{\sqrt{\frac{h_{b2}}{\lambda_2}}d_2}[a_{21}B_3 + a_{22}] \quad \text{(F.13)}$$

$$B_2 = 0.5e^{-\sqrt{\frac{h_{b2}}{\lambda_2}}d_2}[b_{21}B_3 + b_{22}] \quad \text{(F.14)}$$

Adding and subtracting (5) and (6) will yield to equations (15) and (16) in which A_1 and B_1 are expressed through A_2 and B_2

$$A_1 = 0.5e^{\sqrt{\frac{h_{b1}}{\lambda_1}}d_1}\left[A_2(1+\sqrt{\frac{\lambda_1 h_{b2}}{\lambda_2 h_{b1}}})e^{-\sqrt{\frac{h_{b2}}{\lambda_2}}d_1} + B_2(1-\sqrt{\frac{\lambda_1 h_{b2}}{\lambda_2 h_{b1}}})e^{-\sqrt{\frac{h_{b2}}{\lambda_2}}d_1} -\right.$$
$$\left.s_2e^{-2d_1} + \frac{Q_{m2}}{h_{b2}} + s_1e^{-2d_1} - \frac{Q_{m1}}{h_{b1}} - 2\frac{\lambda_2}{\lambda_1}\sqrt{\frac{\lambda_1}{h_{b1}}}s_2e^{-2d_1} + 2\frac{\lambda_2}{\lambda_1}\sqrt{\frac{\lambda_1}{h_{b1}}}s_1e^{-2d_1}\right] \quad \text{(F.15)}$$

$$B_1 = 0.5e^{-\sqrt{\frac{h_{b1}}{\lambda_1}}d_1}\left[\left(1-\sqrt{\frac{\lambda_1 h_{b2}}{\lambda_2 h_{b1}}}\right)A_2\,e^{-\sqrt{\frac{h_{b2}}{\lambda_2}}d_1} + \left(1+\sqrt{\frac{\lambda_1 h_{b2}}{\lambda_2 h_{b1}}}\right)B_2\,e^{\sqrt{\frac{h_{b2}}{\lambda_2}}d_1} -\right.$$
$$\left.s_2e^{-2d_1} + \frac{Q_{m2}}{h_{b2}} + s_1e^{-2d_1} - \frac{Q_{m1}}{h_{b1}} + 2\frac{\lambda_2}{\lambda_1}\sqrt{\frac{\lambda_1}{h_{b1}}}s_2e^{-2d_1} - 2\frac{\lambda_2}{\lambda_1}\sqrt{\frac{\lambda_1}{h_{b1}}}s_1e^{-2d_1}\right] \quad \text{(F.16)}$$

Inserting (13) and (14) in (15) and (16), A_1 and B_1 are expressed through B_3. (17) and (18) can be written as (19) and (20).

$$A_1 = 0.5e^{\sqrt{\frac{h_{b1}}{\lambda_1}}d_1}\left\{B_3\left[b_{21}0.5(1-\sqrt{\frac{\lambda_1 h_{b2}}{\lambda_2 h_{b1}}})\,e^{-\sqrt{\frac{h_{b2}}{\lambda_2}}d_2}e^{-\sqrt{\frac{h_{b2}}{\lambda_2}}d_1} + a_{21}0.5(1+\right.\right.$$
$$\left.\left.\sqrt{\frac{\lambda_1 h_{b2}}{\lambda_2 h_{b1}}})\,e^{\sqrt{\frac{h_{b2}}{\lambda_2}}d_2}e^{-\sqrt{\frac{h_{b2}}{\lambda_2}}d_1}\right] + a_{22}0.5(1+\sqrt{\frac{\lambda_1 h_{b2}}{\lambda_2 h_{b1}}})\,e^{\sqrt{\frac{h_{b2}}{\lambda_2}}d_2}e^{-\sqrt{\frac{h_{b2}}{\lambda_2}}d_1} + \quad \text{(F.17)}$$

$$b_{22}0.5(1-\sqrt{\frac{\lambda_1 h_{b2}}{\lambda_2 h_{b1}}})\,e^{-\sqrt{\frac{h_{b2}}{\lambda_2}}d_2}e^{-\sqrt{\frac{h_{b2}}{\lambda_2}}d_1}-s_2e^{-2d_1}+\frac{Q_{m2}}{h_{b2}}+s_1e^{-2d_1}-\frac{Q_{m1}}{h_{b1}}-2\frac{\lambda_2}{\lambda_1}\sqrt{\frac{\lambda_1}{h_{b1}}}s_2e^{-2d_1}+2\frac{\lambda_2}{\lambda_1}\sqrt{\frac{\lambda_1}{h_{b1}}}s_1e^{-2d_1}\Bigg\}$$

$$B_1=0.5e^{-\sqrt{\frac{h_{b1}}{\lambda_1}}d_1}\Bigg\{\Bigg[b_{21}0.5e^{-\sqrt{\frac{h_{b2}}{\lambda_2}}d_2}(1+\sqrt{\frac{\lambda_1 h_{b2}}{\lambda_2 h_{b1}}})e^{-\sqrt{\frac{h_{b2}}{\lambda_2}}d_1}+0.5e^{\sqrt{\frac{h_{b2}}{\lambda_2}}d_2}(1-\sqrt{\frac{\lambda_1 h_{b2}}{\lambda_2 h_{b1}}})e^{-\sqrt{\frac{h_{b2}}{\lambda_2}}d_1}a_{21}\Bigg]B_3+0.5e^{\sqrt{\frac{h_{b2}}{\lambda_2}}d_2}(1-\sqrt{\frac{\lambda_1 h_{b2}}{\lambda_2 h_{b1}}})e^{-\sqrt{\frac{h_{b2}}{\lambda_2}}d_1}a_{22}+0.5e^{-\sqrt{\frac{h_{b2}}{\lambda_2}}d_2}(1+\sqrt{\frac{\lambda_1 h_{b2}}{\lambda_2 h_{b1}}})e^{-\sqrt{\frac{h_{b2}}{\lambda_2}}d_1}b_{22}-s_2e^{-2d_1}+\frac{Q_{m2}}{h_{b2}}+s_1e^{-2d_1}-\frac{Q_{m1}}{h_{b1}}+2\frac{\lambda_2}{\lambda_1}\sqrt{\frac{\lambda_1}{h_{b1}}}s_2e^{-2d_1}-2\frac{\lambda_2}{\lambda_1}\sqrt{\frac{\lambda_1}{h_{b1}}}s_1e^{-2d_1}\Bigg\} \tag{F.18}$$

$$A_1=0.5e^{\sqrt{\frac{h_{b1}}{\lambda_1}}d_1}\{a_{11}\,B_3+a_{12}\} \tag{F.19}$$

$$B_1=0.5e^{-\sqrt{\frac{h_{b1}}{\lambda_1}}d_1}\{b_{11}B_3+b_{12}\} \tag{F.20}$$

Using (8), (19) and (20) B_3 is obtained. With B_3 known $A_3, A_2, B_2, A_1, and\ B_1$ can be obtained using (2), (13), (14), (19) and (20).

$$B_3=\frac{-a_{12}0.5e^{\sqrt{\frac{h_{b1}}{\lambda_1}}d_1}+0.5c_1b_{12}e^{-\sqrt{\frac{h_{b1}}{\lambda_1}}d_1}+c_2\left(-s_1+\frac{Q_{m1}}{h_{b1}}+T_a-T_{air}\right)+\frac{2\lambda_1c_2s_1}{h}}{\left(0.5a_{11}e^{\sqrt{\frac{h_{b1}}{\lambda_1}}d_1}-0.5b_{11}c_1e^{-\sqrt{\frac{h_{b1}}{\lambda_1}}d_1}\right)} \tag{F.21}$$